Ford/BASF/UM Activities in Support of the Hydrogen Storage Engineering Center of Excellence

Agency:	Department of Energy Office of Energy and Renewable Energy (DOE-EERE) Fuel Cell Technologies Office
DOE Managers:	Jesse Adams, DOE Technology Manager Ned Stetson, Hydrogen Storage Program Manager
DOE Contract Number:	DE-FC36-GO19002
Project Start Date:	February 1, 2009
Project End Date:	June 30, 2015
Prime Contractor:	Ford Motor Company 1201 Village Road Dearborn, MI 48124
Principal Investigator:	Mike Veenstra 313-322-3148 mveenstr@ford.com
Contract Manager:	Melissa Hendra 313-594-4714 mhendra@ford.com
Subcontractors:	University of Michigan (UM), Ann Arbor, MI BASF SE, Ludwigshafen, Germany
Contributors:	Mike Veenstra (PI-Ford), Justin Purewal (Ford), Chunchuan Xu (Ford), Jun Yang (Ford), Rachel Blaser (Ford), and Andreas Sudik (Ford), Don Siegel (UM), Yang Ming (UM), Dong'an Liu (UM), Hang Chi (UM), Manuela Gaab (BASF), Lena Arnold (BASF), and Ulrich Muller (BASF)

Table of Contents

1.0 Executive Summary

Widespread adoption of hydrogen as a vehicular fuel depends critically on the development of low-cost, on-board hydrogen storage technologies capable of achieving high energy densities and fast kinetics for hydrogen uptake and release. As present-day technologies -- which rely on physical storage methods such as compressed hydrogen -- are incapable of attaining established Department of Energy (DOE) targets, development of materials-based approaches for storing hydrogen have garnered increasing attention. Material-based storage technologies have potential to store hydrogen beyond twice the density of liquid hydrogen. To hasten development of these 'hydride' materials, the DOE previously established three centers of excellence for materials storage R&D associated with the key classes of materials: metal hydrides, chemical hydrogen, and adsorbents. While these centers made progress in identifying new storage materials, the challenges associated with the engineering of the system around a candidate storage material are in need of further advancement.

In 2009 the DOE established the Hydrogen Storage Engineering Center of Excellence with the objective of developing innovative engineering concepts for materials-based hydrogen storage systems. The HSECoE was led by Savannah River National Laboratory and involved many other organizations: Pacific Northwest National Lab, Los Alamos National Lab, National Renewable Energy Lab, Jet Propulsion Lab, University of Michigan, Oregon State University, University of Quebec at Trois-Rivieres, United Technologies Research Center, BASF, Hexagon Lincoln, General Motors, and Ford Motor Company.

As a partner in the Hydrogen Storage Engineering Center of Excellence, the Ford-UM-BASF team conducted a multi-faceted research program that addresses key engineering challenges associated with the development of materials-based hydrogen storage systems. First, we developed a novel framework that allowed for a material-based hydrogen storage system to be modeled and operated within a virtual fuel cell vehicle. This effort resulted in the ability to assess dynamic operating parameters and interactions between the storage system and fuel cell power plant, including the evaluation of performance throughout various drive cycles. Second, we engaged in cost modeling of various incarnations of the storage systems. This analysis revealed cost gaps and opportunities that identified a storage system that was lower cost than a 700 bar compressed system. Finally, we led the HSECoE efforts devoted to characterizing and enhancing metal organic framework (MOF) storage materials.

The most noteworthy outcomes of the Ford-UM-BASF project are summarized below:

- Demonstrated MOF-5 as a promising adsorbent material, exceeding activated carbon (MSC-30)
- Successfully scaled lab-quantity synthesis to produce 10 kg of MOF-5 with uncompromised storage performance
- Optimized the compaction of MOF-5 without a binder to increase volumetric storage
- Improved thermal conductivity by 40x via various processing and anisotropic features along with expanded natural graphite layers
- Confirmed transport kinetics through a compacted MOF-5 adsorbent bed are capable for rapid refueling
- Observed MOF-5 is more robust than commonly thought to humid conditions and hydrogen impurities
- Identified with high-throughput computational screening, several adsorbents with promising properties beyond MOF-5, achieving projected densities of 12.4 wt % and 71.4 g/L with the promise of exceeding 700 bar hydrogen systems

This report serves as a final documentation of the Ford-UM-BASF project contributions to the HSECoE during the 6-year timeframe of the Center. The activities of the HSECoE have impacted the broader goals of the DOE-EERE and USDRIVE, leading to improved understanding in the engineering of materials-based hydrogen storage systems. This knowledge is a prerequisite to the development of a commercially-viable hydrogen storage system.

2.0 Introduction

2.1 Background

In October 2008, DOE announced the selection of a new Hydrogen Storage Engineering Center of Excellence in response to Funding Opportunity Announcement DE-PS36-08GO98006. The team was led by Savannah River National Laboratory and consisted of ten partners that included universities, industry and federal laboratories. DOE officially started the HSECoE in 2009 which was anticipated to run for approximately 5 years. It was formed to support the President's Advanced Energy Initiative to reduce our nation's dependence on foreign energy sources by changing the way we power our cars, homes, and businesses. The selected team had the objective to address the significant engineering challenges associated with developing low-pressure, materials-based hydrogen storage systems that will enable fuel cell vehicles to meet customer expectations for driving range and performance. The HSECoE was part of the DOE's National Hydrogen Storage Project, which focused on hydrogen storage materials development. The team leads selected for the HSECoE were:

- Savannah River National Laboratory (Center Lead), Aiken, South Carolina
- Pacific Northwest National Laboratory, Richland, Washington
- United Technologies Research Center, East Hartford, Connecticut
- Los Alamos National Laboratory, Los Alamos, New Mexico
- NASA Jet Propulsion Laboratory, Pasadena, California
- National Renewable Energy Laboratory, Golden, Colorado
- General Motors Corporation, Warren, Michigan
- Ford Motor Company, Dearborn, Michigan
- Oregon State University, Corvallis, Oregon
- Lincoln Composites Inc., Lincoln, Nebraska

As a partner in the Hydrogen Storage Engineering Center of Excellence, the Ford-UM-BASF team conducted a multi-faceted research program that addresses key engineering challenges associated with the development of materials-based hydrogen storage systems, which was organized around the following three tasks:

Task 1: Systems Modeling: Drawing on our extensive expertise in the engineering of fuel cell (FC) and H2-ICE vehicles, we have evaluated and developed system engineering elements with a focus on hydrogen storage system operating parameters. This effort contributed to the creation of a set of dynamic operating parameters and a high-level system model describing the interaction of the fuel storage system with the FC (or H2-ICE) power plant. National Renewable Energy Laboratory and United Technologies Research Center were the leads within the HSECoE for the system modeling analysis and the results along with the contribution from this project can be found in their respective final reports and publications in section 9.

Task 2: Cost Analysis: The unique capabilities of Ford's cost estimating were leveraged to develop and perform hydrogen storage manufacturing cost analyses for various candidate system configurations and operating strategies. This analysis facilitated a technology roadmap for potential cost reductions and manufacturing optimization, while providing important feedback to go/no-go decisions on prototype design and construction. Pacific Northwest National Laboratory was the lead within the HSECoE for the cost analysis and the results along with the contribution from this project can be found in their respective final report.

Task 3: Sorbent Media Assessment & Optimization: We evaluated and optimized the "effective engineering properties" of an important class of sorbent materials known as metal organic frameworks (MOFs) in order to devise improved packing and processing strategies for their use in a storage system. Various mechanical processing routes were examined (ranging from powders to pelletization to extrusion) in an effort to simultaneously maximize packing density, heat and mass transfer, and hydrogen uptake

characteristics. Ford-UM-BASF was the lead within the HSECoE for the sorbent media assessment and optimization. The results and outcome from this task are the focus of this final report.

Since the Ford-UM-BASF team had a significant effort on the adsorbent media, the background and outcomes of this work are summarized below:

Comprehensive characterization of MOF-5 properties: MOFs are a relatively new class of compounds; the first widely cited report focusing on MOFs appeared around the turn of the century. Since that time most MOF-related research has focused on small-scale synthesis of new compositions. Characterization efforts have largely focused on structure analysis, and to a lesser extent, on gas uptake properties. For practical applications, such as in the gas storage systems investigated by the Center, "engineering properties" of the MOF are highly important, yet often overlooked. A major contribution of the Ford-UM-BASF team has been the detailed characterization of several of these properties. We have performed a comprehensive assessment of the primary thermo-physical properties of MOF-5 powders. Characterized properties include:

Thermophysical phenomena: packing density, surface area, pore volume, particle size distribution, and differential enthalpy of H_2 adsorption. In addition, several varieties of hydrogen isotherm models (Unilan, Tóth, Dubinin−Astakhov) were compared for their effectiveness in describing hydrogen adsorption isotherms, which were measured at six temperatures spanning the range 77–295 K, and at pressures of 0–100 bar.

Transport properties: H_2 gas permeation rates, heat capacity, and thermal conductivity. In the latter case, effort was devoted to measuring heat transport at relevant operating temperatures spanning 77 to 300 K, and to assess anisotropies induced by pelletization via uniaxial compression.

Robustness: stability with respect to humidity/water vapor and impurities in the hydrogen fuel stream stability against hydrolysis.

Although some of the characterized properties have been previously reported for laboratory-scale (i.e., small) quantities of MOF-5, variations arising from differences in MOF synthesis and activation pose challenges to achieving a consistent description of these properties. The present study minimized these inconsistencies by analyzing an industrial, pilot-scale version of MOF-5. Consequently, the data should provide a reasonable approximation to the properties expected in industrial applications.

Densification, augmentation, and scale up of MOF-5: MOF-5 is typically obtained as a bulk powder; in this form it exhibits low volumetric density and poor thermal conductivity, both of which are undesirable characteristics for a hydrogen storage material. To improve its thermal and volumetric performance, a series of high-density MOF-5 composites containing 0−10 wt. %expanded natural graphite (ENG, a thermal conduction enhancer) were prepared. Unlike other densified powders, no binders were needed to achieve robust, free-standing pellets. The addition of 10 wt. % ENG to MOF-5 and compaction to 0.5 g/cm^3 was found to increase the thermal conductivity relative to neatMOF-5 of the same density by a factor of 5. Detailed measurements of the hydrogen storage behavior of MOF-5/ENG compositesbetween 77 and 295 K were performed. MOF-5 pellets with 0 wt. % ENG and a density of 0.5 g/cm^3 have a total volumetric hydrogen storage density at 77 K and 100 bar that is 23% larger than powder MOF-5, and 41%larger than cryo-compressed hydrogen. The addition of 10% ENG to 0.5 g/cm3MOF-5 pellets produces only a small decrease (6%) in the total volumetric hydrogen storage compared to neat MOF-5 pellets of equal density.

As previously mentioned, uniaxially compressed MOF-5 pellets exhibit anisotropic thermal transport that is two to four times higher in directions perpendicular to the pressing direction. We demonstrated that this anisotropy can be exploited using two processing techniques. First, a custom die and densification process allowed for reorientation of the preferred heat flow pathway. Second, a layered MOF-5/ENG microstructure increased the thermal conductivity by an order of magnitude, with only minor ENG additions (5 wt.%). These results reveal

that anisotropic thermal transport in MOF composites can be tailored using a judicious combination of second phase additions and processing techniques.

Finally, demonstration of a MOF-5-based prototype relies upon the availability of sufficient quantities of adsorbent media. Indeed, the primary objective of the Center's Third Phase is the construction and evaluation of such a system. Towards this goal, Center partner BASF successfully scaled up its synthesis procedure for MOF-5. Nearly 10 kg of MOF-5 was delivered to the HSECoE for use in the Hex-Cell and MATI prototypes. The performance of the powder was assessed using hydrogen uptake and surface areas measurements, and was found to at least equal the performance of smaller-scale batches.

High-throughput screening of MOF adsorbents: Because of their high surface areas and widely tunable properties, metal−organic frameworks (MOFs) have attracted intense interest as next-generationmaterials for gas capture and storage. Based on available, but limited data, the HSECoE selected MOF-5 as the hydrogen storage medium to be demonstrated in prototype storage systems. Nevertheless, a vast catalog of existing MOFs resides within the CambridgeStructural Database (CSD), many of whose gas uptake properties have not beenassessed. An important question is then: "Do any MOFs exist that out-perform MOF-5?"

To answer this question, this activity employed data mining and automated structure analysis to identify, "cleanup," and rapidly predict the hydrogen storage properties of these compounds.Approximately 20,000 candidate compounds were generated from the CSD using analgorithm that removes solvent/guest molecules. These compounds were thencharacterized with respect to their surface area and porosity. Employing the empirical relationship between excess H_2 uptake and surface area, we predicted the theoretical total hydrogen storage capacity for the subset of ~4,000 compounds exhibiting nontrivial internal porosity.

Our screening revealed that MOF-5 is one of the best, but not the best, hydrogen adsorbent. In particular, several overlooked compounds having high theoretical capacities were identified; these compounds were suggested as targets of opportunity for additional experimental characterization. In addition, screening revealed that the relationship between gravimetric and volumetric H_2 density is concave downward, with maximal volumetric performance occurring for surface areas of 3100−4800 m^2/g. This study showed that H_2 storage in MOFs will not benefit from further improvements in surface area alone. Rather, discovery efforts should aim to achieve moderate mass densities and surface areas simultaneously, while ensuring framework stability upon solvent removal.

Center Leadership: Although not specifically associated with Tasks 1-3, the Ford-UM-BASF team also contributed to the success of the HSECoE by assuming important leadership roles. During Phase 1, Sudik led the Materials Operating Requirements team. Siegel assumed the role of System Architect (SA) for the Adsorbent System shortly before the transition from Phase 1 to 2, and remained in this role until the conclusion of the Center (~4 years). The SA is responsible for all Center activities associated with the development of the adsorbent-based storage systems. Finally, Veenstra served in several critical roles, including: provided an automotive perspective, acted as liaison to U.S. DRIVE hydrogen storage tech team, integrated fuel cell model in the modeling framework, lead in target prioritization , contributed to the cost analysis, and coordinated FMEA along with the design verification plan.

2.2 HSECoE Technical Target Prioritization

As previously indicated, the HSECoE objective was to develop material-based system architectures with the potential to meet the DOE USDRIVE performance and cost targets. As shown in Figure 2.2(1), these targets include about 20 different storage parameters ranging from physical attributes (e.g. weight and volume), cost, durability/operability, charging/discharging rates, fuel purity, and safety criteria.

DOE Targets for Onboard Hydrogen Storage Systems for Light-Duty Vehicles

Table 2 Technical Targets: Onboard Hydrogen Storage Systems

Storage Parameter	Units	2010	2017	Ultimate
System Gravimetric Capacity: Usable, specific-energy from H_2 (net useful energy/max system mass) [a]	kWh/kg (kg H_2/kg system)	1.5 (0.045)	1.8 (0.055)	2.5 (0.075)
System Volumetric Capacity: Usable energy density from H_2 (net useful energy/max system volume)	kWh/L (kg H_2/L system)	0.9 (0.028)	1.3 (0.040)	2.3 (0.070)
Storage System Cost [b]:	$/kWh net ($/kg H_2)	TBD (TBD)	TBD (TBD)	TBD (TBD)
• Fuel cost [c]	$/gge at pump	3-7	2-4	2-4
Durability/Operability:				
• Operating ambient temperature [d]	°C	-30/50 (sun)	-40/60 (sun)	-40/60 (sun)
• Min/max delivery temperature	°C	-40/85	-40/85	-40/85
• Operational cycle life (1/4 tank to full) [e]	Cycles	1000	1500	1500
• Min delivery pressure from storage system; FC= fuel cell, ICE= internal combustion engine	bar (abs)	5 FC/35 ICE	5 FC/35 ICE	3 FC/35 ICE
• Max delivery pressure from storage system [f]	bar (abs)	12 FC/100 ICE	12 FC/100 ICE	12 FC/100 ICE
• Onboard Efficiency	%	90	90	90
• "Well" to Powerplant Efficiency	%	60	60	60
Charging / Discharging Rates:				
• System fill time (5 kg)	min (kg H_2/min)	4.2 (1.2)	3.3 (1.5)	2.5 (2.0)
• Minimum full flow rate	(g/s)/kW	0.02	0.02	0.02
• Start time to full flow (20°C) [g]	s	5	5	5
• Start time to full flow (-20°C) [g]	s	15	15	15
• Transient response 10%-90% and 90% - 0% [h]	s	0.75	0.75	0.75
Fuel Purity (H_2 from storage) [i]:	% H_2	SAE J2719 and ISO/PDTS 14687-2 (99.97% dry basis)		
Environmental Health & Safety:				
• Permeation & leakage [j]	Scc/h			
• Toxicity	-	Meets or exceeds applicable standards		
• Safety	-			
• Loss of useable H_2 [k]	(g/h)kg H_2 stored	0.1	0.05	0.05

Useful constants: 0.2778 kWh/MJ; 33.3 kWh/kg H_2; 1 kg H_2 ≈ 1 gal gasoline equivalent.

Figure 2.2(1): DOE U.S. DRIVE hydrogen storage system targets for Light-Duty Vehicles

The HSECoE recognized that many of the system designs required trade-offs between these many parameters and requested the OEMs to assist in the prioritization of the hydrogen storage targets. The Ford team took the leadership role to brainstorm methods and organized the classification approach. After consideration, the decision was to use a quality function deployment (QFD) method since this tool provides an organized structure for assessing the targets using OEM system engineering disciplines.

The QFD follows the system engineering approach which links the customer musts/wants to the system requirements/targets. The QFD identifies the priorities of the customer attributes and then ranks the relationships of the system targets to the customer attributes. The cause-effect relationships linking the customer and system attributes used a 1 (low effect), 3, 6, 9 (high effect) scale by evaluating the change in the vehicle attribute based on a 40% reduced target. The priority of the customer attributes utilized the analytic hierarchy process (AHP), which uses a series of pairwise comparison judgments to express the relative strength or impact of the element compared to another. The resulting classification values were a product of the cause-effect rankings and AHP

values. In addition, the OEMs recognized that certain parameters are musts (required for basic function) such as safety and certain performance items (e.g. delivery pressures and temperatures to the fuel cell).

The first results of target classification provided some initial observations, but were limited in usefulness since the approach was formulated based on the DOE phase 1 milestone criteria that allowed a hydrogen storage system to meet a 40% target level. Therefore, this ranking approach is only valid to a 40% lower limit of the existing DOE target. When considering this assumption, certain targets were relatively immune to a 40% setting of the value. In addition, the initial target classification was based strictly on a subjective scale for the cause-effect relationships that was unable to provide enough fidelity in assessing the effects of certain parameters such as the gravimetric and volumetric density.

Due to the limitations of the first target classification approach, a second target classification effort was pursued in order to refine the cause-effect rankings between the vehicle and system using models with the goal of developing a utility function to assist in trade-off studies. The refined target prioritization approach still utilized the Quality Function Deployment (QFD) tool. In the previous analysis, the OEMs established the vehicle attribute ratings using an Analytic Hierarchy Process (AHP) which establishes the customer importance of certain vehicle attributes. The refined prioritization used the same AHP values as the original analysis as shown in Figure 2.2(2).

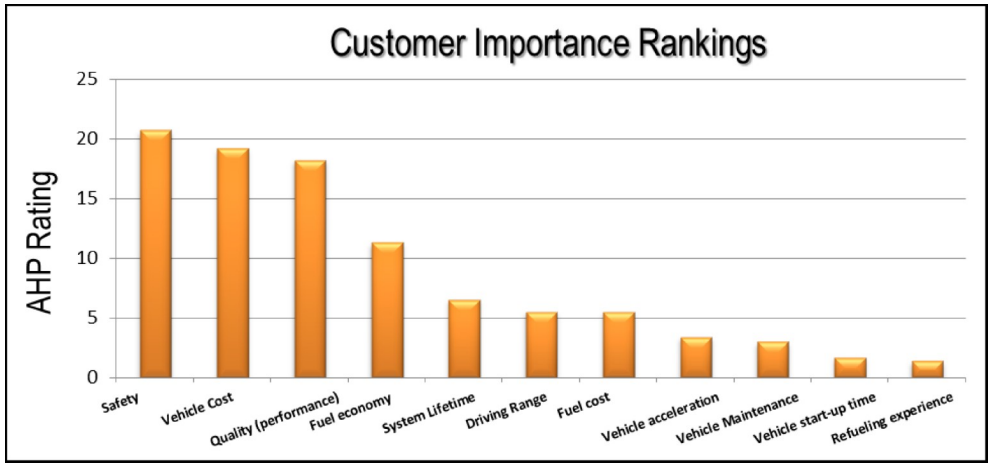

Figure 2.2(2): Vehicle Attribute Ratings based on original Analytic Hierarchy Process

The key difference to this new approach is determination of the linkage between the vehicle attributes and the storage system targets. Previously, a subjective scale was used to identify the relationship between the system targets and vehicle attributes. The deficiency of this previous approach was the cause-effect relationship scale was highly subjective and based on a 40% level of the targets for 2010 (50% level of the targets for 2015) for a specific milestone criteria. The static level does not effectively allow for the development of a continuous objective function. Also, the HSECoE has the Simulink framework that can be utilized to quantify the linkage of the system level targets rather than using the subjective scale. As indicated, the refined analysis utilized the HSECoE Simulink framework to evaluate the changes in the vehicle attributes due to modifying the 2017 targets by +/- 10% increments.

The key system targets that were analyzed based on a brainstorming discussion were the *gravimetric density*, *volumetric density*, and *system cost*. Another important target was the system efficiency but the team believed this was captured within the usable hydrogen ratios within these other parameters. The vehicle attribute (i.e. driving range, fuel economy, etc.) effects were analyzed while varying the system from the specified target values. Since this was a theoretical exercise rather than based on a particular system, it was assumed that only the specific target being analyzed was changing while the other target value remained consistent, such as for the gravimetric case which assumed volumetric remained constant. Figure 2.2.(3) provides examples for the gravimetric case for driving range and fuel economy effects on the left and the volumetric case for driving range on the right. The volumetric case assumed a constrained volume which resulted in the volumetric ratio having a direct impact on driving range. As a result of this analysis, the volumetric energy density can be clearly shown as

having a higher impact to the vehicle driving range than the gravimetric energy density. This general refined analysis was discussed and agreed by the USDRIVE Hydrogen Storage Tech Team.

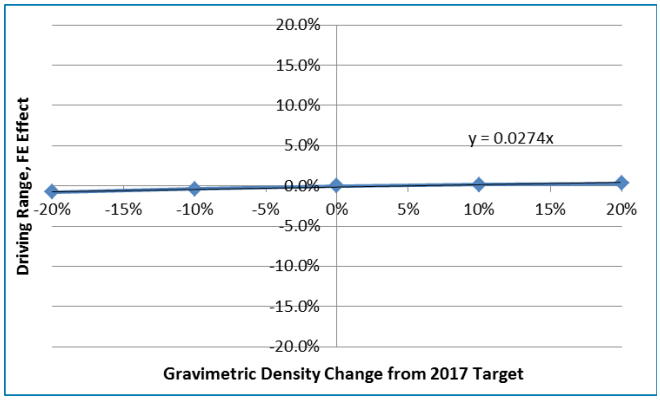

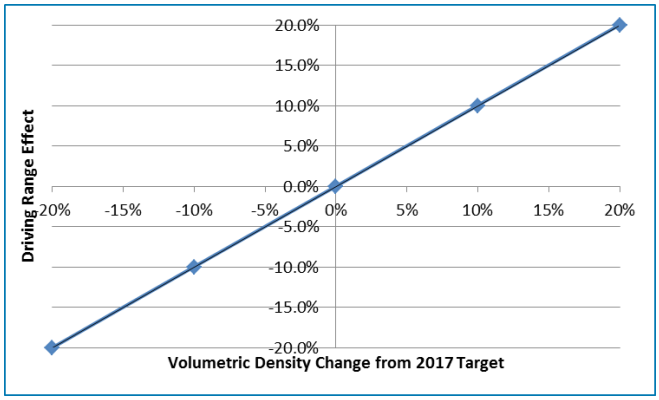

Figure 2.3(3): Refined analysis of system target effects with a gravimetric density case (left) and the volumetric density case (right) in relationship to driving range (and fuel economy).

The final step for determining an objective function was to develop an expression that utilized the percent change from the target values, the customer importance factor, and the correlation slope from the models. The objective function provides a methodology to evaluate the various system designs in a normalized manner and facilitates trade-offs between gravimetric density, volumetric density, and system cost. Figure 2.2(3) provides the calculation overview based on achieving the 2017 target with a system design which produces a system rating of 9.8 or 100% in comparison to the desired target. For comparison, a 700 bar system with 1.5 kWh/kg, $17/kWh, 0.9 kWh/l would have a system rating of 6.7 or 70 %.

System Projections (input variables):

System GD:	**1.8**	**kWh/kg**
System Cost:	**12**	**$/kWh**
System VD:	**1.3**	**kWh/l**

System Rating: **100%** = Gs + Cs + Vs note: normalized based on 100% of 2017 targets

Grav Score (Gs): 1.4 = I_{FE} x C_{GFE} x $S_{GD\%}$ + I_{DR} x C_{GDR} x $S_{GD\%}$ + I_{VA} x CGV_A x $S_{GD\%}$ + I_{VC} x C_{GVC} x $S_{GD\%}$

Cost Score (Cs): 2.9 = I_{VC} x C_{CVC} x $S_{C\%}$

Vol. Score (Vs): 5.5 = I_{DR} x C_{VDR} x $S_{VD\%}$

$S_{GD\%}$	**100%**	= % gravimetric density system target from 2017 target
$S_{C\%}$	**100%**	= % system cost target from 2017 target
$S_{VD\%}$	**100%**	= % volumetric density system target from 2017 target

I_{FE}	**11.3** = importance rating for fuel economy (vehicle level)
I_{DR}	**5.5** = importance rating for driving range (vehicle level)
I_{VA}	**3.4** = importance rating for vehicle acceleration (vehicle level)
I_{VC}	**19.2** = importance rating for vehicle cost (vehicle level)

C_{GFE}	**0.03** = correlation % change in gravimetric density for fuel economy (% system to % vehicle)
C_{GDR}	**0.03** = correlation % change in gravimetric density for driving range (% system to % vehicle)
C_{GVA}	**0.04** = correlation % change in gravimetric density for vehicle acceleration (% system to % vehicle)
C_{GVC}	**0.04** = correlation % change in gravimetric density for vehicle cost (% system to % vehicle)
C_{CVC}	**0.15** = correlation % change in cost for vehicle cost (% system to % vehicle)
C_{VDR}	**1** = correlation % change in volumetric density for driving range (% system to % vehicle)

Figure 2.2(3): Target prioritization objective function for normalized comparisons with 2017 targets.

3.0 Adsorbent System Designs

In Phase 3 HSECoE partners built and tested two MOF-5-based hydrogen storage systems, the so-called 'Hex-cell' system and the 'MATI' system. Schematics of the storage vessel components of these systems are shown in Fig. 3.0(1); an example of a full system layout is given in Fig. 3.0(2). Both systems use a Type I (aluminum) pressure vessel with a maximum working pressure of 100 bar. The relatively low operating pressure of an adsorbent-based system allows for use of a lower-cost metallic vessel. This approach differs from the higher-cost Type 3 or Type 4 composite vessels used to store compressed H_2 at 350 and 700 bar.

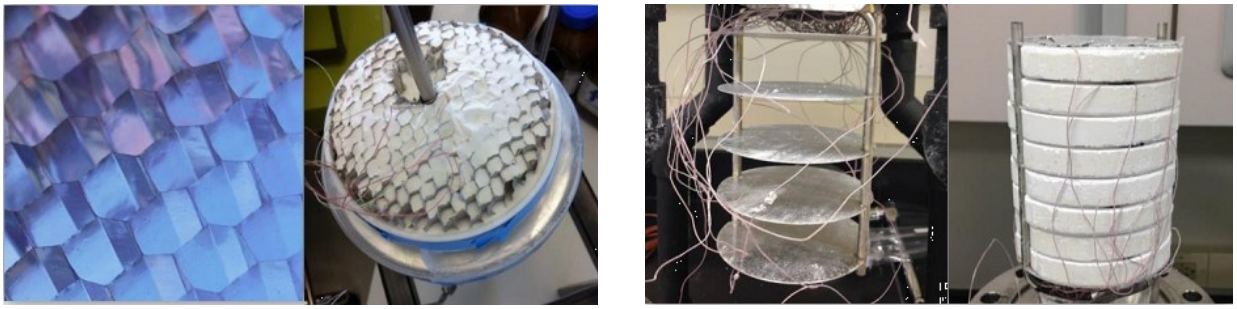

Fig 3.0(1): Photographs of the two prototype hydrogen storage systems. (Left) Hex-cell prototype, showing magnified view of hexagonal-cells of the heat exchanging manifold and top-view of the manifold filled with MOF-5 powder. The vertical rod in the center of the manifold is the resistive heating element. (Right) MATI prototype, showing the empty manifold and the manifold loaded with 8 MOF-5 pucks.

Although the Ford-UM-BASF team was not directly involved in the construction of these systems, the team was heavily involved in the characterization and optimization of the MOF-5 media, as well as with the development of system-level performance models and cost estimates associated with these prototypes. To facilitate subsequent discussion, here we briefly introduce the fundamental aspects of these systems.

Hex-cell system: The Hex-cell system uses a flow-through strategy for cooling during fueling. More specifically, pressurized cryogenic H_2 gas (nominal temperature, 77 K) is inserted into the top of the storage vessel and used to convectively cool the system as it passes over the MOF-5 storage medium. The gas is warmed as some portion of the H_2 adsorbs during fueling; finally the gas leaves the system through an outlet at the opposite end of the vessel. The adsorbent is employed in a powder form to facilitate permeation of the cold H_2. This powder is packed into the cells of an aluminum heat-exchanging manifold assembled in a honeycomb structure. The hexagonal cells of the manifold are aligned along the axial direction of the cylindrical storage vessel. Hydrogen can be liberated during vehicle operation using a pressure swing or via a combined temperature/pressure swing. In the latter case, heat is added to the vessel by way of a resistive heating rod. This rod is positioned at the center of the vessel; the metallic heat exchanger allows for heat produced by the rod to be transmitted throughout the vessel via conduction. The nominal operating range for this system is from 0 to 100 bar and 77 to ~160 K. The simple design of the heat exchanger, combined with the possibility of using an "off the shelf" heating rod, suggest that the Hex-cell system may be advantageous from a cost perspective.

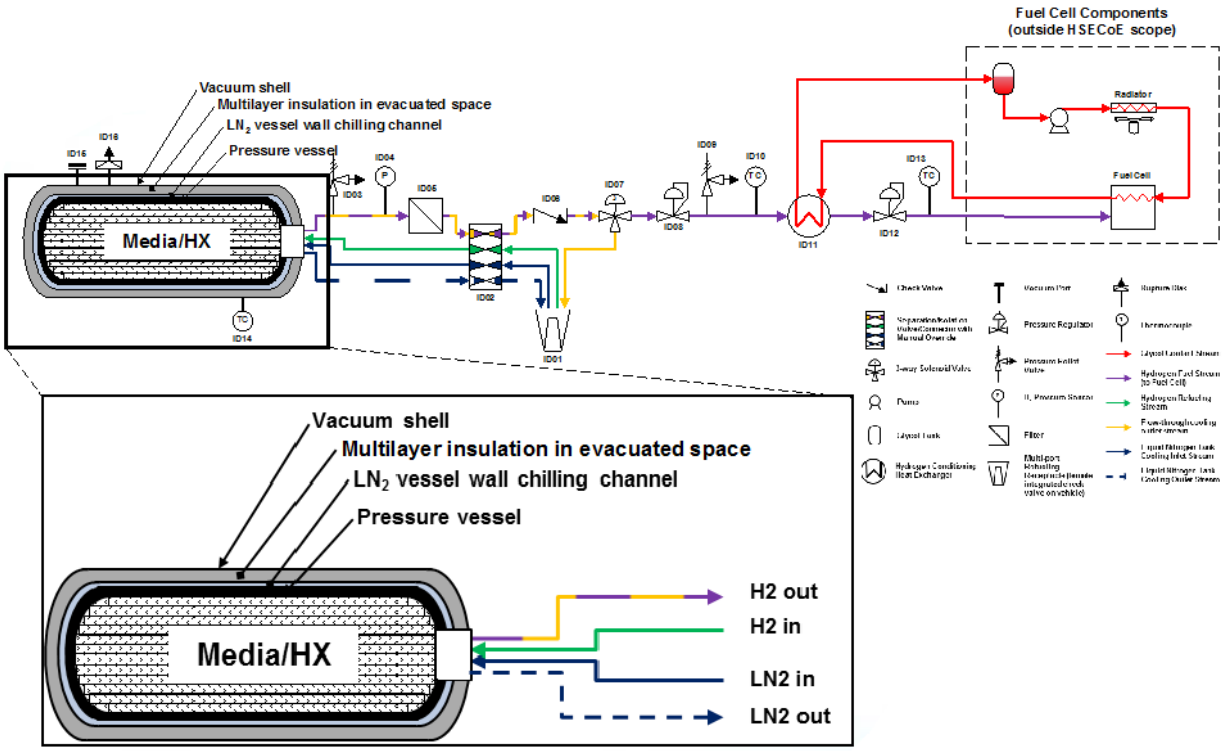

Fig. 3.0(2): Schematic of the layout for a MOF-5-based hydrogen storage system. (Adapted from D. Anton, AMR 2015.)

MATI system: The so-called MATI system derives its name from its distinctive heat exchanger, a Modular Adsorption Tank Insert. This system is distinguished from the Hex-cell in two fundamental ways: first, it uses densified MOF-5 pucks (rather than powder) as the storage medium; second, it relies on conductive heat exchange with a flowing, but isolated working fluid (rather than convection). During fueling, liquid nitrogen flows across parallel cooling plates positioned between stacked MOF-5 pucks. Meanwhile, a separate, but interleaved set of plates distributes the hydrogen gas. As with the Hex-cell system, desorption can be triggered with a pressure swing, or via a pressure/temperature swing. In the latter case warm hydrogen (heated using an external burner) is circulated through the heat exchanger. Operating conditions (temperature, pressure) for the MATI are also similar to those of the Hex-cell. Advantages of the MATI system include higher volumetric density (due to the use of densified MOF-5), and more efficient refueling (due to the controlled nature of the coolant flow). On the other hand, the more complex design of the MATI suggests that it will be the more expensive of the two options.

4.0 FMEA

Based on the system engineering disciplines, the HSECoE completed the formulation of Design Failure Mode Analysis (FMEA) for the adsorbent and chemical hydride systems. This effort was led by Ford but was certainly a team effort over multiple meetings including face-to-face discussions. The FMEA is a recognized tool by the OEMs used to identify potential failure modes related to the primary system functions and interfaces. In addition to failure mode identification, OEMs recognize the FMEA can assist in prioritizing potential risk, improving system designs, and guiding the validation test plan. The HSECoE also acknowledged these benefits and desired to ensure the design was robust and the testing covered the potential failure modes.

The industry has a standardized process for completing a FMEA as defined in SAE J1739. The based approach is shown in Figure 4.0(1). The FMEA consists of three main steps which are the following: identification of failure modes along with their severity rating, brainstorming potential causes along with their occurrence rating, and document the current controls along with their detection ratings.

Item/Function	Potential Failure Mode	Potential Effect(s) of Failure	Sev	Class	Potential Cause/ Mechanism of Failure	Occ	Current Controls	Det	RPN	Recommended Action	Responsibility and Target Completion Date	Action Results				
												Actions Taken	S	O	D	RPN
What are the Functions, Features, or Requirements? List in Verb-Noun-Metric format	What can go wrong? - No Function - Partial, Over, Under Funtion - Intermittent Funtion - Unintended Funtion	**STEP 1** What are the Effect(s)?	How bad is it?		**STEP 2** What are the Cause(s)?	How often does it happen?	**STEP 3** How can this be prevented or detected?	How good is the method at detecting it?		What can be done? - Design Changes - Process Changes - Additional Testing - Special Analysis - Revise Standards or Procedures or Test Plans						

Figure 4.0(1): Overview of the FMEA form and the multiple step approach.

The functions within the FMEA were directly aligned with the DOE U.S. DRIVE system targets and the effects along with the severity (1-10 scale from best to worst) were completed based on prior OEM assessment. The potential failure modes were determined as the anti-functions. The critical step is the identification of the causes for the failure modes and occurrence rankings (1-10 scale from best to worst) or chance the cause would occur. The HSECoE adsorbent and chemical hydrogen teams evaluated their respective designs and documented these causes and rankings. For the adsorbent system (included MATI and HexCell), a total of 109 potential causes were identified and ranked by the adsorbent team. Next, the teams evaluated their current tests in the design control column and determined the detection ranking (1-10 scale from best to worst) based on how effective the planned tests will be in detecting the cause of failure. In some cases, the team discovered the HSECoE didn't have a test in the current plan to address a certain cause of failure which resulted in the worst case rating of 10. The result of the FMEA was the development of the Risk Priority Number (RPN) which is the product of the severity, occurrence, and detection ratings. The RPN number allows the team to identify the highest potential risks of failure modes. Figure 4.0(2) provides a graphical Pareto summary of the RPN ratings after the first version of the adsorbent system FMEA in phase 1.

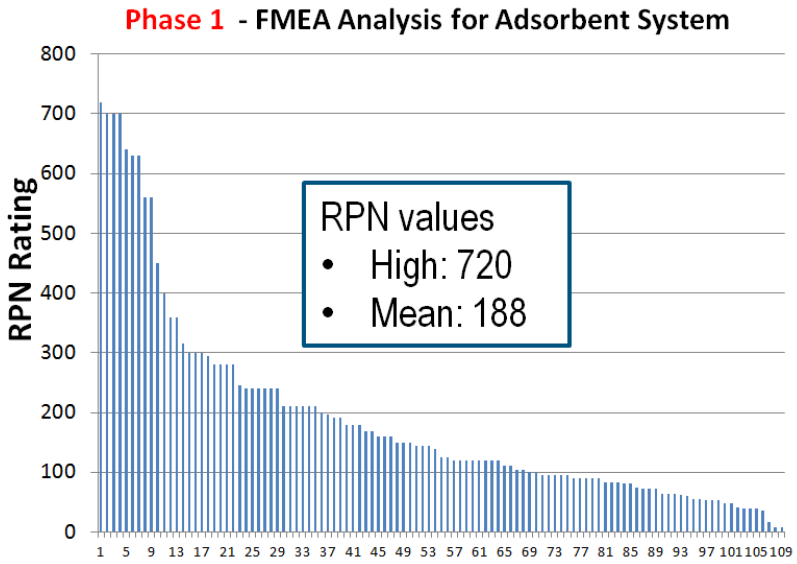

Figure 4.0(2): Adsorbent FMEA in-process Pareto chart of RPNs

The relative ranking allows the team to visualize that there are clearly some failure modes that have higher risk than others. Some of these high RPN rankings are directly related to a lack of a defined test to assess a certain cause. As a result, several action items were documented to assist in reducing the risks by either defining a test or modifying the design to reduce the RPN values. The highest grouping of RPNs from 720 to 400 is shown in Figure 4.0(3).

Potential Cause	Failure Mode (RPN)	Actions
Material release rate insufficient due to non-homogenous materials at end of life	Hydrogen supply unable to achieve full flow rate (720) Storage system only accepts partial fill (630) Storage system on-board efficiency < 90% (560) System only supplies partial capacity (560) Storage system fills in > 3.3 minutes (450)	Consider a vibration test Need to evaluate bed packing metric Use system models to evaluate sensitivity of contact resistance
Type IV tank liner incompatible with adsorbent or in-service activation	System unable to contain hydrogen due to component rupture (700) System exceeds allowable external leak rate limit (700)	Need to discuss a in-service process and evaluate the HDPE out-gassing
Material release rate insufficient due to impurities (from station at single time or lifetime)	Hydrogen supply unable to achieve full flow rate (640) Storage system only accepts partial fill (560) Storage system fills in > 3.3 minutes (400)	Consider adding a cycle test with spec hydrogen at the limits of J2719
Fuel cell system requires higher delivery pressure at same temperature	System only supplies partial capacity (560)	Need to confirm with the fuel cell tech team regarding the probability of the min. pressure increase

Figure 4.0(3): Highest RPN items in FMEA for adsorbent system from Phase 1

The next grouping of potential causes that should be evaluated is items with RPNs greater than 180 and occurrence ratings greater than 7 as shown in Figure 4.0(4).

Potential Cause (Occ)	Failure Mode (RPN)	Actions
Hydrogen station using hydrogen supply to cool the adsorbent (10)	Storage system Wells to PowerPlant efficiency < 60% (180)	Need to confirm the assumptions for fueling to calculate the WPP
Hydrogen station using flow-through auxiliary cooling media to cool the adsorbent (10)	Storage system Wells to PowerPlant efficiency < 60% (180)	Need to confirm the assumptions for fueling to calculate the WPP
Material release rate insufficient due degradation in heat transfer at end of life (9)	System only supplies partial capacity (315)	Use system models to evaluate sensitivity of contact resistance
Material uptake insufficient rate due to performance of thermal isolation system (8)	Storage system only accepts partial fill (280) System only supplies partial capacity (245) Loss of useable hydrogen is greater than .05 [g/hr]/kg (240) Storage system fills in > 3.3 minutes (200)	Conduct reliability assessment of vacuum system integrity over the lifetime Consider vibration and/or durability test for isolation system
Material release rate insufficient due to initial material selection - form factor (8)	Hydrogen supply unable to achieve full flow rate (192)	Need to define experimental permeability test at cryogenic temperatures
Component interfaces and connections between BOP (7)	System exceeds allowable external leak rate limit (210)	Evaluate the leakage levels of interfaces and connections
Extended periods of non-operation (beyond 4 days) (7)	Loss of useable hydrogen is greater than .05 [g/hr]/kg (210)	*See thermal isolation system*

Figure 4.0(4): RPN >180 and occurrence > 7 items in FMEA for adsorbent system from Phase 1

In Phase 2, the initial FMEA was updated based on the actions and activities within this phase. The RPN values were changed by the team, shown in figure 4.0(5), based mainly on modified detection and occurrence ratings. The peak RPN value and mean in phase 1 (720 and 188, respectively) was revised to 512 and 157, respectively. Phase 2 actions involved in these RPN revisions included: initial homogenous material analysis, heat exchanger testing, revised tank construction from composite to aluminum, and completed cryogenic testing. Designs were developed with deep-dive technical reviews, controls, and test plans for Phase 3.

The FMEA ratings were further modified based on the Phase 3 activities by the adsorbent team as shown in figure 4.0(5). Some of the key actions that facilitated the reduction in the Risk Priority Numbers (RPN) include the following:

- Completed testing to reduce occurrence ratings associated with hydrogen impurity concerns
- Assessed tank robustness with adsorbent material and cryogenic operating conditions
- Conducted thermal management evaluation testing to assess performance in adsorbent bed
- Performed system testing to assess material variability and effects of non-homogenous bed

The final outcome of the FMEA provided the potential top failure modes that should be considered in further research efforts. The HSECoE made significant progress from Phase 1 by reducing the peak RPN to 288 and a mean RPN to 114 for the adsorbent system. The top failure modes that are identified in figure 4.0(6) include: non-homogenous adsorbent bed, leaks at cold temperature, insulation performance, and degradation of the thermal management system over the system life. From these failure modes, adsorbent system researchers should ensure future material-based system designs avoid these potential failure modes.

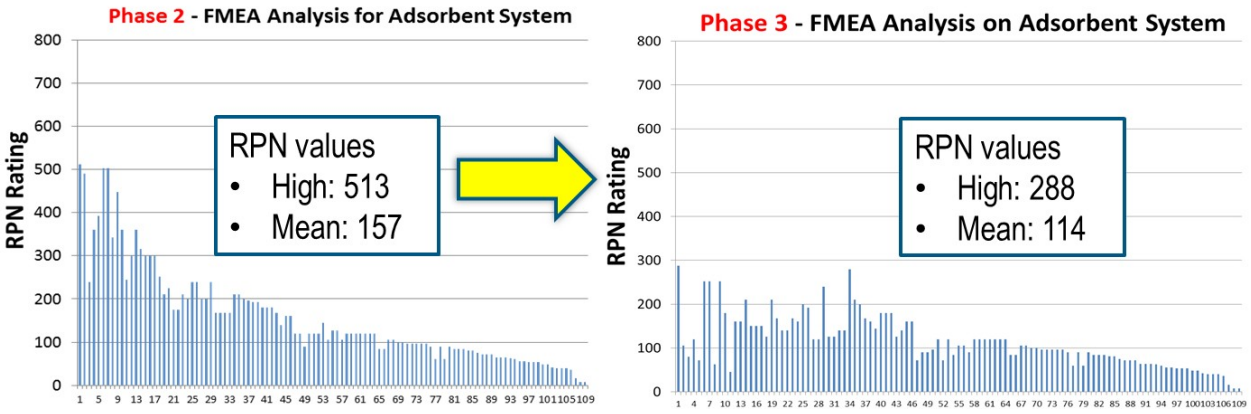

Figure 4.0(5): Phase 2 versus Phase 3 progressive Pareto summary of RPN values

Potential Cause	Failure Mode (RPN)	Comments
(1) Material release rate insufficient **due to non-homogenous materials** at end of life	Hydrogen supply unable to achieve full flow rate (288) Storage system only accepts partial fill (252) Storage system on-board efficiency < 90% (252) System only supplies partial capacity (252)	Confirmed performance was stable after material cycle and Phase 3 system testing. Further key life tests should be considered.
(2) Component interfaces and connections between BOP parts **leak at cold temperatures**	System exceeds allowable external leak rate limit. (280)	Further development of cryogenic sealing solutions should be considered.
(3) Material uptake insufficient rate due to **performance of thermal isolation system** such as vacuum stability	Loss of useable hydrogen is greater than .05 [g/hr]/kg H2 (240) System only supplies partial capacity (assumes complete fill) - from initial use through lifetime (1,500 cycles) (210)	Further reliability assessment of vacuum system integrity over the lifetime should be considered.
(4) Material release rate insufficient due **degradation in heat transfer in bed** and to the thermal management system at end of life	System only supplies partial capacity (assumes complete fill) - from initial use through lifetime (1,500 cycles) (210)	Confirmed performance of thermal management during Phase 3 system testing. Further key life tests should be considered.

Figure 4.0(6): Highest RPN items >200 in FMEA for adsorbent system from Phase 3

5.0 Materials

5.1 Selection of a Prototype Adsorbent

The selection of MOF-5 by the Hydrogen Storage Engineering CoE was driven by a number of factors, including the following list of requirements:

1. Performance: gravimetric hydrogen density (wt.%), volumetric hydrogen density (g/L), thermal conductivity, and ability to be densified.
2. Demonstration of scaled-up production. Approximately 5-10 kg of material (total) were required for Phase 2-3 of the project.
3. Future Prospects: An optimal hydrogen storage system will operate at near-ambient temperatures and pressures, while exhibiting high hydrogen storage densities. Reaching these goals will largely depend on the development of improved storage materials. The "future prospects" criterion is a subjective assessment of which materials classes are most likely to demonstrate significant improvements in their hydrogen storage properties given additional R&D. Factors that suggest that MOFs have the potential to exhibit improvements in performance include: existence of a large phase space of compounds, tunability of composition, and tunability of structure.

Table 5.1(1) lists MOFs which are either commercially supplied, or for which some kind of pilot production process has been demonstrated. Included for comparison is a commercially-available KOH superactivated carbon, MSC-30, which is frequently used as a benchmark for high-capacity H_2 and CH_4 adsorbent materials.

Table 5.1(1) Commercially-produced MOFs

Commercial Name	Names Commonly Used in Literature	Manufacturer	Metal Center	Langmuir Surface Area (m^2/g)	N_2 BET Surface Area (m_2/g)
A100	MIL-53 (Al)	BASF	Al	1100-1500	1286
A300	MIL-110 (Al)	BASF	Al	1790	
A520	MIL-88a (Al)	BASF	Al		
C300	Cu-BTC, HKUST-1	BASF	Cu	1500-2100	1290
F300	Fe-BTC	BASF	Fe	1300-1600	
M050	Mg Formate	BASF	Mg	400-600	
N125	MOF-74 (Ni)	BASF	Ni	1500-1600	
Z100	MOF-5, IRMOF-1	BASF	Zn	3650-4300	2700-3800
Z377	MOF-177	BASF	Zn		3965-4100
Z1200	ZIF-8	BASF	Zn	1300-1800	1100
MTA1	Al(fumarate)(OH)	MOF Technologies	Al		
MTA2	ZIF-8	MOF Technologies	Zn	1650-1800	
MTA3	ZIF-67	MOF Technologies	Co	1500-1800	
MTZ4	HKUST-1	MOF Technologies	Cu	1500-1600	
Cat.# 40-1105	UiO-66	Strem Chemicals	Zr	1150	
Cat. # 30-4015	ZIF-8	Strem Chemicals	Zn		
KRICT-Fe100	MIL-101 (Fe)	Strem Chemicals	Fe	2120	1950
MSC-30	MSC-30	Kansai Coke & Chemical			3250-3470

Among the MOFs where scaled-up production has been demonstrated, MOF-177 is the candidate with the highest surface area, pore volume and excess H_2 adsorption at 77 K. It is closely followed by MOF-5 in second place. However, MOF-5 ($\rho_{crys}=0.61$ g/cm^3) has a crucial advantage over MOF-177 ($\rho_{crys}=0.43$ g/cm^3) in terms of its higher crystal density. As a result, MOF-5 has a larger hydrogen storage capacity on a volumetric basis. When synthesized under anhydrous conditions, MOF-5 is reported to have a BET surface area of 3800 m^2/g and a maximum excess hydrogen uptake of 7.6 wt. % at 77 K [Kaye 2007].

MOF-5 is attractive in terms of cost for scaled-up production. One of the predominant factors limiting the scale-up of MOF synthesis is the availability of organic linker precursors in sufficient quantity and quality. The linker for MOF-5, benzene-1,4-dicarboxylic acid (terephthalic acid), is a commodity chemical. As we describe next in Section 5.4.1, BASF demonstrated a large increase in space-time-yield in moving from the laboratory scale (kg/m^3/d) to industrial scale production (299 kg/m^3/d) of MOF-5.

Downselect: Based on the available materials and the considerations summarized above, the HSECoE deliberated amongst two shortlisted materials:

1. **MOF-5:** MOF-5 is a crystalline microporous material with the chemical formula $Zn_4O(BDC)_3$ (BDC = 1,4-benzene dicarboxylate). First reported by Prof. Omar Yaghi's group in 1999, MOF-5 is a well characterized metal-organic framework. Published information exists regarding: (i) Characterization of optimal synthesis conditions; (ii) Studies of durability/robustness under various conditions; (iii) Simulations and computational work; (iv) Experimental gas adsorption measurements. Having this large pre-existing body of published information provided additional motivation for selecting MOF-5 over other MOFs
2. **MAXSORB** (MSC-30): MSC-30 is an amorphous activated carbon produced by the Kansai Coke & Chemical Company. This is a finely powdered material. It is very similar to the much-studied AX-21, a "superactivated" carbon originally developed by AMOCO and commercialized by the Anderson

Development Company (although the surface area of MSC-30 is somewhat higher). There is thought to be some batch-to-batch variability regarding surface area and pore volume. Petroleum coke is generally used as the carbon precursor, which is mixed with an excess amount of potassium hydroxide, and followed by several heating and washing steps. The intercalation of K^+ ions into the carbon, and their subsequent removal, is what creates much of the microporosity. Apparently produced using a continuous process, MSC-30 was available well in excess of the quantities required for the project.

Selected Material and Justification: Based on the selection criteria described above the Center chose MOF-5 as the primary material for further analysis and application in Phases 2 and 3. Work involving MAXSORB was brought to a logical conclusion, with the results of those studies documented in publications and/or DOE reports. The justification for this choice is summarized below.

1. **Performance**: MOF-5 outperforms MSC-30 in gravimetric and volumetric density. For example, H_2 uptake measurements and system modeling by the Center estimated that the gravimetric capacity of a powder-based Type III system operating at $P_{max} = 60$ bar and $T = |40\,\mathrm{K} - 120\,\mathrm{K}|$ is 5.5 wt. % for MSC-30 and 7.3 wt. % for MOF-5. Projected volumetric densities for the same systems are: 27 g H_2/L (MSC-30) and 31 g H_2/L (MOF-5). MOF-5 also holds an advantage over MSC-30 in terms of densification; MOF-5 can be compacted without the use of binders, whereas MSC-30 cannot. (Use of binders lowers the surface area and hydrogen storage capacity, and may result in an increase in cost.) Although spark-plasma methods can densify MSC-30 without binders, this method results in a large loss of surface area and may not be scalable to kg quantities in the near term.
2. **Availability**: Both MOF-5 and MAXSORB were determined to meet the criterion for availability. As described above, MSC-30 is produced industrially by Kansai Coke and Chemical. Sufficient quantities (9 kg) of MOF-5 were available to the Center from BASF.
3. **Future Prospects**: MOF-5 is a member of the larger class of Framework Materials, FM, of which there are now several thousand known and theoretical compounds. The large potential compositional space of FMs, coupled with the ability to tune their structure and composition, suggests that new FMs with improved properties are likely to be identified. Given these factors, the demonstration of a MOF-based adsorbent system by the HSECoE could have significant benefits for identifying those materials properties that most strongly impact the efficiency of a hydrogen storage system, making future materials discovery efforts more efficient. To our knowledge a FM-based hydrogen storage system has never been reported, whereas several activated-carbon-based systems have been built and successfully demonstrated. Consequently, a hydrogen storage system based on a MOF adsorbent would be unique, and would offer new opportunities to uncover design tradeoffs specific to this material.
4. **Safety**: Neither MOF-5 nor MAXSORB are believed to present extreme safety hazards. For example, neither is pyrophoric. While a full safety assessment of both materials is beyond the scope of the Center, for the purposes of materials down-selection we consider both materials to be sufficiently safe.

5.2 Safety

5.2.1 Introduction

From the point of view of safety, a risk assessment was conducted based on evaluating the potential hazards of a storage tank filled with MOF-5 and hydrogen, particularly with respect to national and international standards and regulations. To identify the required safety data for a sound risk assessment two main situations were identified of the above mentioned application: (a) handling of the pure MOF-5 powders/granules (b) release from the storage tank filled with MOF-5 and hydrogen. The safety assessment of these scenarios should address both the production filling process of MOF-5 into the hydrogen storage tank and the release of MOF-5 from the tank due to an accident situation during vehicle operation.

5.2.2 Safety Assessment Method

The assessment of handling of the pure MOF-5 powders/granule followed the standard procedure for potentially combustible dusts which includes the following:

1) DSC (differential scanning calorimetry) measurement of the solid MOF-5 to obtain the hazard potential (onset temperature and energy release of the reaction) for thermal decomposition reactions, additionally screening test for storage and transportation of MOF-5 in air.

2) Dust explosiveness of the MOF-5 dust dispersed in air. If the test is positive (that means if MOF-5 is rated as explosive dust) additional measurements have to be performed (e.g. minimum ignition temperature MIT, minimum ignition energy MIE, maximum explosion pressure p_{max}, maximum rate of explosion pressure rise K_{ST}, lower explosion limit LEL, limiting oxidiser concentration LOC).

When hydrogen is filled into a storage tank containing solid MOF-5 particles (in form of granules, dust etc.) one has to ensure that no chemical reaction with significant energy release between the hydrogen and the MOF-5 will occur. The DSC measurements in hydrogen atmosphere can also identify any potential chemical reactions (including their energy release and onset temperature).

For an accidental release from the tank, mixtures containing combustible gases and combustible dusts may occur. If the concentration of the gaseous component (hydrogen) in the total mixture of combustibles and air is above the LEL of the gas, the explosion properties of the mixture are dominated by the properties of the gas. Considering a worst case concentration of hydrogen in air (30 vol. %) means that the effect of the MOF-5 dust on a potential explosion is negligible. The scenario for a safety assessment of the storage tank can be simplified in a conservative way assuming pure hydrogen (without MOF-5 dust) as combustible. Based on the abovementioned and relevant standards, the safety assessment required the following data of MOF-5: dynamic scanning calorimetry in a hydrogen atmosphere and dust explosibility along with minimum ignition energy and minimum ignition temperature if positive.

The generation of safety data was conducted by the BASF safety engineering group. The laboratory is accredited according to DIN EN ISO / IEC 17025. All standard test methods are performed according to official guidance documents (national and international standards like VDI, TRBS, DIN EN, ISO, IEC).

For differential scanning calorimetry, BASF used a standard procedure according to DIN EN 51007. For maximum explosion pressure (P_{max}), BASF used a standard procedure according to DIN EN 14034-1. The apparatus is a 20 L sphere. The procedure and the test apparatus meet the requirements of DIN IEC 60079-20-2 and ASTM E 1226. For maximum rate of explosion pressure rise (K_{ST}), BASF used a standard procedure according to DIN EN 14034-2. The apparatus is a 20 L sphere. The procedure and the test apparatus meet the requirements of DIN IEC 60079-20-2 and ASTM E 1226 (5 L sphere).

For minimum ignition energy (MIE), BASF uses a standard procedure according to DIN EN 12821. The standard procedure meets the requirements according to DIN IEC 60079-20-2 and ASTM E 2019. DIN EN 12821 and ASTM E 2019 differ in the sample preparation only: the product sample is sieved with a 63 µm sieve according to DIN EN 12821 and a 75 µm sieve according to ASTM E 2019. This is a conservative deviation from what ASTM E 2019 demands for sample preparation. The standard apparatus is a Hartmann-tube.

For minimum Ignition temperature (MIT), BASF uses a standard procedure according to VDI 2263. The BASF apparatus is a standard BAM-oven. According to DIN IEC 60079-20-2 section 1.1 a Godbert-Greenwald-oven is recommended for use to determine the minimum ignition temperature of a dust cloud. Considering DIN IEC 60079-20-2 section 1.1 note 2: “The method is not applicable to dusts which may, over a longer period of time than provided for in the test method, produce from deposits gases generated during pyrolysis or smouldering.” using a BAM-oven for measuring the minimum ignition temperature gives usually the more conservative values of the MIT. The time of the dust particles facing the high temperature of the BAM-oven exceeds that of the Godbert-Greenwald-oven. That means the BAM-oven meets the requirements of DIN IEC 60079-20-2 and ASTM E 1491 in a conservative way.

5.2.2 Safety Assessment Results

The initial safety assessment conducted a dust explosibility screening of the MOF-5 using a Hartmann Tube Apparatus. This devise had a continuous arc ignition source with an effective energy of 4 Joules (J). A sample would be classified as exposable if a flame was observed to propagate away from the ignition source. The result of the MOF-5 test was unable to ignite at 4 J. The next step was to increase the ignition energy to 2 kJ which was

able to ignite the MOF-5 in the 20 L sphere. Therefore, the minimum ignition energy of MOF-5 is between 4 J and 2 kJ. As a reference, materials that ignite above 0.50 J are not considered sensitive to ignition by electrostatic discharge. Other ignitable dust particles have significantly lower minimum ignition energy such as coal at 30 to 60 mJ. The DSC measurements in air and under hydrogen at 10 bar don't indicate any particular risk when handling MOF-5, nor do they indicate any chemical reaction between MOF-5 and hydrogen.

The dust classification of MOF-5 in regards to explosion severity was determined in a 20 liter sphere based on the deflagration index (K_{ST}) which is the normalized pressure rise rate during the explosion and expressed by the following equation:

$$K_{st} = (dP/dt)_{max} V^{1/3} \quad \text{[bar m/s] where V is the volume of the test vessel}$$

The K_{st} value is obtained using the optimum deflagration conditions that can occur with a dust. Therefore, a series of tests were conducted over various concentrations to determine what dust concentration is optimum for a deflagration. Once the optimum dust concentration was determined with the then the $(dP/dt)_{max}$ value can be found and K_{st} can then be calculated, which essentially represents the optimum deflagration concentration for MOF-5 or other dust being tested. The MOF-5 tested for ignition had a particle size distribution the range of about 5 microns to 1000 microns. The ignition source used a pyrotechnic detonator at an energy level of 10 kJ, ambient pressure at ignition was 1 bar absolute, and temperature was between 20° C to 24° C. The resulting P_{max} at dust explosion was 6.3 bar absolute and K_{st} value was found to be 48 bar m/s for MOF-5. Based on this information, the dust explosion classification for MOF-5 is St 1 which is characterized as week to moderately explosive. Figure 5.2 (1) provides the table for dust explosion classifications. For reference, MOF-5 at a K_{st} value of 48 is comparable to the rating of activated carbon (44) or paper tissue dust (52) while an order of magnitude lower than other dusts such as aluminum powder (400). The safety assessment concluded that MOF-5 required a very high ignition energy level and produced a low explosion risk. Other typical aspects regarding handling MOF-5 can be found on the Material Safety Data Sheets (MSDS).

Dust Explosion Class	**K_{st} (bar * m/s)**	**Characterization**
St 0	0	Non-explosible
St 1	$0 < K_{st} < 200$	Weak to moderately explosible
St 2	$200 < K_{st} < 300$	Strongly explosible
St 3	$K_{st} > 300$	Very strongly explosible

Figure 5.2(1): Dust explosion classification per ASTM E 1226

5.3 Scale-up

Initial scale-up tests
Synthesis trials at BASF were carried out in a 1000 L-scale reactor to produce several kg of MOF-5 per batch. Initially, the kg-scale MOF-5 batches showed deviations compared to laboratory-scale MOF-5 batches. MOF-5 crystals were considerably smaller for the kg-scale batches. This affects the MOF's filterability and resulted in long filtration times during which MOF-5 decomposed. MOF-5 degrades when being exposed to the mother liquor too long. Two approaches were tested on laboratory-scale to circumvent this: improvement of the filtration process and stabilization of the MOF in the mother liquor. A combination of both might improve the filterability.

It was demonstrated that MOF-5 can be milled under technically relevant conditions while managing to preserve its surface area. The obtained powder was used for compaction trials. It was found that the milled MOF-5 is particularly sticky. Sticking originates from the electrostatic properties of the MOF-5 powder. It is very likely that the pelleting machinery would be blocked by the sticky mixture when compacting larger amounts. Further compaction trials were carried out to identify a way that would allow to compensate the electrostatics and enable

manufacturing of pellets on several kg-scale. In contrast to what was observed for the laboratory material (GW0117), the addition of ENG alone was not sufficient to compensate the electrostatics. It was found that a mixture of 5 wt.% ENG and 5 wt.% magnesium stearate can completely suppress it. Pellets with crush strengths between 13 and 24 N and surface areas ranging from 2100 m²/g to 2600 m²/g were obtained. The hydrogen uptake of those pellets ranged from 4.2 to 4.9 wt.% at 100 bar, 77K (compared to GW117 with 5 wt.% ENG only: 4.6 wt.%).

Demonstration of MOF-5 scale-up
Three scaled synthesis trials (200 L) were carried out to produce about 10 kg MOF-5 powder. A summary of the product properties is given in the table below:

Table 5.3(1) Overview of MOF-5 properties from scaled batches:

Batch	Product characteristics				
	Isolated yield [kg]	BET surface [m²/g]	LSA surface [m²/g]	Zn content [wt%]	C content [wt%]
1	3.1	2937	3838	32	37
2	3.5	2870	3794	34	37
3	3.2	2955	3896	34	37
Final	9.3	2937	3877	30	37

The surface areas of all batches were excellent (Langmuir SA > 3700 m²/g) and even slightly better than for laboratory material. The size of primary crystals was reduced compared to the laboratory scale due to non-optimized stirring in the pilot plant. Addressing this would have required engineering effort that was beyond this project's scope.

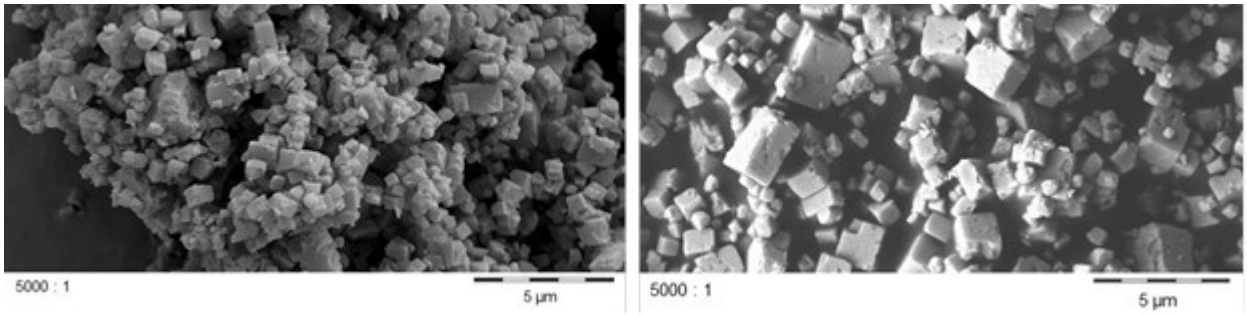

Figure 5.3(1) SEM microscope pictures of MOF-5 from a 200 L batch (left) and a laboratory batch (right)

Crystal morphology of the three batches varied due to varying washing times in the manually operated pilot plant, leading to partial dissolution of the crystals' surface.

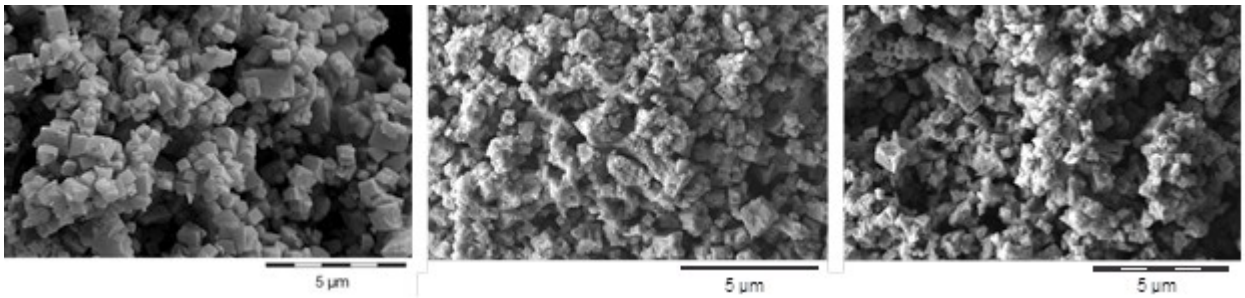

Figure 5.3(2) SEM microscope pictures of the three 200 L batches

The MOF-5 lumps obtained from the three batches were milled, yielding 9.3 kg of a homogenized sample (BET SA = 2937 m^2/g; Langmuir SA = 3877m^2/g; He-density = 2.19 g/cm^3).

In contrast to the crystallite morphology, particular size distribution appeared to be less dependent on the synthesis method. Both the scaled-up MOF-5 powder and experimental was subjected to particle size characterization by the cyclonic separation method. The particle size distributions (PSD) of the MOF-5 powder samples are sensitive to dispersing pressure. As shown in Fig. 5.3(3), the apparent particle size distribution changes when the dispersing pressure is increased from 0.2 bar to 3.5 bar. (It is likely that the higher dispersing pressures are breaking up the MOF-5 agglomerates into smaller particles, resulting in new peaks at 1 µm and 10µm). From a practical viewpoint, the PSDs measured at the 0.2 bar dispersion pressure are more reflective of the actual MOF-5 powders that are encountered during handling and measurement. Notwithstanding the measurement artifact, there is no major difference in the measured PSDs for the MOF-5 powders synthesized using the lab-scale method and the 200 L method.

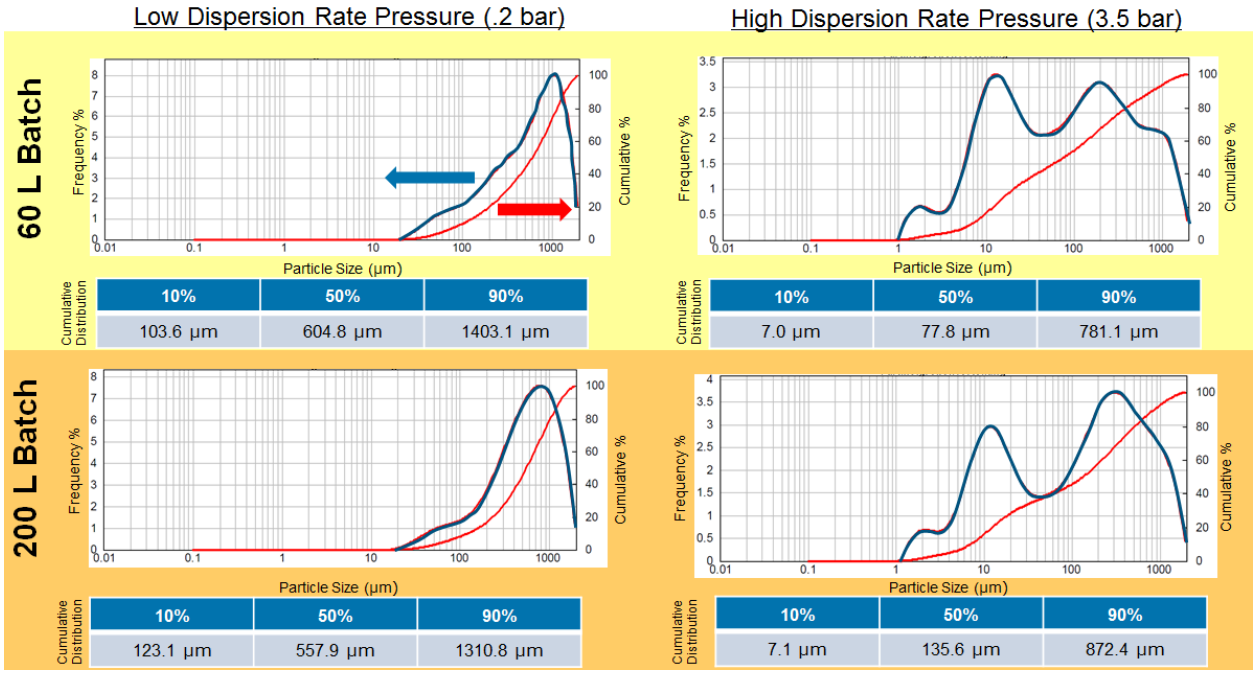

Figure 5.3(3) Particle size distribution of (top) laboratory-scale MOF-5 and (bottom) 200 L-scale MOF-5 after cyclonic separation at different dispersion rate pressures.

Hydrogen adsorption isotherms were measured on the 9 kg batch of MOF-5 and compared against previously measured data for the laboratory-scale batch of MOF-5. Results are summarized below in Figure 5.3(4). Excess hydrogen adsorption properties were essentially indistinguishable for the lab-scale and 200 L batches of MOF-5 powder.

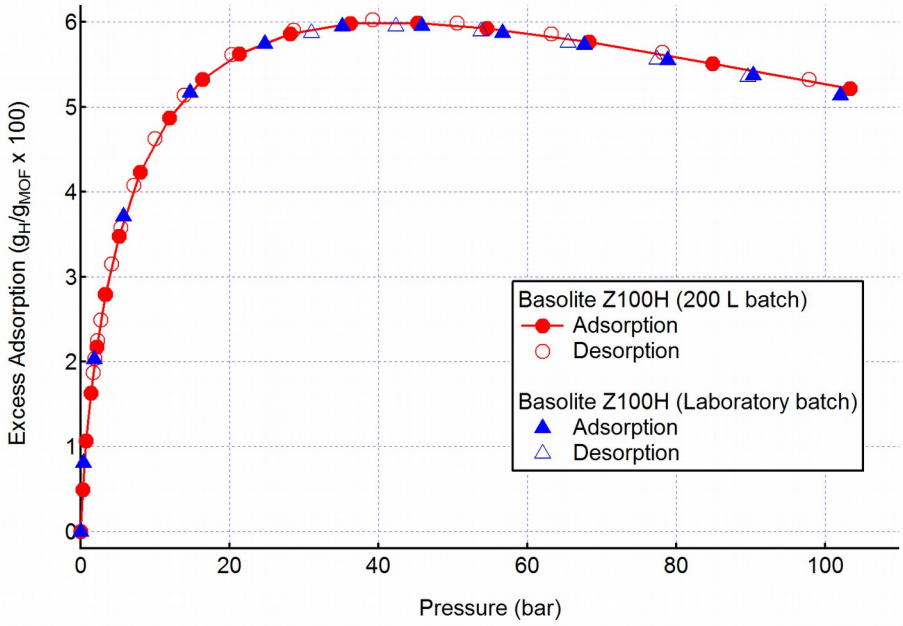

Figure 5.3(4) Hydrogen adsorption isotherms at 77 K of two batches of MOF-5 (Basolite Z100H) supplied by BASF. Red circles correspond to data measured on a 200 L batch of MOF-5. Blue triangles correspond to data measured for a batch produced using a laboratory-scale synthesis. Excess adsorption units are g/g × 100, as defined in Section 5.4.4

5.4 Characterization

5.4.1 Synthesis: The conventional synthesis process for MOFs involves combining metal salts (e.g., metal nitrates, sulfates, or acetates) with organic linkers, the latter most commonly consisting of mono-, di-, tri- or tetracarboxylic acids. These constituents are dissolved together and stirred in a polar organic solvent such as an amine [e.g. triethylamine (TEA)] or amide [e.g. *N,N*-diethylformamide (DEF), *N,N*-dimethylformamide (DMF)]. MOF crystallites then form via self-assembly and subsequently precipitate from the solution within minutes to hours. Typical synthesis temperatures range from ambient up to approximately 200°C. After filtration, washing, and drying, the crystalline product is obtained in the form of a powder. Depending on the desired application, the powder can be further processed into compacts (e.g., pellets, strands, *etc*.).

Laboratory-scale MOF synthesis procedures have recently been scaled from multi-kg to tons of product per batch, which will facilitate commercial applications of these materials. Moreover, sustainability is a big concern and was achieved by replacing solvent-based by water-based procedures. Example space-time-yields (STY) for the synthesis of MOF (and other framework) materials observed in laboratory and industrial settings are given in Table 5.4(1). Up to three orders of magnitude improvement in STY is observed in transitioning from laboratory to commercial settings.

Table 5.4(1) Comparison of space-time-yields (STY) for synthesis of various framework materials in both laboratory and commercial settings.

Composition	Literature Name	Laboratory STY ($kg/m^3/d$)	Commercial Name	Industry STY ($kg/m^3/d$)
$Zn_4O(BDC)_3$	MOF-5 IRMOF-1	0.21	Basolite Z100H	299
$Cu_3(BTC)_2$	HKUST-1	8.6	Basolite C300	225
$Zn(MeIM)_2$	ZIF-8	1.3	Basolite Z1200	160
Aluminum-fumarate	Aluminum-fumarate MOF	~30	Basolite A520	up to > 3600

MeIM=2-Methylimidazolate, BTC=benzene-1,3,5-tricarboxylate , BDC=1,4-benzene dicarboxylate

For this project, MOF-5 powders were synthesized by BASF at room temperature using a procedure described by Yaghi and coworkers starting from 1,4-benzene dicarboxylic acid (H_2BDC, $C_8H_6O_4$, Merck), zinc acetate dihydrate ($Zn(CH_3COO)_2 \cdot 2H_2O$, Merck), and *N,N*-dimethylformamide (DMF, BASF AG). In a glass reactor equipped with a teflon-lined stirrer, 130 g of $Zn(CH_3COO)_2 \cdot 2H_2O$ was dissolved in 1200 ml DMF. Within 2 hours, a solution of 37.5 g of H_2BDC in 950 ml DMF was added under rigorous stirring. The precipitate was filtered off, washed three times with 1 L of dry acetone and dried under a stream of flowing nitrogen. Given the low vapor pressure of conventional MOF synthesis solvents (e.g. DMF has a vapor pressure of approximately 4 torr at 25ºC), solvent exchange to a more volatile solvent (e.g. acetone has a vapor pressure of approximately 270 torr at 25ºC) has been shown to be an effective method for solvent removal. Prior to characterization, MOF-5 was heated and evacuated at 130ºC and 50 mtorr for 1-3 hrs, yielding the desolvated or so-called 'activated' form of the material. The wet chemical analysis of the obtained solid yielded 34 wt% Zn, equivalent to 92% molar yield of MOF-5 calculated as $Zn_4O(BDC)_3$. Cubic shaped crystals, smaller than 1 μm, were observed by scanning electron microscopy.

MOF-5 is one of the most thoroughly studied metal-organic frameworks, and its properties (particularly pore volume and surface are) can vary significantly due to differences in sample quality and synthesis methods. Depending on synthesis, post-processing and activation methods, the maximum excess hydrogen adsorption at 77 K for MOF-5 has been measured at values ranging from 4.3 wt.% on the low end to 7.1 wt.% on the high end. The sample with an excess adsorption of 7.1 wt.% was synthesized and desolvated in a water-free process using a nitrogen glovebox and anhydrous solvents [Kaye, 2007]. This particular high-quality sample had a BET surface area of 3800 m^2/g, which is in fact higher than the simulated surface area of 3580 m^2/g calculated from molecular modelling [Snurr, 2007].

The MOF-5 powders used in this project (synthesized by the method described above) have BET surface areas within the range 3300-3500 m^2/g (for $0.02 < P/P_0 < 0.1$), slightly lower than the simulated value for an ideal MOF-5 crystal structure. The fact that it is somewhat lower is likely due to defects in the intra-crystalline pore structure (such as blocked pores). Nonetheless, the MOF-5 materials used in this project actually have the highest measured H_2 uptakes in the literature, aside from the material characterized in [Kaye, 2007].

5.4.2 Crystallite and Particle size. Particle and crystallite size can have implications for packing density in a packed bed hydrogen storage system. (We use "crystallite" to refer to a single crystal grain of MOF-5, and "particle" to refer to an agglomerate of crystallites.) Particle sizes of less than 100 μm have been associated with increased inter-particle friction; contributions from short-range electrostatic forces can also lead to agglomeration and inhibit packing. Small particle size can also lead to an increased contribution of external surface area and intra-particle porosity, as well as decreased permeability and particle strength.

Scanning electron microscopy (SEM) was used to characterize the crystallite size for as-synthesized MOF-5 powder. A representative SEM image is shown in Figure 5.4(1) (inset), where a cubic morphology is observed. The crystallite size histogram comprising data from three separate SEM images is also shown in Figure 5.4(1). Based on a total of 182 crystallites, the mean crystallite size is 0.36 ± 0.011 μm. As described below, this small crystal size of MOF-5 results in a relatively small bulk density (~30% of the single crystalline value) as compared to other MOFs possessing larger crystal sizes

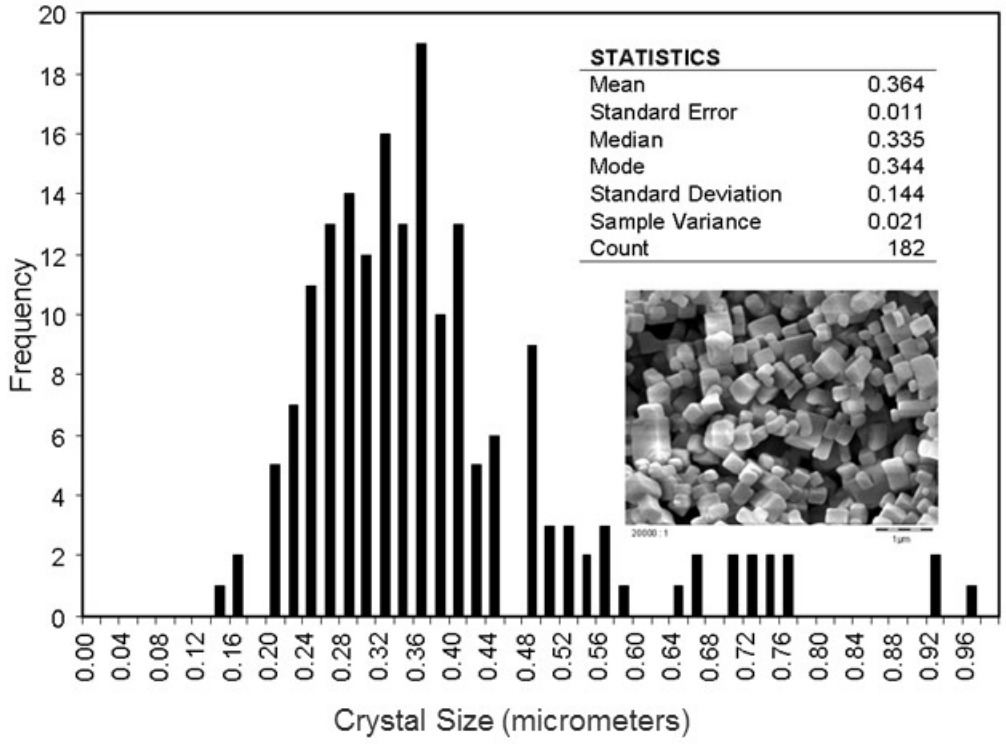

Figure 5.4(1). Crystal size histogram and statistics for MOF-5 powder. The distribution has a mean diameter of 0.36 μm and standard deviation of 0.144 μm.

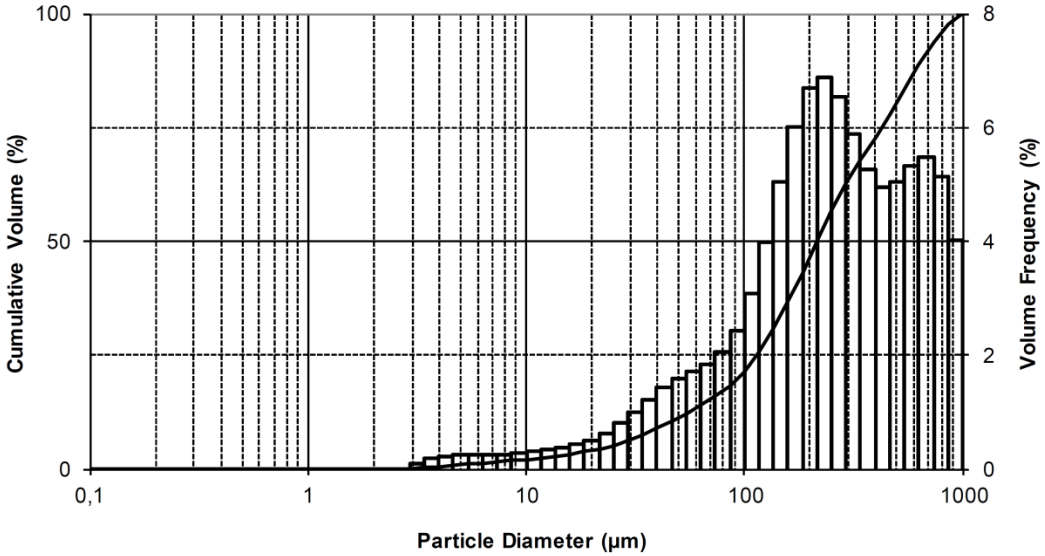

Figure 5.4(2). Particle size distribution and cumulative volume percentage for a MOF-5 powder produced using a lab-scale setup. The distribution has a mean diameter of 215 μm; 99% of the particles have a diameter less than 857 μm.

In addition to measuring the crystallite size, the dimensions of agglomerated particles were also measured. Results are essentially identical to those presented earlier in Fig. 5.3(3). The distribution of particle sizes and the cumulative percentage of their volume fraction is shown in figure 5.4(2). The mean of the particle size was found to be 0.22 mm, and 99% of the particles were found to have a diameter less than 0.86 mm. Comparison of the crystallite and particle size distributions indicates that due to inter-particle cohesion, essentially all sub-micron sized MOF-5 crystallites aggregate into particles having diameters larger than 3 micron.

We note that since a single MOF-5 particle is actually an aggregate of individual crystallite grains, the density of a single particle should be lower than the crystallographic density. This is due to the void spaces which are present between the agglomerated crystallite grains. Therefore, when we compare the bulk tap density of MOF-5 powder to its theoretical crystallographic density, there are actually two levels of packing efficiencies which need to be considered: (1) the local packing efficiency within a single particle; (2) the bulk packing efficiencies of the powder.

5.4.3 Density: The volumetric density of stored hydrogen is an important performance metric for mobile fuel cell applications. The densities of high-surface-area materials can be quite low, ranging from 0.1 to 0.4 g/cm^3. Consequently densification into pellets or custom-molded monoliths has been explored for such materials as MOF-177, MOF-5 and activated carbons, resulting in higher densities of 0.5–0.8 g/cm^3.

Careful attention needs to be paid to defining the density of a porous material. At least FIVE different types of density exist for these materials, each with a distinct meaning. These include: skeletal density, single crystal density, apparent density, envelope density and bulk density. In our usage of density definitions we have tried to be consistent with technical guidelines published by Micromeritics [Webb, 2002].

Skeletal density **(** ρ_{sk} **)** is the highest limiting density of a porous material. It includes only the "hard volume" of the porous material which is impenetrable to helium gas. However this volume can also include closed pores in addition to the solid pore framework. Skeletal density is typically measured by helium pycnometry. For MOF-5 the skeletal density value was measured at $\rho_{sk} = 2.01$ **g/cm^3** using an AccuPyc 1330 Pycnometer (Micrometritics). For this measurement 8.0 mL of MOF-5 was placed in the standard sample holder at ambient temperature. The measurements were repeated until the reproducibility was within +/- 0.005 g/mL. This value was confirmed many times by the helium free space measurements performed before each H_2 isotherm experiment. A number of alternative names for skeletal density exist, including true density, absolute density and Helium density. We emphasize that having an accurate value for skeletal density is critical to making meaningful measurements of excess H_2 adsorption, BET surface area and pore volume.

Single crystal density **(** ρ_{crys} **)** is an ideal density calculated from the crystallographic structures of the porous material. An alternative name frequently used for crystalline materials is the *crystallographic density*. It is equal to the mass of atoms contained with the unit cell, divided by the unit cell volume. Therefore, this unit cell volume includes all open and closed pore volumes. Since MOFs are crystalline materials, ρ_{crys} is commonly used as a basis of comparison between different MOFs, as it can be considered an intrinsic material property which is independent of measurement technique. The crystallographic density of MOF-5 is $\rho_{crys} = 0.61$ g/cm^3. Therefore, if a large, defect-free cubic crystal of MOF-5 were somehow grown in a lab, and it had dimensions of 1 cm × 1 cm × 1cm, the crystal would weigh only 0.61 g. Unfortunately, MOFs are actually synthesized as powders comprising tiny agglomerated crystallite grains, and have a packing density far below that of the single crystal density.

Apparent density **(** ρ_a **)** is a measurable version of the single crystal density which includes crystal defects, blocked pores and other non-idealities. In theory, we should be able to estimate the open pore volume from the measured skeletal density (ρ_{sk}) and known single crystal density (ρ_{crys}),

$$v_{pore}^{¿} = \frac{V_{crys} - V_{sk}}{m} = \frac{1}{\rho_{crys}} - \frac{1}{\rho_{sk}}, \qquad (5.4.1)$$

where $v_{pore}^{¿}$ is a *specific* pore volume (i.e., pore volume per unit mass of adsorbent). Note that v_{pore} is the specific pore volume while V_{pore} is the pore volume for some arbitrary mass m of porous material. In theory, $v_{pore}^{¿}$ should agree with the measured pore volume (v_{pore}) determined experimentally by N_2 adsorption at 77 K or argon adsorption at 87 K. A large difference between the measured v_{pore} and calculated $v_{pore}^{¿}$ indicates that the apparent density should be used in place of the crystal density.

Considering a sample of m grams of MOF-5, the apparent density is defined as the sum of the total pore volume (V_{pore}) and skeletal volume (V_{sk}) present in that sample,

$$V_a = V_{pore} + V_{sk} \tag{5.4.2}$$

where V_{pore} is measured by N_2/Ar isotherms and V_{sk} is measured by Helium pycnometry. After some algebraic manipulation, this expression can be alternatively written in terms of the apparent density. First equation (5.4.2) is inverted, multiplied by m ,

$$\frac{m}{V_a} = \frac{m}{V_{pore} + V_{sk}} \times \frac{1/V_{sk}}{1/V_{sk}} \tag{5.4.3}$$

Some additional rearranging is done to the RHS of equation (5.4.3),

$$\frac{m}{V_a} = \frac{m/V_{sk}}{\left(\frac{m}{V_{sk}}\right)\left(\frac{V_{pore}}{m}\right) + 1}. \tag{5.4.4}$$

This yields the expression for apparent density,

$$\begin{aligned} \rho_a &= \frac{\rho_{sk}}{\rho_{sk} v_{pore} + 1} \\ &= \frac{2.01\,\text{g/cm}^3}{2.01\,\text{g/cm}^3 \cdot 1.2\,\text{cm}^3/\text{g} + 1} \\ &= 0.59\,\text{g/cm}^3 \text{(for MOF-5)} \end{aligned} \tag{5.4.4}$$

In this case, the apparent density is close to the single crystal density of MOF-5 ($\rho_{crys} = 0.61$ g/cm^3). We note that the apparent density is often used in lieu of crystal density for non-crystalline porous material such as activated carbons. For example for the well-studied MSC-30 benchmark material apparent density values have been measured in the range $\rho_a = 0.39 - 0.43$ g/cm^3.

Bulk density **(** ρ_{bulk} **)** includes all inter-particle voids, along with all open and closed pore intra-particle volumes, as part of the total sample volume. The bulk density is the value you obtain if you fill a large graduated cylinder with powder and tap it until the level settles to a stable value. Measurements of bulk density can result in a range of values due to differences in the number of taps, size of the container, packing force, particle shape, electrostatic interactions, and particle size distribution.

In gas storage applications it is desirable to completely fill the storage vessel with MOF powder in a manner that minimizes the presence of large voids. Repeated tapping and/or vibration of the powder and vessel can accomplish this. A standardized value for the packing or tap density can be measured using DIN, ISO 787 Part II, ISO 3953, or ASTM B 527-93 using a jolting volumeter or tap density measurement instrument. By this method we measured a bulk density of MOF-5 of around $\rho_{bulk} = 0.21$ g/cm^3 for a particular batch of MOF-5 powder.

A conventional approach is to write the bulk density in terms of the theoretical (i.e., single crystal or apparent density) and a packing efficiency f ,

$$\rho_{bulk} = f \times \rho_{crys}. \tag{5.4.5}$$

The packing efficiency for an single sized spheres in an ordered hexagonal close packed arrangement is $f = 0.74$. For random close packed spheres, the upper limit of the packing efficiency typically has an upper

limit of around $f \approx 0.63$ or lower. As evident in the SEM images presented in earlier sections, MOF-5 crystallites actually have a cubic shape rather than a spherical shape.

However, as we noted in Sec. 5.4.2, it is difficult to apply this standard packing arrangement to a powdered material such as MOF-5 since the individual particles are not single crystallites, but are instead aggregates of many crystal grains stuck together. The density of a single MOF-5 particle is likely to contain inter-crystallite voids, and would therefore be significantly lower than ρ_{crys} or ρ_a . Recent guidelines from NREL recommend using the term *packing density* in place of *bulk density* [Parillo, 2015]. However, to remain consistent with our previously published work, we continue to use the term bulk density in this report.

The bulk density of MOF-5 powder was initially measured using a small container (.75 ml) which was filled with MOF-5 and then tapped for approximately 5 seconds. This procedure resulted in a low density of 0.13 g/cm^3. To assess the effect of tapping upon bulk density, we loaded a known mass of MOF-5 powder into a larger graduated cylinder (25 cm^3), and manually tapped the cylinder on the floor of the glovebox; the cylinder elevation for each tap was 2–3 cm. The tapping process was repeated for an increasing number of taps, and the volume and mass of MOF-5 powder in the cylinder was recorded afterwards.

Figure 5.4(3) shows the bulk density as a function of the number of manual taps. It is clear that the powder density increases with the number of taps, starting from a value of 0.18 g/cm^3 at 200 manual taps and increasing to 0.21 g/cm^3 after 2000 taps. The MOF-5 tap density was also measured using a standardized jolting volumeter. In this case a series of 2000 taps were used, and the resulting density of 0.22 g/cm^3 was found to be in very good agreement with the manually-tapped sample. Additional testing demonstrated that the tap density can depend on the volume of the graduated cylinder employed and on the particle size. These tests resulted in a range of MOF-5 powder densities spanning 0.13 to 0.22 g/cm^3.

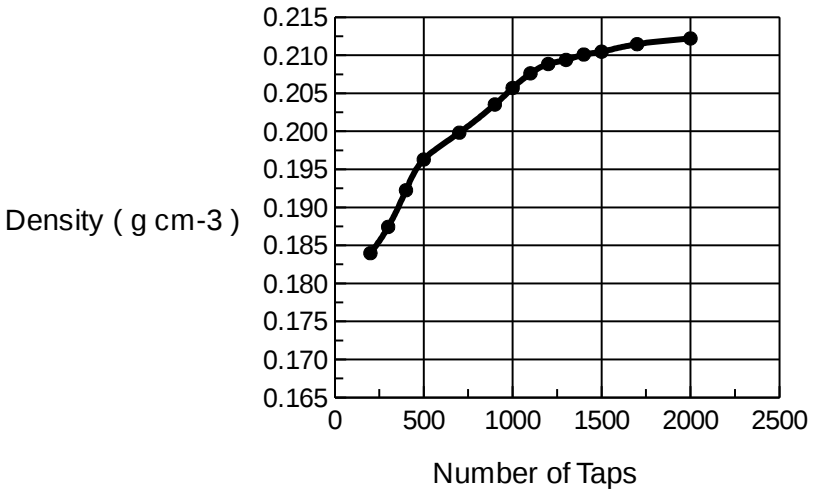

Figure 5.4(3). Tap density of MOF-5 as a function of the number of taps.

Envelope density **(** ρ_{env} **)** is yet another type of density with a specific meaning for porous materials. For this density, the sample mass is divided by the volumes which lies within a close-fitting envelope enclosing a single granule, particle, tablet *etc*. For a cylindrical pellet, we envision a tight-fitting envelope enclosing the cylinder, with volume $V = \pi \times r^2 \times h$. If an irregularly shaped granule were dropped into some media such as a fluidized sand bath (or some other fluid-like media which does not penetrate into the granule pores), the displaced volume would correlate to the envelope density. However, in this report the envelope density is used strictly for pellets, and is equivalent to a geometric density.

Table 5.4(2). Density examples for representative MOFs

Material	Skeletal Density (g/cm^3)	Apparent Density (g/cm^3)	Single Crystal Density (g/cm^3)	Bulk Density (g/cm^3)

MOF-177	1.6	0.44	0.427	0.33
MOF-5	2.0*	0.59*	0.61	0.21*
MIL-53	1.4	0.74		0.55
HKUST-1	1.72	0.87	0.881	0.64
MSC-30	2.2	0.39-0.49	N/A	0.29

*Our measurements; All other values taken from [Beckner, 2015]

5.4.4. Hydrogen Storage Density

Excess adsorption is the quantity which is directly measured by the standard static volumetric method (alternatively called the manometric method). Many detailed explanations of this method exist in the literature. The basis of this method is that a known amount (N moles) of gas is expanded from a calibrated reservoir volume (V_r) into a sample cell containing the adsorbent material (with a free space volume V_S at the beginning of the experiment). Some of the pressure drop in this step is due to the gas expansion, and some is due to adsorption. Since the temperatures and pressures are measured during the experiment, we know initial (ρ_i) and final density (ρ_f) of the bulk gas phase. Multiplying the gas density with the volume gives the gas amount in moles. The excess adsorbed amount is therefore defined as

$$N_{ex} = V_r \times \rho_i - \left(V_s + V_r\right) \times \rho_f \tag{5.4.6}$$

During adsorption this value is positive. It means that the hydrogen density near the adsorbent surface (and inside the adsorbent pores) is higher than the bulk gas density (ρ_f¿ . Thus, the excess adsorbed amount is equal to the "extra" moles of hydrogen within the higher density phase, beyond what we would expect if it were simply at the bulk gas density. We call the high density phase the *adsorbate phase*.

We employ three types of units for expressing the excess adsorption is this report.

(1) mol/kg: Moles of excess adsorbed H_2 per kilogram adsorbent

$$\frac{\text{mol}}{\text{kg}} = \frac{N_{ex}\left(\text{moles } H_2\right)}{m_{sorbent}\left(\text{g}\right)} \times \frac{1\,\text{kg}}{1000\,\text{g}} \tag{5.4.7}$$

(2) wt.%: Mass of excess adsorbed hydrogen divided by the combined adsorbent mass and hydrogen mass. For a H_2 molar mass of $MM = 2.0159$ g/mol, and a sorbent mass of $m_{sorbent}$ in grams,

$$\text{wt.\%} = \frac{N_{ex} \cdot MM}{m_{sorbent} + N_{ex} \times MM} \times 100 \tag{5.4.8}$$

This is often a source of confusion in the literature, as many authors use the wt.% label without actually including the hydrogen mass ($N_{ex} \times MM$) in the denominator

(3) g/g×100: Mass of H_2 divided by mass of adsorbent times 100. This unit is easier to fit to models, and is easier to compare to data in the literature (which often do not include hydrogen mass in the denominator). At low excess adsorption amounts, the distinction between wt. % and g/g×100 is small. However, for the case of MOF-5, the maximum excess H_2 adsorption at 77 K (for our samples using our measurements) is 5.7 in units of wt.%, and 6.0 in units of g/g×100.

To convert the units from *n*[g/g×100] to *n*[wt.%], a simple expression can be used

$$n_{wt.} = \frac{100}{\frac{100}{n_{g/g\times 100}} \pm 1}, \tag{5.4.9}$$

where $+1$ is used going from g/g×100 to wt.%, and -1 is used to convert from wt.% to g/g×100.

Absolute adsorption is related to excess adsorption by $n_a = n_{ex} + v_a \rho_g$, where v_a is the volume occupied by the adsorbate phase, and ρ_g is the bulk hydrogen gas density. We cannot measure the adsorbate volume, but we can be envision it as enclosing the regions around the adsorbent surface where local H_2 density exceeds the bulk gas H_2 adsorptive density. We can also interpret it as the volume near the surface that is subjected to the potential field of the solid. We assume that v_a is constant with respect to adsorption amount. In the context of hydrogen adsorption well above the critical point (where the adsorption mechanism should have some likeness to monolayer formation rather than pore filling), the assumptions of constant adsorbate volume and average adsorbate density appear reasonable.

Near ambient conditions (e.g., low pressure and/or above cryogenic temperatures), ρ_g will be significantly lower than the density of the adsorbed phase (ρ_a). Under such conditions, the approximation $n_{ex} \cong n_a$ holds. However, at higher pressures and/or cryogenic temperatures the density of the gas phase (ρ_g) increases at a faster rate than the density of the absorbed phase (ρ_a), and thus n_a will continue to increase while n_{ex} reaches a maximum (plateau).

Total storage (volumetric) is a measure of practical hydrogen storage capacity of an adsorbent when it is inserted into a high pressure tank. It counts the total amount of hydrogen (both adsorbed and gaseous) which is present in the tank, and is an important metric for determining the actual hydrogen which can be delivered from the system. We start by assuming that a high pressure tank has been completed filled with MOF-5 powder (mass = m), and which is packed at its bulk density $\rho_{bulk} = m/V_{tank}$. The amount of free space remaining in the tank which can be occupied by hydrogen gas, is given by

$$V_{free} = V_{tank} - \frac{m}{\rho_{sk}} = \frac{m}{\rho_{bulk}} - \frac{m}{\rho_{sk}} \tag{5.4.10}$$

The total moles of hydrogen inside the tank (N_t) is equal to the excess adsorbed amount (N_{ex}) plus the amount of hydrogen gas (at the gas density ρ_{gas}) which occupies the free space V_{free} within the tank. This amount is written out as,

$$N_t = N_{ex} + \rho_{gas} V_{free} \tag{5.4.11}$$

To get the specific total storage on a volumetric basis ($n_{t,vol}$) both sides of Eq. 5.4.11 are divided by the internal tank volume V_{tank} (which we assume is equal to m/ρ_{bulk}).

$$\frac{N_t}{V_{tank}} = \frac{N_{ex}}{V_{tank}} + \frac{m \cdot \rho_{gas}}{V_{tank}} \left(\frac{1}{\rho_{bulk}} - \frac{1}{\rho_{sk}} \right) \tag{5.4.12}$$

Simplifying this further, using the assumption that $V_{tank} = m/\rho_{bulk}$,

$$n_t, vol \wedge ¿ \frac{N_{ex}\rho_{bulk}}{m} + \rho_{gas} \cdot \rho_{bulk}\left(\frac{1}{\rho_{bulk}} - \frac{1}{\rho_{sk}}\right)$$
$$¿ = n_{ex}\rho_{bulk} + \rho_{gas}\left(1 - \frac{\rho_{bulk}}{\rho_{sk}}\right). \quad (5.4.13)$$

To obtain $n_{t,vol}$ in units of grams hydrogen per liter (g/L), the quantities in equation 5.4.13 need to be written in the units shown in Table 5.4(4). A typical calculation of $n_{t,vol}$ for hydrogen adsorbed in MOF-5 at 77 K, 45 bar is included for illustration.

Table 5.4(3). Units used for parameters in Equation 5.4.13.

Quantity	Units	Equivalent Units	Typical Value
n_{ex}	g H_2 / kg sorbent	mol/kg × 2.0159 g/mol	60 g/kg (45 bar, 77 K)
ρ_{bulk}, ρ_{sk}	kg/L	g/cm^3	$\rho_{bulk} = 0.21, \rho_{sk} = 2.0$
ρ_{gas}	g/L	-	14.8 g/L (45 bar, 77K)
$n_{t,vol}$	g/L	-	25.9 g/L (45 bar, 77 K)

As defined here, the total volumetric storage quantity can be considered as a quasi-material property which depends on material post-processing step such as powder settling and mechanical compaction or molding. When we are considering a pellet or custom-molded monolith, we replace the bulk density ρ_{bulk} with the envelope density ρ_{env}. We do not employ the *gravimetric* total storage density in this report.

Total storage (volumetric) in an ideal MOF-5 crystal

We cannot directly measure an excess hydrogen adsorption isotherm for an ideal, single MOF-5 crystal. Therefore, to estimate the total volumetric hydrogen storage density for an ideal MOF-5 crystal we need to make several assumptions.

1. The excess adsorption isotherm (n_{ex}^{crys}) of the crystal is equal to that of powder MOF-5 (n_{ex}^{pwd})
2. The bulk/geometric density of the material is equal to the single crystal density

Based on these assumptions, the total volumetric storage is equal to

$$n_{t,vol}^{crys} = n_{ex}^{pwd}\rho_{crys} + \rho_{gas}\left(1 - \frac{\rho_{crys}}{\rho_{sk}}\right), \quad (5.4.14)$$

The assumption $n_{ex}^{crys} = n_{ex}^{pwd}$ has not been directly confirmed by measurement, but numerous GCMC simulations have suggested its validity.

Hydrogen Delivery (volumetric)

Hydrogen delivery (or the *usable* hydrogen density) is defined as the difference in the system total volumetric storage between an initial temperature and pressure ($T_1, p_1 ¿$ and final temperature

$$n_{del,vol} = , n_{t,vol}(T_2, p_2) - n_{t,vol}(T_1, p_1) \quad (5.4.15)$$

For the special case of isothermal delivery, $T_1 = T_2$. A typical lower limit to the hydrogen delivery pressure for PEM fuel systems is $p_2 = 5$ bar. At low temperatures such as $T_1 = T_2 = 77$ K, the delivered H_2 amount can often be significantly lower than the total stored amount, owing to the remaining adsorbed amount in low-pressure region of the isotherm.

5.4.5 Surface area and pore volume:

A frequently reference rule in the hydrogen storage field is that a BET specific surface area of 500 m^2/g should correlate to 1 wt.% of excess hydrogen adsorption at 77 K. Initially, the rule was simply a correlation observed in activated carbons between their BET surface area (measured by N_2 at 77 K) and their excess hydrogen adsorption at 77 K and 35 bar in units of (mg hydrogen)/(g of sorbent). This correlation was later extended to consider the *maximum* excess hydrogen adsorption at 77 K in units of wt.% (g hydrogen) / (g hydrogen + g sorbent) × 100. It was extended to include materials beyond activated carbons as well.

While this correlation is approximately valid for a surprisingly wide range of sorbents (including MOFs), large experimental comparisons of adsorbent materials have generally demonstrated a wide range of scatter in plots of the maximum H_2 uptake versus BET surface area plots. Deviations from this rule are sometimes due to a simple observation. Materials that lie *above* the 1 wt.% per 500 m^2/g line (more H_2 adsorbed than predicted from SA) often have a larger fraction of their total pore volume consisting of micropores and ultra-micropores. This is a reflection of the well-known importance of micropores in supercritical hydrogen adsorption.

We can suggest additional reasons for the large scatter in the maximum excess wt.% versus BET surface area plots. Intuitively, the BET surface area should actually be correlated to the H_2 adsorption at *full surface coverage*. Surface coverage is more closely related to the absolute adsorption rather than the excess adsorption. Further, at higher pressures, the deviation between excess adsorption and fractional surface coverage becomes quite significant. The maximum excess adsorption point can occur at different pressures for different materials (not necessarily 35 bar). Trying to correlate the specific surface area with hydrogen adsorption for a variety of materials does not make sense if we are doing this comparison at different levels of fractional hydrogen surface coverage. To get around this issue, some authors have tried to use the excess hydrogen uptake at a low fractional coverage (usually at 1 bar, 77 K) as a basis of comparison, rather than the maximum excess uptake. In many ways, this approach is even worse, because low pressure hydrogen uptake is strongly influenced by the heat of adsorption, particularly if there are coordinatively unsaturated metal sites as in certain MOFs.

Experimental error in both the excess hydrogen uptake and BET surface areas can cause scatter in the wt.% versus BET surface area plots. Errors in high-pressure, supercritical hydrogen adsorption isotherms (particular for small sample sizes) are not uncommon. While the 77 K N_2 isotherms used for the BET surface area modeling are generally less susceptible to error, inconsistencies in how the isotherm is fitted to the BET model can be a source of confusion in the literature. As described later in this section, the BET surface areas reported in the literature often have significant variability (even for the same material). Part of this is variation is due to that fact that authors fit the BET model to different $\left\{ p/p_0 \right\}$ regions.

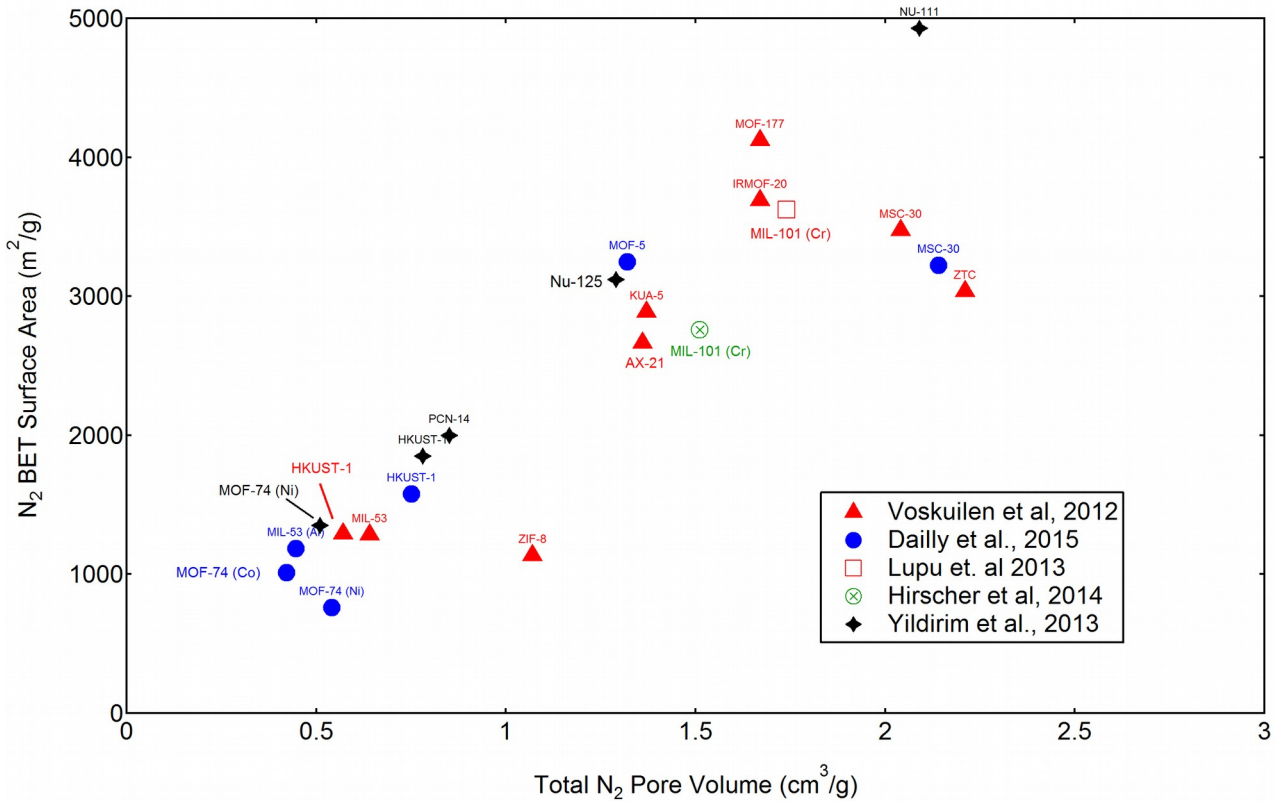

Figure 5.4(4). Relationship between total pore volume and BET specific surface area for a number of well-studied metal-organic frameworks, ZIFs and activated carbons. The legend indicates the references that the data points were taken from. The p/p_0 ranges used for the BET model fitting were stated for all these data. (ZTC refers to zeolite templated carbon, while KUA is an activated carbon).

We performed a quick survey of the published BET surface areas and total N_2 pore volumes in the literature. We focused on studies where $\{p/p_0\}$ ranges used for the BET model fits were clearly stated (and were consistent or nearly-consistent with the Rouquerol consistency rules). Further, we focused on comparison studies, where all the measurements were performed by the same group (presumably using a consistent methodology). A summary of these values is shown above in Figure 5.4(4).

As is evident in Figure 5.4(4), Framework materials with ultra-high specific surface areas have been reported. The group of Prof. Yaghi reported MOF-210 which has a BET surface area of 6240 m^2/g and total pore volume of 3.60 cm^3/g. Similarly, the group of Prof. Hupp reported a BET surface area of 7140 m^2/g and pore volume of 4.40 cm^3/g for NU-110. As our team demonstrated in [Goldsmith, 2013] however, higher specific surface areas do not necessarily result in a higher practical H_2 storage capacity. Typically, such improvements to surface area occur via creation of larger micropores, thereby decreasing the crystal and bulk densities, which limits any increase to the volumetric storage density.

During the course of this project, we characterized the surface areas and micropore volumes for numerous batches of MOF-5 synthesized and activated at BASF. In most cases we measured N_2 isotherms at 77 K, while in a few cases we measured Ar isotherms at 87 K. Based on the standard pressure range for BET analyses ($0.05 < P/P_0 < 0.2$) we obtained BET surface areas between 2763 m^2/g and 3000 m^2/g, depending on the particular batch of MOF-5 used in the measurement. However, if we instead use a pressure range ($0.02 < P/P_0 < 0.1$) which is consistent with the BET consistency criteria, the resulting BET surface areas fall in the range of 3300-3600 m^2/g.

Table 5.4(4). Measured surface areas from N_2 isotherms at 77 K. Isotherms measured on a Micromeritics ASAP2420 instrument. Free space calculations were accomplished by assuming $\rho_{sk} = 2.01\ g/cm^3$, and using a pre-calibrated sample cell.

MOF-5	BET Model	Langmuir Model

Batch	p/p_0	# Points	SA (m2/g)	p/p_0	# Points	SA (m2/g)
GP0378	[0.01, 0.05]	5	3539	[0.01,0.1]	8	3814
GP0378	[0.05, 0.2]	5	2920	—	—	—

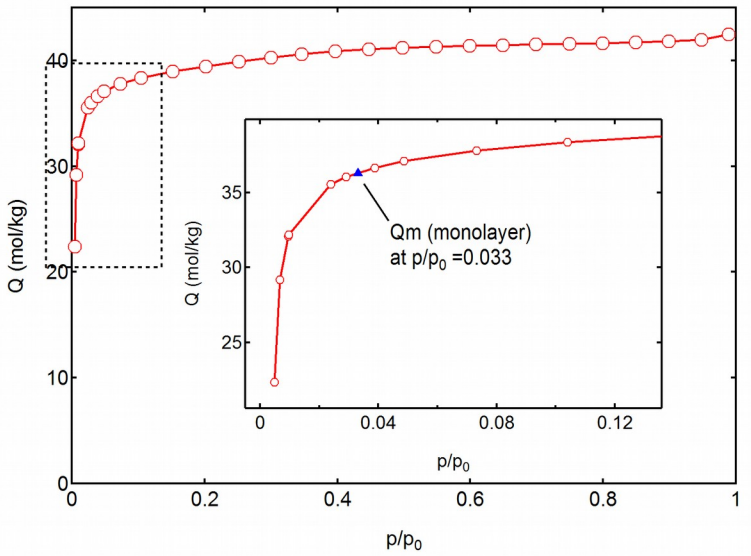

Figure 5.4(5) N_2 isotherms for powder MOF-5 (200 L batch) measured at 77 K. The inset shows the low pressure region of the isotherm, and indicates the estimated monolayer completion point (triangle) from the BET model.

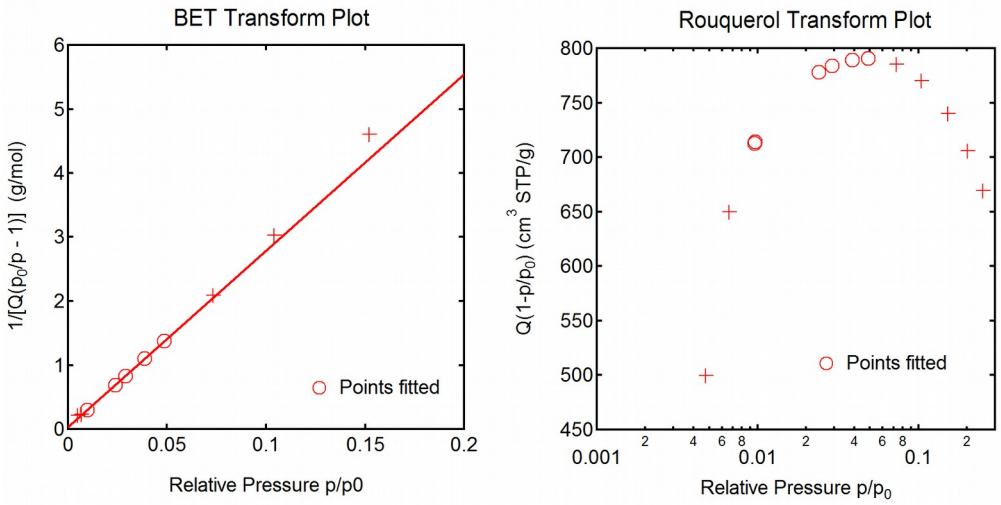

Figure 5.4(6) (left) BET transform plot of the N_2 isotherms, with indicated points to the model (right) Rouquerol transform plot showing a monotonic increase for fitted points

An example of a surface area measurement for powder MOF-5 (200 L batch) is shown in Figs 5.4(5-6). The instrument that we used for the nitrogen isotherm measurements (Micromeritics, ASAP2420) was not equipped with a high-resolution pressure gauge capable of accurate low-pressure measurements. This placed a practical lower limit on pressure measurements of around 20 Torr (i.e., a relative pressure of $p/p_0 = 0.003$). Consequently, much of the steep, low-pressure region of the MOF-5 isotherm was not directly measurable. Nonetheless, we could still map out the "knee" region of the isotherm in order to estimate the monolayer completion point.

The recommended BET consistency criteria are summarized below:

1. There should be a linear region in the BET transform plot,

$$\frac{p/p_0}{Q(1-p/p_0)} \text{ vs. } p/p_0, \tag{5.4.16}$$

where Q is the adsorbed N_2 amount in units of cm^3[STP]/g, and p/p_0 is the relative pressure.

2. The BET constant C should be positive
3. The Rouquerol transform, $Q(1-p/p_0)$ vs. p/p_0, should be monotonically increasing within the pressure range fitted to the BET model
4. The monolayer capacity Q_m should fall within the $p_1 < p/p_0 < p_2$ range used for fitting to the BET model
5. The pressure at which the monolayer capacity Q_m is reached, i.e., $(p/p_0)_m$, should roughly be equal to,

$$(p/p_0)_m \approx \frac{1}{\sqrt{C}+1}. \tag{5.4.17}$$

The consistency criteria were met for powder MOF-5 by choosing data in the pressure range $\{0.01 < p/p_0 < 0.05\}$. As shown in Figure 5.4(6), the BET transform is linear in this region, and the Rouquerol transform is monotonically increasing. Fitting to this data yields the parameters which are summarized in Table 5.4(5). From the values in the second column of this table, we confirm that fourth and fifth consistency criteria are met for this pressure range. In contrast, the "standard" BET pressure range of $\{0.05 < p/p_0 < 0.2\}$, with fit values summarized in the third column, clearly does not meet any of the consistency criteria outlined above (apart from the linearity of the BET transform plot). Therefore, values of the BET surface area depends very strongly on the pressure range chosen for fitting. As a comparison, the computed surface area for the ideal MOF-5 crystal structure has been previously reported as 3580 m^2/g [Snurr, 2007].

Table 5.4(5) Impact of pressure range on the fitted BET model parameters for MOF-5 (for N_2 isotherms at 77 K)

BET Parameters/FOMs	$\{0.01 < p/p_0 < 0.05\}$	$\{0.05 < p/p_0 < 0.2\}$
C	790.6	-77.4
Q_m (cm^3_{STP}/g)	813.2	675.7
$(p/p_0)_m$	0.033	0.0075
$1/(\sqrt{C}+1)$	0.034	NAN
BET Surface Area (m^2/g)	3540	2941

5.4.6 Thermal Properties

Although significant attention has been focused on improving the gas storage capacity of MOFs, relatively little effort has been devoted to assessing their thermal properties. The thermal conductivity and heat capacity of MOFs (and other adsorbents) are significant because they will impact the design, performance, and cost of MOF-based storage systems. For example, hydrogen uptake and release reactions involve the liberation (adsorption) or consumption (desorption) of heat; therefore efficient dissipation and delivery of heat is critical. Typically, adsorbent systems incorporate a heat exchanger for managing the temperature during fueling and delivery. The thermal conductivity properties of the storage media will have a direct influence on the heat exchanger design. If the thermal conductivity is low, the heat exchanger design requires additional complexity, which may add weight and cost. As a counter-measure, material enhancements can be added to the material to increase the thermal conductivity. These additions displace some fraction of the storage material, resulting in a decrease in storage capacity and an increase in the system weight. Therefore, it is important to accurately evaluate thermal conductivity to minimize the amount of the enhancement materials. Moreover, the creation of accurate system models relies on the determination of thermal properties for materials of interest.

Heat capacity. The specific heat capacity (c_p) describes to the ability of a material to store thermal energy, and indicates the amount of energy needed to heat the material to a specified temperature. It is an important property for systems whose operation involves a temperature swing, such as in the thermal desorption of stored gasses. The heat capacity of powder MOF-5 in the temperature range of 220 – 370 K was determined using the procedure described in Section 5.6.4, and is plotted in Figure 5.4(7). At 300 K, c_p for MOF-5 was measured to be 0.72 $Jg^{-1}K^{-1}$, which is comparable to that of alumina (0.77 $Jg^{-1}K^{-1}$) and graphite (0.71 $Jg^{-1}K^{-1}$). c_p increases approximately 33% over the measured temperature range, from approximately 0.6 $Jg^{-1}K^{-1}$ at 220 K to 0.8 $Jg^{-1}K^{-1}$ at 340 K.

Thermal conductivity. The thermal conductivity of most microporous materials (e.g. zeolites and MOFs) is low, stemming from their large pore size (>20 Å in diameter) and high free volume (>90% free volume). McCaughey *et al* have pointed out that the atomic number density for MOFs is even lower than that for zeolites (2.46×10^{28} atoms/m^3 for MOF-5 versus 5.13×10^{28} atoms/m^3 for sodalite), suggesting that MOFs will have an even lower thermal conductivity than other highly porous compounds. Single crystal thermal conductivity measurements have been previously measured on 1-2 mm crystals of MOF-5 over a temperature range of 6-300 K. This data, obtained using a longitudinal steady-state heat flow method, shows a peak thermal conductivity at 20 K of ~0.37 W/m·K and a minimum at 100 K of ~0.22 W/m·K. From 100 to 300 K, the thermal conductivity increases by 30%, attaining a value at 300 K of ~0.32 W/m·K. This value is much lower than that for other microporous single crystals such as zeolites (3.53 and 2.07 W/m·K for sodalite and faujasite, respectively).

The intrinsic thermal conductivity for MOF-5 single-crystals represents an upper limit for the pure material. Data from powder samples includes the effects of interparticle porosity which will reduce the thermal conductivity below the single crystal value. We have measured the thermal conductivity for compacted MOF-5 powder at temperatures from 300 to 335 K and at three densities: 0.35, 0.52, and 0.69 g/cm^3. The thermal conductivity (k) was calculated as the product of heat capacity (c_p), thermal diffusivity (α), and bulk density (ρ).

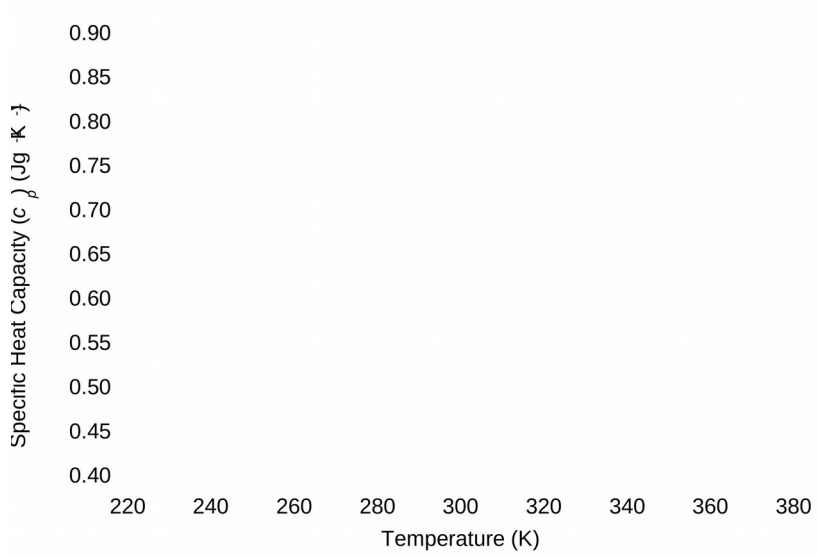

Figure 5.4(7). Specific heat capacity (cp) ($Jg^{-1}K^{-1}$) for powder MOF-5 as a function of temperature (K).

Measured thermal conductivity data is plotted in Figure 5.4(8). The thermal conductivity for MOF-5 remains relatively constant over the measured temperature range for all three densities. Values at 300 K for each density are as follows: 0.091 $Wm^{-1}K^{-1}$ (ρ = 0.35 gcm^{-3}), 0.11 $Wm^{-1}K^{-1}$ (ρ = 0.52 gcm^{-3}), and 0.16 $Wm^{-1}K^{-1}$ (ρ = 0.69 gcm^{-3}). (As the highest density pellets exceed the single-crystal density we presume some plastic deformation such as pore collapse has occurred in these samples during the compression process.) Based on these data, a modest improvement in k can be achieved via compression of the neat powder (e.g. ~20% improvement in k in going from ρ = 0.35 to 0.52 gcm^{-3}). The thermal conductivity for the 0.52 gcm^{-3} compact at 300 K is only 35% of the value of that for the single crystal (ρ = 0.61 gcm^{-3}) and is comparable to that of other hydrogen storage materials such as sodium alanate (~0.5 $Wm^{-1}K^{-1}$). Since higher thermal conductivities are desirable, the addition of conductive additives such as graphite or aluminum (e.g. graphite has a thermal conductivity of 1390 $Wm^{-1}K^{-1}$

at 400 K) are required to improve heat transfer. The augmentation of materials for improved thermal conductivity is extensively developed and discussed in section 5.6.

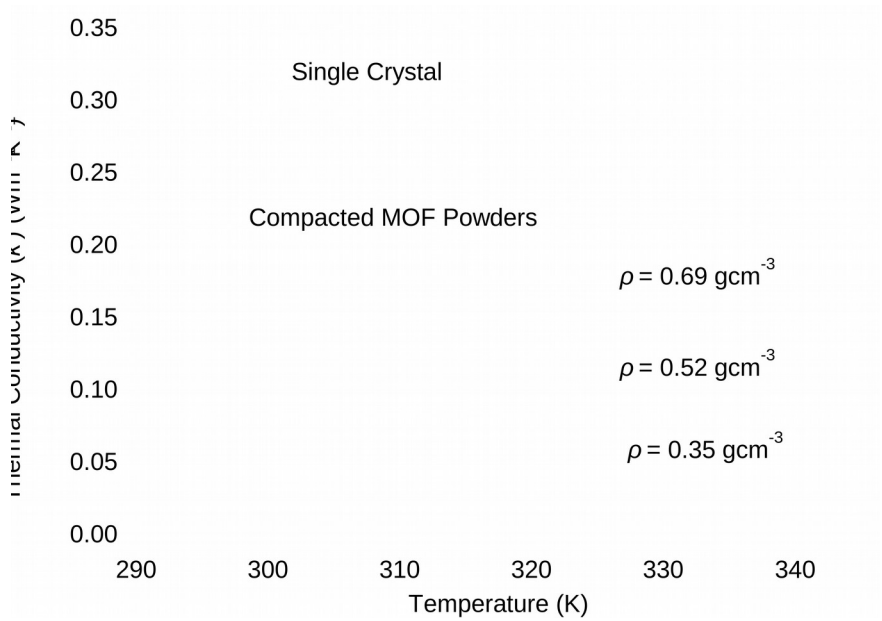

Figure 5.4(8) Thermal conductivity data for MOF-5 powders as a function of temperature and bulk density: 0.35 g cm^{-3} (diamonds), 0.52 g cm^{-3} (triangles) and 0.69 g cm^{-3} (circles). The thermal conductivity for a single crystal of MOF-5 at 300 K (square) is provided for reference.

It should be acknowledged these thermal conductivity measurements along with section 5.6 are based on characterizing strictly the material without the influence of hydrogen. In the application, the thermal conductivity of hydrogen should be considered since hydrogen has the highest thermal conductivity among other gases. Hydrogen thermal conductivity as shown in Figure 5.4(9) ranges from 0.08 to 0.15 $Wm^{-1}K^{-1}$ within the operating conditions of interest for an adsorbent system. Semelsberger *et al* as part of the HSECoE conducted thermal conductivity measurements of MOF-5 in combination with hydrogen at the desired temperature and pressure conditions for an adsorbent system. The transient plane source technique was used to measure the *in-situ* thermal conductivity measurement at temperatures from -180 to 40 °C and pressures from 0 to 100 bar. The result was a two times increase in the thermal properties within the initial 10 bar of hydrogen compared to the neat material measurements at ambient pressures. The experiments were also conducted with helium that exhibited a reduction in performance concluding the gas-specific thermal properties of hydrogen along with pressure effect directly influence the thermal conductivity.

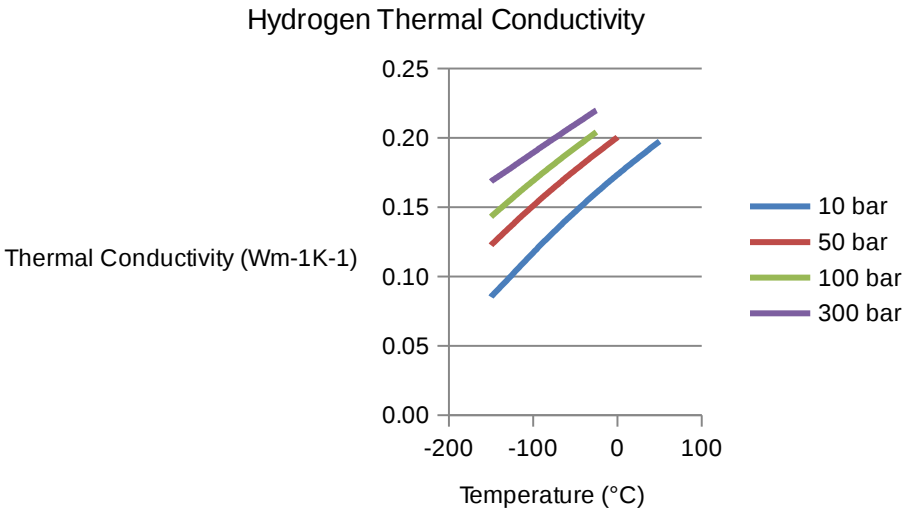

Figure 5.4(9) Thermal conductivity data for hydrogen as a function of temperature at various pressures. Source: NIST Reference Fluid Thermodynamic and Transport Properties Database (REFPROP): Version 8.0

5.4.7 Hydrogen Adsorption Isotherms

Hydrogen isotherm data is essential for constructing system models for capacity and dormancy under various operating scenarios. Toward this end, materials-level models that can describe empirical hydrogen adsorption isotherm data are needed. In this work, a continuous flow controlled cryostat is employed for collection of adsorption data at several intermediate temperatures: 103, 118, and 138 K. Cryogenic baths are used for 77 K and 200 K, while measurements at 295 K are performed without active temperature control. The resulting data is then used to determine model parameters that in turn provide an analytic expression for the adsorption properties in MOF-5 at arbitrary temperatures.

Modeling approach. Most thermodynamics-based adsorption models (with the exception of the Ono-Kondo lattice model) specify the adsorption amount in terms of a surface coverage or site occupancy, both of which are types of *absolute adsorption*. What is experimentally measured however is the *excess adsorption* amount. Trying to reconcile these two different formulations of adsorption has been a major roadblock to modeling supercritical hydrogen adsorption, since the absolute and excess adsorption diverge at higher pressures (e.g., higher ρ_g values). The pragmatic solution adopted for this project has been to utilize an effective adsorbate volume (v_a) which is determined by fitting to H_2 isotherms measured over at least four or more temperatures. We recall from Sec 5.4.4, that the excess and absolute adsorption can be equated by

$$n_{ex} = n_a - \rho_g v_a \qquad (5.4.17)$$

where v_a is the volume occupied by the adsorbed phase. While there may be some concerns about this modeling approach from a theoretical viewpoint, this approach has proved very pragmatic.

The Dubinin-Astakhov (D-A) model is pore-filling model for adsorption of subcritical gases in microporous adsorbents, i.e., those whose pore diameter is less than 2 nm. This model has been adapted to describe supercritical H_2 adsorption for a variety of microporous materials (e.g. carbons and MOFs). For these compounds the adsorption enthalpy is influenced by the superposition of attractive forces from neighboring walls of the adsorbent. In such microporous materials, the adsorption process is often interpreted as a volume of liquid adsorbate filling the pores. The D-A model can be readily applied to most MOFs given that their pore diameters (0.5 to 1.5 nm) fall within the applicable range. (The diameters of the two pores in MOF-5 are 1.5 and 1.1 nm.). We convert the D-A model to units of excess adsorption using the approach described above,

$$n_{ex} = n_{max} \exp\left[-\left(\frac{RT}{a+bT}\right)^m \ln\left(\frac{p_s}{p}\right)^m\right] - p_g v_a \qquad (5.4.18)$$

where α and β are considered as the enthalpy and entropy contributions to the characteristic free energy of adsorption, $m=2$ is a heterogeneity factor, and p_0 is considered as a pseudo-saturation pressure (conceptually, it's the saturation pressure extrapolated to supercritical conditions. Despite some difficulties in applying it to MOF-5, this modified D-A model was selected by the center as a lumped-parameter-model which captures the essential adsorption thermodynamics of the H_2/MOF-5 system (allowing it to be used as a module within a higher-level system model).

Experimental and modeling results for excess capacity. The excess hydrogen adsorption by MOF-5 as a function of temperature (77 to 295 K) and pressure (0 to 100 bar) is shown in Figure 5.4(9). The storage capacities are expressed as excess gravimetric capacity (expressed as wt.%) and excess volumetric capacity ($g \cdot H_2/L \cdot$MOF-5). The experimental data are represented by symbols and the modeled fits by the solid lines. The measured excess adsorption at 77 K shows a maximum value of 5.7 wt. % (29.9 mol/kg) at 48 bar.

Parametric description of the excess hydrogen stored in MOF-5 as a function of temperature and pressure was achieved by fitting the modified D-A model. Values for the five parameters were obtained by non-linear regression using the measured isotherm data at 77, 138, 200 and 295 K. The resulting values for the model parameters are listed in Table 5.4(5), and the fits are represented as solid lines. As shown in the table below, the fitted parameters are of comparable magnitude to those previously established for microporous activated carbons (AX-21, CNS-201) and a Cu MOF with an exposed unsaturated metal centers (HKUST-1).

Table 5.4(5): Fit parameters of the modified D-A model [Richard, 2009] for different adsorbent materials.

Parameters	Units	MOF-5[1]	AX-21[2]	CNS-201[3]	HKUST-1[3]
n_{max}	mol/kg	125.4	71.6	24.5	34.7
a	J/mol	2239	3080	4750	4430
b	J/mol·K	19.5	18.9	16.7	14.1
v_a	cm^3/g	2.01	1.43	0.485	0.648
p_0	bar	16920	14700	21100	12900
m	—	2	2	2	2

[1]Our measurements; [2]from [Chahine, R., 2009, Adsorption]; [3]from [Chahine, R., 2009, AIChE]

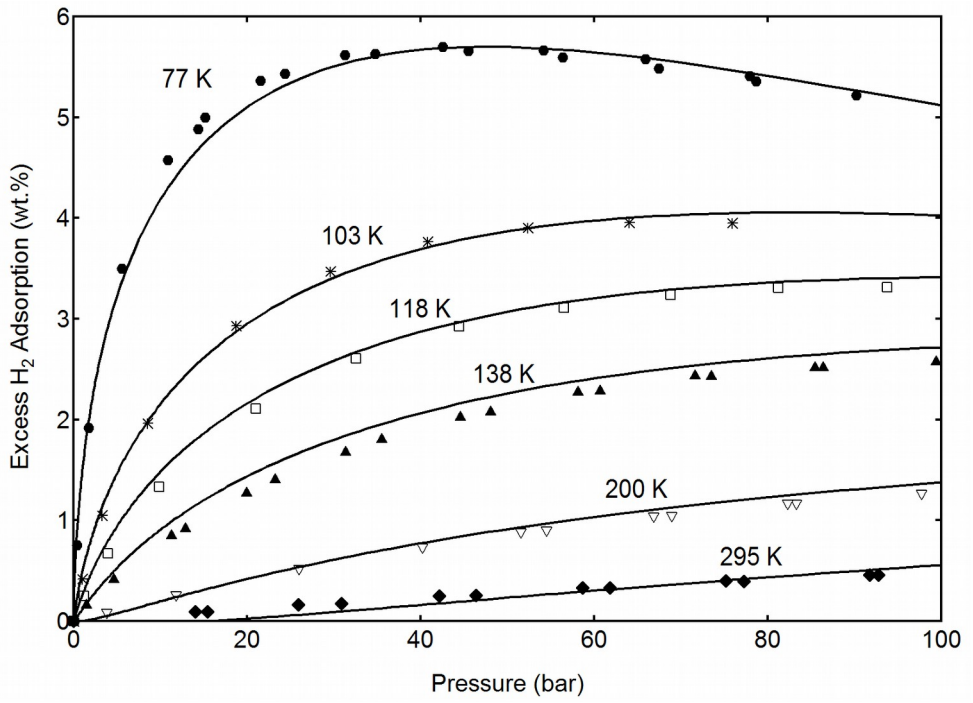

Figure 5.4(9) Excess hydrogen adsorption isotherms for powder MOF-5 at five temperatures (77, 103, 118, 138, 200 and 295 K). Measured data corresponds to symbol points, and solid lines are fits using the modified D-A equation using the specified fit parameters. Gravimetric excess H_2 adsorption in wt. %.

The D-A model parameters for MOF-5 reproduce the empirical data across the most of the temperature-pressure conditions shown in Figure 5.4.(9), although there are some visible discrepancies at higher temperatures. Nevertheless the original intent of the various adsorption models was to impart physical insight into the adsorption process. Given the empirical nature of the model, its various modifications, and its applicability to the MOF materials class, the clear physical meaning of the parameters becomes more ambiguous. In particular, we find the fitted adsorbate volume ($v_a = 2.01$ ml/g) is significantly larger than both the intra-crystalline free volume (given by $1/\rho_{crys} - 1/\rho_{sk} = 1.16\,\text{ml/g}$), and the experimentally-measured total N_2 pore volume ($V_{micro} = 1.2$ ml/g).

The modeled excess adsorption at 295 K is negative below a pressure of approximately 20 bar. Thus caution should be exercised in applying these parameterizations to operating conditions outside of the ones used here. Other models, including the Unilan model, have been found to better describe H_2 adsorption by MOF-5 over a wider temperature range.

Adsorption Enthalpy. The term *differential enthalpy* of excess adsorption is often used interchangeably with the term *isosteric heat*, and we denote it as $\Delta \acute{h}_{ex}$ to be consistent with [Rouquerol, 1999]. Conceptually, it is the change in adsorbate enthalpy after an infinitesimal increase in the excess adsorption amount $d n_{ex}$ at constant temperature and volume. In other words, the amount of heat that is released during H_2 adsorption is related to $\Delta \acute{h}_{ex}$. Therefore, $\Delta \acute{h}_{ex}$ is an important parameter that, together with thermal attributes discussed in Sec 5.4.x, affects the overall design and performance of on-board and/or forecourt thermal management systems. In this section we calculate $\Delta \acute{h}_{ex}$ as a function of excess hydrogen adsorption in MOF-5 by applying the Clausius-Clapeyron equation to the excess adsorption isotherms in Fig. 5.4(9).

Isosteric heats derived from experimental excess adsorption data (particularly at supercritical conditions) are very sensitive to both the data accuracy and the calculation method. For that reason we have included our methodology for calculating it. The first step is to interpolate the $n_{ex}(T, p)$ data so that they can be sliced along constant n_{ex} lines (which are called *isosteres*). For this purpose, we re-plot the MOF-5 isotherms in Fig.

5.4(10) with excess adsorption on the *x*-axis (log-scale) and equilibrium pressure on the *y*-axis (log-scale). Log scale is used here because many of the important data points occur at low pressures which are difficult to discern on a linear scale plot of the isotherms. Data points at higher pressures for the 77 K, 103 K, and 118 K isotherms are masked from the fits, as they are not useful for estimating the adsorption enthalpy by the isosteric method. To minimize bias from models, each isotherm is fitted individually to a rational function of the form

$$p = \frac{a \cdot n + b \cdot n^2 + c \cdot n^3}{1 + d \cdot n + e \cdot n^2} \tag{5.4.19}$$

where n is the excess adsorption, p is the equilibrium pressure, and $\{a, b, c, d, e\}$ are coefficients to be fitted. The 77 K isotherms shown in panel (a) include low pressure data measured with a high-resolution pressure gauge for improved accuracy, but which are not shown in Fig. 5.4(9). The points where the dashed vertical lines intersect the fitted curves at each temperature represent the isosteres.

Plots of the isosteres for excess adsorption amounts (n_{ex}= 1,3,5,…,13 mol/kg) at the temperatures 77, 103 and 118 K are plotted along with the linear fits are shown in panel (b) of Fig 5.4(10). The isosteric heat is estimated from the slope of the linear fits using the Clausius-Clapeyron equation,

$$-\Delta \acute{h}_{ex} = R \left[\frac{\partial \ln p}{\partial (1/T)} \right]_{n_{ex}} \tag{5.4.20}$$

where it is assumed that the differential enthalpy is constant over a small temperature interval. This equation is an approximate form of the exact Clausius-Clapeyron equation

$$\left[\frac{\partial p}{\partial T} \right]_{n_a} = \frac{\Delta \acute{h}}{T \Delta v} \tag{5.4.21}$$

where Δv is the difference in molar volume between the gas and adsorbed phases and n_a is the absolute surface coverage. The approximate form is derived by assuming the molar volume of the adsorbed phase is negligibly small compared to that of the gas, and that the gas molar volume is given by the ideal gas law, (i.e., $\Delta v = RT/P$). We note that these two assumptions are more valid at low pressures and higher temperatures.

To illustrate the sensitivity of the experimental $\Delta \acute{h}_{ex}$ to the calculation method, 3 different estimates of the isosteric heat are plotted in Panel C of Figure 5.4(10). The three estimates differs in terms of the temperature range included in the isosteres. A larger temperature range can increase accuracy by including more data isostere points in each linear regression fit. However, too large of a temperature range may be inconsistent the assumption of a constant differential enthalpy. A temperature range of 10 K between the three isotherms is considered a good compromise [Rouquerol, 1999]. As shown in the plot, all three estimates are relatively consistent at small adsorption amounts. The experimental differential enthalpies actually start to increase at higher loadings. This occurs when the isosteric method is applied to excess adsorption at supercritical temperatures, and is due to the fact that the excess adsorption curves have a maximum value.

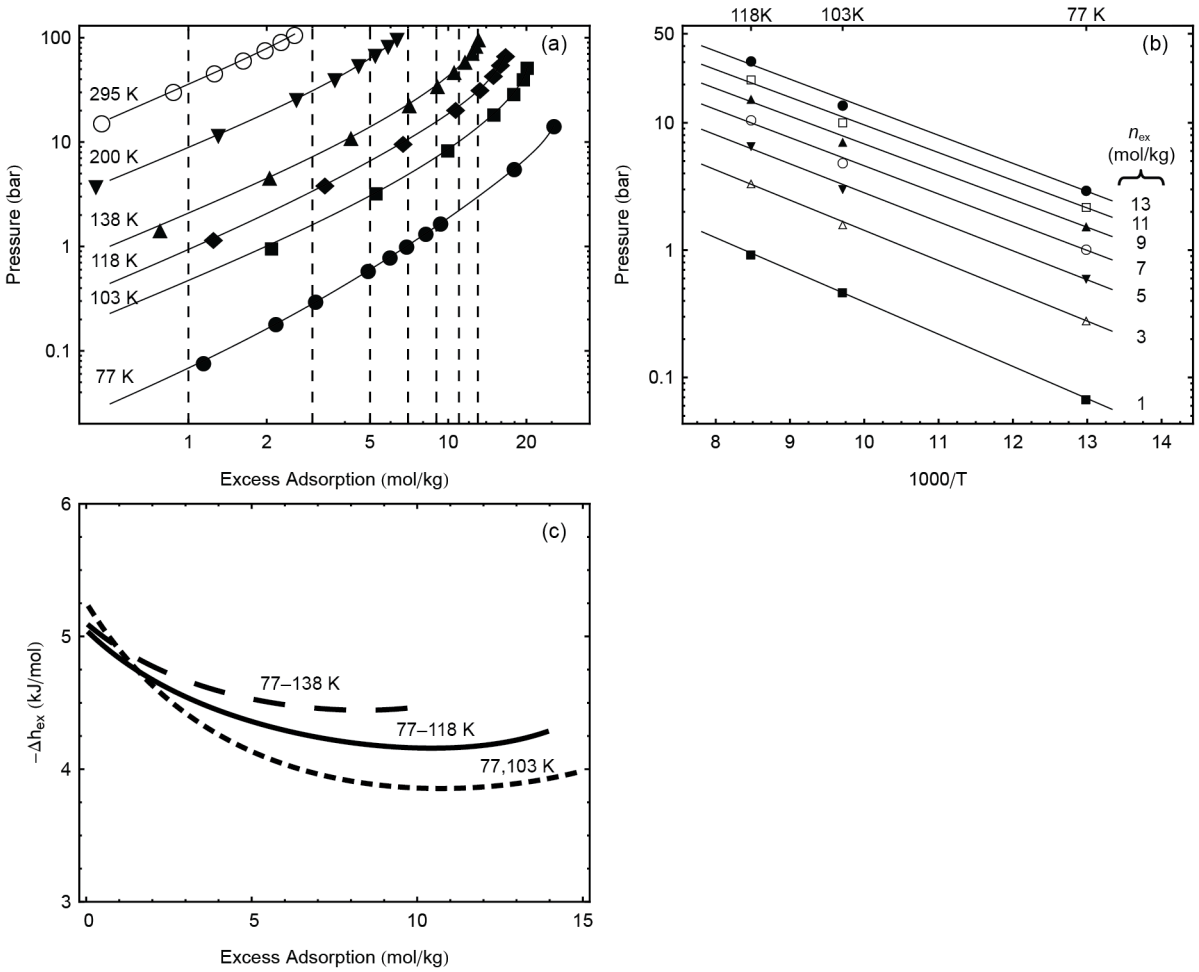

Figure 5.4(10) Calculation of the isosteric heat for H_2 adsorption in MOF-5 from excess adsorption isotherms measured between 77 K and 298 K.

The isosteric heat can be calculated analytically for the modified D-A model as a function of absolute adsorption:

$$\Delta \acute{h}_a = -a\sqrt{-\ln\left(\frac{n_a}{n_{max}}\right)} \qquad (5.4.22)$$

Equation 5.4.22 is plotted in Figure 5.4(11) using the D-A parameters listed in Table 5.4(5). At low pressures, the excess and absolute adsorption amounts are similar, and thus the experimental and modeled $\Delta \acute{h}_a$ can be directly compared. Agreement between the experimental and modeled enthalpy is fairly good. These results confirm that adsorption models such (as the D-A model) can be effective in describing the thermodynamic properties of hydrogen adsorption in MOF-5. With care, these D-A parameter values can be used in the heat/mass balance equations in a hydrogen storage model for MOF-5.

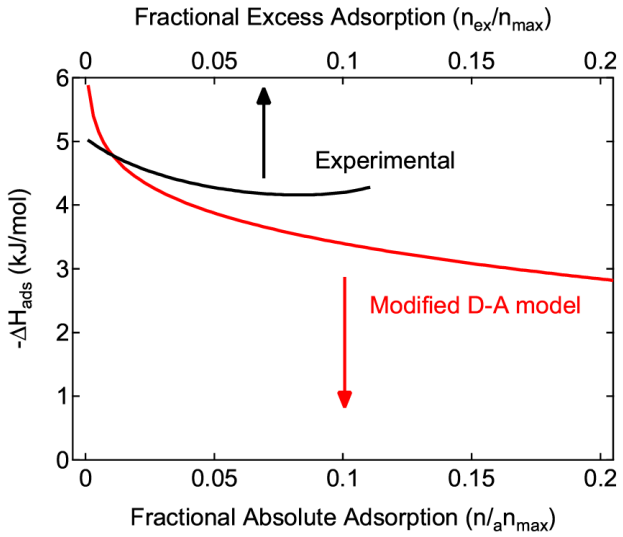

Figure 5.4(11). Differential H_2 adsorption enthalpy ($-\Delta H_{ads}$) of powder MOF-5. Experimental estimates of $-\Delta H_{ads}$ are plotted on the top axis versus the fractional excess adsorption. The modeled $-\Delta H_{ads}$ is plotted on the bottom axis versus fractional absolute adsorption.

Shortcomings of modified D-A Model for MOF-5:

Modified D-A model: Conceptually, the D-A model considers the adsorbed species within the micropores as similar to a liquid, although with properties that differ from the bulk liquid due to the presence of the adsorbent forcefield. It is considered a pore-filling model because the adsorbed volume of fluid is correlated to the differential molar work of adsorption. When the D-A model is modified for excess adsorption within a constant adsorbate volume, the resulting equation is given by

$$n_{ex} = n_{max} \exp\left[-\left(\frac{RT}{a+bT}\right)^m \ln\left(\frac{p_s}{p}\right)^m\right] - p_g v_a \qquad (5.4.23)$$

where $E = a + bT$ is the characteristic energy of adsorption (i.e., assumed here to vary linearly with temperature), p_s is a pseudo-saturation pressure, and m can be interpreted as a micropore heterogeneity parameter. A value of $m = 2$ appears adequate to describe hydrogen adsorption on the activated carbons AX-21 and CNS-201, and Cu-BTC (i.e., HKUST-1). For subcritical adsorption, the adsorption potential $A = -RT \ln(p/p_{sat})$ is considered as the difference in free energy between the adsorbate phase and the saturated liquid at the same temperature (i.e., the differential molar work of adsorption).

At supercritical temperatures a pseudo-saturation pressure is used in place of p_s. Various methods of extrapolating the saturation pressure to supercritical temperatures have been proposed. One of the attractions of the D-A model is that the characteristic free energy E is generally temperature-invariant in the absence of adsorbent-adsorbate interactions. For a non-polar adsorbate such as H_2, however, small temperature variations of E has been rationalized as the entropic contribution to the free energy. The linear variation $E = a + bT$ assumed in Eq. 5.4.23 has been found to work well empirically for hydrogen adsorption in activated carbons. An inherent weakness of the D-A model is that it does not reduce to Henry's law in the low concentration limit. Further, the absolute differential enthalpy of adsorption derived from the modified D-A model using the Clausius-Clapeyron equation has a logarithmic singularity at $n_a = 0$.

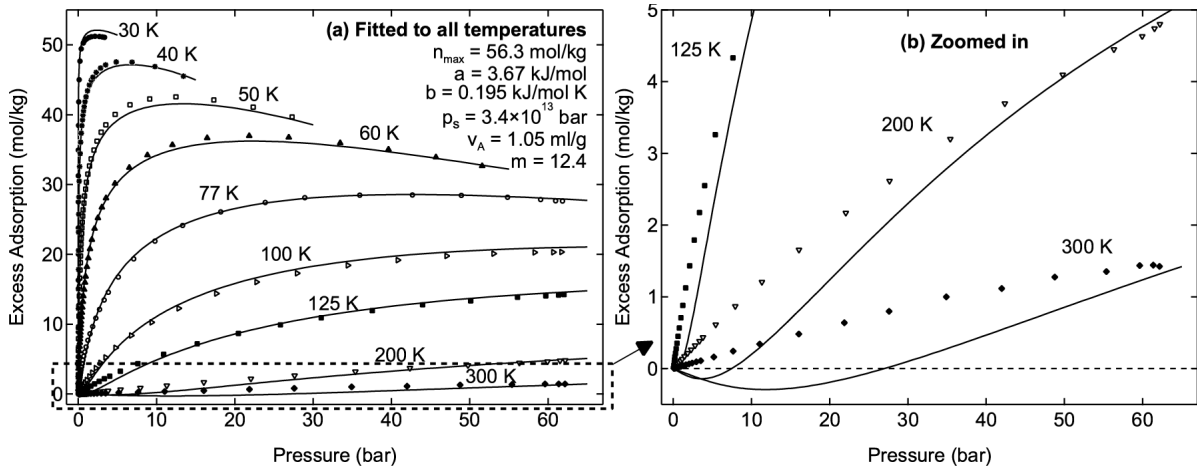

Figure 5.4(12). Fits of the modified D-A equation (Eq. 5.4.23) to experimental MOF-5 isotherms from Ref. [Zhou, 2007] (a) Model fitted to all temperatures with no constraint on m. (b) Same fits, zoomed in to the adsorption range 0–5 mol/kg

While the modified D-A model has been found to work well for activated carbons such as AX-21 over a wide temperature range, we found that it is not particularly effective for modelling hydrogen adsorption in crystalline porous materials such as MOF-5 which lack strong adsorption sites.

We evaluated the effectiveness of the modified D-A model on a set of benchmark MOF-5 hydrogen adsorption isotherms available over a wide temperature range of 30 to 300 K [Zhou, 2007]. We attempted to fit the modified D-A model to the reference data using many different approaches, such as fitting only to high and low temperature data, and fitting only to 77 K – 300 K data. A representative fit to the complete 30 K -300 K reference data set is displayed above in Fig. 5.4(12). Full detail on other fits is available in the Supporting Information section of an earlier article [Purewal, 2012].

We concluded it was impossible to accurately fit MOF-5 isotherms across the entire temperature range while keeping the heterogeneity parameter fixed at $m=2$. One frustrating feature of the model is that is yields negative adsorption values for MOF-5 at 200 K and 300 K. To reasonably fit the MOF-5 isotherm across the entire temperature range, it was necessary to set $m=12.4$, as shown in Fig. 5.4(12).

However, this results in an unrealistically large values for the characteristic free energy, $E=3.67+0.195\times T$, with values of 18.6 kJ/mol at 77 K and 61.2 kJ/mol at 295 K. As visible in the figure, the model at 300 K is actually negative up to a pressure of 27 bar, and has an unusual convex curvature. The assumptions of a temperature-independent p_s and a linear temperature variation for $E=a+bT$ cause the modified D-A model to consistently underestimate the adsorbate density at 200 K and 300 K, resulting in negative excess adsorption values at low pressures.

To obtain satisfactory fits for Eq. 5.4.23 to MOF-5 across the complete 30 K – 300 K temperature range, while retaining reasonable values for the model parameters, it is necessary to fit p_s and E independently for each temperature. The temperature variation of p_s is described by a power law expression, varying by five orders of magnitude between 30 K and 300 K. It appears that E does not vary linearly with temperature as originally assumed, but is described instead by a second order polynomial, increasing from 2.4 kJ/mol at 30 K, to 18.2 kJ/mol at 300 K.

These results demonstrate that the modified D-A model is not an effective tool for modeling H_2 adsorption in MOF-5 over a wide temperature range. Since the empirical temperature variations of p_s and E are not known in advance, a total of twenty one adjustable parameters are required to fit the nine experimental temperatures (since p_s and E are fitted independently for each temperature, they contribute 18 of the parameters).

The unexpected temperature dependence of the p_s and E parameters is more than just an inconvenience however. The thermodynamic properties derived from the modified D-A model, (which are required by the system model), assume a linear variation of E versus temperature and a constant p_s value.

Non-modified D-A model: The original, unmodified D-A model has been previously applied to MOF-5 hydrogen uptake over a limited 50–87 K temperature range. Instead of assuming a constant adsorbate volume, as in Eq. 5.4.23, the fractional volume-filling interpretation is used in which micropores are gradually filled with a liquid-like hydrogen adsorbate phases, similar in density to liquid hydrogen but with a thermal expansion factor. The adsorbate specific volume increases with the adsorption amount up to a maximum of v_a . Excess adsorption then has a clear meaning as the difference between the adsorbate and gas density within the adsorbate volume,

$$n_{ex} = (p_a - p_g) v_a \exp\left[-\left(\frac{RT}{E}\ln\frac{p_s}{p}\right)^m\right] \tag{5.4.24}$$

where the adsorbate density and pseudo-saturation pressure are both assumed to vary with temperature according to

$$\rho_a \wedge ¿ \rho_0 \exp\left[-a(T - T_0)\right]$$
$$p_s \wedge ¿ p_c \left(\frac{T}{T_c}\right)^\gamma \tag{5.4.25}$$

We tested the fits of the Eqs. 5.4.24-25 using the same set of benchmark MOF-5 isotherms.

Two representative fits are shown in Fig. 5.4(13). As is apparent from both panels below, this model is useful for describing narrow, cryogenic temperature ranges such as 50–100 K. But at higher temperatures, the assumption of a liquid-like hydrogen adsorbate phase cannot fit data between 125 K and 300 K.

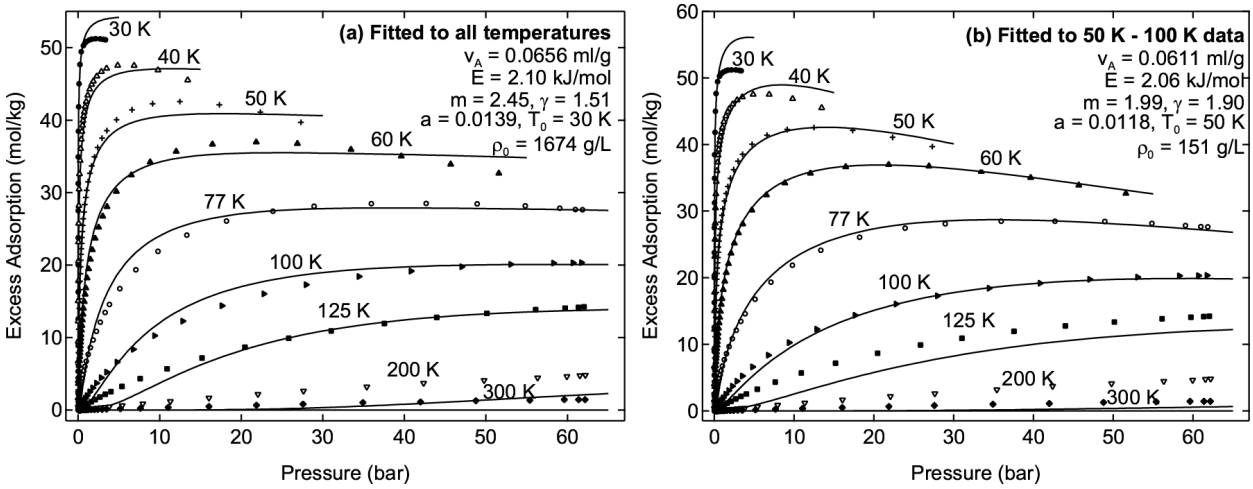

Figure 5.4(13). Fits of the D-A equation (Eq. 5.4.24) to the benchmark MOF-5 experimental hydrogen adsorption data from Reference [Zhou, 2007]. (a) Model fitted over the complete data set, including all the temperatures (b) Model fitted only to data between 50 K and 100 K temperature range.

In panel (a), where the model was fitted to all temperatures, the fidelity between model and experimental data was poor for all temperatures. Further, this approach yielded unrealistic values for some parameters, such as a characteristic adsorbate density $\rho_0 = 1674\ \text{g/L}$. In panel (b) of the same figure, the model was fitted only to the 50–100 K data, resulting in poor fits outside of that temperature range.

To obtain satisfactory fits of Eqs. 5.4.24-25 across a wide temperature range, it is necessary to fit the characteristic free energy E independently for each temperature. However, the temperature variation of E is not known beforehand (which defeats the main advantage of the D-A model in furnishing a single, temperature-invariant characteristic adsorption energy). Therefore, a total of *fourteen* adjustable parameters are required to effectively fit Eq. 5.4.24 to the *nine* experimental temperatures in the MOF-5 reference isotherms. These results suggest this model is not a significant improvement upon the modified D-A equation (Eq. 5.4.23) in terms of fitting MOF-5 hydrogen isotherms across a wide temperature range.

The Unilan Model—An Alternative Model for MOF-5: In light of the limitations of the pore-filling models in reproducing the MOF-5 experimental isotherms, we have investigated whether MOF-5 hydrogen adsorption isotherms may be better described by monolayer models. The motivation for this is that the MOF-5 crystalline pore structure contains comparatively large channels (7.8 Å) and pore cavities (12.1 Å and 15.2 Å), and lacks unscreened CUMC sites, resulting in lower adsorption at low pressures. The simplest surface adsorption model is the Langmuir equation, where absolute adsorption is given by

$$n_a = \frac{n_{max}}{1 + K/p} \tag{5.4.26}$$

The equilibrium constant is given by

$$K = p^\circ \exp\left(\frac{-\Delta S}{R} + \frac{\Delta H}{RT}\right), \tag{5.4.27}$$

where ΔH is equal to the (constant) molar differential enthalpy of adsorption, and ΔS can interpreted as the molar integral entropy at $n_a = n_{max}$. The standard-state pressure is $p^\circ = 1\,\text{bar}$.

The Langmuir model neglects surface heterogeneity and therefore does not provide a realistic description of supercritical hydrogen adsorption by most microporous materials. However fitting data to a superposition of two Langmuir isotherms typically provides good fits to supercritical adsorption isotherms across broad temperature ranges. For integrating into system-level models, it is preferable to develop an adsorption model which has fewer parameters (e.g., than a superposition of two or more Langmuir isotherms) and for which there is a clearer physical interpretation of the parameter values.

The Unilan model (i.e., *uni*form energy distribution and *Lan*gmuir local isotherm) is an attractive empirical model for describing hydrogen adsorption in MOF-5. It can be classified as a monolayer adsorption model since it uses the (monolayer) Langmuir equation as to describe the local isotherms. This model treats energetic heterogeneity by assuming a uniform distribution of adsorption enthalpies between E_{max} and E_{min}, and zero elsewhere. The probability density function that an adsorption site has enthalpy q is given by,

$$N(q) = \begin{cases} \dfrac{1}{(E_{max} - E_{min})} & \text{if} \quad E_{min} < q < E_{max} \\ 0 & \text{if} \quad \text{elsewhere} \end{cases} \tag{5.4.28}$$

where the positive-valued q has been substituted for $-\Delta H$. Adsorption at a local site with enthalpy q is assumed to follow the Langmuir equation. Rather than taking a discrete superposition of Langmuir equations, this model instead averages the Langmuir equation over a continuous interval from E_{min} to E_{max}.

The expression for the Unilan model is obtained by evaluating the average

$$n_a \wedge ¿ n_{max} \int_0^{\infty} \frac{N(q)}{1+\frac{a}{p}\exp\left(\frac{-q}{RT}\right)} dq$$

$$¿ = \frac{n_{max} RT}{E_{max} - E_{min}} \ln\left(\frac{a + p\exp\left(\frac{E_{max}}{RT}\right)}{a + p\exp\left(\frac{E_{min}}{RT}\right)}\right) \qquad (5.4.29)$$

where $a = \exp(-\Delta S/R)$. The function increases monotonically versus p, and meets the required properties $n_a(0) = 0$ and $n_a(\infty) = n_{max}$. As required, it reduces to Henry's law (i.e., $n_a = k_H p$) to first order in p in the limit of low pressure. An implicit assumption is that the adsorption entropy is constant for all sorption sites. To calculate the excess adsorption, the standard expression $n_{ex} = n_a - \rho_g v_a$ is used. When fitted to excess adsorption data, therefore, the Unilan model contains five temperature-independent parameters: { ΔS , E_{max} , E_{min} , n_{max} , v_a }.

A fit of the Unilan model to reference powder MOF-5 isotherms at all temperatures is displayed in Fig. 5.4(14). The fit quality for the Unilan model clearly outperforms that of the D-A models. Further, the fit parameters have physically-meaningful values. The entropy difference ($-7.8R$) is very close to the $-8R$ value that is typically observed for H_2 adsorption in many adsorbents. The values of E_{max} (4.63 kJ/mol) and E_{min} (2.14 kJ/mol) are consistent with the reported experimental values of the MOF-5 isosteric heat (which decreases from 4.8 kJ/mol to 3.3 kJ/mol). The estimated adsorbate volume v_a varies between 1.2 g/cm^3 and 1.4 g/cm^3 depending on the fit criteria, consistent with the open pore volumes that we have measured for various batches of MOF-5. Unlike the modified D-A models, the Unilan model accurately predicts hydrogen adsorption near room temperature with no negative values.

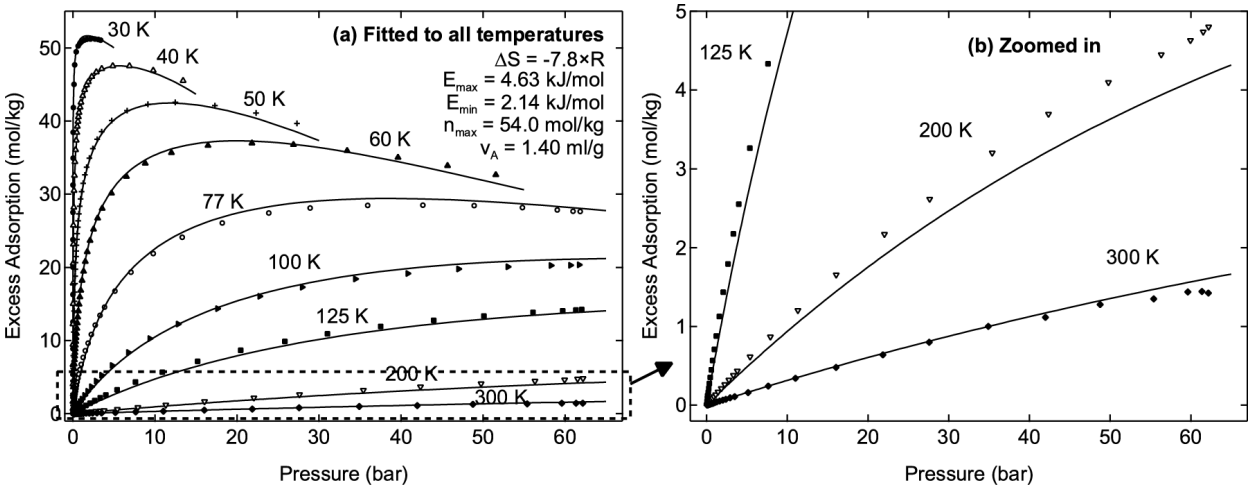

Figure 5.4(14): Fits of the Unilan equation to the benchmark experimental MOF-5 isotherm data from Reference [Zhou, 2007]. (a) Model fitted to all temperatures. (b) Same fits, zoomed in to the excess adsorption range of 0–5 mol/kg

Using only five temperature-independent parameters, and without recourse to a pseudo-saturation pressure parameter, the Unilan model provides an accurate description of supercritical hydrogen adsorption across a wide temperature range. (Presumably, the fits could be improved even further by allowing either ΔS or ΔH to vary with temperature, but this appears unnecessary.) Furthermore, parameters determined from fits only to the 77 K, 200 K and 300 K temperatures still provide accurate estimates for intermediate temperatures between those limits (see the Supporting Information for [Purewal, 2012] for additional details).

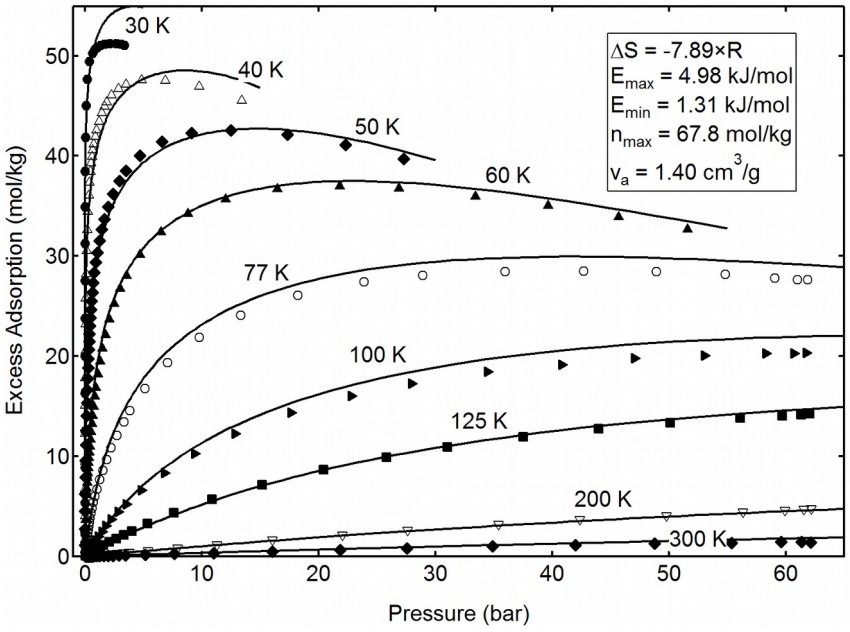

Figure 5.4(15). Modeled MOF-5 isotherms (lines) were based on fits to Ford data. They are compared against reference MOF-5 isotherms (markers).

A cross-comparison between our modeled isotherms for powder MOF-5, and the reference MOF-5 isotherms [Zhou, 2007] is displayed in Figure 5.4(15).

- The solid lines in the figure above correspond to the Unilan model fitted to excess adsorption data measured in our laboratory between temperatures of 77 K and 295 K, using a powder MOF-5 sample synthesized and activated by BASF. The Unilan model was then evaluated at the temperatures presented in the reference data.
- The reference data, in contrast, was measured on a well-validated Sieverts instrument at NIST (Gaithersburg MA) between 30 K and 300 K, using an independently synthesized MOF-5 sample.
- The agreement between the two data sets is quite good down to a temperature of 40 K. The excellent agreement between the two data sets is somewhat surprising, given the large variability in published MOF-5 data in the recent past.

In concluding this section we note that the maximum adsorbate density ($n_{max}/v_a = 77$ g/L) predicted by the Unilan model exceeds the density of liquid H_2 at the 20.1 K and 1 bar pressure (71 g/L). Interestingly, the predicted adsorbate density is close to the density of liquid H_2 at 21 K and 70 bar (77.2 g/L). Due to the large compressibility of liquid (and solid) hydrogen, it is reasonable that at higher pressures the hydrogen adsorbate density within MOF-5 pores may exceed the liquid H_2 density at 1 bar, and approach the densities of liquid H_2 at high pressures.

5.5 Compaction

5.5.1 Introduction: Total hydrogen storage capacity (on a volumetric basis) is the metric which is most relevant from a system perspective. As described earlier in Section 5.4.5, the total capacity includes both the excess adsorbed hydrogen plus the bulk hydrogen gas residing throughout the entire free volume (intra-crystalline pores, inter-crystalline voids, interstitial spaces). In short, it includes all of the hydrogen stored within a tank which has been fully packed with an adsorbent material. Since MOF-5 is synthesized as a powder with a low bulk packing density (0.13 to 0.2 g/cm^3), it is advantageous to process the powder into pellets or monoliths which minimize the presence of interstitial spaces and reducing the interfacial thermal resistance between loosely-packed particles. Ideally, a custom-molded MOF-5 monolith will completely fill the storage tank and have good thermal contact with system walls and heat exchangers.

5.5.2 Objectives: Compacted pellets, rather than loose powders, are attractive for on-board gas storage applications due to the greater *total volumetric* hydrogen storage density, enhanced thermal contract, and the improved ease of handling. Compacting microporous materials using a large mechanical force is known to reduce the micropore volume in MOFs and (even in activated carbons). This is due to pore collapse, pore blockage and (for MOFs) amorphization of crystal structure. In other words, MOF-5 compaction is expected to yield small reductions in the gravimetric hydrogen storage capacity. If this reduction is modest, however, it will be compensated by a larger increase in the volumetric capacity. By carefully controlling the final pellet density and applied compaction force, it therefore may be possible to optimize the total volumetric capacity.

5.5.3 Design: Pellets were prepared with bulk densities between 0.27 and 0.79 g/cm^3 from desolvated MOF-5 powder using a cylindrical punch and die set having a bore diameter of either 6.35 mm, 4.5 mm or 12.7 mm. A specified mass of powder was loaded into a cylindrical die and compressed using a manual pellet press. The resulting pellets are cylindrical with flat ends. By raising or lowering the anvil which supports the die, it is possible to control the penetrating depth of the punch and thereby control the final pellet thickness. Pellet bulk densities are calculated from the mass and geometric dimensions of individual pellets. Maximum error in the measured pellet density is approximately 3%.

All handling of the material was done inside a high-purity glovebox with an H_2O and O_2 concentration below 0.1 ppm. Particles of MOF-5 cohere well and it is not necessary to introduce binder additives to form pellets. Individual pellets typically weigh less than 100 mg, so it is necessary to produce a set of pellets of constant density in order to obtain a cumulative mass large enough for hydrogen adsorption measurements. The variation of the measured density within a single set of pellets is typically below 5%.

An additional set of pellets shown in Fig. 5.5(1) was prepared using a 6 mm die set and a 12 ton hydraulic press (Carver, 4350 manual pellet press). This bench-top press was located outside of the glovebox. To minimize exposure of the MOF-5 to humid air, dry nitrogen gas was blown across the sample during compaction.

Final pellet densities versus applied pressure (using pellets prepared with a 6 mm die and 12 ton hydraulic press) are summarized in Fig. 5.5(1). The approximate applied forces varied from 1.3 kN to 9.8 kN. As expected, the density does not increase indefinitely, but instead approaches a limiting value of 1.7 g/cm^3. This is nearly three times the single crystal density $\rho_{crys} = 0.61$ g/cm^3. The holding time for applied loads was typically 1 min, but it was not possible to control the pressure release rate with the manual pellet presses.

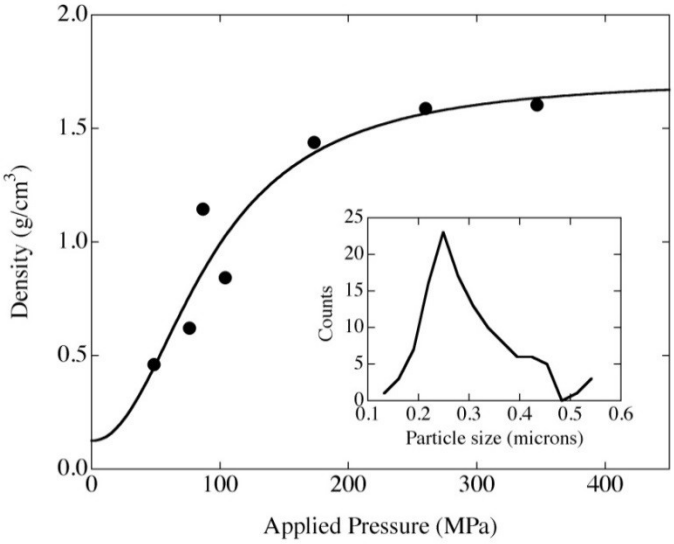

Figure 5.5(1): Density of MOF-5 pellets versus uniaxial compaction pressure. Pellets prepared in air using a 6 mm die set and a 12 ton hydraulic press. Inset: Particle size distribution of the MOF-5 powder used to prepare pellets.

5.5.4 Pellet Mechanical Robustness:
Mechanical strength is a consideration in determining an optimum pellet density. Pellets with inadequately low densities tend to crumble and break apart upon repeated handling. This is undesirable for pellets that have been designed to optimize heat transfer, kinetics, hydrogen density and other properties.

Crush strength measurements were performed on a mechanical testing system (Instron model 3366) equipped with a 500 N load cell following the procedure described ASTM D4179-01. For radial crush tests, pellets of diameter 0.635 cm and height 0.49 ± 0.01 cm were compressed on their side between two platen anvils at a rate of 0.5 mm/min until mechanical failure, detectable as a drop in applied load. Measurements were collected for 5 pellets of a given density

The radial crush strengths of several sets of identically sized MOF-5 pellets (within an error of 1%) are compared in Fig. 5.5(2). Pellets with a density of 0.31 g/cm^3 show almost no resistance to compressive loads applied along their radius. However, tablets with larger densities have greatly improved crush strength. For the 0.41 g/cm^3 pellets, the average crush strength was 24 N. This increases to 71 N and 106 N for pellets having densities of 0.51 g/cm^3 and 0.60 g/cm^3, respectively. A density of 0.4 g/cm^3 was found to be sufficient for routine handling (and even dropping on the floor). These findings were later used in preparing larger-scale MOF-5 pellets (31 mm and 50 mm diameter)

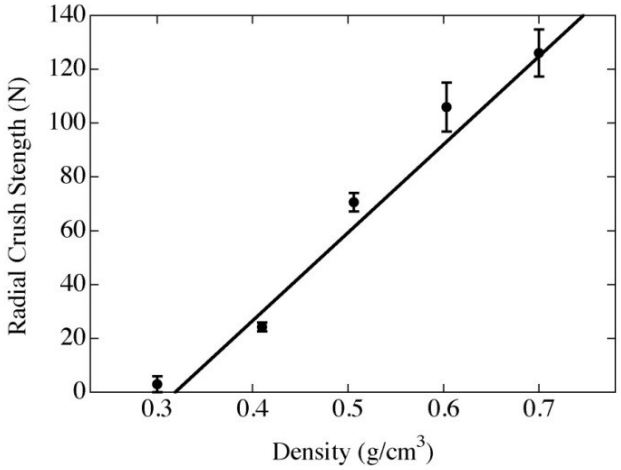

Figure 5.5(2): Radial crush strength of MOF-5 pellets as a function of pellet density.

5.5.5 Compaction Impact on MOF-5 Crystallinity: Figure 5.5(3) shows powder XRD curves for MOF-5 tablets with varying densities. While the intensities of the diffraction peaks decrease with density, there are no other notable changes in the XRD patterns except for a slight increase in the diffuse scattering. Although the MOF-5 crystal structure was previously reported to collapse to an amorphous phase at an applied pressure of 3.5 MPa [Zhang, 2010], this transformation is not observed here. Based on the calibration curve in Fig. 5.5.(1), a density of 0.75 g/cm^3 corresponds to an applied pressure of around 80 MPa. While the consistent decrease in diffraction intensity does indicate a progressive transformation from crystalline to amorphous, even at 0.75 g/cm^3 a considerable fraction of the crystalline phase remains intact. As evident in the Figure 5.5(3) inset, there is a slight shift decrease in d-spacing. We attribute this to sample displacement error due to the difficulty in getting pellets of the exact same thickness. It is not likely caused by an actual decrease in MOF-5 lattice parameter.

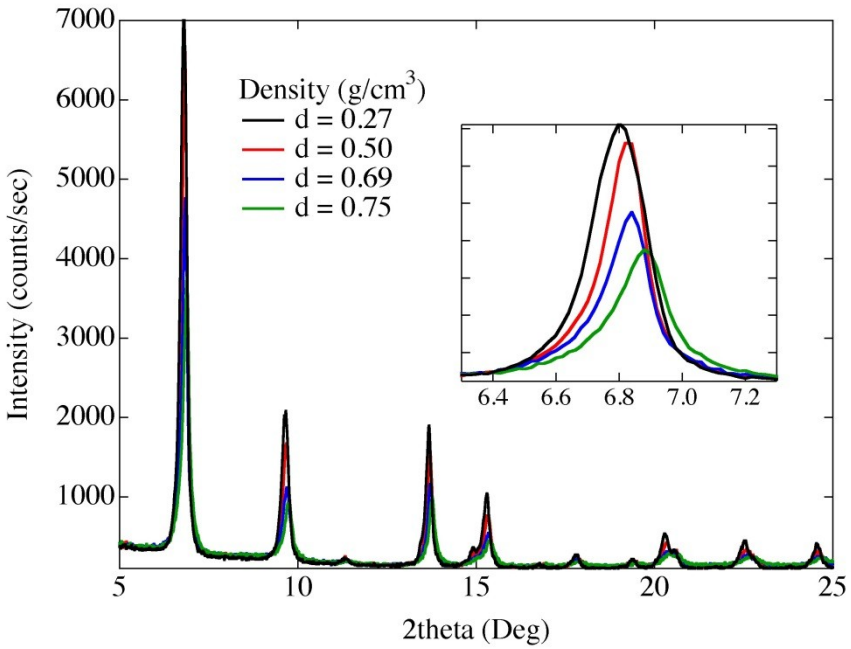

Figure 5.5(3): Powder X-ray diffraction patterns for MOF-5 pellets. Inset: magnified view of the 6.8° peak.

5.5.6 MOF-5 Density versus BET Surface Area:

Nitrogen isotherms at 77 K were measured for the MOF-5 pellets and were used to calculate the BET surface area and total pore volume. We note that the BET surface areas reported here were obtained by fitting to a pressure range of $\left[0.05 < p/p_0 < 0.2\right]$, which results in a significantly lower value for the BET surface area. However, direct comparisons between these values is still valid as all samples were fitted using the same p/p_0 range.

Compacting MOF-5 powder into pellets is expected to reduce the surface area and total pore volume. Figure 5.5(4) summarizes the variation of N_2 BET specific surface area versus pellet density for MOF-5. Up to a density of $\rho = 0.31$ g/cm^3 there is essentially no loss of surface area compared to the powder MOF-5. However, surface are and pore volume begin to decrease somewhere between 0.3 g/cm^3 and 0.4 g/cm^3. Pellets with densities of 0.51 g/cm^3 and 0.90 g/cm^3 exhibit a 18% and 57% decrease in surface area, respectively relative to the baseline surface area. Trends in total pore volume closely follow those for surface area.

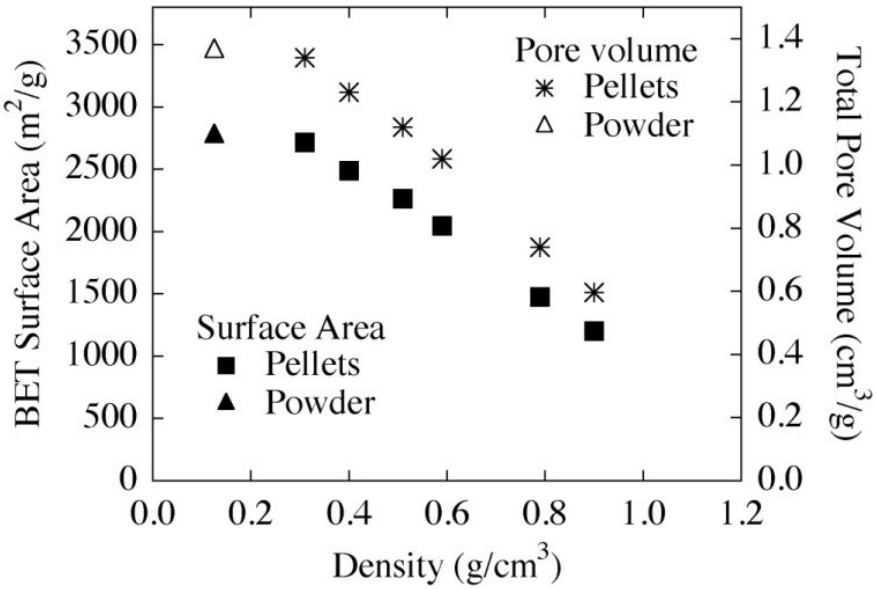

Figure 5.5(4): MOF-5 pellet BET specific surface area (▪) and total volume (▴) versus density. The BET surface area (□) and total volume (△) of powder MOF-5 is also shown.

Hydrogen adsorption properties for MOF-5 pellets are summarized in Figure 5.5(5). Excess adsorption is shown in the left pane, while total storage (volumetric) is displayed in the right panel. Not surprisingly, the excess adsorption follows the same trends as the BET surface area. The excess adsorption is essentially unchanged in the 0.31 g/cm^3 pellet relative to the powder. However, decreases of 15% and 42% are observed for the 0.51 g/cm^3 and 0.79 g/cm^3 samples, respectively. The onset of micropore loss appears to occur between a pellet density of 0.3 g/cm^3 and 0.4 g/cm^3, which is fully consistent with the trends visible in the N_2 surface area/pore volume data in the previous figure.

The total amount of hydrogen storage by MOF-5 pellets on a volumetric basis is shown in the right panel of Figure 5.5(5). For comparison, the bulk density of compressed H_2 gas at 77 K is included in the figure. While there is a notable improvement in total hydrogen storage going from powder to a low density $\rho_{env} = 0.31$ g/cm^3 pellet, further compaction appears to provide little benefit.

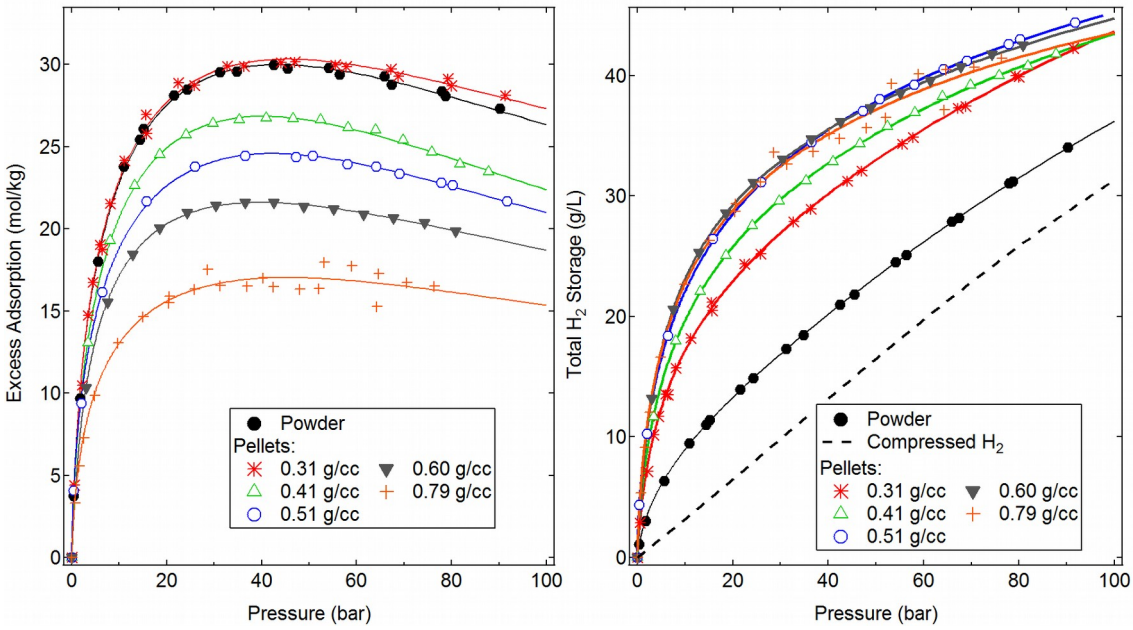

Figure 5.5(5): Excess hydrogen adsorption by MOF-5 powder ($\rho = 0.13$ g/cm^3) and of neat MOF-5 pellets of indicated densities at 77 K. Gravimetric adsorption (left) expressed in mol/kg, and volumetric storage (right) in g/L.

The improvement in total hydrogen storage produced through densification of MOF-5 powder is summarized more succinctly in Figure 5.5(6) below. Recalling the MOF-5 crystal density $\rho_{crys} = 0.61$ g/cm^3, an ideal compacting process would result in a dense, defect-free crystal without any micropore losses or packing losses. Such an ideal compaction process is shown in the Figure 5.5(6) as the dashed line. The total volumetric storage of an ideal MOF-5 crystal is computed using Eq. 5.4.14, as described in Section 5.4.3 previously. However, our measurements on mechanically compacted MOF-5 samples do not follow that idealized trajectory. Rather, the total volumetric storage density of the MOF-5 pellets reaches a plateau which is close to 45 g/L, drawn as the solid horizontal line in the figure below. Beyond a threshold pellet density of 0.3 to 0.4 g/cm^3, further mechanical compaction of MOF-5 provides little improvement in terms of volumetric storage capacity.

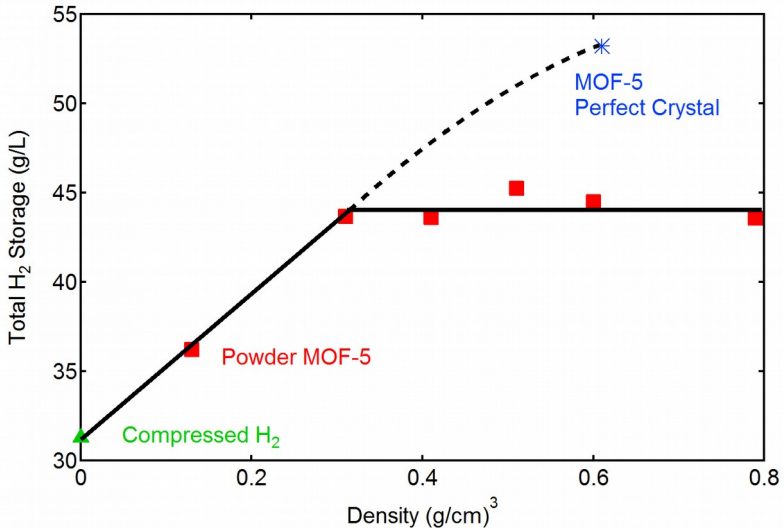

Figure 5.5(6): Total volumetric hydrogen storage density at 77 K and 100 bar for MOF-5 pellets. The values for powder MOF-5 ($\rho_{pwd} = 0.13$ g/cm^3) and bulk H_2 gas are included for comparison. The value for the MOF-5 perfect crystal was calculated using the assumptions in Sec. 5.4.4.

5.5.7 Variable temperature hydrogen adsorption in MOF-5 pellets

Variable temperature H_2 adsorption isotherms (77 K-295 K) were measured for MOF-5 pellets with density 0.31 g/cm^3, 0.4 g/cm^3 and 0.52 g/cm^3. The results are shown below in Figure 5.5(7). For these measurements, temperature control was provided by liquid N_2 (77 K), liquid Ar (87 K) and acetone/solid CO_2 (192 K). Solid CO_2 without acetone was used for sample temperatures of 200 K. A continuous flow liquid N_2 cryostat was used for the remaining temperatures.

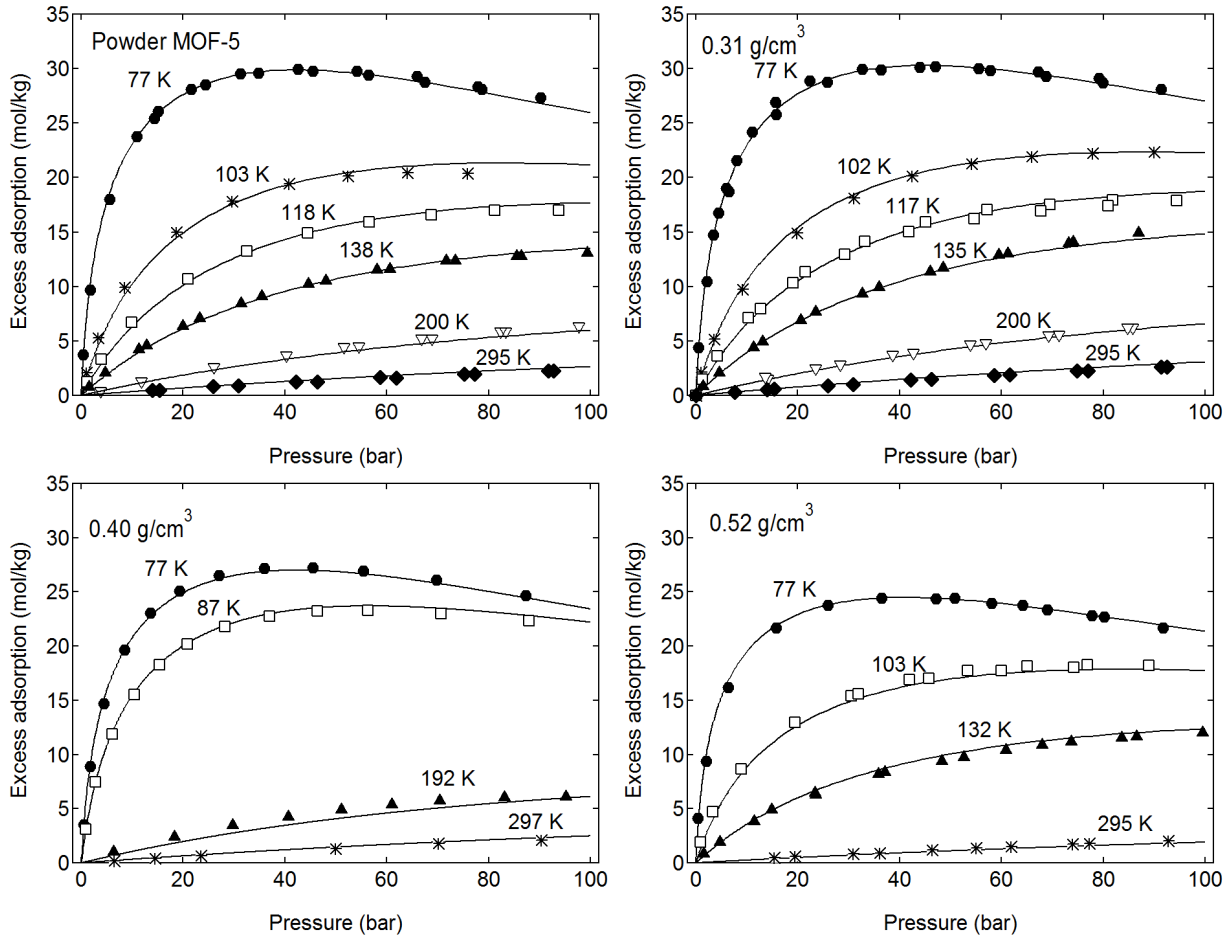

Figure 5.5(7). Hydrogen adsorption isotherms for MOF-5 pellets measured at variable temperatures. Measured data is plotted as markers. Solid lines are fits to Unilan model.

Table 5.5(1): Fitted Unilan model parameters to MOF-5 isotherms

	$\Delta S/R$	E_{max} (kJ/mol)	E_{min} (kJ/mol)	n_{max} (mol/kg)	v_a (cm^3/g)
Powder	-7.89	4.98	1.31	64.1	1.40
$\rho_{env}=0.31$ g/cm^3	-7.89	4.98	1.31	63.3	1.28
$\rho_{env}=0.40$ g/cm^3	-7.89	4.98	1.31	57.6	1.24
$\rho_{env}=0.52$ g/cm^3	-7.89	4.98	1.31	53.9	1.21

As was the case for powder MOF-5, the variable-temperature excess H_2 adsorption data was fitted to the modified D-A model to provide parameters for system-level modelling. The solid lines shown above in Figure 5.5(7) are fits to the Unilan model, as it provided better fits to the data between 150 K and 298 K. Three of the parameters in the Unilan model ($\Delta S, E_{min}, E_{max}$) are material parameters which are unlikely to be affected by simple mechanical compaction of a powder. Therefore, these parameters are held fixed as constraints, allowing only n_{max} and v_a to be adjustable. Best-fit parameters are summarized in Table 5.5(1). The trends in both n_{max} and v_a closely parallel the trends in the BET surface areas and total N_2 pore volumes, as expected.

5.5.8 Hydrogen Permeability in neat MOF-5 pellets:

Compacting MOF-5 (or any microporous adsorbent) into large monolithic structures will reduce the permeability of H_2 gas through the material (in comparison to a loosely packed powder bed). Any significant reduction in gas permeability will have a direct impact on refueling kinetics, and on the assurance of a 100% SOC fill (due to H_2 concentration gradients within the sorbent bed). While H_2 has a small kinetic diameter (0.3 nm) and can rapidly permeate small micropores, we found that there was insufficient data available regarding H_2 permeation through dense, monolithic micropore-based adsorbent materials. We carried out extensive testing to quantify the hydrogen permeation rate through MOF-5 pellets. Results on this work have been previously published [Xu 2012].

Experimental methods: The H_2 permeability measurement setup is shown below in Fig.5.5(8). A MOF-5 cylindrical pellet was secured in the sample holder using silicone adhesive sealant sealing around the sample edge in the glove box. The effective gas flow diameter *d* was 1.00 cm, and the sample thickness *h* was 0.5 cm (Fig.1b). Two pressure transducers P1 and P2 were connected adjacent to the sample holder in upstream and downstream positions, respectively.

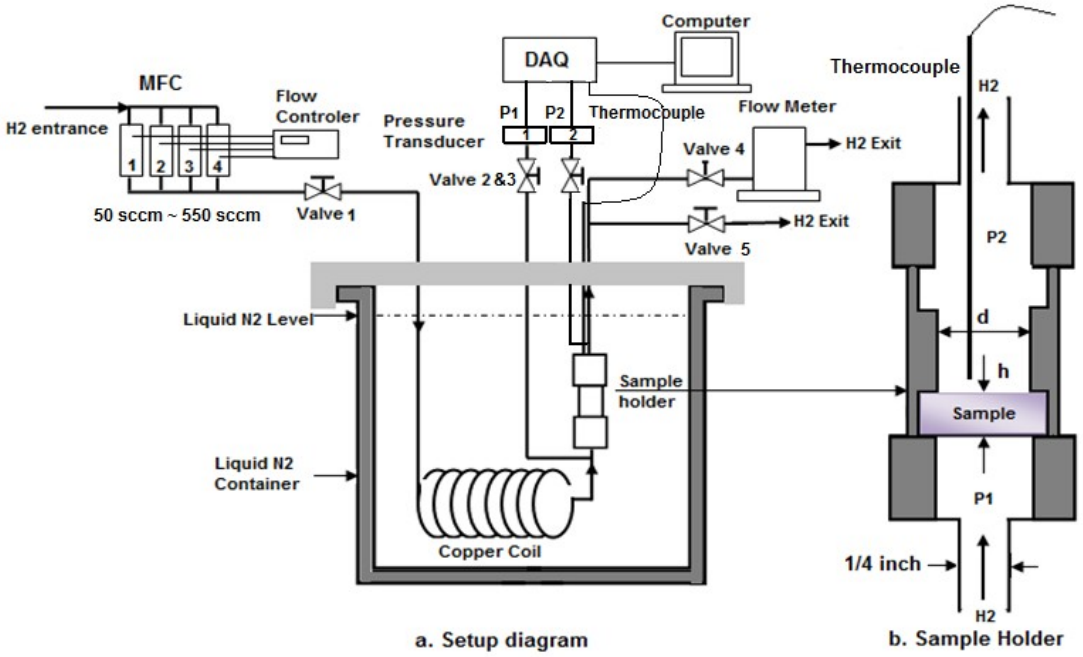

Figure 5.5(8) Schematic of hydrogen permeability test apparatus. The expanded view on the right illustrates the placement of MOF-5 pellet within the sample holder. P1 is the pressure upstream of the MOF-5 pellet, and P2 is downstream pressure.

A thermocouple was positioned downstream about 5 mm near the sample to measure the gas temperature. Since the thermocouple is positioned close to the sample, we assume that the measured temperature reflects the temperature of the sample. The temperature, H_2 inlet and outlet pressure were recorded by a data acquisition module.

For the cryogenic H_2 transport measurements at 77 K, the sample holder were completely submerged in a liquid N_2 (LN) Dewar, and the liquid N_2 level was kept constant. MOF-5 has a negative thermal-expansion coefficient which helps to secure the seal between the sample and the sample holder. Hydrogen gas flowed through 1/4 inch stainless steel tubing and then through copper coil within the liquid N_2 Dewar to ensure that the H_2 gas was cooled down to 77 K before flowing through the sample. The measured H_2 outlet temperature was between 77-79 K upon exiting the copper tube with a flow rate of up to 550 standard cubic centimeters per minute (sccm), which was the maximum flow rate used in this study. For the measurements at 296 K, the pressure drop was taken without using LN. We note that a flow rate of 1 sccm is roughly equivalent to 9×10^{-8} kg H_2/min.

The measurement set-up had four mass flow meters (MSK) which were set at H2 flow rates of 50 sccm, 100 sccm, 200 sccm and 200 sccm to create a H_2 flow rate from 0 sccm to 550 sccm (i.e., 4.9×10^{-5} kg H_2/min). A bubble flow meter was connected to the H_2 exit to confirm the flow rate. At steady state, the H_2 inlet pressure

P_1 and outlet pressure P_2 are constant. P_2 is very close to the ambient pressure between 745 and 755 torr, as read from a barometer. $\Delta P = P_1 - P_2$ is the measured pressure-drop when H_2 flows through the sample. The steady flow is reached when the inlet flow rate equals outlet flow rate. For each sample, 11 pressure-drops corresponding to 11 flow rates from 50 sccm to 550 sccm at 50 sccm increments were measured (see Figure 5.5(9) for an example). The H_2 flow was allowed to reach steady state at each step. In order to evaluate the effects of degassing on permeability, some samples were degassed at 130°C using heating tape attached to the sample holder and a mechanical pump connected through the H_2 exit. The valves 1 to 5 were used to control H_2 flow and prevent air from leaking into the sample holder during degassing and subsequent cooling down.

Results: For a comparison analysis, the Darcy permeability was calculated using two approaches by assuming H_2 gas as incompressible and compressible. For an incompressible gas, the Darcy permeability (κ) is given by the Darcy equation:

$$\kappa\left[cm^2\right] = \frac{v\left[cm^3\,\mathrm{STP}/g\right] \times \mu\left[Pa \cdot s\right] \times h\left[cm\right]}{\Delta P\left[Pa\right] \times A\left[cm^2\right]} \tag{5.5.1}$$

where v is the H_2 flow velocity through the sample, μ is the H_2 viscosity, h is the sample thickness, and $\Delta P = P_1 - P_2$ is the pressure drop across the porous MOF-5 pellet under steady state flow, and A is the cross-sectional area of the pellet. The units of each parameter are indicated in brackets. The Darcy unit (Da) is given by $1\,\mathrm{Da} = 9.87 \times 10^{-9}\,\mathrm{cm}^2$.

When we include the assumption that H_2 is a compressible ideal gas, the expression for the pressure drop through the porous media simplifies to

$$\Delta P = \frac{P_1^2 - P_2^2}{2P_2} \tag{5.5.2}$$

Substituting this into the Darcy equation,

$$\kappa = \frac{2P_2}{\left(P_1^2 - P_2^2\right)} v\mu h \tag{5.5.3}$$

Therefore, by measuring the pressure drop and flow rate, the Darcy permeability for H_2 both as an incompressible and compressible gas can be calculated using Eq. 5.5.1 and Eq. 5.5.3, respectively.

To calculate the Darcy permeability, κ , the following physical parameters were used. The dynamic (absolute) viscosity of H_2 gas at 298 K is given by $\mu_0 = 8.41\,\mu\mathrm{Pa \cdot s}$, while at 77 K is it given by $\mu_0 = 3.47\,\mu\mathrm{Pa \cdot s}$. The hydrogen flow velocity is calculated from $v\left[cm^3\,\mathrm{STP}/sec\right] = v\left[sccm\right]/60\left[sec/min\right]$. The pellet dimensions are 0.5 cm in thickness and 0.785 cm^2 in cross-sectional area.

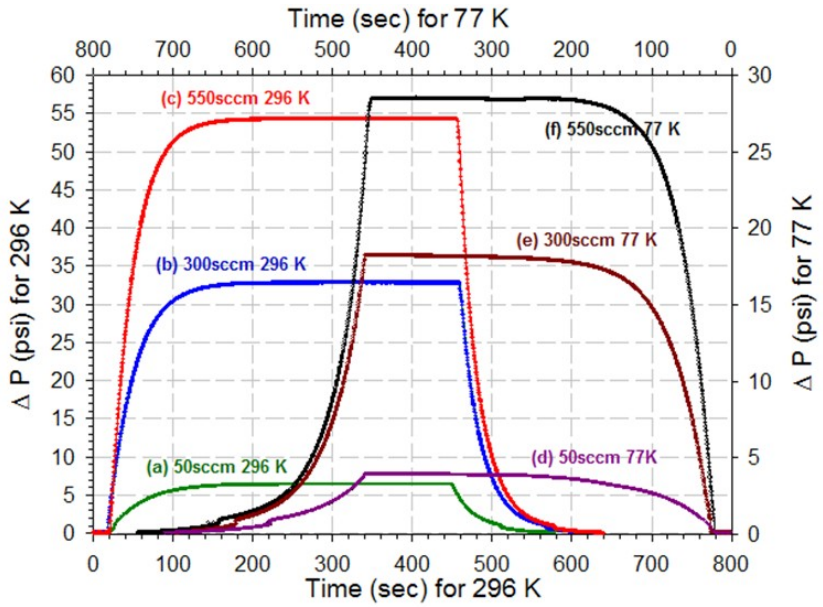

Figure 5.5(9). The pressure drop ΔP versus time for a neat MOF-5 sample with $\rho_{env}=$¿ 0.47 g/cm^3. The curves (a), (b) and (c) data are taken at 296 K (left & bottom axis), while the curves (d), (e) and (f) data are taken at 77 K (right & top axis) under H_2 flow rate 50 sccm, 300 sccm and 550 sccm, respectively.

Pressure drops as a function of time are plotted in Fig. 5.5(9) for a MOF-5 pellet ($\rho_{env}=0.47$ g/cm^3) with a hydrogen flow rate from 50 to 550 sccm. Measurements taken at 296 K are presented on the left y-axis, while measurements taken at 77 K are plotted versus the right y-axis. The pressure drop ΔP at steady H_2 flow state was used to calculate the Darcy permeability. A calculation of the Darcy permeability (assuming an incompressible gas) for this sample at 296 K and $v=300\,\text{sccm}=5\,\text{cm}^3[\text{STP}]/\text{sec}$ is given by

$$\kappa=\frac{(5\,\text{cm}^3[\text{STP}]/\text{s})(8.41\times10^{-6}\,\text{P}\cdot\text{s})(0.5\,\text{cm})}{(2.28\times10^5\,\text{Pa})(0.785\,\text{cm}^2)}=1.17\times10^{-10}\,\text{cm}^2=0.012\,Da \qquad (5.5.4)$$

The Darcy permeability for each MOF-5 pellet sample was determined experimentally by plotting either ΔP (for incompressible gas) or $2P_2/(P_2^2-P_1^2)$ (for compressible gas) versus the flow rate v . The value of κ is determined from the slope of the fitted line.

Tables 5.5(2) lists the Darcy permeability (κ) of neat MOF-5 samples of various densities. The results show that H_2 permeability decreases significantly with the density of the pellet. In addition, the permeability measured at 296 K is higher than that measured at 77 K for the same sample. The results also demonstrate that degassing the pellet *in situ* immediately before to measurement does not change the H_2 permeability significantly.

Table 5.5(2) Values of the Darcy permeability assuming either an incompressible gas (κ) or compressible gas (κ_c).

$T=296\,K$			$T=77\,K$		
ρ_{env} (g/cm^3)	κ (Da)	κ_c (Da)	ρ_{env} (g/cm^3)	κ (Da)	κ_c (Da)
0.301	0.2030	0.1875	0.3003	0.0477	0.0456
0.311	0.1473	0.1322	0.3068	0.0406	0.0387
0.321	0.1220	0.1081	0.3417	0.0153	0.0138
0.342	0.0593	0.0423	0.4000	0.0040	0.0035
0.349	0.0462	0.0349	0.4732	0.0033	0.0024
0.401	0.0173	0.0094	0.4829	0.0026	0.0017
0.462	0.0132	0.0064	0.4973	0.0012	0.0006
0.473	0.0121	0.0056			

0.490	0.0098	0.0046			

The effects of gas compressibility on H_2 permeation were demonstrated by calculating the Darcy permeability using incompressible gas Eq. 5.5.1 and compressible ideal gas Eq. 5.5.3 for the MOF-5 samples. The results are plotted versus sample density in Fig. 5.5(10). At 296 K, the compressible gas Darcy permeability is 7.5% lower than the incompressible gas Darcy permeability for the low density (0.301 g cm^{-3}) sample and 52% lower than that for the high density (0.490 g cm^{-3}) sample. At 77 K, the compressible gas Darcy permeability is still smaller than the corresponding incompressible gas Darcy permeability, the difference ranges from 5% to 56% for low density pellet and high density pellet, respectively.

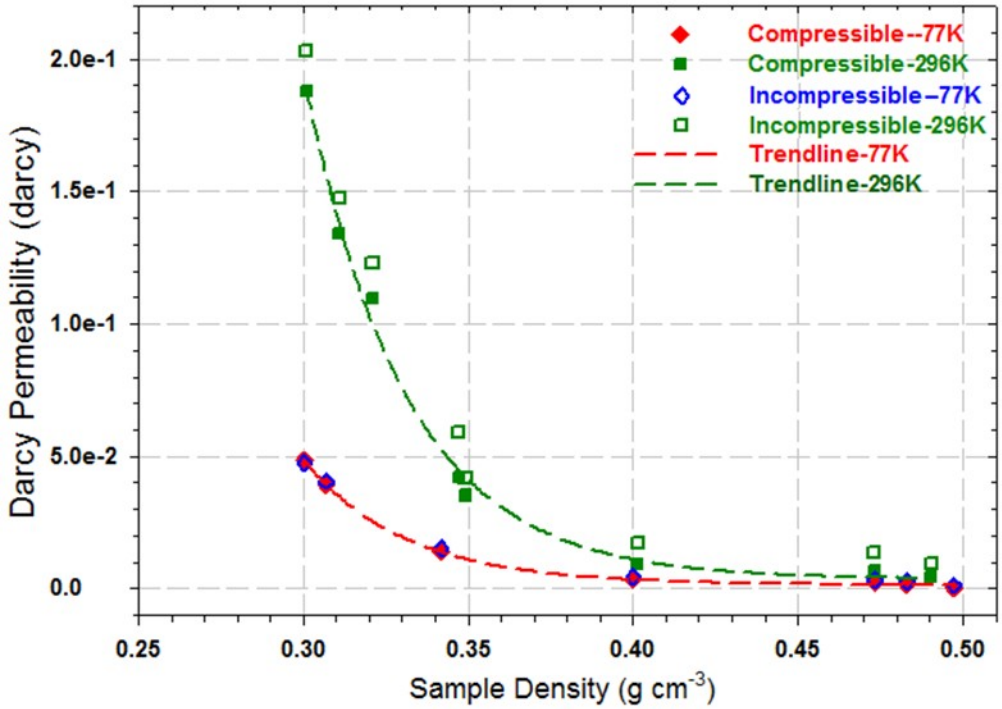

Figure 5.5(10). Comparison of incompressible and compressible ideal gas Darcy permeability of hydrogen for MOF-5 pellets.

These differences come from the fact that higher density samples lead to larger H2 pressure drops, which result in a larger difference between compressible and incompressible gas permeability. The results of the compressible gas Darcy permeability (κ_c) for the various samples are also listed in Tables 5.5(2) along with the incompressible gas Darcy permeability (κ). The Darcy permeability values provide a direct comparison of H_2 permeation through MOF-5 samples with different density and ENG content at 77 K and 296 K. The results confirm as expected that lower density samples will have better H_2 mass transport properties.

The approaches for calculating the Darcy permeability have some aspects that need to be further evaluated. The incompressible Darcy permeability approach assumes the fluid to be incompressible Newtonian fluid with a constant viscosity μ. In fact H_2 is a compressible gas, the modified compressible fluid Darcy permeability approach should give more accurate results. However the gas viscosity μ and flow velocity v are assumed to be constant, which will lead to some error. In practical applications, the hydrogen filling pressure could be much higher, as high as 150 bar. At such high pressure, the assumptions for the Darcy permeability calculation may not be satisfied, consequently, the obtained Darcy permeability data at low H_2 pressure may need to be modified for a practical storage system.

5.5.9 Hydrogen Diffusivity in Compacted MOF-5 Powder:

The Darcy permeability does not fully characterize the hydrogen transport dynamics which are needed for a complete system model. Convective H_2 flow (which is driven by pressure gradients) is the dominant mass transport mode for hydrogen gas in many, if not most, scenarios. However, a highly compacted MOF-5 material can effectively block the convective flow through the material, allowing diffusion to become the dominant mass transport mode. The driving force for diffusion in this scenario is concentration gradients rather than pressure gradients.

The diffusivity of bulk dilute H_2 gas in an open volume is a starting point for this consideration. From the kinetic theory of gases, the diffusion of hydrogen gas near ambient pressures depends on the mean velocity of the H_2 gas particles,

$$\acute{v} = \sqrt{\frac{8kT}{\pi m}} = \sqrt{\frac{8\left(1.38\times10^{-23}\,\text{J/K}\right)\left(295\,\text{K}\right)}{\pi\left(3.34\times10^{-27}\,\text{kg}\right)}} = 1761\,\text{m/s} \qquad (5.5.5)$$

(where we assume ambient conditions $T = 295\,\text{K}$ and $p = 1\,\text{bar}$), and on the mean free path between collisions of individual H_2 molecules,

$$\lambda = \frac{1}{\sqrt{2}\,\pi\,a^2 C} = \frac{1}{\sqrt{2}\,\pi\left(3\times10^{-10}\text{m}\right)^2\left(2.46\times10^{25}\,1/\text{m}^3\right)} = 1.02\times10^{-7}\,\text{m} \qquad (5.5.6)$$

where $a \approx 0.3$ nm is the van der Waals hard sphere diameter for H_2, and $C = p/kT = 2.46\times10^{25}\,\text{atoms/m}^3$ is the concentration in molecules per unit volume (ideal gas law). The diffusion constant is equal to

$$D = \frac{1}{3}\acute{v}\,\lambda = \frac{1}{3}\left(1761\,\text{m/s}\right)\left(1.02\times10^{-7}\,\text{m}\right) \approx 0.6\,\text{c m}^2\text{/s at 1 bar, 295 K} \qquad (5.5.7)$$

Extensive measurements of the binary diffusion for the H_2-N_2 mixture yield a value between 0.78 cm^2/s and 0.8 cm^2/g based on the H_2:N_2 stoichiometry [Matsunaga, 2002]. In other words, these are the values that are measured using conventional techniques, such as the two bulb method, where two reservoirs containing different stoichiometric mixtures of H_2 and N_2, are separated by a closed valve. Both reservoirs are at equal pressure, and the concentration of each species can be monitored by an analytical instrument. After the valve is open, the time dependent concentration profile of the H_2 gas species is driven by the diffusion coefficient D in accordance with Fick's Second Law.

Gas diffusivity inside a porous material is slower compared to that of the bulk gas. The gas cannot diffuse directly down a concentration gradient, but must travel through the complex pore network between and around particles. (This assumes that the gas cannot diffuse through the particle itself). The resulting *effective* diffusivity is related to the bulk diffusivity by the equation

$$D_{eff} = \frac{\theta\,D_{bulk}}{\tau} \qquad (5.5.8)$$

where θ is the porosity (volume fraction of open pore space in the solid), and τ is the tortuosity (which is an indicator of the irregular geometric path a particle must percolate through). Estimating the value of θ for MOF-5 is not straightforward, since it should include the free space between and around individual crystallites and particles, but *not* the intra-crystalline pore volume itself. A good estimate is roughly $\theta \approx 0.35$ for the close-packing of spheres. The tortuosity must be greater than 1, and can be as large as $\tau = 8$ for compacted powders. Therefore a worst-case estimate of the H_2 diffusivity within a compacted MOF-5 powder at 295 K and 1 bar is,

$$D_{eff} = \frac{\theta D_{bulk}}{\tau} = \frac{(0.3)(0.78\,\mathrm{cm}^2/\mathrm{s})}{8} = 0.03\,\mathrm{cm}^2/\mathrm{s} \qquad (5.5.9)$$

In the case of MOF-5, the gas can also diffuse *through* the porous MOF-5 crystal structure. However since the sizes of these pores (12Å, 15Å) are much smaller than the mean free path ($\lambda = 1000\,\text{Å}$) at ambient conditions, this diffusion mechanism is dominated by *Knudsen diffusion*, which is much slower compared to bulk diffusion. The Knudsen diffusivity is calculated by replacing the mean free length (λ) with the width of the channel or pore (r),

$$D = \frac{1}{3} \acute{v} r \qquad (5.5.10)$$

This value is meaningful in the limiting case of dilute concentrations, since it does not take into account the self-blocking of the narrow MOF pore windows by the H_2 molecules themselves. Additionally, at low temperatures such as 77 K, a significant amount of H_2 will adsorb onto the pore surfaces. This can lead to mass transport by an even slower mechanism called *surface diffusion*, where an H_2 molecule hops from site to site along the adsorbent surface. Finally, thermal effects arising from the exothermic heat of adsorption adds to the complexity of the hydrogen diffusion mechanism. Separating out all of these different diffusion modes is difficult. However, a detailed analysis of the microscopic diffusion mechanisms of H_2 adsorbed within porous solids is typically more important for applications such as gas separations than it is for high-pressure gas refueling. While surface diffusion and Knudsen diffusion are likely to have a moderate impact on the localized H_2 concentrations within MOF particles, they are less important in describing the macro-scale H_2 transport throughout an entire storage system.

5.5.10 Conclusions:

1. Forming MOF-5 bulk powder into pellets involves compromises between crush strength, gravimetric adsorption and volumetric adsorption.
2. BET surface area, total pore volume and *excess adsorption* of hydrogen begin to decrease beyond a density range of 0.3–0.4 g/cm^3
3. Pellets with ρ = 0.79 g/cm^3, for example, have the greatest crush strength, but also have the lowest excess gravimetric H_2 adsorption.
4. Total volumetric hydrogen storage at 77 K reaches a plateau around 0.3–0.4 g/cm^3
5. A density of $\rho_{env} = 0.4$ g/cm^3 appears to deliver the best compromise between the three factors among the densities considered here
6. As described in Section 5.4, increasing the density of MOF-5 pellets does not significantly increase the thermal conduction. Introducing highly conductive additives, such as expanded natural graphite, are required. (This work is described in the next section.)
7. Hydrogen gas is highly permeable through a low density MOF-5 pellet of roughly $\rho_{env} = 0.3$ g/cm^3. The Darcy permeability decreases exponentially as the pellet density increases to $\rho_{env} = 0.4$ g/cm^3.

5.6 Augmentation for Thermal conductivity

5.6.1 Introduction

A five minute refueling time is critical to the commercial success of FCV's, but heat management issues intrinsic to hydrogen storage materials can prolong the refueling time beyond the 5 minute window. Cryo-adsorbent based systems typically have the most favorable hydrogen adsorption/desorption kinetics among the material-based storage options, but even they are not exempt from this problem. If the storage systems arrives at the refueling station with near the maximum operating temperature, it is necessary to cool the entire tank system down to the re-fueling temperature in order to guarantee a successful >95% SOC fill. The low thermal conductivity of MOF-5 (and cryo-adsorbents in general) can therefore place limitations on the design of cryo-adsorption based storage systems. The main components which need to be cooled the base temperature are (1) the MOF-5 material, (2) the high-pressure tank and (3) cryogenic insulation.

In addition to cooling the storage system to the base temperature, it is necessary to remove heat released during refueling itself. These heat sources include (1) the released heat of adsorption, (2) the compression work and the (3) thermal mass from the inlet hydrogen gas, must also be dissipated to prevent a temperature increase in the storage material. While the heat dissipation problem for cryo-adsorbents is not extreme, the unusually low heat conduction properties of MOFs present a significant materials engineering challenge. Thermal modeling of the MATI system indicates that an effective thermal conductive of 1 W/m·K may be sufficient for the MOF-5 monoliths to meet the refueling targets.

Unfortunately, MOF-5 pellets have a thermal conductivity below 0.1 W/m·K at room temperature. This is slightly lower than the value of 0.3 W/m·K previously measured for a single crystal of MOF-5. To improve thermal conduction, we explored MOF-5 based composites containing 0 to 10 wt.% of conductive carbon additives, such as expanded natural graphite (ENG). ENG has been successfully used as a thermal conduction enhancer in variety of metal and complex hydride materials.

5.6.2 Designs and Objectives

The objective is to increase the bulk, isotropic thermal conductivity of a MOF-5 compacted pellet to 1 W/m·K, with the least impact on the gravimetric/volumetric hydrogen storage capacity.

Table 5.6(1) Thermal Properties of common thermal conductivity additives, compared to MOF-5

Property	Lattice Direction	Natural graphite	Aluminum 1100 Alloy	Copper 11000 Alloy	MOF-5 Single crystal
Density		1.1-1.7	2.71	8.89	0.61
Thermal Conductivity (W/m·K)	a,b	140-500	220	388	0.32
Thermal Conductivity (W/m·K)	c	3-10	220	388	0.32
Specific heat capacity (J/kg·K)		846	904	385	0.73

As summarized in Table 5.6(1), natural graphite is an effective, though highly directional, heat spreading material. In addition to thermal conductivity, graphite provides additional benefits to a compacted MOF-5 hydrogen storage media. Compared to the Al- and Cu-based thermal conductivity additives:

- Graphite is lightweight, and has a minimal effect on the MOF-5 gravimetric hydrogen storage capacity
- Graphite works well as a binder and lubricant in forming MOF5 into pellets by a pellet press.

We investigated two different forms of graphite-based thermal conduction enhancing additives.

- Expanded natural graphite (large worm-shaped particles, extremely low density)

- Graphene-aggregate carbon powder (extremely fine particles, similar in texture to carbon black)

While both carbons additives owe their high conductivity to their graphitic nature, their morphologies are quite different. The ways that they impact the thermal conductivity are distinct as well.

The expanded natural graphite (ENG) used in this work was obtained from SGL Group. Due to its larger size and springy, worm-like morphology (i.e., *very* low density), ENG does not blend easily with MOF-5. Extensive mechanical mixing using a milling instrument is required to create a MOF-5/ENG blend. In this process, stoichiometric amounts of MOF-5 and ENG powders were loaded into a SS milling vial (without grinding media), and then mixed using a Spex 8000 high energy mixer/mill for roughly 30 sec. The vigorous mixing breaks up the ENG into smaller particles, enabling better dispersion into the MOF-5 powder. When the resulting mixture is pressed into a pellet, the ENG forms a visibly inhomogeneous fiber-like network through the pellet.

The large size of ENG particles is a source of anisotropy. Within a pellet, the ENG worms tend to align perpendicular to the direction of compaction. The resulting pellets have a notable anisotropy in the thermal conductivity, with the radial direction being more conductive that the axial direction. This is not necessarily a detriment, however, as some thermal management designs can benefit from a directional heat spreader. We exploited this anisotropy by creating a layered MOF|ENG|MOF heat spreader structure, which improves the thermal conductivity nearly twenty-fold in the direction of the ENG heat spreaders (NOTE: this should actually have an insulating effect perpendicular to the heat spreaders)

We obtained a series of graphene-aggregate carbon powders from Cabot Corporation, which we refer to by their trade name *GPX*. The macroscopic texture of this material is very similar to that of a fine carbon black powder, with BET surface areas of around 50 m^2/g. At the microscopic levels they are composed of small graphene platelets aggregated into particles in a random fashion. They are synthesized using either chemical exfoliation (for GPX-103) or mechanical exfoliation processes (for GPX-203), and can differ in terms of their isotropic or two-dimensional character. The GPX line is claimed to offer superior performance compared to carbon blacks when used as a thermal conductive additive within a low conductivity material (e.g., such as a polymer).

Similar to a carbon black, the GPX materials disperse well when mixed with MOF-5 and coat the surface of the individual particles with a thin carbon layer. The MOF-5/GPX blends can be mixed by hand, and do not require a mechanical mixer/mill. When the mixture is pressed into a pellet, this yields a continuous network of conductive carbon black through the entire pellet. The resulting pellets appear more visibly homogenous compared to the ENG/MOF5 composite. Since the GPX particles do not have a strong preferred orientation relative to the direction of compaction, the thermal conductivity of the MOF-5/GPX pellet is considerably less anisotropic compared to the MOF-5/ENG composite.

However, the GPX can only coat the outer surface of MOF5 aggregate-crystallites. The overall pellet homogeneity is therefore limited by the particle size distribution of the MOF-5 powder itself (i.e., large MOF-5 particles embedded in the pellet will create regions of inhomogeneity). This effect is visible is Figure 5.6(13), in which the MOF-5 powder contained a mixture of large and small particles. Even in this case, the MOF-5 particles are still small enough that they are unlikely to create large temperature variations within a monolith. The homogeneity can be improvement by grinding and sieving the MOF-5 powder prior to mixing with GPX.

5.6.3 Study of thermal conductivity versus ENG %, density

A test matrix was developed to study the effect of two factors (ENG%, pellet density) on the axial thermal conductivity. Additionally, the radial thermal conductivity was characterized for a small subset of samples. The experimental design for this work is summarized in Table 5.6(2), along with the measured thermal conductivities at room temperature.

Table 5.6(2): Thermal Conductivity of MOF-5/ENG Composite Pellets Measured by Flash Diffusivity at 25°C

Axial Thermal Conductivity(W/m·K)			
ENG (wt %)	ρ_{pellet}=¿ 0.37-0.4 g/cm^3	ρ_{pellet}=¿ 0.5 g/cm^3	ρ_{pellet}=¿ 0.7 g/cm^3
0	0.07	0.12	0.14
1	0.08	0.13	0.15
5	0.15	0.30	0.46
10	0.39	0.60	0.91

Radial Thermal Conductivity (W/m·K)			
0	0.08	—	—
1	—	—	—
5	0.3	—	—
10	0.95	—	—

As described in more detail in the following sections, the main findings of this experiment are:

1. Thermal conductivity increases with pellet density due to an improvement interfacial contact between particles
2. The thermal conductivity increases with ENG content in both axial and radial directions, with the most significant increases for 5% ENG and 10% ENG. Addition of 1% ENG did not appear to provide a significant improvement in thermal conduction
3. As shown in Fig. 5.6(1), there is a positive interaction between the two factors: ENG loading and pellet density. At higher ENG loadings, the thermal conductivity increases at a fast rate versus pellet density.
4. The maximum thermal conductivity was achieved for a 0.7 g/cm^3 density and 10 wt.% ENG loading, and was close to 1 W/m·K.
5. As expected, there is significant directional affect for ENG-containing pellets. Heat conduction is higher in the radial compared to the axial direction due to alignment of the rod-like ENG particles perpendicular to axial compaction direction.

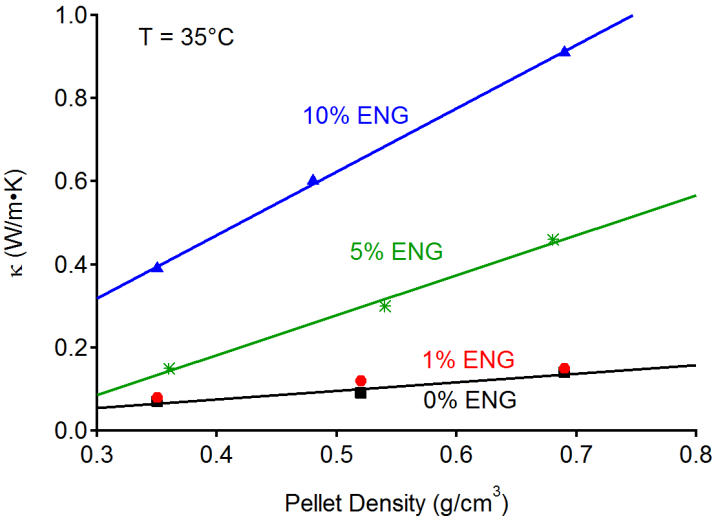

Figure 5.6(1) Thermal conductivity of MOF-5/ENG composite pellets in the axial direction at 35°C.

5.6.4 Methods: Sample preparation, heat capacity and thermal diffusivity measurements

Expanded natural graphite, ENG, was provided by SGL Group. Synthesis of ENG proceeds by soaking natural graphite flakes in sulfuric acid, which intercalates between the graphite basal planes, expanding the structure in the c-axis direction. The intercalated molecules are then violently removed by heating at 700^{0}C for 12-15

minutes. ENG consists of relatively large black vermicular particles ranging in length from approximately 0.5 to 4 mm. The density of ENG (~0.1 g/cm^3) is approximately 20 times smaller than normal graphite (2.25 g/cm^3). The worm-like structure of the ENG arises from the expansion of natural graphite's lamellar structure. ENG particles exhibit a high aspect ratio (length/diameter), ranging from 18 to 25.

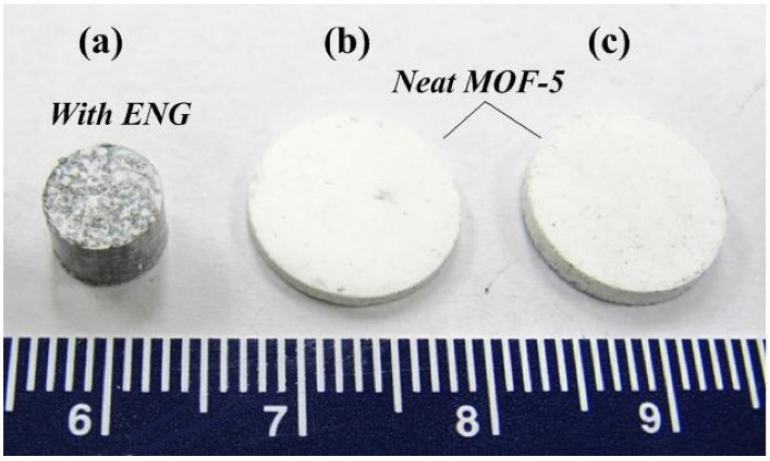

Figure 5.6(2). Cylindrical pellets of neat MOF-5 and MOF-5+ ENG composites (a) pellet of 4.5mm diameter for specific heat capacity measurement (b) pellet of 6.35mm diameter for surface area measurement (c) pellets of 12mm diameter and 1mm thickness for XRD measurement

Specimens were compressed using a manual pellet press housed inside an Ar-filled glovebox. Cylindrical and rectangular shaped pellets were formed and characterized. Cylindrical samples were used for microstructure characterization and room temperature thermal diffusivity measurements; rectangular samples were primarily used for steady-state heat flow thermal conductivity measurements, where a rectangular geometry best accommodates the size of the stainless-steel contacts of the instrument. To examine the impact of compression direction, two different types of die were designed for each sample shape. In the case of the cylindrical geometry, this allowed for pellets to be processed using uniaxial compression along either the radial or axial directions. Likewise, for the rectangular geometries, compression was performed parallel, or perpendicular to, the long axis of the pellet.

The thermal conductivities of all pellets are calculated at 26, 35, 45, 55 and 65 °C with three densities based on the following equation:

$$\lambda = \alpha \cdot C_p \cdot \rho$$

where α is the thermal diffusivity, ρ is the density and C_p is specific heat capacity.

Specific heat capacity measurements were performed with a calibrated DSC (SENSYS DSC, Setaram) on single 4.5 mm pellet. Pellets were placed inside aluminum-oxide crucibles in the glove box and data were collected using a heating rate of 5 K/min and a He carrier gas flow of 20ml/s.

Thermal diffusivity measurements at room temperature and above were performed using a xenon thermal flash diffusivity instrument (Anter Flashline, FL3000S2) with N_2 as a protective gas, and with pellets having a 12.8 mm diameter and 3mm average thickness. In this method the temperature of the rear surface of the sample is measured as a function of time after a laser pulse with known power is shined on the sample's opposite surface. The method of Clark and Taylor, which accounts for heat loss of the sample during the measurement, was used to estimate the thermal diffusivity. The instrument was calibrated using an iron standard. A thin copper sheet, or a thin layer of silver paint, was applied to the top surfaces to prevent the pellets from fracturing during measurement due to the temperature probes, For some measurements, a thin copper sheet was adhered to the top surface of the pellet using silver paint. Graphite was coated on the lower surface of the pellet to improve light absorption.

Prior to measurements, the pellets were degassed at room temperature for at least 3 hours. Two measurements were taken for each pellet at the following temperatures: 25 °C, 35 °C, 45 °C, 55 °C, and 65 °C. Notice that for this measurement technique the heat flow is along the axial direction of the pellet. It is therefore possible to characterize anisotropies in thermal conductivity by performing measurements on pellets pressed in distinct (i.e., axial or radial) directions. For pellets pressed axially, the thermal flash sample geometry results in a heat flux which is largely perpendicular to the average ENG orientation. Conversely, pellets pressed radially exhibit ENG orientations more closely aligned with the heat flow direction.

5.6.5 Density vs Applied Pressure

As shown in Figure 5.6(3), the relationship between pellets density and applied pressure is largely independent of the ENG concentration. The pellet density increases linearly with the increase of applied pressure at applied pressure below 150 MPa. Above this point, the MOF-5 density starts to approach a limited value of 1.7 g/cm^3 (nearly three times of the single crystal density of 0.605 g/cm^3).

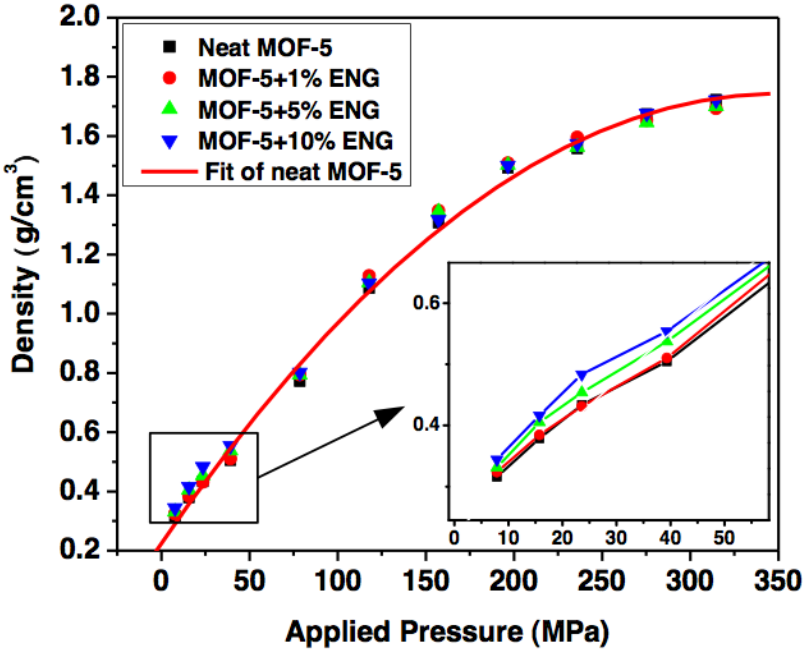

Figure 5.6(3): Pellets density vs. applied pressure for different contents of ENG

From the inset in Fig.5.6(3), it can be seen that when the applied pressure is in a lower range (i.e., less than 50 MPa), the density increases with the content of ENG increasing under the same pressure. This is because the ENG is easier to be compressed compared with MOF-5 due to its vermicular microstructure, which makes the pellets volume decrease with the content of ENG increasing under the same pressure. We speculate that the highly-compressible ENG can absorb more the compression force, and protect MOF-5 to some extent. When the applied pressure becomes larger, the compression of MOF-5 takes the leading position, which, therefore, makes the pellet density almost the same despite of different contents of ENG.

5.6.6 Specific Heat of MOF-5/ENG Composites

The specific heat capacity (C_p) equals the amount of energy one must put into the system in order to heat 1 g of a material to a certain temperature, and is therefore an indicator of the effective *thermal mass* of a material. Heat capacity can be an important property for gas storage systems relying on temperature-swing operation. The heat capacity of pellets of neat MOF-5 and MOF-5/ENG composites at temperatures of 26, 35, 35, 55 and 65°C were measured and are plotted in Fig. 5.6(4).

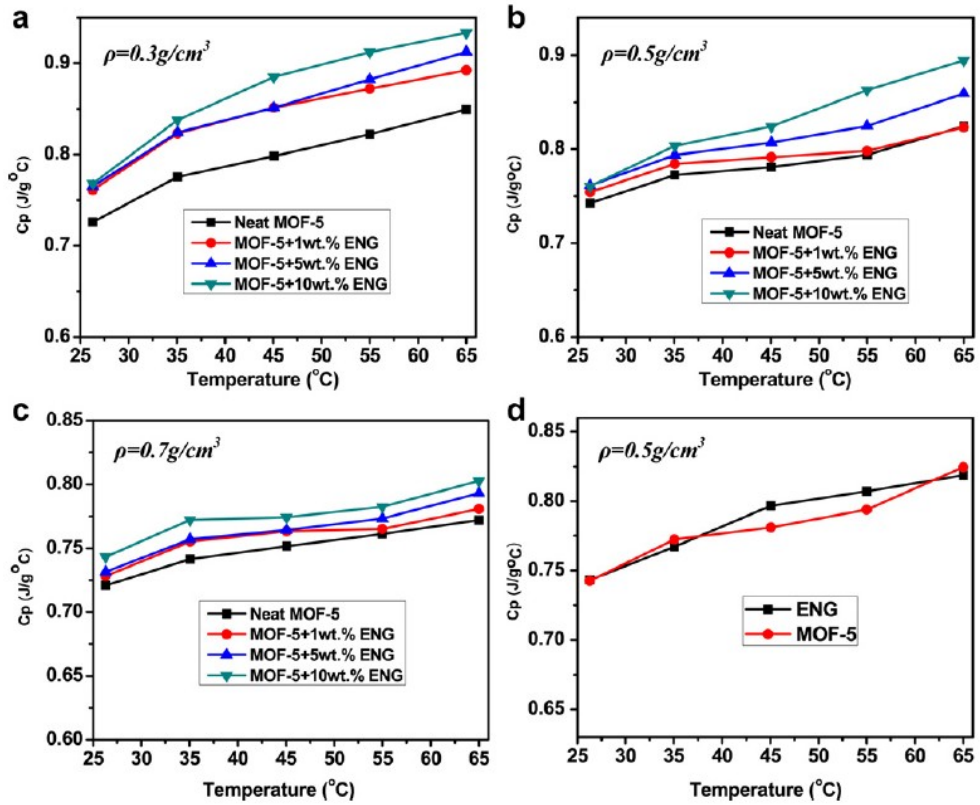

Figure 5.6(4): Specific heat capacity of pellets of neat MOF-5 and MOF-5/ENG composites as a function of density, ENG content, and temperature. (a)-(c) Pellets with densities of 0.3, 0.5, and, 0.7 g/cm^3, respectively; (d) comparison of neat MOF-5 pellets with neat ENG pellets, both with density of 0.5 g/cm^3.

The specific heat capacities increase with increasing temperature for all the samples examined. The value of C_p at 26°C for MOF-5 with density of 0.3 g/cm^3 is 0.73 J/g°C, and is comparable to that of graphite (0.71 J/g°C). For a fixed density, the specific heat capacity increases with increasing ENG concentration. For example, at the density of 0.5 g/cm^3 the heat capacity for the MOF-5 compact with 10 wt.% ENG increases by almost 6% at 26 °C (from 0.73 to 0.77 J/g°C) and almost 10% at 65°C (from 0.85 to 0.93 J/g°C) relative to neat MOF-5 compact. However, the C_p of neat ENG is comparable to that of neat MOF-5, suggesting that the C_p of the MOF- 5/ENG blends should not be altered relative to the neat MOF-5 compacts. A possible explanation for the observed increase in C_p with increasing ENG additions may be traced to ENG's ability to preserve the crystallinity of MOF-5 during the compaction process (as discussed above). In support of this hypothesis we note that for a fixed ENG content C_p decreases with increasing compact density; presumably this is due to a decrease in MOF-5 crystallinity.

5.6.7 Axial Thermal Conductivity of MOF-5/ENG Composites

Thermal conductivity data in the axial direction were determined for pellets of MOF-5 and MOF-5+ENG composites, as shown in Fig. 5.6(5). The axial thermal conductivities of all pellets show a weak temperature dependence. The neat MOF-5 pellets present a very low thermal conductivity, around 0.1 W/m·K at a density of 0.515 g/cm^3, which is about one third of the single crystal MOF-5 (0.31W/m·K).

Adding 1 wt.% ENG has little effect on the improvement of thermal conductivity due to the small amount of ENG. With ENG increasing to 5wt.% and 10wt.%, the thermal conductivity shows a significant increase. For 5 wt.% ENG, the thermal conductivity, compared with neat MOF-5, increases by around 3 times and 3.33 times for density of 0.54 g/cm^3 and 0.68 g/cm^3 respectively. For 10 wt.% ENG, it increases by around 5.5 times and 6.33 times for density 0.486 g/cm^3 and 0.697 g/cm^3 respectively.

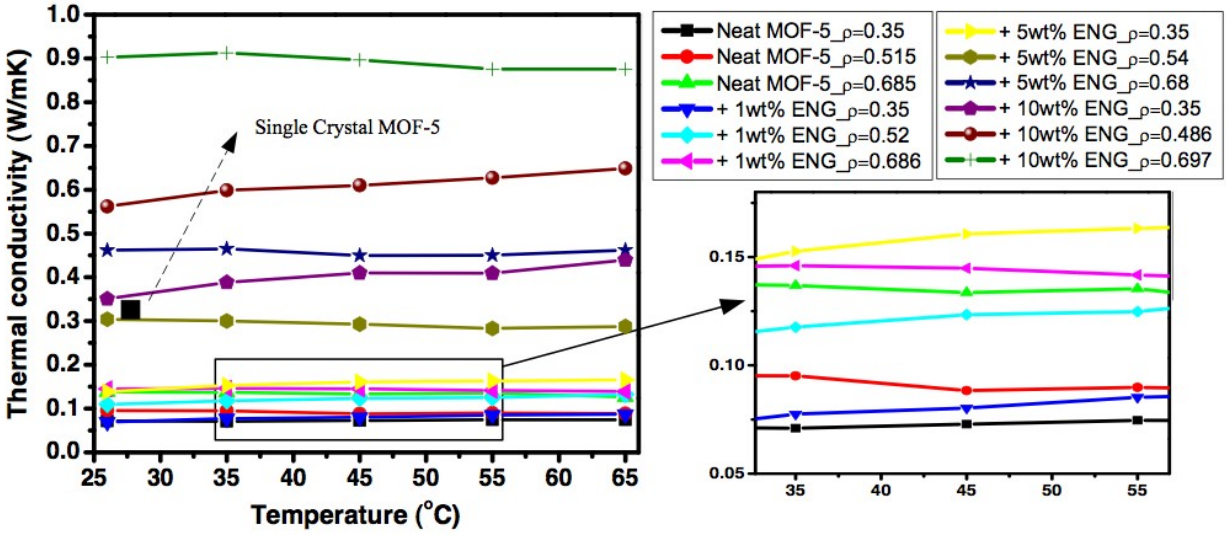

Figure 5.6(5). Axial thermal conductivity of pellets of neat MOF-5 and MOF-5+ENG composites with different pellet densities and ENG contents (1wt.%, 5wt.% and 10wt.%), measured at temperatures from 26°C to 65°C

Increasing the pellet density clearly improves the thermal conductivity. For example, for adding 5 wt.% and 10 wt.% ENG, the thermal conductivities increase by around 1.67 times and 1.73 times from density of 0.5 g/cm^3 to 0.7 g/cm^3 respectively. This is due the improvement in interfacial contact resistance as individual particles are pressed more closely together.

5.6.8 Radial versus Axial Thermal Conductivity of MOF-5/ENG Composites

Preparation of anisotropic samples: In the flash thermal diffusivity technique the heat flow is along the axial direction of the pellet. It is therefore possible to characterize anisotropies in thermal conductivity by performing measurements on pellets pressed in distinct (i.e., axial or radial) directions. For pellets pressed axially, the thermal flash sample geometry results in a heat flux which is largely perpendicular to the average ENG orientation, Figure 5.6(7ab). Conversely, pellets pressed radially exhibit ENG orientations more closely aligned with the heat flow direction, Figure 5.6(7c).

To examine the impact of compression direction, two different types of die were designed for each sample shape. In the case of the cylindrical geometry, this allowed for pellets to be processed using uniaxial compression along either the radial or axial directions, as illustrated in Figure 5.6(6).

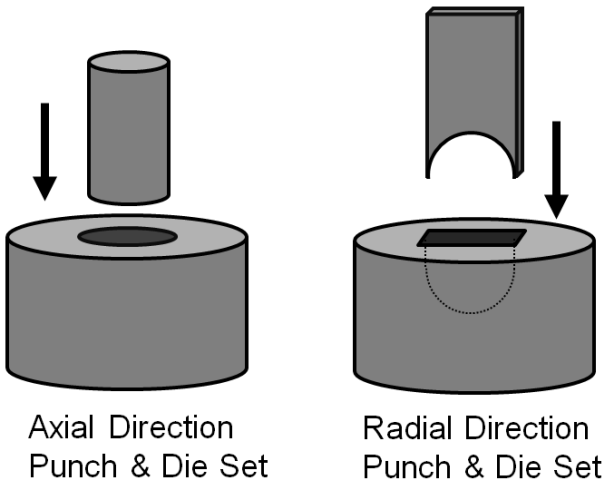

Figure 5.6(6). Methods for compacting MOF-5 into pellets along the standard axial direction (left), or non-standard radial direction (right).

Figure 5.6(7) shows micrographs of cross sections for three pellets formed using different pressing directions and amounts of ENG. The pressing direction in specimens (a) and (b) is along the axial direction of the pellet, while the specimen (c) was pressed radially. The images at the top of Figure 5.6(7) are of cross-sections obtained from cutting the pellet along the rectangular plain shown in the lower sketch. Arrows overlaid on the microscopy images indicate the compression direction.

The relationship between ENG orientation and the pressing direction was calculated using image processing software. The average angle of the ENG in all three cases approximately 70 degrees, confirming that the ENG within the pellets has a tendency to align perpendicular to the pressing direction. This behavior should encourage the formation of a percolating network in directions perpendicular to the pressing direction, resulting in higher thermal conductivity in the same directions.

To assess the directional properties of heat conduction in MOF-5/ENG composite pellets, , thermal conductivity measurements were performed on pellets synthesized using different compression directions. Figure 5.6(8) shows near-ambient temperature thermal conductivity data for MOF-5/ENG pellets having different mass fractions of ENG and orientations of the pressing direction with respect to the direction of heat flow. At 30 °C the thermal conductivities of pellets containing 0%, 5% and 10% ENG are 0.08, 0.38, and 0.99 W/m·K, respectively, for pellets in which the ENG is aligned parallel to the heat flow direction. A similar trend holds for the other ENG orientation and at other temperatures. As expected, the highest conductivity (0.99 W/m·K) is found for pellets containing the highest concentration of ENG (10 wt.%), in which the ENG is oriented parallel to the heat flow direction.

This confirms that pellets having the same ENG composition, but different ENG orientations, exhibit differing thermal conductivities. Pellets with ENG orientations parallel to the heat flow (filled symbols) exhibit conductivities that are 2 to 4 times higher than in pellets where the orientation is perpendicular (open symbols). For the ENG concentrations considered here, this anisotropy appears to be independent of the amount of ENG added. As a comparison, pure ENG compacted into pellets have a thermal conductivity of 1.40 W/m·K (axial) and 3.13 W/m·K (radial), which is consistent with the alignment of vermicular graphite perpendicular to the pressing direction.

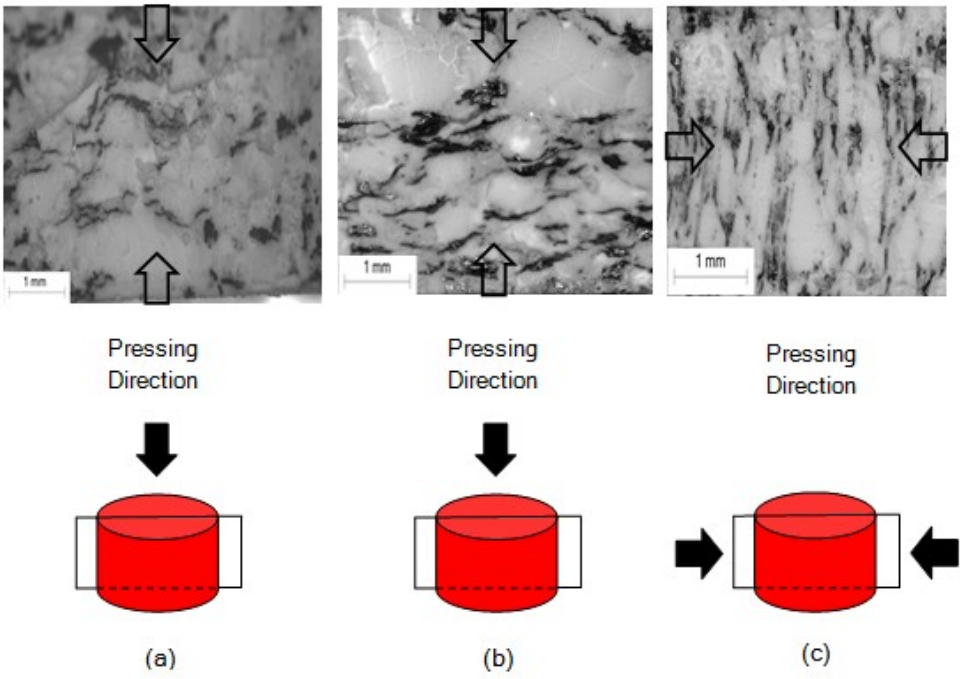

Figure 5.6(7) Cross section of a MOF-5/ENG pellet from optical microscopy. Arrows indicate the pressing direction. The sketch below each image shows the relationship of the cross-section plane to the pressing direction. (a) MOF-5 mixed with 5% ENG, pressed axially; (b) MOF-5 mixed with 10% ENG, pressed axially; and (c) MOF-5 mixed with 5% ENG, pressed radially

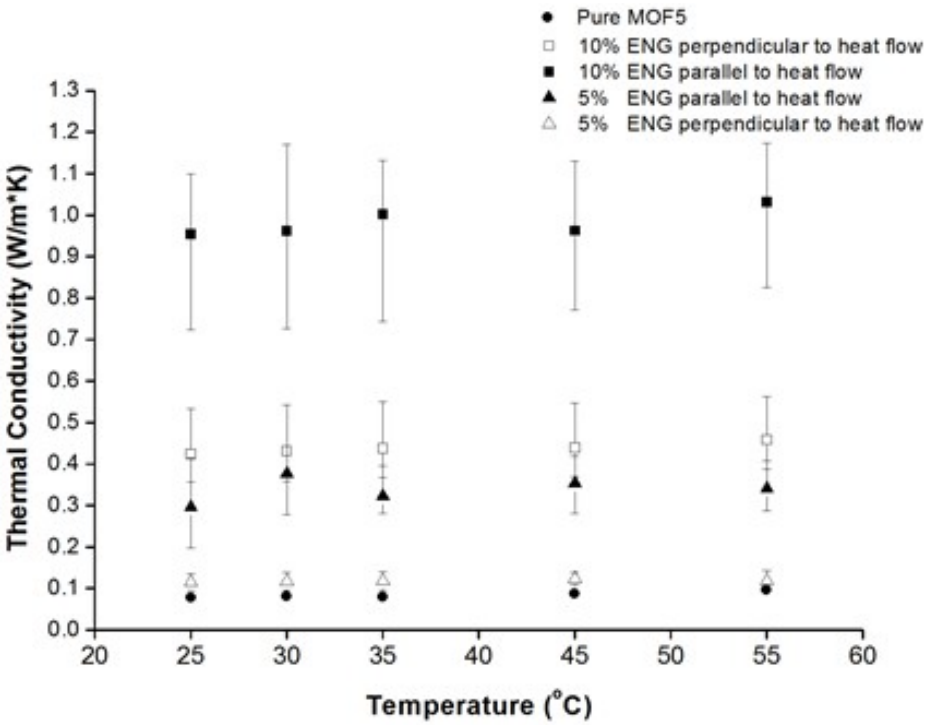

Figure 5.6(8) Near-ambient temperature thermal conductivity for MOF-5/ENG pellets (0.4g/cm^3) as a function of temperature, ENG content, and pressing direction. Error bars correspond to the range of measured values.

5.6.9 Low-temperature thermal conductivity of MOF-5/ENG Composites

Methods for the low-temperature thermal conductivity measurement

Low-temperature thermal conductivity were measured using a different experimental method, distinct from the flash or TPS methods used for the other measurements in this section. These low temperature measurements (80 to 300 K) were performed using a steady-state heat flow method that is well-suited for materials having low thermal conductivity. For this setup, rectangular-shaped pellets were prepared having a cross section of 5 mm × 5 mm and length of 3 mm. For the rectangular geometries, compression was performed parallel, or perpendicular to, the long axis of the pellet. The rectangular pellets were sandwiched between two stainless-steel contacts (SS304) with the same cross section and thickness of 10 mm. The temperature-dependent thermal conductivity of the stainless-steel contacts have been previously measured. Stycast epoxy was used to reduce the contact resistance between the sample and the steel contacts, and did not permeate the samples. A strain gauge heater was mounted on top of one steel contact, while the other contact (placed under the sample) was connected to the heat sink, thereby generating a heat flux from the top of the pellet to the bottom.

Measurements were conducted in vacuum to prevent parasitic convection and adsorption within the MOF pores. Two copper cylinders were mounted outside the cold finger as radiation shields. The temperature of the sample holder was controlled by a Lakeshore 340 temperature controller. Six thermocouples (TC1–TC6) were inserted into small-bore holes in the top (TC1, TC2) and bottom (TC5, TC6) steel plates and affixed to the top and bottom of the sample (TC3, TC4) [see Supporting Information, Section 5]. These probes were used to determine the heat fluxes through the steel contacts (TC5, TC6, TC1, and TC2) and the temperature drop across the sample (TC3, TC4) upon heating, from which the sample's thermal conductivity was derived. The sample's thermal conductivity κ was determined using the 1D Fourier law,

$$\kappa = \frac{Q \cdot t_s}{A_s (T_3 - T_4)}$$

where t_s and A_s are the sample thickness and cross-sectional area, and Q is the power through the sample. Q was estimated using the power, $A_b k_b (T_5 - T_6)/t_b$, transferred through the bottom steel plate, where k_b is the thermal conductivity of the steel contact and t_b is the distance between TC5 and TC6. T_3, T_4, T_5, T_6 are the temperatures measured using the thermocouples TC3, TC4, TC5 and TC6, respectively. Three major sources of error are associated with Q: uncertainty due to parasitic black-body radiation losses from the sample, uncertainty due to parasitic conduction losses through the thermocouples, and uncertainty in t_b due to the nonzero thermocouple diameter. Uncertainty in t_s due to surface roughness, uncertainties in temperature and voltage measurements, and the interfacial temperature drops at each end of the sample also contribute to the error. Accounting for the above sources of uncertainty, we estimate the maximum error in the thermal conductivity to be 18%.

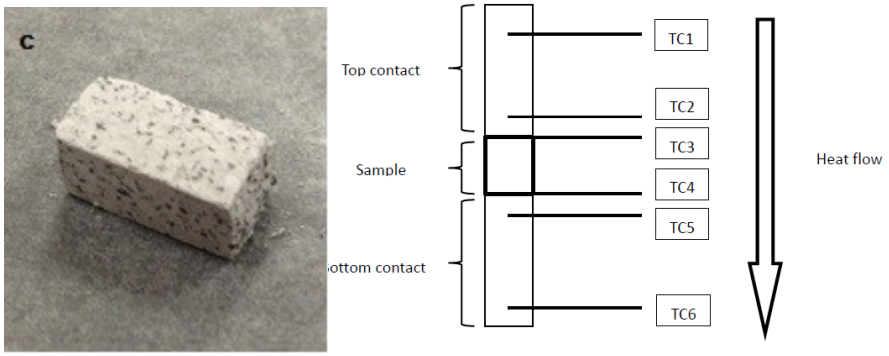

Figure 5.6(9) (*left*) Rectangular sample used for low-temperature measurements (80 – 300 K). The sample dimensions are 10 × 5 × 5 mm. Sample density = 0.35 g/cm^3. (*right*) Thermocouple positions for the steady-state heat flow method.

Figure 5.6(9) shows the thermal conductivity measured from cryogenic to room temperature (80 K to 300 K). The increasing thermal conductivity at low temperatures (80 - 200 K) arises from phonon excitations, while the moderate decrease above 200K is due to a reduction in the average phonon mean free path. The sample having ENG aligned parallel to the heat flow direction (white sample) exhibits the highest value of thermal conductivity 0.68 W/m·K. A much lower maximum conductivity is observed 0.17 W/m·K in the case of perpendicular ENG alignment. This factor of four improvement in thermal conductivity is consistent with the range we observed for room temperature measurements. These data further signify the presence of significant transport anisotropies arising from ENG orientation and/or MOF-5 boundary effects caused by anisotropic compression

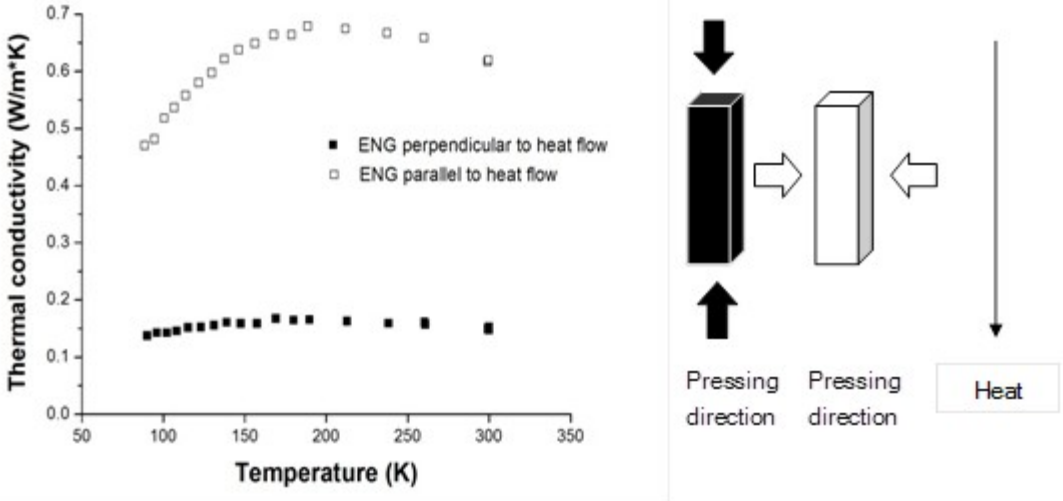

Figure 5.6(10). Thermal conductivity of 0.35 g/cm^3 pellets containing 5% ENG over the temperature range of 80 - 300K. Measurements performed using the steady-state heat flow method. Pellets were formed using two orthogonal pressing directions.

The differences in room temperature thermal conductivities obtained with the transient and steady-state heat flow method (SSHFM) (0.38 W/m·K for the transient method vs. 0.62 W/m·K for SSHFM) can be explained by the different sample making and measuring method. Black-body radiation can be described by Stefan–Boltzmann law,

$$j = \sigma T^4$$

where j is the total power radiated per unit area, T is the absolute temperature and $\sigma = 5.67 \times 10^{-8}$ W/m^2·K^4 is the Stefan-Boltzmann constant. This equation indicates that the radiation at 300 K is 198 times larger than that at 80 K. To minimize the radiation loss across the sample, we have to cut the sample to decrease the heat path length between two steel contacts. However, the cutting process increases the surface roughness of the pellet, thus introducing uncertainty of t_s . The Stycast epoxy accumulated in the hollow part of the sample will also contribute to the error of the calculated thermal conductivity. On the other hand, the transient flash method employs a sample with very flat surface, as well as Clark and Taylor corrections for radiative losses near room temperature, leading us to conclude that the latter method is more reliable at higher temperatures.

5.6.10 Layered MOF-5/ENG Pellets

ENG particles tend to align perpendicular to the direction of uniaxial compaction, making them ideal as a directional heat conductor. Certain system designs could benefit from this highly anisotropic thermal conductivity. We tested the effectiveness of ENG as a directional heat conductor embedded within a MOF-5 pellet by fabricating pellets containing a layered MOF-5|ENG|MOF-5 structure.

Pellets with a layered MOF-5/ENG microstructure were fabricated using the radial pressing method illustrated in Figure 5.6(6). Before compression, known masses of pure MOF-5 and ENG were separated according to the desired final ENG mass %, and then divided into equal parts. These parts were then added into the die alternatively and pressed into pellet form. The total mass fraction of ENG in the pellet was 5%. A pellet containing four ENG layers is shown in figure 5.6(11) below.

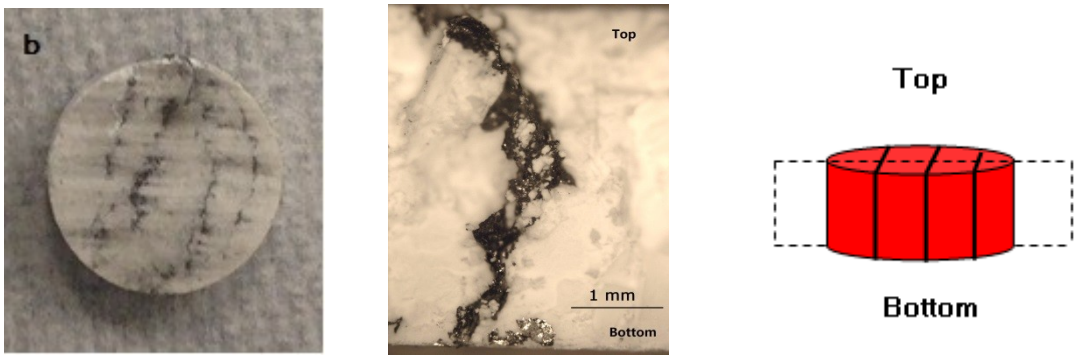

Figure 5.6(11). Cylindrical pellet with layered 5% ENG distribution. (left) Pellet diameter = 1.28 cm, thickness = 3 mm, density = 0.4g/cm3; (center) Cross section of pellet after being cut perpendicular to the ENG layers; the top and bottom surfaces of pellet are labeled. MOF-5 layers are white, while the ENG layers are black; (right) Orientation of the ENG layers. The dashed rectangle shows the cross-sectional plane

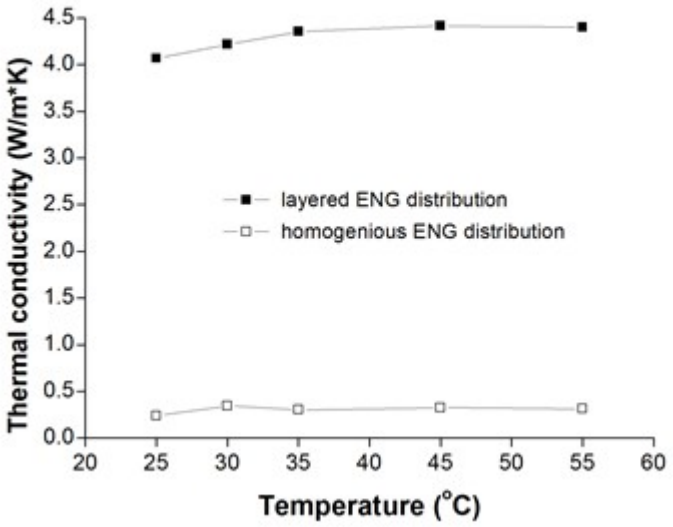

Figure 5.6(12). Thermal conductivity of pellets with two different ENG distributions (layered and homogeneous) at near-ambient temperatures. Both pellets contain approximately 5 wt. % ENG. Layered pellets contain ENG layers which are parallel to the heat flow direction. Data for the homogeneous pellets are reproduced from Fig. 5, and refer to the samples identified as "5% ENG parallel to heat flow."

The thermal conductivity of this layered pellet was measured at near-ambient temperatures using the transient Xe flash method. Results are summarized in Figure 5.6(12), and compared with those for a homogenous mixture of 5 wt.% ENG. The measured value at 35 °C is 4.35 W/m·K. Therefore, the layered pellet exhibits more than an order of magnitude (~20x) increase in thermal conductivity compared to a pellet having a homogeneous ENG distribution. As previously mentioned, this impressive jump in thermal conductivity can be attributed to the layered microstructure of the pellet. This microstructure provides a very efficient, high thermal conductivity pathway, and does so without requiring an increase in the mass fraction of ENG.

5.6.11 Comparison of MOF-5/GPX composites to MOF5/ENG composites

As described earlier in Section 5.6.3, we characterized MOF-5 composite pellets containing an alternate conductive carbon additive, GPX-103. This material belongs to family of graphene-aggregate powders developed by Cabot Corporation, and which we refer to by their trade-name GPX. (Further details on this class of material was provided in Section 5.6.3). At the microscopic level, GPX-103 particles are platelet shaped. But at the macroscopic level, GPX powders appear similar to carbon black powders, and disperse well when mixed with MOF-5 powder.

Figure 5.6(13) displays a horizontal cross-section and vertical cross-section of a MOF-5 pellet with 10 wt.% GPX-103, and with density 0.4 g/cm^3. As shown in the figure, the GPX-103 powder appears to completely coat the individual MOF-5 particles with a thin layer of conductive carbon. When the resulting MOF-5/GPX mixture is pressed into pellets, it forms a continuous network of conductive carbon in both the axial and radial directions (visible as the dark regions in the figure). The large white particle sin each figure are actually large single MOF-5 particles. Therefore, the homogeneity of the MOF-5/GPX-103 particles in this case is limited by the particle size distribution of the MOF-5 itself. While such a local, small-scale heterogeneity is not necessarily a large detriment to either the thermal or mass transport properties of the monolith. However, it is possible to improve the homogeneity by sieving the MOF-5 powder (described in greater detail in Section X).

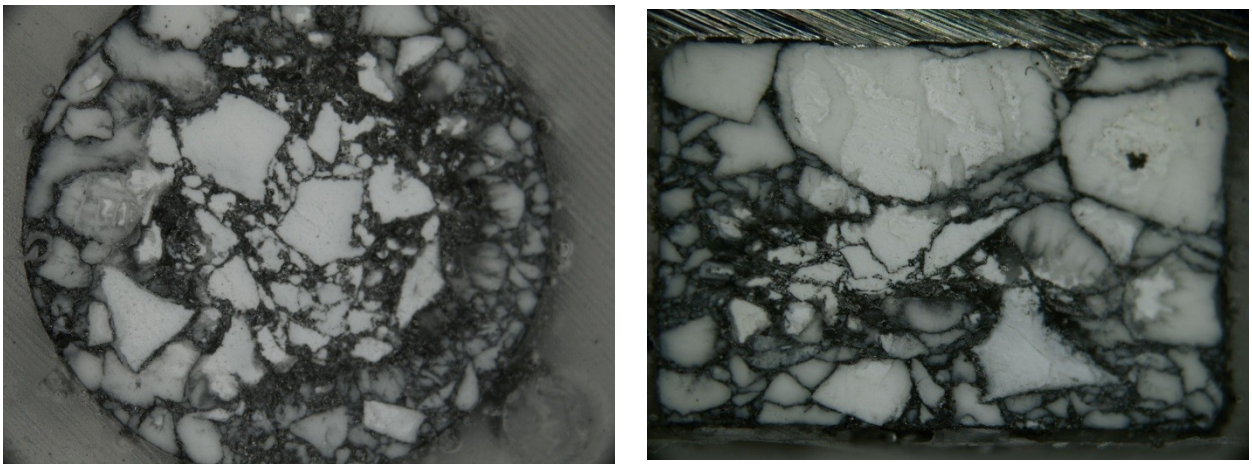

Figure 5.6(13) Optical micrograph of a radial cross-section (left) and axial cross-section (right) of a MOF-5 pellet containing 10 wt.% GPX-103 powder. The density of the pellet was 0.4 g/cc. The dark regions correspond to the conductive carbon. The large white regions correspond to single MOF-5 particles.

The thermal conductivity of neat MOF-5 pellets, and composite pellets containing 5% ENG or GPX-103 by mass were measured and compared using the transient plane source (TPS) measurement method. The results are shown in Figure 5.6.(14). When combined with the test material's volumetric heat capacity, this method can be used to measure the radial and axial thermal conductivity (κ) of a cylindrical pellet simultaneously. Note that values of κ presented in sections 5.6.7 through 5.6.10 were all measured by either a transient Xe flash method, or steady-state heat flow method. The κ values obtained by each method seems to have a small, constant offset which should be taken into consideration when making a direct comparison. Compared to the flash method, the TPS method is considered to have better fidelity for porous materials with low thermal conductivities. But a complete discussion of the relative merits of each method is beyond the scope of this report.

Unlike ENG, the GPX particles do not appear to orient as strongly with respect to compaction direction. As a result, the anisotropy in thermal conductivity is less pronounced compared to ENG, as evident in the figure below. While the radial conductivity is roughly the same for both the ENG- and GPX-containing pellets, the axial conductivity is nearly 65% larger in the GPX-containing pellet.

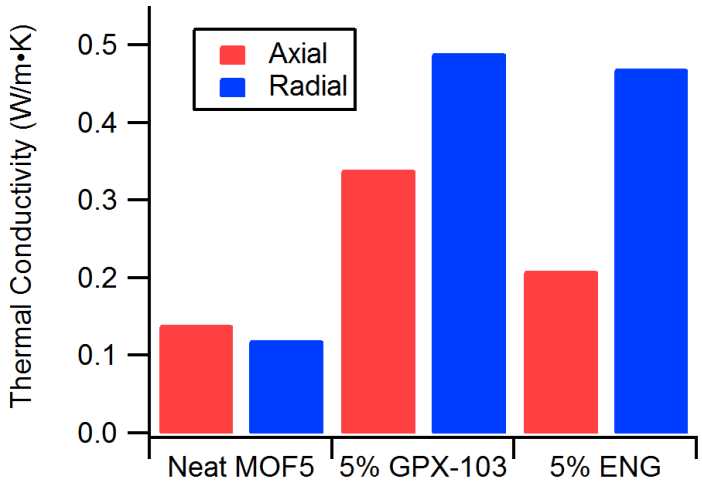

Figure 5.6(14). Thermal conductivity in the axial and radial directions for MOF-5 pellets, and composite MOF-5 pellets at 0.4 g/cc density (sample environment: 1 atm, 23°C). Pellets compacted uniaxially in the axial direction.

A comparison was made of the hydrogen storage properties of GPX and ENG-containing pellets, with the results summarized in the figure below. Because ENG and GPX-103 both possess a negligible surface area relative to MOF-5, there was not expected to be any difference in the hydrogen uptake properties of the ENG- and GPX-containing pellets. This is confirmed in the excess hydrogen adsorption isotherms at 77 K shown below. More detailed information on the hydrogen storage properties of MOF-5/ENG composites is provided in the next section.

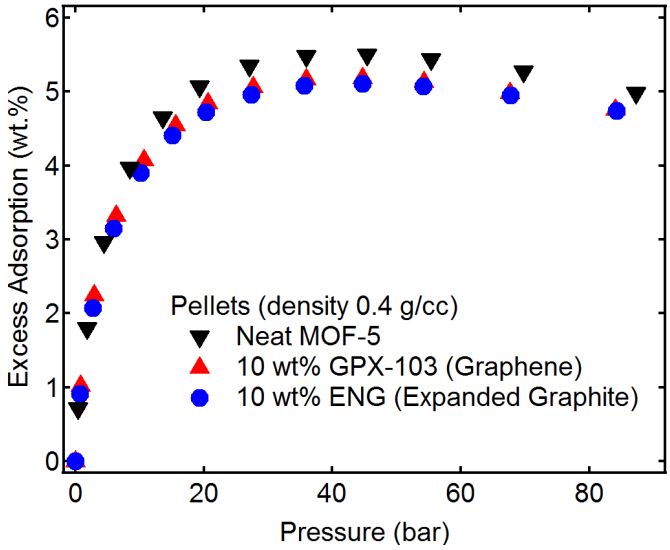

Figure 5.6(15) Excess hydrogen adsorption at 77 K for three pellet samples (each with density 0.4 g/cm^3).

5.6.12 Hydrogen Storage Properties of MOF-5/ENG Composite Pellets

Introduction

The test matrix for hydrogen adsorption characterization of the MOF-5/ENG composite pellets is shown in Table 5.69(4). The temperatures at which the H_2 adsorption measurements were performed are indicated in each box. Because the 1% ENG composites did not show significant improvement in thermal conduction properties, hydrogen isotherms were measured for only a single density. Empty boxes in the test matrix due to time constraints or instrument availability.

Table 5.6(4) Test matrix for hydrogen sorption characterization of MOF-5/ENG composite pellets. Temperatures at which H_2 adsorption measurements were performed are indicated in each box. Sample densities were rounded the nearest 0.1 g/cm^3 for categorization.

ENG %	Approximate Pellet Density					
	0.3 g/cm^3	**0.4 g/cm^3**	**0.5 g/cm^3**	**0.6 g/cm^3**	**0.7 g/cm^3**	**0.8 g/cm^3**
0 wt. %	77, 102, 117, 135, 200, 295	77, 87, 192, 297	77, 103, 132, 295	77	—	77
1 wt. %	—	77		—	—	—
5 wt. %	77, 200, 295	—	77, 103, 111, 132	—	77	—
10 wt. %	77, 200, 298	—	77, 200, 298	—	77	—

At first glance, there is not expected to be any strong interaction between the two factors in this experiment (ENG concentration, and pellet density). Expanded graphite contributes a negligible amount of surface area relative to the MOF-5, and is expected to simply lower the overall surface area by an amount proportional to its concentration (x).

$$SSA_{Total} \wedge ¿\, x \cdot SS\,A_{ENG} + (1-x) \cdot SS\,A_{MOF\,5}$$
$$¿ \approx (1-x) \cdot SS\,A_{MOF\,5}$$

In other words, a MOF-5/ENG composite containing 10% ENG should have a roughly 10% lower BET surface area compared to a neat MOF-5 pellet of equal density.

In reality we found a slight positive interaction between the ENG concentration and pellet density. Pellets containing 10% and 5% ENG experienced a lower rate of surface area loss versus density when compared against the neat MOF-5 pellets. This (relatively small) effect was attributed to the role of ENG as a lubricant during the MOF-5 compaction, and to its high compressibility which allowed it to absorb force during mechanical compaction

Results

An example of the hydrogen storage measurements for the $\rho_{env} \approx 0.5$ g/cm^3 composite pellets is shown below in Figure 5.6.(16). Excess adsorption are compared in the top panel, while the lower panel contains a comparison of the total volumetric storage at 77 K and 100 bar H_2 pressure. ENG concentrations are displayed as a mass percent (wt.%). The excess isotherms follow the expected trends, with the maximum uptake decreasing with ENG amount, $0 > 1 > 5 > 10$. The lower panel indicates both the total storage amount at 100 bar, and the isothermal delivery amount between 100 bar and 5 bar.

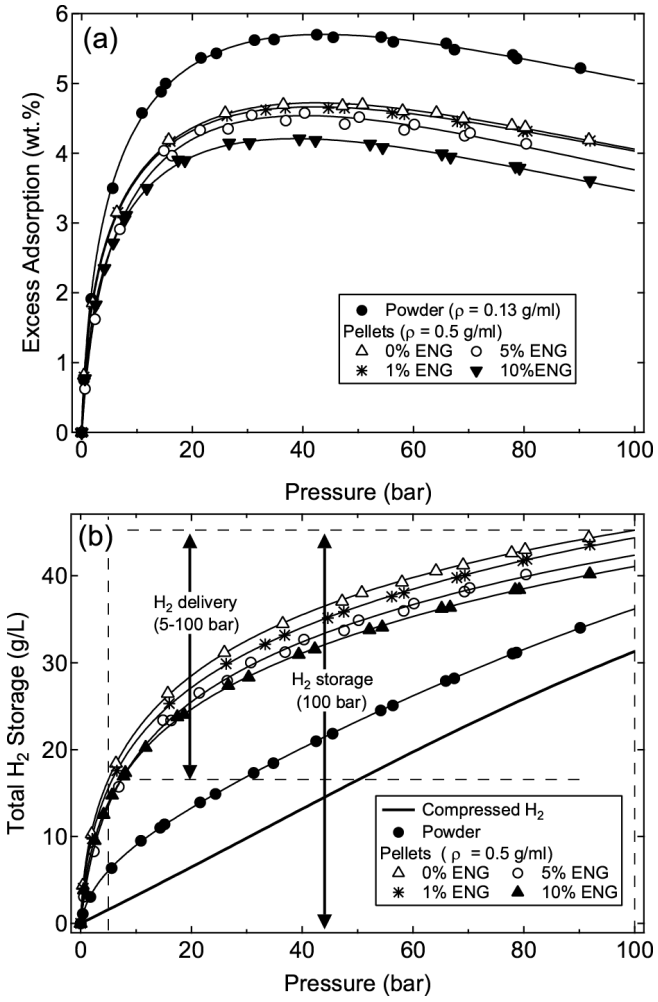

Figure 5.6(16): Hydrogen adsorption isotherms measured at 77 K for medium density ($\rho_{env} \approx 0.5$ g/cm^3) composite pellets. (a) Excess adsorption isotherms, where the excess amounts are presented in units of wt.% (b) Total volumetric

hydrogen storage; cryo-compressed hydrogen is included for comparison. Hydrogen storage at 100 bar and delivery at 5 bar is illustrated for the 0% ENG data series.

The lower panel in Figure 5.6(16) indicates a significant improvement in the total volumetric hydrogen storage amount for compacted MOF-5/ENG pellets, compared to compressed H_2 and powdered MOF-5. This is consistent with the findings for neat MOF-5 pellets presented earlier in Figure 5.5(5). As visible in the lower panel, isothermal delivery of hydrogen from the MOF-5/ENG is hampered by the retention of adsorbed H_2 gas at pressures below 5 bar. However, there are simple engineering solutions for the non-desorbed hydrogen gas at 5 bar, such as moderately heating the system to temperatures in the 80 K to 140 K range using the vehicle cell coolant system.

Summary of H_2 Storage at 77 K — Figure 5.6(17) provides a summary of the excess hydrogen adsorption in MOF-5/ENG pellets at 77 K. The y-value is simply the maxima for the hydrogen excess adsorption isotherm at 77 K, which typically occurs at pressures between 35 bar and 45 bar. As suggested earlier in this section, there appears to be a slight interaction between the two factors, ENG% and pellet density. The rate of capacity loss versus density is smaller for the 5% and 10% ENG materials (i.e., their slopes in Fig. 5.6(17) are smaller). The addition of ENG actually appears to mitigate the reduction of hydrogen adsorption capacity at higher densities. We suggest that ENG additions may protect MOF-5 crystallites from plastic deformation and/or amorphization during uniaxial compaction due to its properties as a lubricant, or due to its highly compressible properties.

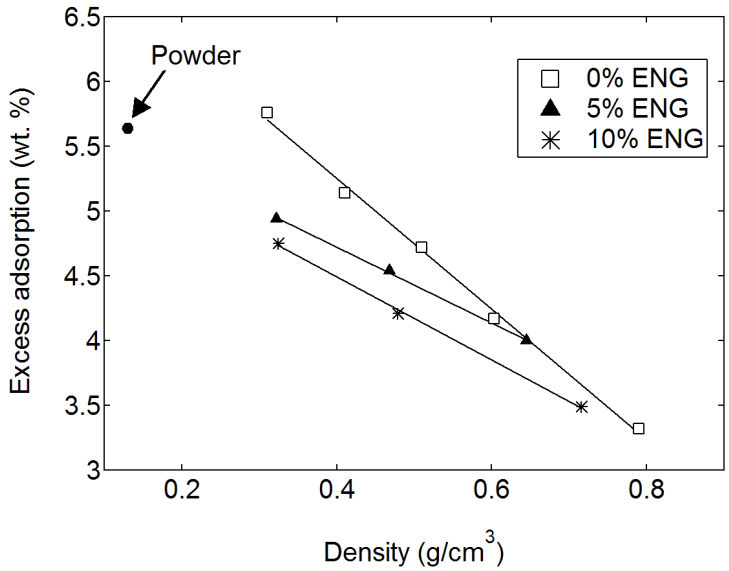

Figure 5.6(17) Maximum excess adsorption at 77 K plotted versus the pellet density for MOF-5+ENG pellets.

The maximum excess hydrogen adsorption (wt.%) at 77 K is plotted versus the BET specific surface area in Figure 5.6(18) shown below. Variation between the two variables roughly follows the empirical 500 m^2/g per 1 wt.% Chahine rule. As noted earlier, these values of BET surface area were obtained from fits to $0.05 < p/p_0 < 0.2$, which results is significantly lower values.

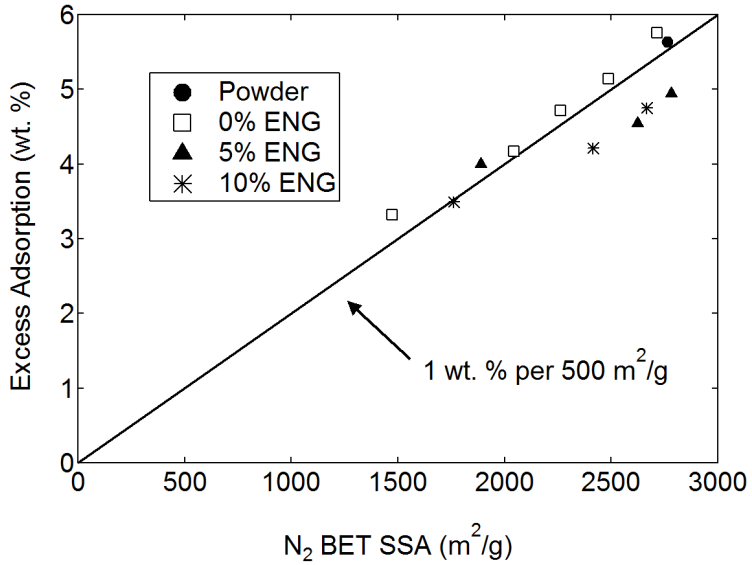

Figure 5.6(18) Maximum excess H_2 adsorption at 77 K plotted versus the BET specific surface area

The total (volumetric) H_2 storage at 100 bar and 77 K is shown in the Fig. 5.6(19) below. As derived previously in Eq. 5.4.13, this value is equal to the total mass (kg) amount of hydrogen present in the tank at 100 bar and 77 K, divided by the internal volume of the tank (L). For comparison the density of compressed hydrogen at 77 K (lower line) is included in the figure. The theoretical hydrogen storage for a single crystal MOF-5 monolith occupying the entire storage tank is drawn as the upper line in Fig. 5.6(19). The calculation of this value is given by Eq. 5.4.14, in an earlier section of the report.

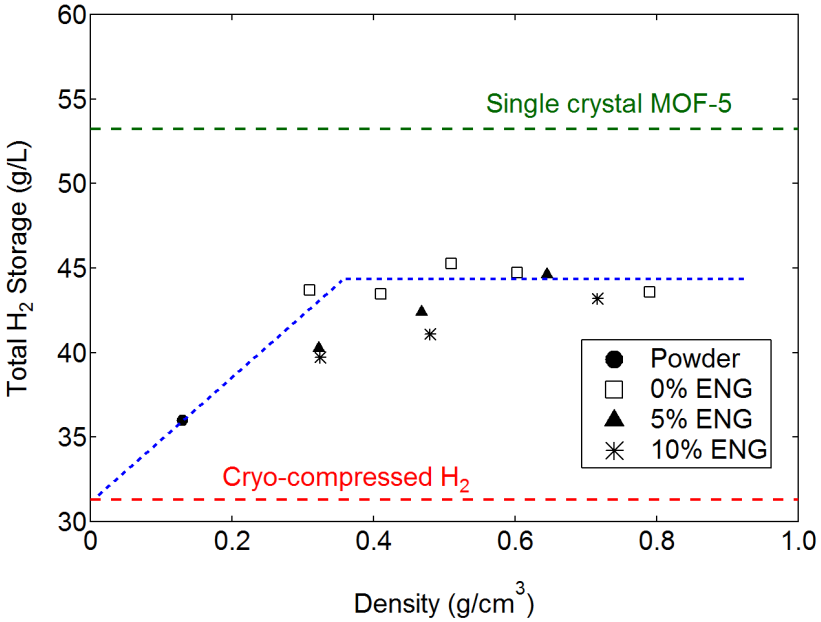

Figure 5.6(19) Total volumetric hydrogen storage in MOF-5/ENG composite pellets at 77 K and 100 bar H_2 pressure. Values for compressed H_2 and single-crystal MOF-5 (both at 77 K and 100 bar) are included for comparison

The results for MOF-5/ENG composite pellets shown in the figure above are more or less consistent the results reported earlier for neat MOF-5 pellets. Total hydrogen storage reaches a plateau of about 45 g/L, which is below the theoretical amount that can be stored in MOF-5. The presence of up to 10 wt.% of conductive ENG does not appear to have a significant effect on this parameter. Neat MOF-5 pellets with a density between 0.3 g/cm^3 and 0.7 g/cm^3 achieved approximately 83% of the volumetric hydrogen storage of a MOF-5 single crystal. This is a promising development given the simplicity of uniaxial mechanical compaction and its potential for scale-up.

Table 5.6(5). Hydrogen Adsorption Properties of MOF-5/ENG Composites

Sample		BET Surface Area (N_2)	Maximum Excess Adsorption		Deliverable Hydrogen	
ENG %	*ρ (g/cm³)*	*m²/g*	*Gravimetric (wt%)*	*Volumetric (g/L)*	*100–0 bar (g/L)*	*100–5 bar (g/L)*
0	0.31	2716	5.76	19.1	43.7	31.3
0	0.41	2486	5.14	22.2	43.5	29.1
0	0.52	2263	4.72	25.7	45.3	28.7
0	0.60	2045	4.17	26.3	44.7	27.5
0	0.79	1473	3.32	27.1	43.6	26.4
1	0.49	2584	4.66	24.1	44.4	28.8
5	0.32	2781	4.94	16.7	40.3	29.0
5	0.47	2623	4.54	22.3	42.4	28.9
5	0.65	1888	4.00	26.9	44.6	27.5
10	0.32	2665	4.75	16.1	39.7	28.8
10	0.48	2413	4.21	21.0	41.1	27.2
10	0.72	1760	3.49	25.9	43.2	26.6
Powder		2762	5.64	7.8	36.0	30.0
Single-Crystal		2762	5.64	36.2	53.2	30.9
Cryo-compressed		—	—	—	31.3	29.7

Variable temperature hydrogen adsorption

As summarized in Table 5.6(4), multi-temperature isotherms were measured for six of the MOF-5/ENG composite samples, in addition to powder MOF-5. Fitting the Unilan model to 77 K, 200 K and 300 K hydrogen isotherms was generally sufficient to accurately predict the excess adsorption data at temperatures and pressures between 77 K and 300 K. However, the Unilan model parameters summarized in Table 5.6(6) were obtained by fits of the Unilan model to all available temperature isotherms. The two fitted parameters n_{max} and v_a decrease versus ENG% and density. This is consistent with our findings that micropore volume decreases with compaction and decreases to a lesser degree with ENG addition.

Table 5.6(6). Unilan Model Parameters for H_2 Adsorption by MOF-5/ENG Composites

Sample		(a) Best Fits					(b) Constraints [a]	
ENG %	ρ (g/cm³)	$-\Delta S/R$	E_{max} (kJ/mol)	E_{min} (kJ/mol)	n_{max} (mol/kg)	v_a (cm³/g)	n_{max} (mol/kg)	v_a (cm³/g)
Powder	0.13	7.93	5.04	1.06	67.8	1.40	64.1	1.4
0	0.31	7.89	4.98	1.31	63.3	1.28	63.3	1.28
0	0.52	8.08	5.30	2.05	42.4	0.91	53.9	1.21
5	0.32	7.88	5.03	2.03	44.7	1.03	55.3	1.23
5	0.47	7.88	4.76	2.11	41.3	0.95	48.0	1.00
10	0.32	7.87	4.95	1.93	44.7	1.04	53.0	1.19
10	0.48	7.86	4.96	1.55	44.6	1.08	47.5	1.11

[a] Constraints: $\Delta S = -7.89 \times R$, $E_{max} = 4.98\,\text{kJ/mol}$, $E_{min} = 1.31\,\text{kJ/mol}$

Note: Parameters corresponding to a minimum SSR between fits and data are summarized in the columns labelled "(a) Best Fits". In these fits, all 5 model parameters were allowed to vary independently without any constraints until a minimum SSR was reached. Some trends in the model parameters for the MOF-5/ENG composites are purely artifacts arising from parameter correlation. In particular, there is an inverse correlation between the E_{min} and n_{max} model parameters. To find more meaningful trends in the parameters, some must be held constant during the fit. The entropy and enthalpy parameters are not expected to change significantly with density and small ENG additions. Fits were therefore performed with ΔS, E_{max} and E_{min} held constant at the values for neat 0.31 g/cm³ pellets, leaving n_{max} and v_A as the only adjustable parameters. These constraints do not significantly decrease the quality of fits.

Using the fitted Unilan variables summarized above, it is possible to explore the hydrogen storage trends within the MOF-5/ENG composites as a function of temperature. From Eq. 5.4.13 we know that there are two components to the stored hydrogen in MOF-5. The first component in the surface excess hydrogen (i.e., the adsorbed phase). The second component is the "free" hydrogen which exists at the bulk hydrogen density throughout the free space of the MOF-5 sample, recalling that $v_{free} = 1/\rho_{bulk} - 1/\rho_{sk}$). The relative fraction of these two components is summarized in Figure 5.6(20) for both a loosely packed powder MOF-5 bed, and a compacted MOF-5 pellet. As expected, the powder MOF-5 has a much large contribution from the free H_2 which occupies the inter-particle voids. In the compacted MOF-5 pellets (with $\rho_{env} = 0.52$ g/cm^3) the surface excess hydrogen constitutes a much larger fraction of the total stored amount. This is expected since compaction of the MOF-5 powder reduces the amount of the inter-particles voids.

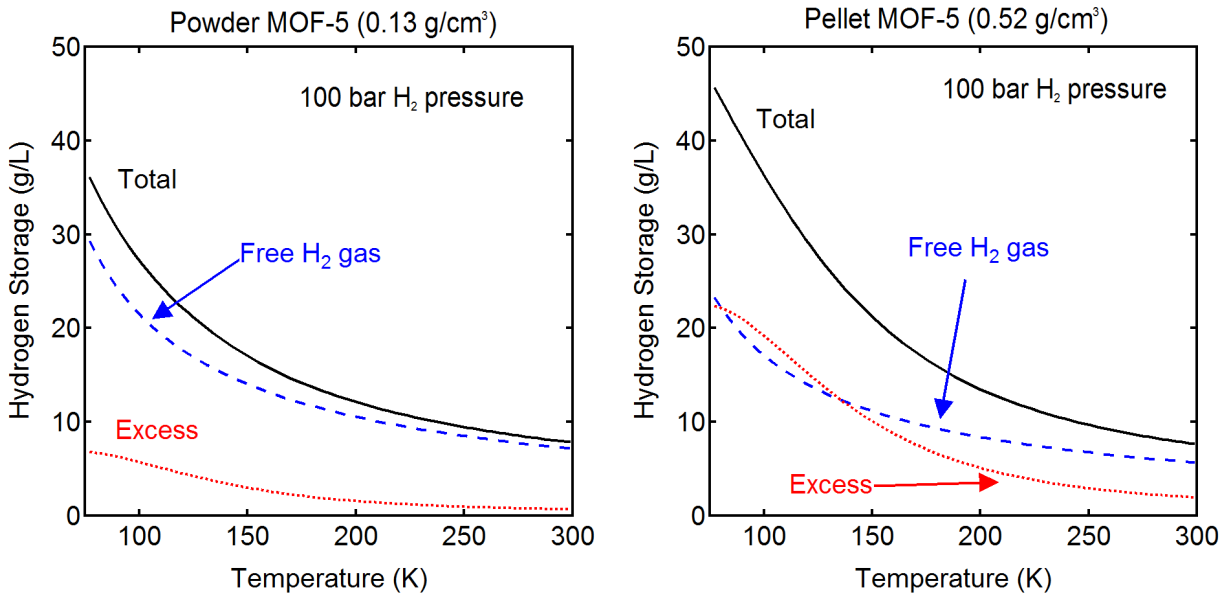

Figure 5.6(20) Breakdown of the stored hydrogen within a powder MOF-5 bed (left) and compacted MOF-5 monolith (right) into the two components: surface excess hydrogen and bulk free hydrogen.

The Unilan model parameters were used to compared the total hydrogen storage (volumetric) amounts for the MOF-5/ENG composites as a function of temperature. Results are summarized below in Fig. 5.6(21).

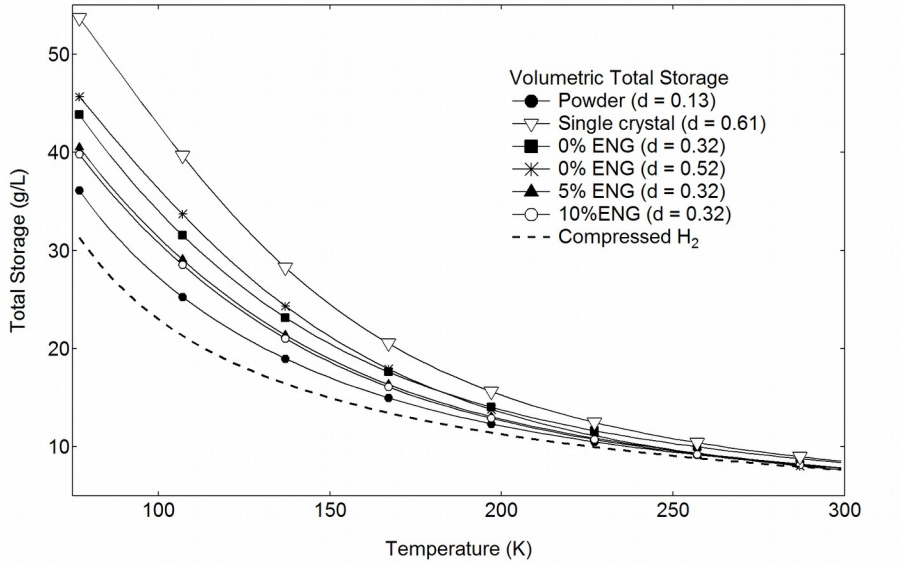

Figure 5.6(21). Total volumetric hydrogen storage for MOF-5/ENG materials plotted as a function of temperature using Unilan model parameters.

Single crystal MOF-5 values represent an upper limit for volumetric hydrogen storage of compacted MOF-5. Among the samples measured, volumetric storage is highest for the 0% ENG pellets of density 0.52 g/cm^3. Relative to powder MOF-5 and compressed H_2, the largest improvement in volumetric H_2 storage by MOF-5/ENG composites occurs at temperatures close to 100 K. Neat MOF-5 pellets with density 0.52 g/cm^3 have a total volumetric storage of 36 g/L at 100 K, which is roughly 33% and 58% larger than the respective values for powder MOF-5 and compressed H_2. The addition of 5% and 10% ENG to the ~ 0.5 g/cm3 MOF-5 pellets decreases the total volumetric storage at 100 K by about 6% and 11%, respectively.

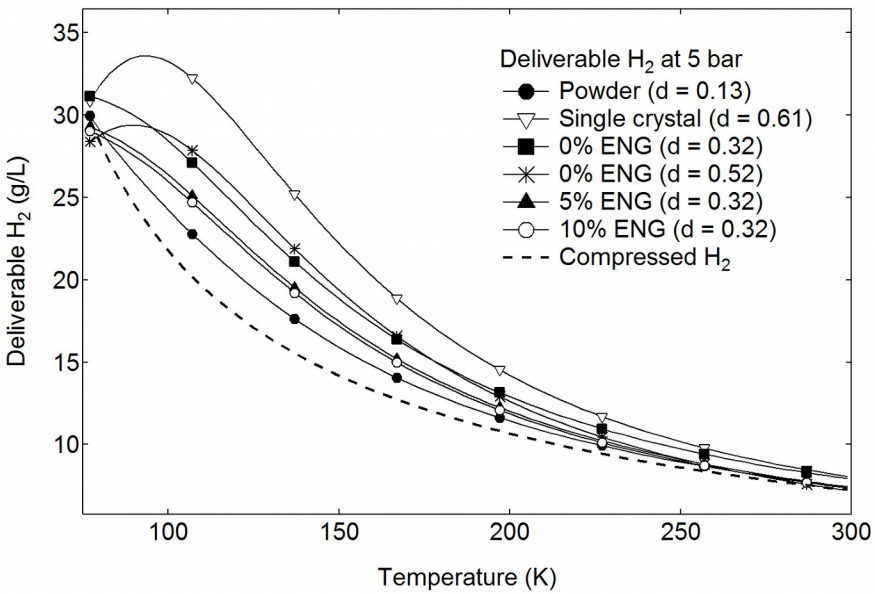

Figure 5.6(22) Total isothermal hydrogen delivery between 100 bar and 5 bar, at the temperature on the *x*-axis.

Isotherm hydrogen delivery between 100 and 5 bar is plotted as a function of temperature in Fig. 5.6(22) above. Cryo-compressed has more deliverable hydrogen at 77 K than most MOF-5/ENG composites (with the exception of 0% ENG 0.5 g/cm^3 pellets and single-crystal MOF-5). However, above 77 K the MOF-5/ENG composites exceed cryo-compressed hydrogen in terms of deliverable hydrogen capacity. The largest improvement in isotherm delivery (relative to powder MOF-5 and compressed H_2) occurs at a temperature of approximately 122 K. The 0% ENG 0.52 g/cm^3 pellets have the isothermal delivery at 122 K of 25.0 g/L, about 23% and 41% larger than the respective values for powder MOF-5 and compressed H_2. Addition of 5% and 10% ENG to the ~ 0.5 g/cm^3 MOF-5 pellets reduces the total isothermal H_2 delivery by about 6% and 10%, respectively.

5.6.13 Hydrogen Permeability in MOF-5/ENG Composites

Hydrogen permeability was measured experimentally for MOF-5/ENG composites using the setup and methods described earlier in Sec 5.5.8. Permeability values of the samples with varying ENG content measured at 77 K and 296 K versus sample density are shown in Fig. 5.6(23). As was the case with neat MOF-5 pellets, the results show H_2 permeability decreases exponentially with the density of the pellet. In addition, the permeability measured at 296 K is higher than that measured at 77 K for the same sample. At 296 K, the 5 wt.% ENG sample has higher permeability than neat MOF-5 sample. Similarly, the 10 wt.% ENG sample has slightly higher permeability than the 5 wt.% ENG up to a pellet density of around 0.4 g/cm^3. At 77 K, the permeability of neat MOF-5, 5 wt.% ENG and 10 wt.% ENG samples do not differ significantly

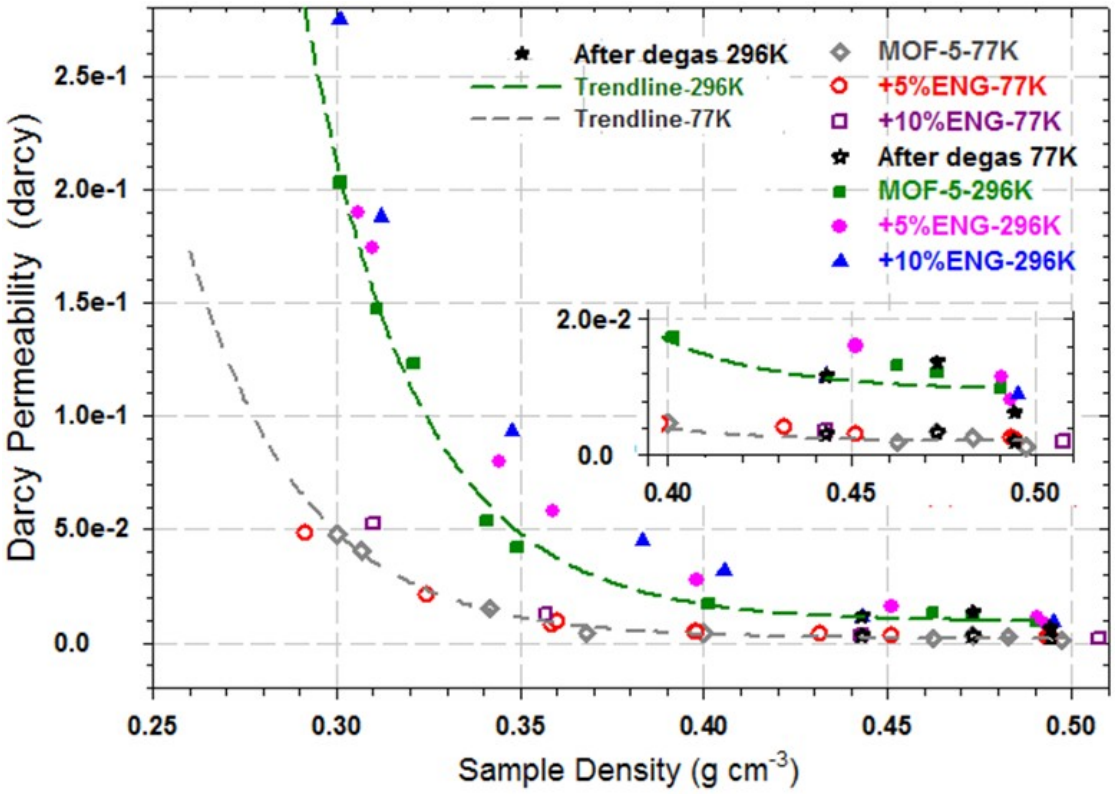

Figure 5.6(23) Darcy permeability of hydrogen versus sample density for MOF-5/ENG pellets

Measured values of the Darcy permeability constant for H_2 permeation through MOF-5/ENG pellets are tabulated below in Tables 5.6(7-8).

To summarize the effect of ENG additions on hydrogen permeability through compacted MOF-5 powder:

1. At 296 K, the addition of ENG enhances the H_2 permeability when the pellet density is below 0.4 g/cm^3. The enhancement is greater for 10% ENG than 5% ENG.
2. Any ENG-based enhancement in H_2 permeability is suppressed in pellets with a density greater than 0.4 g/cm^3.
3. At 77 K, additions of ENG do not affect the measured Darcy permeability for H_2 gas. The modified compressible Darcy permeability is lower than incompressible Darcy permeability of the same sample.

Table 5.6(7) Values of the Darcy permeability for a MOF-5+5 wt.% ENG pellet. Assuming either an incompressible gas (κ) or compressible gas (κ_c).

$T=296\,K$			$T=77\,K$		
ρ_{env} (g/cm^3)	κ (Da)	κ_c (Da)	ρ_{env} (g/cm^3)	κ (Da)	κ_c (Da)
0.3057	0.1896	0.1743	0.2914	0.0486	0.0465
0.3096	0.1741	0.1717	0.3244	0.0209	0.0193
0.3244	0.0796	0.0689	0.3587	0.0081	0.0068
0.3587	0.0581	0.0461	0.36	0.0094	0.0081
0.3981	0.0278	0.0185	0.3974	0.0044	0.0032
0.451	0.016	0.0087	0.3981	0.0046	0.0036
0.4908	0.0114	0.002	0.4317	0.0041	0.0031
0.4933	0.0081	0.0036	0.451	0.0029	0.002
0.4942	0.0064	0.0029	0.4933	0.0026	0.0018
			0.4942	0.0022	0.0015

Table 5.6(8) Values of the Darcy permeability for a MOF-5+10wt.% ENG pellet. Assuming either an incompressible gas (κ) or compressible gas (κ_c).

$T = 296\,K$			$T = 77\,K$		
ρ_{env} (g/cm^3)	κ(Da)	κ_c(Da)	ρ_{env} (g/cm^3)	κ(Da)	κ_c(Da)
0.3008	0.2748	0.2578	0.31	0.0534	0.0513
0.3123	0.188	0.173	0.357	0.0125	0.0111
0.3477	0.0936	0.082	0.4429	0.0036	0.0016
0.3833	0.0453	0.0328	0.5076	0.002	0.0012
0.4054	0.0321	0.0224			
0.4429	0.0117	0.0056			
0.4952	0.0091	0.0041			

5.6.14. Conclusions:

(1) ENG is excellent for directional heat conduction within MOF-5 pellets and monoliths. When incorporated into a layered alternating MOF|ENG|MOF compacted structure, it offers about twenty-fold improvement in heat conduction in the ENG planar direction. This design can be scaled up, and combined with an internal aluminum pin matrix

(2) GPX (graphene-aggregate carbon powder) is good for isotropic heat conduction in a MOF-5 pellets, and coats individual MOF-5 particles with a conductive layer. Homogeneity is limited by the particle sizes of MOF-5.

(3) The impact on micropore volume, surface area, and hydrogen adsorption properties is identical for both ENG and GPX, and depends only on the mass % loading and pellet density.

5.7 Impurity Degradation

5.7.1 Introduction

A commonly assumed advantage of cryo-adsorbents over other hydrogen storage materials (e.g., metal hydrides, complex hydrides) is their chemical stability with respect to gas impurities and moisture.
However, while most conventional adsorbents are chemically stable (requiring only regeneration to remove adsorbed water and other impurities), MOFs such as MOF-5 may be less robust against common impurities in hydrogen fuel streams.

For example, zinc-based MOFs with carboxylate linkers (e.g., MOF-5) are known to be susceptible to chemical degradation in humid conditions, owing to the weak metal-ligand bond between Zn and O. Past studies have also identified MOFs which are unstable in the presence of high concentrations of hydrogen sulfide, ammonia, and other common impurities in industrial gas streams. In most cases, MOF degradation is manifested as a decrease in storage capacity due to a reduction in the surface area and pore volume, changes in crystal structure, or local chemical bonding.

While most studies have focused on scenarios in which MOFs are exposed to high concentrations of harmful impurities, these environments are far more severe than what would be typically encountered in an on-board hydrogen storage system. As is the case for semiconductor and Li-ion battery production, strict environment controls can be implemented at the production and packaging phases. Once installed in a vehicle, hydrogen storage materials would be subjected only to impurities in the hydrogen fuel stream itself.

Hydrogen gas from the fueling station is required in the U.S. to be is compliant to fuel quality standards outlined in SAE J2719. (The international standard ISO 14687-2 provides identical purity standards.) Impurity limits set by J2719 are driven primarily by the need to protect the catalyst and polymer electrolyte components in the fuel

cell stack. As a result, threshold limits for ammonia (0.1 ppm), carbon monoxide (0.2 ppm), sulfur species (0.004 ppm), and halogenates (0.05 ppm) are exceptionally stringent. Complete threshold limits are summarized in Table 5.7(1). Although SAE J2719 does recognize impurities that are known to poison and/or deactivate conventional metal hydride-based storage materials (e.g., CO and O_2), the impact of impurities on adsorbent materials such as MOFs are currently not accounted for.

The identity and concentration of impurities in the hydrogen fuel stream depends on the hydrogen production method. For example, hydrocarbons, carbon monoxide, and sulfur species are more likely to be present in hydrogen produced by steam methane reformation, the predominant method. Field data from existing hydrogen stations confirms that the J2719 impurity limits are achievable, although some station samples still exceed the requirements. Nitrogen, oxygen, and water are contaminants likely to leak in from the atmosphere during refueling process itself.

To our knowledge, no systematic studies exist regarding the chemical stability of MOFs after exposure to hydrogen streams containing impurities identified in J2719. The utilization pattern of the hydrogen storage system will strongly influence the mechanism by which degradation can occur. For example, if a MOF-based system is cycled frequently at cryogenic temperatures (i.e. cycling), it may accumulate the more strongly-bound impurity species by selective adsorption, potentially reducing the available storage capacity for hydrogen molecules. However, chemical degradation side-reactions involving the adsorbed impurities will proceed slowly at cryogenic temperatures. For MOFs stored at higher temperatures for extended periods (i.e. storage), chemical side-reactions will proceed faster, but the accumulation of impurities will be considerably smaller.

As a zinc-based metal-organic framework material with a carboxylate linker, MOF-5 is susceptible to water-induced degradation. Of particular importance, however, is the fact that MOF-5 synthesis methods have been optimized, meaning that high-quality, fully-desolvated samples of MOF-5 are commercially available. This is particularly important because it enables the systematic study of impurity-induced degradation, without having to account for degradation caused or accelerated by poor sample quality.

Table 5.7(1) Impurity test gas mixtures used in this study.

Gas Mixture	Impurity	Test Gas Concentration *(ppm)*	J2719 Threhold Limit *(ppm)*	Cycle Test Performed	Storage Test Performed	Concentration factor over J2719
1	NH_3	7	0.1	Y	N	70
2	H_2S	1	0.004[a]	Y	Y	250
3	HCl	9	0.05[b]	Y	N	180
4	H_2O	8	5	Y	Y	1.6
5	CO	2	0.2	Y	N	10
	CO_2	5.7	2			2.85
	CH_4	8.3	2[c]			4.15
	O_2	9.6	5			1.92
	N_2	119	100			1.19
	He	505	300			1.7
Not Tested	HCHO	-	0.01	-	-	
Not Tested	HCOOH	-	0.2	-	-	

a Total sulfur category in J2719 includes hydrogen sulfide (H_2S), carbonyl sulfide (COS), carbon disulfide (CS_2) and mercaptans

b Total halogenates category in J2719 includes hydrogen bromide (HBr), hydrogen chloride (HCl), chlorine (Cl_2) and organic halides (R-X)

c Total hydrocarbons category in J2719 includes ethylene, propylene, benzene, phenol (paraffins, olefins, armoatic compounds, alcohols, aldehydes)

We examined the degradation potential of 10 impurities listed in SAE J2719. These impurities were mixed with nominally pure hydrogen gas at a concentration of up to several ppm, and include: NH_3, H_2S, HCl, H_2O, CO, CO_2, CH_4, O_2, N_2, and He. We subject MOF-5 powder samples to these gas mixtures for pressure cycle testing at 77 K, and ambient temperature static exposure testing for 1 week. The hydrogen storage capacity of the MOF-5 is tested at regular intervals during the pressure cycling, and is tested at the start and end of each static exposure test. Powder XRD and FTIR spectra of the MOF-5 are collected on the post-test samples to check for changes in the crystal structure, and confirm the absence of new phases. The results indicate that common hydrogen fuel impurities at low levels do not lead to significant degradation of MOF-5 powder in either the pressure cycling or ambient static exposure tests.

5.7.2 Methods

Impurity test gases: The SAE J2719 requirements for fueling stations are summarized in table 5.7(1). This standard is based on the potential constituents from hydrogen production. It is improbable that a single production method would result in a mixture with all twelve of the contaminants listed in the standard. In addition, preparation of a single gas mixture containing all J2719 contaminants is impractical due to the interactions of the impurities with each other. For example, hydrogen chloride and hydrogen sulfide will react together and with water. Therefore, five separate hydrogen impurity gas mixtures were prepared according to the J2719 levels that could be formulated and qualified by the specialty gas company (Airgas). The separate mixtures allowed for independent analysis of the effect of each impurity. Formulation and qualification of the impurity test gas mixtures at the trace levels in SAE J2719 also proved a challenge, necessitating the use of higher impurity levels.

Consequently, the following 5 gas mixtures were examined (in all cases the balance of gas is H_2):

- Mixture 1: Ammonia (NH_3), at 5 to 10 ppm
- Mixture 2: Hydrogen sulfide (H_2S), at 1 ppm
- Mixture 3: Hydrogen chloride (HCl), at 5 to 10 ppm
- Mixture 4: Water (H_2O), at 5 to 10 ppm.
- Mixture 5: Carbon monoxide (CO), at 2 ppm; Carbon dioxide (CO_2) at 5 ppm; Methane (CH_4) at 2 ppm; Oxygen (O_2) at 5 ppm; Nitrogen (N_2) at 100 ppm; Helium (He) at 500 ppm. We note that the 6 impurities present in this mixture are presumed to not react with each other.

The delivered impurity test gas levels are shown in Table 5.7(1). Since the majority of these levels exceed the impurity limits defined in J2719, the test gas mixtures used in this study provide a more stringent test of MOF-5 robustness.

Cycle test procedures: Pressure cycling protocols utilized in this study borrow from methods previously used to study conventional hydride materials. Previous work has established numerous cycle test methods. These include intrinsic cycling, where the same hydrogen gas is re-used each cycle, and extrinsic cycling, where a fresh aliquot of hydrogen is introduced in each cycle. Many of the existing cycle test methods were developed to study aging mechanisms unique to metal hydrides, including alloy disproportionation and particle breakup. The present study employs only extrinsic pressure cycling, as this method best simulates the MOF-5 degradation mechanisms expected in on-board hydrogen storage systems.

Pressure cycle testing at 77 K was performed using an automated manometric sorption instrument, following a programmed routine. Each cycle starts with a 5 min adsorption period, where a 168 ml reservoir is filled with a fresh dose of 100–105 bar impurity gas mixture, which is then expanded into an evacuated sample cell containing MOF-5. The empty sample cell has a free space of approximately 15 ml, with the MOF-5 sample displacing a volume of approximately 200 µl. At the end of the 5 min adsorption period, the sample cell is closed off. The equilibrium pressure at this point is in the 75–85 bar range, which corresponds to 5.5–5.8 wt.% excess hydrogen at 77 K. This is followed by a 5 min desorption period in which the hydrogen in the sample cell is expanded into an evacuated 1174 ml reservoir. Following the desorption period, the hydrogen pressure in the entire instrument is slowly ramped down to 1 bar, and then opened to continuous vacuum for 5 min. During the active vacuum period nearly all of the adsorbed hydrogen should be removed. This cycle pattern is repeated 300 times in total for each test gas. Cycling is interrupted approximately every 60 cycles to measure the hydrogen adsorption capacity of the sample.

Pressure cycle tests were conducted for all five test gas mixtures listed in Table 5.7(1). Throughout each period of continuous cycling the sample cell is immersed in a liquid nitrogen (LN2) bath, and is allowed to warm up only for the capacity test. To prevent MOF-5 powder from being blown out of the sample cell during the repeated desorption steps, which involve a large pressure differential, a 2 micron sintered metal filter gasket was placed immediately above the sample cell. The filter has a 0.125 inch hole drilled in it to allow an internal PRT sensor to extend into the sample cell. Fresh samples of MOF-5 powder were utilized for each gas mixture test and then remained for the entire 300 cycles.

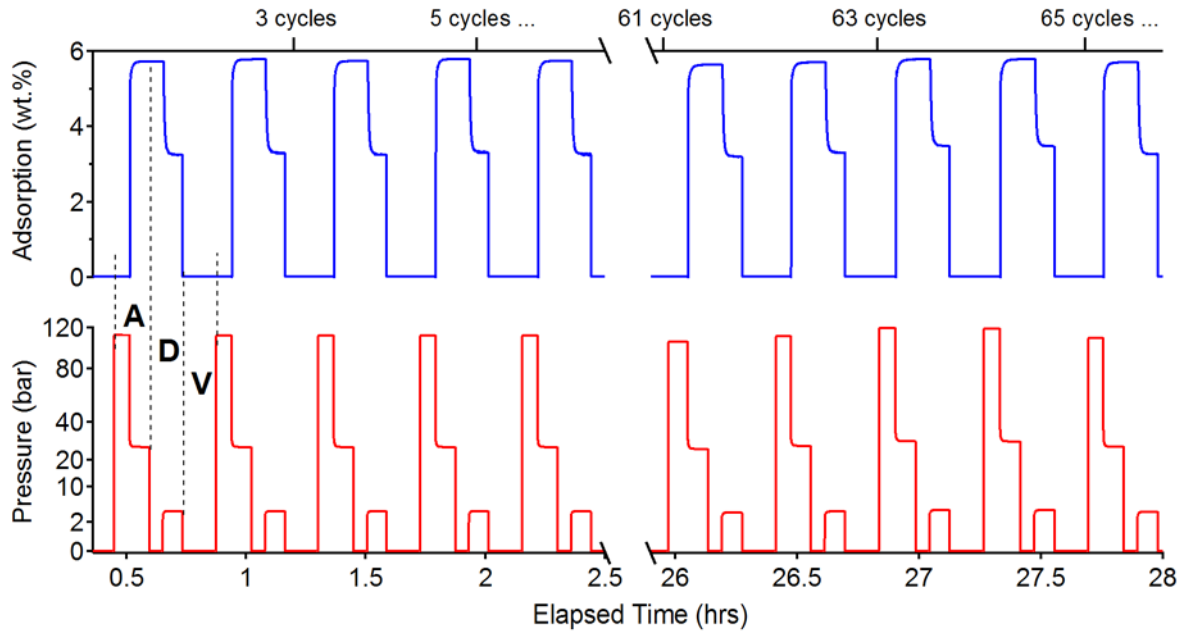

Figure 5.7(1). An example of the pressure cycling procedure for the exposure of MOF-5 to impure hydrogen gas. The lower panel displays the reservoir pressure, plotted on a square root scale. The upper panel displays the excess gas adsorbed in the MOF-5 sample. Both panels are plotted versus total elapsed time (bottom axis) and cycle number (top axis). For the second cycle the adsorption phase (labelled A), desorption phase (labelled D) and vacuum phase (V) are identified. The x-axis is split so as to show the first 5 and last 5 cycles from the experiment

An example of the pressure cycling procedure is provided in Figure 5.7(1). To accurately track the adsorbed hydrogen amounts during this particular cycling experiment, smaller volumes were employed for both the adsorption (Vr =12.31 ml) and desorption (Vr = 167.63 ml) phases. During the 5 min adsorption phase (labeled A), the pressure drops to about 26 bar and the adsorbed amount reaches 5.8 wt. %, on average. During the 5 min desorption period (labeled D), the average equilibrium pressure is 3.8 bar, which corresponds to an excess hydrogen concentration of 3.2 wt.%. During the 5 minute vacuum period (labeled V), it is assumed that the hydrogen concentration drops to approximately 0 wt.% (although the value was not directly measured). This confirms that the MOF-5 sample adsorbs around 5.8 wt.% (excess basis) of hydrogen gas each cycle. Importantly, the hydrogen uptake between the first five and last five cycling periods in this particular experiment appears to be unchanged. **In contrast to the rest of the report, in Section 5.7 the unit of weight percent (wt. %) refers to the mass of adsorbed hydrogen per 100 g of adsorbent. The mass of adsorbed hydrogen is not included in the denominator**

Storage test procedure: Long-term impurity storage tests were performed for impurity mixtures using a manometric sorption instrument. The sample cell containing powder MOF-5 sample was charged with the test gas mixture up to an equilibrium pressure of approximately 40 bar, with the sample cell initially immersed in liquid nitrogen. The sample cell was then valved off and allowed to warm to room temperature. It was left under hydrogen pressure at room temperature for 1 week. Storage tests were performed for the H_2O and H_2S test gas mixtures.

Capacity Test Procedure: Capacity tests consist of measuring a single hydrogen adsorption isotherm at 77 K, up to a maximum pressure of approximately 90 bar. Hydrogen adsorption measurements were performed using a

manometric sorption instrument (PCT-Pro 2000, Setaram) with an oil-free scroll vacuum pump (Anest Iwata model ISP90). Free space measurements were performed using helium at room temperature for each sample. The sample cell was immersed in a liquid nitrogen bath, with the LN2 level filled to a calibrated height.

Initial capacity tests were collected prior to starting the pressure cycling and storage procedures. Before being loaded in the sample cell, MOF-5 powder samples were degassed to remove any weakly-bound water. Samples were evacuated at room temperature for at least 6 hours, then evacuated and heated to 130 °C overnight.

Final capacity tests were collected at the end of both pressure cycling and storage. For pressure cycling, capacity tests were measured approximately every 60 cycles until the end of the 300 cycle tests. With the exception of the initial capacity tests, the MOF-5 samples were degassed only by pulling vacuum on the sample at room temperature (no heating) before capacity tests. (For the initial capacity tests the freshly loaded MOF-5 sample was degassed at 130°C, as described in the previous paragraph.)

Settings, dose increments and step times were identical for all capacity test measurements. Due to the difficulty in switching test gas bottles in the middle of storage and pressure cycle testing, capacity tests were performed using the same impurity gas mixtures utilized in the corresponding cycle and storage procedures. **In contrast to the rest of the report, in Section 5.7 the unit of weight percent (wt. %) refers to the mass of adsorbed hydrogen per 100 g of adsorbent. The mass of adsorbed hydrogen is not included in the denominator.**

XRD and FTIR Characterization: Powder X-ray diffraction (XRD, Rigaku Miniflex II diffractometer using Cu Kα radiation, $\lambda = 1.5418$ Å) was used to assess changes in crystallinity resulting from exposure to testing gas containing impurities. Fourier transform infrared spectrometry (FTIR) was used to assess changes in bonding resulting from exposure to impurities. Measurements were made using a Thermo Scientific Nicolet FTIR spectrometer. A scan range of 4000 to 600 cm-1 was used, with a scan time of 5 minutes. Powder samples were loaded and scanned in air.

5.7.3 Maximum Impurity Accumulation:

We first estimate the maximum impurity accumulation that could occur in the MOF-5 adsorbent bed on a worst-case basis during repeated refueling and operation. In this scenario, we assume that the impurity concentrations in the fuel stream are at the maximum allowable levels in J2719, as summarized in Table 5.7(2). The tank is assumed to be filled with 5.6 kg usable hydrogen during each cycle based on the DOE target capacity for a driving range of 300 miles. At this capacity, the storage vessel would contain about 25 kg of MOF-5 with the full condition at 100 bar and 80 K while the empty condition is 5 bar and 140 K (similar to the temperature excursion expected on the on-board vehicle system). Since the temperature of the MOF-5 media is assumed to rise to 140 K by the end of each fuel cycle, in a real system the lightly bound gaseous impurities (He, N_2, O_2) will be removed along with the hydrogen at each cycle (i.e., no accumulation). However the more strongly bound gas species have the potential to accumulate as cycling progresses. For the purposes of illustrating a worst-case scenario, we assume that all species dosed into the storage tank at each cycle are retained regardless of their strength of interaction with MOF-5.

Worst-case estimates of impurity accumulation amounts are listed in Table 5.7(2) based on the assumption outlined above. These assumptions are worst case since every fill would not occur from an empty state, stations are not expected to provide impurities consistently at or above the SAE J2719 specification, and the impurities would not expect to accumulate. Regardless, an assessment at 300 cycles and 1,500 cycles was conducted to provide worst-case impurity accumulation. The 300 cycles is an initial screening level (as agreed by DOE) based on the cycles represent the majority of the vehicle life a 90K miles using the assumption of 300 miles driving range on each fill. The 1,500 cycles is the DOE and USDRIVE hydrogen storage system target for operation cycle life.

Table 5.7(2) Estimated maximum impurity accumulation in MOF-5 (wt. %) following 300 and 1500 adsorption/desorption cycles assuming an impure gas with impurity levels set equal to the SAE J2719 specification threshold.

SAE J2719 Constituents	J2719 Specification PPM level	Maximum Accumulation (wt. %)		Potential degradation mechanisms
		After 300 cycles	After 1500 cycles	
Water	5	0.034	0.168	Pore structure degradation
Hydrocarbons	2	0.013	0.067	Surface area blocking
Oxygen	5	0.034	0.168	No accumulation effect
Helium	300	2.016	10.080	No accumulation effect
Nitrogen, Argon	100	0.672	3.360	No accumulation effect
Carbon dioxide	2	0.013	0.067	Surface area blocking
Carbon monoxide	0.2	0.0013	0.007	Surface area blocking
Total sulfur	0.004	0.00003	0.0001	Structure damage possible Not significant at accumulation level
Formaldehyde	0.01	0.00007	0.0003	No accumulation effect
Formic acid	0.2	0.0013	0.007	Not detectable at accumulation level
Ammonia	0.1	0.0007	0.003	Structure damage possible Not significant at accumulation level
Total halogenates	0.05	0.0003	0.002	Structure damage possible Not significant at accumulation level

After 300 cycles the maximum H_2O concentration in the MOF-5 pores is less than 0.03 wt.%. In contrast to water, which can irreversibly insert to the MOF framework at high loadings, hydrocarbons, carbon dioxide and carbon monoxide are expected to affect MOF-5 primarily by competing with hydrogen for active sorption sites. These species are not expected to initiate chemical side-reactions that degrade the crystalline pore structure. After 300 cycles, however, the maximum attainable concentrations do not appear high enough to have a significant effect on the hydrogen storage capacity. Given the lack of test data, however, a cycling experiment using an impurity mixture of He, O_2, CH_4, N_2, CO, and CO_2 was performed.

The trace impurities with the lowest concentrations (including sulfur, halogenates, ammonia, formic acid, formaldehyde) accumulate only to levels of 0.0003–0.002 wt.% after 300 cycles. It is unclear whether such low amounts are detectable, or capable of impacting MOF-5 hydrogen storage attributes. Rather than individually test all of these ultra-low concentration fuel impurities, we omitted formic acid and formaldyde from the test sequence on the assumption that any possible degradation mechanisms would be equal to or less than that of the other impurities.

The estimations described above suggest that repeated exposure to a hydrogen gas stream containing impurity levels equal to the J2719 maximum will not adversely affect a hydrogen storage system based on MOF-5. Below, we test this hypothesis directly by performing cyclic and static exposure tests for the five ‘impure’ hydrogen gas mixtures listed in Table 5.7(1). In all cases the mixtures contain impurity concentrations that are much higher than allowed for in the specification; consequently, these experiments constitute more stringent tests of the robustness of MOF-5.

5.7.4 Impurity cycle testing (Ammonia)

The ammonia impurity mixture (Mixture 1) contains a concentration of 7 ppm, which is roughly 70 times larger than the 0.1 ppm threshold in J2719. Hydrogen capacity tests measured on the MOF-5 sample during pressure cycling with the ammonia test gas are summarized in figure 5.7(2a). The adsorption isotherms after 63, 125, 183, 247, 309 cycles are unchanged (within measurement error), indicating no hydrogen uptake capacity loss after pressure cycle testing.

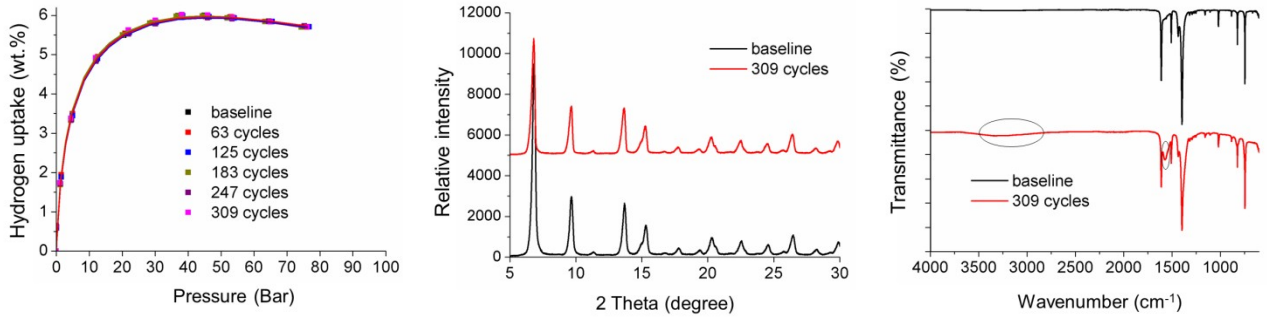

(a) (b) (c)

Figure 5.7(2). (a) Adsorption isotherms for MOF-5 powders with test gas mixture 1 including NH_3 as the impurity. Capacity measurement are taken every 60 cycles; (b) XRD spectra for MOF-5 powders before and after the cycle test; (c) FTIR spectra for MOF-5 powders before and after the cycle test.

The powder XRD spectra shown in figure 5.7(2), measured before and after cycle testing, does not show any significant change to the long-range crystal structure due to the cycling. Nevertheless, two small changes are present in the FTIR spectra shown in panel (c). These changes correspond to the emergence of two new peaks: The broad, weak peak around 3300 cm^{-1} (circled on plot) can be attributed to the O-H bond stretching in carboxylic acid, while the peak near 1600 cm^{-1} arises from the C=O bond in carboxylic acid. A possible reaction signaled by the emergence of these peaks is that the Zn-O bond between the metal cluster and organic linker has been broken, with a proton from NH_3 combining with COO^- to form carboxylic acid. It appears as though this reaction only effects a small fraction of Zn-O bonds, given that neither the powder XRD spectrum nor the hydrogen storage capacity are altered. This maybe because the amount of impurities accumulated during the cycle test is small, and can only affect a small fraction of the Zn-O bonds in the sample.

5.7.5 Impurity Cycle Testing (Halogenates)

The characterization results of MOF-5 powder before and after pressure cycling with hydrogen chloride are shown in figure 5.7(3). As noted in Sec. 5.7.2, the 9 ppm impurity concentration of hydrogen chloride in this hydrogen test gas (Mixture 3) is 180 times larger than the 0.05 ppm threshold limit in J2719. Despite these relatively high levels, hydrogen adsorption isotherms in figure 5.7(3) indicate only a small apparent decrease in hydrogen uptake after 307 cycles. The maximum excess H_2 adsorption amount at 77 K decreases 2.5% from 6.0 wt.% to 5.85 wt.% (excess) after 307 cycles.

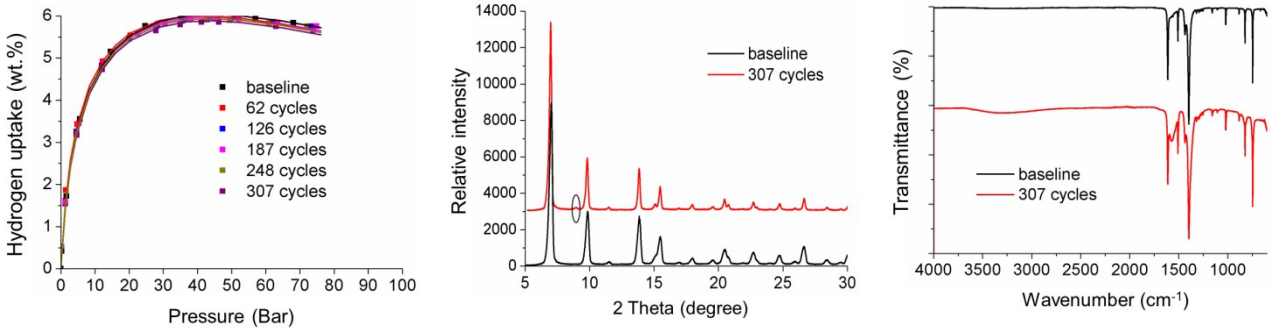

(a) (b) (c)

Figure 5.7(3) (a) Adsorption isotherm of MOF-5 powders with test gas mixture 3 including HCl as the impurity. Capacity measurement are taken every 60 cycles (b) XRD spectra for MOF-5 powders before and after cycle test (c) FTIR spectra for MOF-5 powders before and after cycle test.

Further characterization confirms that this capacity loss can be traced to MOF-5 structure decomposition. The powder XRD pattern of the post-cycling sample has a new peak emerging at 2θ=9°, as shown in panel (b) above. This peak also appears in the powder XRD spectrum for MOF-5 following water-induced structure degradation. The emergence of the 9°C peak indicates degradation and/or amorphization of the MOF-5 crystal structure. In addition to this change in the XRD patter, the FTIR spectrum in panel (c) shows the same impurity-induced peaks at 3300 cm-1 and 1600 cm-1 that are present for the ammonia-containing test gas in figure 5.7(2c). This suggests a common reaction pathway leading to the structure decomposition of MOF-5 following exposure to ammonia, hydrogen chloride, and water impurities.

5.7.6 Water, Hydrogen Sulfide (Sulfur), and Inerts Mixture

Results for the remaining three mixtures (2, 4 and 5) are summarized figure 5.7(4). Mixture 2 contains hydrogen sulfide, while mixture 4 contains water. Mixture 5, which includes a set of mostly inert impurity species is denoted "inerts" for identification. For all three of these mixtures there was no measurable change in the hydrogen adsorption capacity tests measured during the course of pressure cycling. Likewise, for all three impurity mixtures the MOF-5 crystal structure and bonding network appears unchanged following 300 pressure cycles. The powder XRD patterns (panels b,e,h) and FTIR spectra panels c, f, i) collected on the pre-cycling and post-cycling MOF-5 samples do not show any significant changes.

Mixture 2 (Hydrogen Sulfide)

(a) (b) (c)

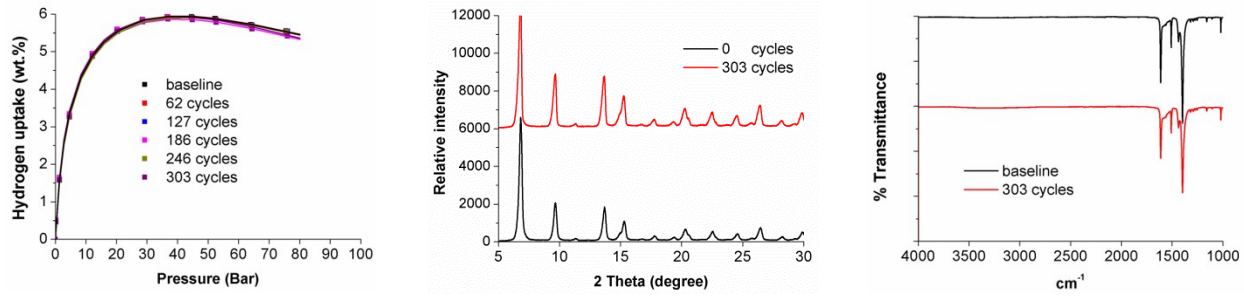

Mixture 4 (Water)

(d) (e) (f)

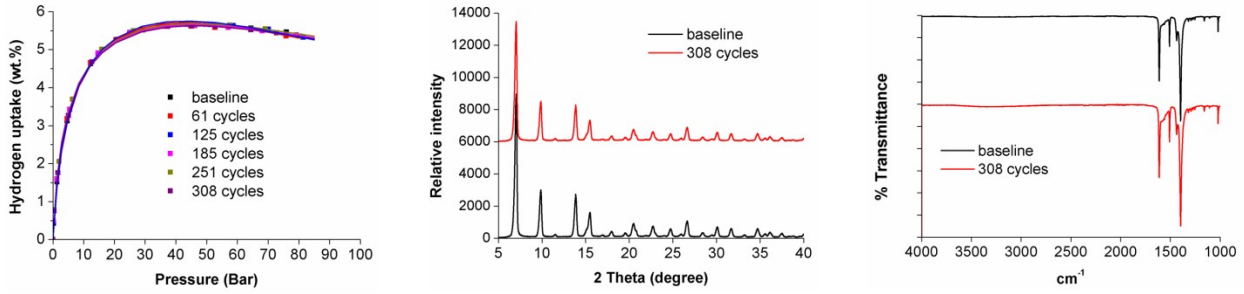

Mixture 5 (Inerts)

(g) (h) (i)

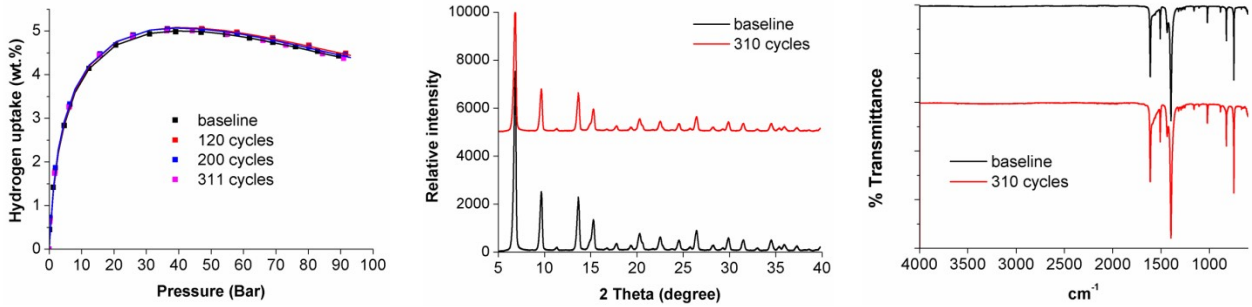

Figure 5.7(4) (a,d,g) Hydrogen adsorption isotherms for during cycling of MOF-5 powder using the indicated impurity gas mixture. (b,e,h) Powder XRD patterns following impurity cycling for the respective impurity mixtures. (c,f,i) FTIR patterns of MOF-5 powders before and after impurity cycling with the respective impurity gas mixture

Since the impurity concentrations in Mixtures 2, 4 and 5 significantly exceed the threshold levels specified in J2719, we conclude that these contaminants will not impact the adsorption capacity of MOF-5 powders within 300 cycles.

5.7.7 Summary of impurity cycling tests

Figure 5.7(5) provides a summary of the hydrogen capacity measured during pressure cycling tests for all five impurity gas mixtures. We reiterate that each hydrogen adsorption capacity test consisted of measuring an excess adsorption isotherm at 77 K, using the same impurity gas employed in the ongoing cycling sequence. The capacity is therefore defined in terms of the maximum excess adsorption at 77 K. The hydrogen capacities plotted on the y-axis are expressed as a percentage of the initial capacity measured at the beginning of the cycle testing (i.e., capacity at cycle 0). For all five of the impurity gases tested, the capacity retention was above 97% after 300 cycles.

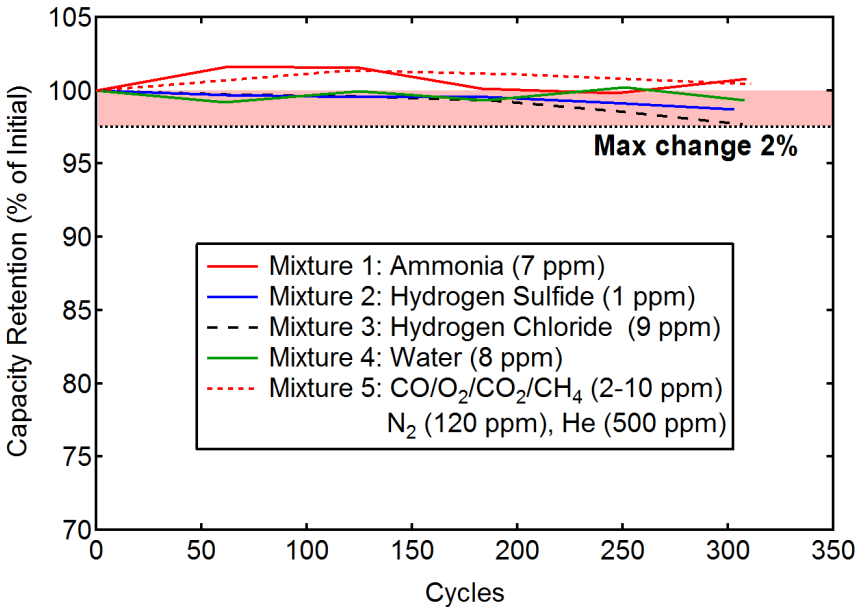

Figure 5.7(5) Summary of maximum hydrogen excess adsorption in MOF-5 (expressed as a percentage of the maximum adsorption before the start of testing) measured at 77 K and 80 bar as a function of cycle number with impurity gas mixtures.

5.7.8 Static Exposure Test (water)

A one-week static exposure test was performed at room temperature using the water impurity mixture (mixture 4), and was carried out according to the procedure described in section 5.7.2. Figure 5.7(6) summarizes the pre- and post-storage characterization results for this MOF-5 sample. The hydrogen uptake curves indicate that there was no adsorption capacity change following the one-week exposure. The XRD and FTIR profiles also indicate a stable bonding and crystal structure of MOF-5 samples following the test. When combined with the earlier pressure cycling test results, the static exposure test results confirm that H_2O concentrations up to 8 ppm in the hydrogen fuel do not affect hydrogen storage performance of MOF-5 within 300 cycles and 1 week exposure. According to J2719 standard, the content of H_2O should be less than 5 ppm, which presents an even safer threshold.

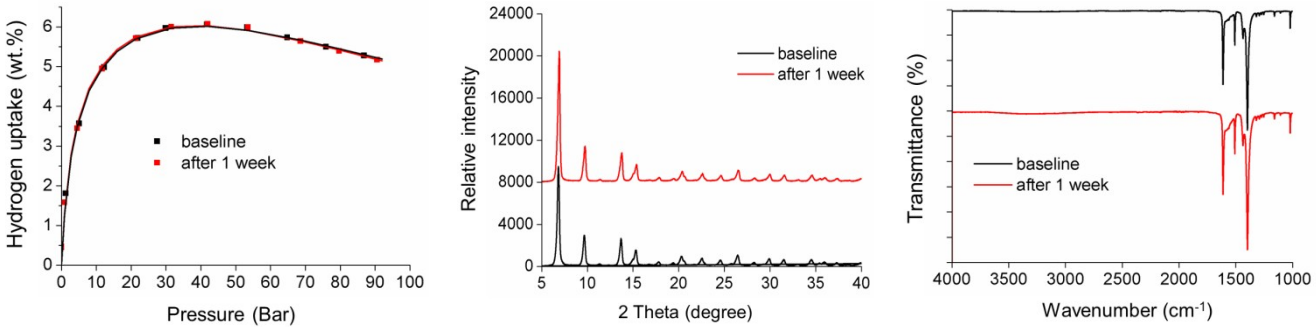

(a) (b) (c)

Figure 5.7(6) (a) Adsorption isotherm of MOF-5 powders with test gas mixture 4 including H2O as the impurity. Capacity measurement are taken before and after 1 week static exposure (b) XRD spectra for MOF-5 powders before and after static exposure (c) FTIR spectra for MOF-5 powders before and after static exposure.

5.7.9 Static exposure test (hydrogen sulfide)

MOF-5 was subjected to a one-week static exposure test at room temperature using the hydrogen sulfide impurity mixture (mixture 2). Figure 5.7(7) summarizes the characterization results of the MOF-5 powder before and after the test. The hydrogen uptake isotherms in panel (a) indicate no decrease in adsorption capacity. The unchanged peaks in XRD and FTIR in panels (b) and (c) also show that the bonding network and crystal structure of MOF-5 samples are not altered during the exposure test. Combining the result of cycle test and static exposure with hydrogen including H_2S, we can conclude that 0.9 ppm H_2S in hydrogen does not significantly affect the hydrogen storage performance of MOF-5 within 300 cycles and 1 week of static exposure. According to the J2719 standard, the concentration of H_2S in the hydrogen fuel stream should be less than 0.004 ppm. This level is more than 200 times lower than in the test mixture, signaling that a gas stream that meets the specification will be even less likely to result in degradation.

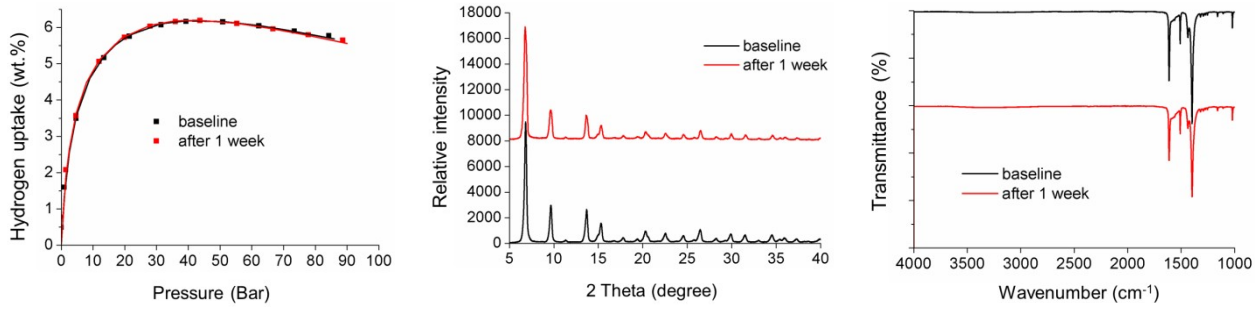

(a) (b) (c)

Figure 5.7(7) (a) Adsorption isotherm of MOF-5 powders with test gas mixture 2 including H_2S as the impurity. Capacity measurement are taken before and after 1 week static exposure (b) XRD spectra for MOF-5 powders before and after static exposure (c) FTIR spectra for MOF-5 powders before and after static exposure

5.7.10 Conclusion

Hydrogen gas conforming to purity standards outlined in SAE J2719 can contain certain allowable contaminants in the fuel stream. We studied the effect of these impurities on the hydrogen storage capacity, bond network, and crystal structure of MOF-5 using cyclic and static exposure tests. Four impure hydrogen gas mixtures were prepared by introducing ammonia, hydrogen sulfide, hydrogen chloride, and water, respectively. Six additional (mostly inert) impurities were combined into a fifth hydrogen mixture.

Only the hydrogen chloride mixture yielded a measurable (though small) decrease in hydrogen storage capacity during the course of pressure cycle testing at 77 K. No measurable decrease was noted for the other hydrogen impurity mixtures during pressure cycling. Cycling with hydrogen chloride amounts also induced small changes to the MOF-5 crystal structure and local chemical structure, as indicated by XRD and FTIR, respectively. Changes to the chemical bonding structure were also observed for samples cycled with trace ammonia, but corresponding changes to the long-range crystal structure or hydrogen storage capacity could not be detected.

Static exposure of MOF-5 to water and hydrogen sulfide impurities for 1 week had no measurable effect on the sample.

The impurity levels used here exceeded the J2719 threshold by at least of a factor of 10, and in some cases exceed them by a factor of 200. The robustness observed at these higher concentrations demonstrate that hydrogen from a fueling station compliant with J2719 should not impact the performance of a MOF-5-based hydrogen storage system for up to 300 cycles and 1 week's static exposure.

5.8 The Stability of MOF-5 at Variable Water Vapor Concentrations

5.8.1 Introduction

Exposure of MOF-5 to air with a high water vapor concentration (e.g., "humid air") is known to induce degradation of MOF-5 crystal structure, thereby reducing capacity and cycle life. In these instances it is important to know not only that degradation can occur, but to also quantify the degree of degradation and its dependence on operating conditions. This information is essential for establishing a material's "stability window," which indicates the conditions under which suitable performance can be maintained.

The first objective was to determine the humidity threshold level for MOF-5 degradation. We quantified the impact of humid air exposure on the properties of MOF-5 as a function of exposure time, humidity level, and powder vs. pellet morphology. Properties examined include hydrogen storage capacity, surface area, and crystallinity.

The second objective is to elucidate the connection between water uptake in MOF-5 and its hydrolysis, using density functional theory (DFT) calculations. This is accomplished by calculating the energetics of water insertion as a function of water coverage. Distinguishing features of our approach are the use of a van der Waals-aware density functional and full treatment of the MOF crystal structure (i.e., without structure simplifications or cluster model approximations). As a first step we calculate the thermodynamics of water adsorption at various sites in MOF-5. Subsequently, the energetics for hydrolysis are evaluated as a function of the local coverage of water near the Zn-O insertion point. Water insertion is found to be exothermic only after a critical number of H_2O molecules are adsorbed in close proximity on a given Zn-O cluster. This finding corroborates experimental observations of an induction period – presumably associated with nucleation of small, adsorbed water clusters – preceding hydrolysis. Finally, the reaction pathway for water insertion into the framework was evaluated in the presence of explicit, adsorbed water molecules. For coverages where insertion is thermodynamically favorable, the barrier for insertion is predicted to be low, only 0.17 eV. Such a small barrier indicates the likelihood for rapid hydrolysis at moderate humidity levels, in agreement with our experimental measurements.

5.8.2 Experimental Methods:

Stability testing under humid conditions was performed at 22°C using two relative humidity (RH) levels: 45% and 61%. These conditions were maintained using a gas flow system that mixed dry air with water vapor. The flow apparatus employs a Bronkhorst W303A Liquid flow controller with a Controlled Evaporator Mixer (CEM). The flow rate for dry air was set to 20 L/minute (1.2 m^3/hr), and the water vapor flow rate was 10.7 g/h for 45% RH, and 16.9 g/h for 61% RH. These two streams were mixed and connected to a large Erlenmeyer flask, which served as a controlled humidity chamber.

The standard definition of relative humidity

$$Relative\,humidity = \frac{actual\ vapor\ density}{saturation\ vapor\ density} \times 100 = \frac{\rho_{vap}}{\rho_{sat}} \times 100$$

where the saturation vapor density of H_2O (in units of g/m^3) between 0 °C and 40 °C is given by,

$$\rho_{sat} \wedge ¿ 5.018 + (0.32321)T + (8.1847 \times 10^{-3})T^2 + (3.1243 \times 10^{-4})T^3$$
$$¿ = 19.4\ \mathrm{g/m^3}\ at\ 22°C.$$

The value of $\rho_{sat}(22°C) = 19.4$ g/m^3 is used to convert the vapor and air flow rates into RH values

H_2O Vapor Flow Rate	Air Flow Rate	H_2O Vapor Density	RH (at 22°C)
10.7 g/hr	1.2 m^3/hr	8.91 g/m^3	46 %
16.9 g/hr	1.2 m^3/hr	14.08 g/m^3	73 %

Samples were transferred to the humidity chamber after first being loaded into a bottle within the glovebox. The bottle was placed inside the flask and opened. The bottle opening was positioned so as to block the impingement of the humid airflow directly onto the sample; this geometry was intended to minimize convection effects, and mimic water adsorption from a quasi-static atmosphere. A given sample was exposed for a specified time, with exposure times of 30 min., 2 h, 24 h, 48 h and 66 h for powders, and 30 min, 2 h, 24 h, 66 h for pellets. The mass of the sample used for each measurement was approximately 0.37 g. For powders, fresh samples were used for each exposure experiment; for pellets, samples underwent a cumulative exposure process in which (for example) a pellet exposed for 2 h was removed from the humidity chamber, characterized, and then returned to the chamber for another 22 h, to achieve a total exposure of 24 h.

5.8.3 Effects of humidity exposure – BET Surface Area

The BET surface areas of MOF-5 powders with different exposure times to the two relative humidity levels are shown in Figure 5.8(1). The pressure interval used for fitting to the BET model was $\{0.05 < p/p_0 < 0.2\}$. As described in previous sections, this data range results in smaller surface area for powder MOF-5 (i.e., 2900 m^2/g versus 3500 m^2/g, see Sec.5.4.5). Nonetheless, all of the data were fitted using the same p/p_0 range, to allow for a meaningful comparison between values. We note that the batch of MOF-5 powder used for this experiment had a slightly lower surface area compared to some of the other batches used for this work. The initial measured surface area was 2355 m^2/g for this particular batch of MOF-5.

Results are summarized below in Fig. 5.8(1). For the RH = 45% samples, relatively small changes in SA are observed for exposure times up to 48 h. At 66 hours the surface area then drops more precipitously to a value which is half (1217 m^2/g) its initial maximum. It is also evident that the pellets (discussed in more detail below) exhibit enhanced robustness to humidity; the pellets maintain higher BET surface areas compared to those of powders for the same exposure conditions. (Note: The initial surface area of the unexposed pellets is slightly above that of the unexposed powders due that media being sourced from a different batch of MOF-5 material.) In contrast, for the RH = 61% samples the BET surface area decreases more rapidly, achieving a value of nearly zero (34 m^2/g) after 66 hours. The declining surface area for both RH values indicates that the porosity of the MOF-5 powders is continuously reduced upon exposure to humid conditions.

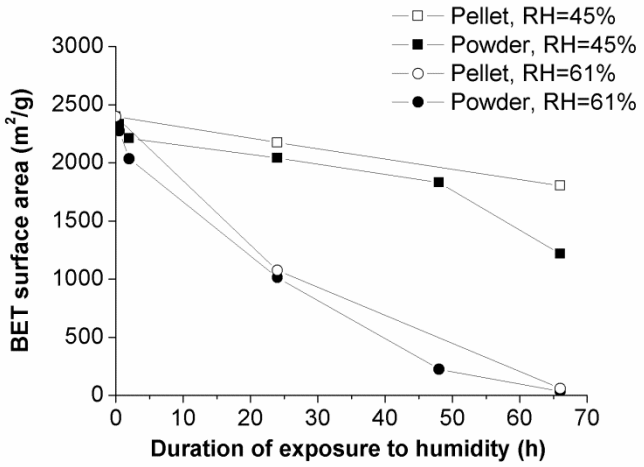

Figure 5.8(1). BET surface area of MOF-5 powders (filled data points) and pellets (open symbols) as a function of exposure time to humid air with relative humidity (RH) of 45% (square symbols) and 61% (circular symbols). T = 22°C in all cases. Data points at $t = 0$ correspond to samples which were not exposed to humidity.

Effects of humidity exposure – Hydrogen adsorption

Hydrogen adsorption isotherms at 77 K were measured for MOF-5 powders exposed to humidity (RH = 45% and 61% at 22°C) for various exposure times. Results are shown below in Figure 5.8(2). The x-axis specifies the equilibrium hydrogen pressure, and y-axis is the excess adsorbed hydrogen.

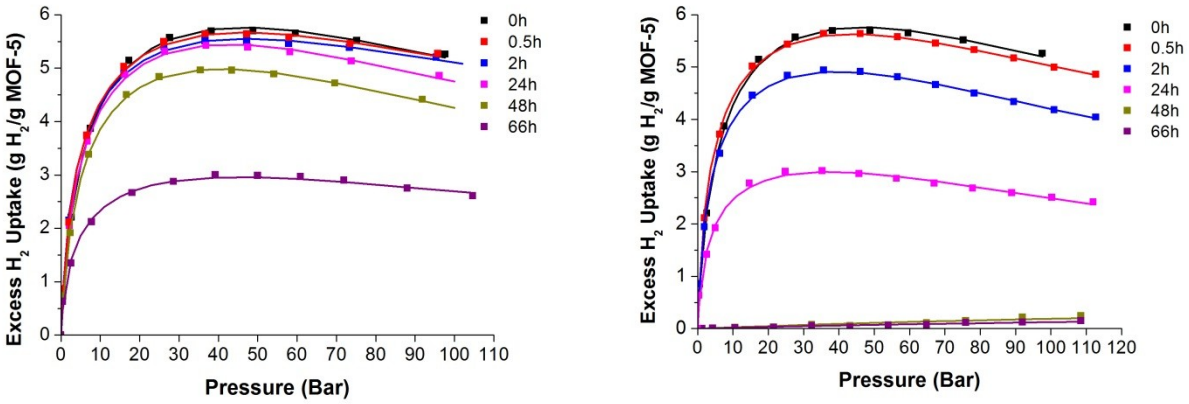

(a) Relative humidity = 45% (b) Relative humidity = 61%

Figure 5.8(2) Excess gravimetric hydrogen uptake in MOF-5 powders at $T = 77\ K$ as a function of relative humidity and exposure time. *Left*: relative humidity = 45%, T = 22°C; *Right*: relative humidity = 61%, T = 22°C. Isotherms are plotted before exposure to humid air (0 h), and after 5 increasingly longer exposure times: 0.5 h, 1.5 h, 24 h, 48 h and 66 h. Solid symbols represent experimental data.

The left panel shows data for the lower humidity level, RH = 45%. For samples exposed for the two shortest time periods, 0.5 h and 2 h, the decrease in maximum hydrogen uptake is less than 3% compared to the baseline (unexposed) material. This indicates that the MOF-5 powders do not undergo "sudden death" when exposed to moderately humid conditions for short times. For a 24-hour exposure, the peak in the adsorption isotherm also decreases by only slightly (~5%), from 5.7 to 5.4 wt.%. However, more significant changes are observed for longer exposures; for example, uptake drops to half of that for the pristine material after 66 hours exposure. In contrast, at the higher RH value (61%), significant decreases in hydrogen storage capacity appear after 2 hours of exposure. After 24 h uptake decreases by approximately 50%, which is an order of magnitude larger than the losses seen at RH = 45%. After 48 hours the powder has lost essentially all of its gas storage capability (uptake below 0.5 wt. %).

The results demonstrate that exposure to humid environments for periods longer than approximately ~2 h negatively impacts the adsorption of H_2 in MOF-5 powders. Two possible explanations for this behavior are: (i) water molecules preferentially adsorb in MOF-5, and thereby block sites for H_2 uptake, or (ii) water molecules react irreversibly with MOF-5, for example, by decomposing/insertion into its crystal structure. The first scenario is unlikely given that each sample exposed to humid conditions is evacuated and heated over night to remove any adsorbed water before hydrogen isotherm measurements are performed. Therefore, we hypothesize that the most likely explanation for the observed decrease in H2 uptake is an irreversible structure change wherein MOF-5 transforms into a new composition/structure that is less amenable to gas storage, presumably due to loss of porosity, surface area, etc.

5.8.4 Effects of humidity – Powder X-ray diffraction

Powder X-ray diffraction was used to assess changes to the crystallinity of MOF-5 associated with exposure to humidity. Figure 5.8(3) shows diffraction patterns for MOF-5 powders as a function of exposure time for the RH = 45% and RH = 61% cases. For RH = 45%, during exposures up to 48 hours there are not significant changes in the XRD pattern relative to the unexposed material. After 66 hours, a new peak appears at $2\theta = 9^0$, consistent with the formation of a new phase. The position of the new peak is in agreement with prior studies, and resembles the pattern for ZnBDC•xH_2O. (We note that the full crystal structure of the emergent phase has not been completely determined.) In contrast, for the RH = 61% case the same peak appears much sooner, after only 24 hours of exposure. Additional changes to the diffraction pattern are evident at longer exposure times. Comparing the XRD patterns for both RH conditions it is clear that the extent of the change in crystallinity/structure with respect to exposure time closely follows the trends observed in both the H_2 uptake isotherms and the surface area.

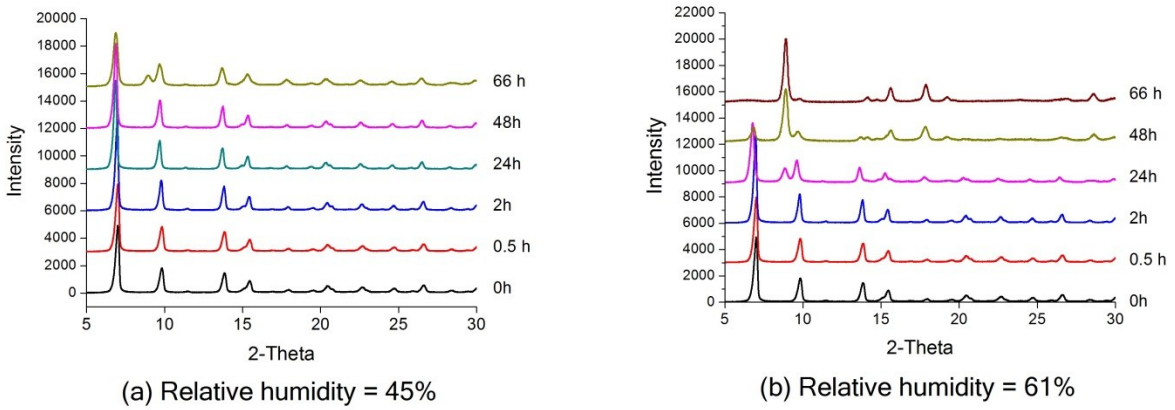

Figure 5.8(3). XRD spectra for MOF-5 powders as a function of exposure time to humid air with relative humidity values of 45% (left) and 61% (right).

5.8.5 Effects of humidity – H_2O Vapor Isotherm for MOF-5

Water adsorption and desorption isotherms were measured on MOF-5 at 25ºC using a gravimetric apparatus, with the results summarized below in Figure 5.8(4). Here the x-axis represents RH, and the y-axis represents the mass fraction of adsorbed water ([m(water)/m(MOF-5)] x 100). Three adsorption/desorption cycles were performed using the same powder sample. During the first uptake cycle less than 1 wt.% of water is adsorbed for RH up to 45%. The water uptake then jumps dramatically to more than 12 wt.% at RH values between 45 – 55 %. For higher RH the uptake saturates at capacities of 12-14 wt.%. The initial isotherm (adsorption 1 in the figure below) has a Type V character, with a steep rise at $p/p_0 \approx 0.5$, which is expected for systems exhibiting relatively strong adsorbate-adsorbate interactions in comparison to (weaker) adsorbate-adsorbent interactions.

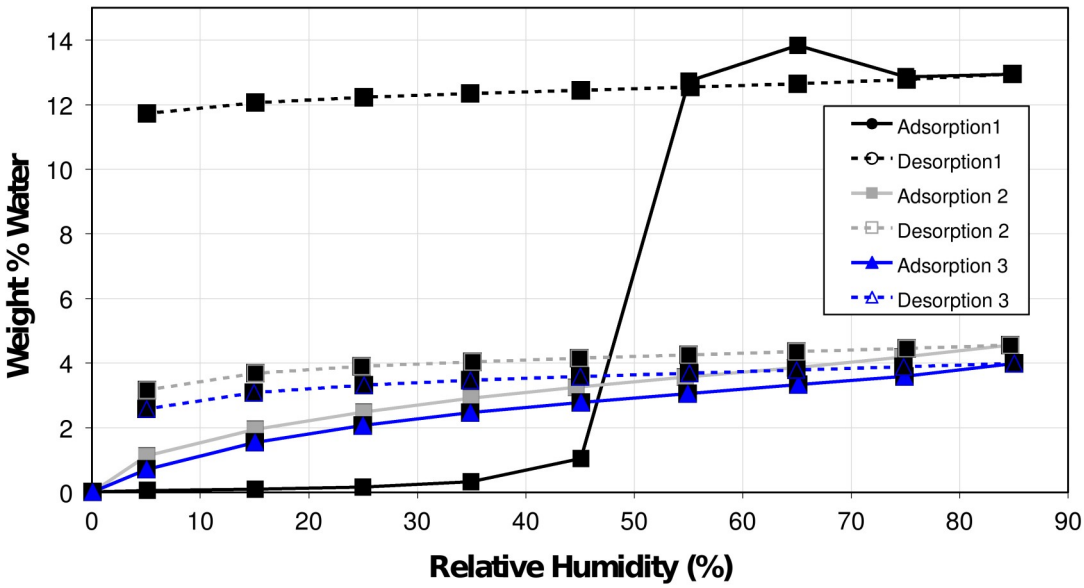

Figure 5.8(4) Water adsorption in MOF-5 powder at 25°C vs. relative humidity. The consecutive adsorption/desorption cycles are plotted.

The steep increase in water uptake in MOF-5 evident in the isotherm over the relatively narrow region of RH spanning 45 – 55% explains the dramatic differences in H_2 uptake, surface area, etc. observed for the two humidity levels (RH = 45 and 61%) in the exposure experiments. These two levels fall, respectively, just below and just above the transition region in Fig. 5.8(4), indicating that these measurements can be rationalized by the sudden increase in the adsorbed water content of the MOF as RH increases from 45 to 61%.

Figure 5.8(4) also shows that the isotherm for the first adsorption-desorption cycle exhibits a large hysteresis; this is because the amount of adsorbed water decreases only slightly during the desorption cycle, ~1 wt.%, suggesting

a strong chemisorption-like binding of H_2O to the MOF-5 framework. In the subsequent 2nd and 3rd cycles relatively little water adsorption occurs; the sample has lost approximately 2/3 of its water uptake ability. As previously described, these latter cycles were performed following separate sample activation steps. Therefore, the low uptake observed for these cycles likely reflects the failure of the activation procedure to remove strongly bound H_2O from the first uptake cycle, in concert with a structure change as suggested by XRD.

5.8.6 Effects of humidity – FTIR Spectroscopy

FTIR spectroscopy was used to examine changes to bonding in MOF-5 resulting from humidity exposure. Figure 5.8(5) shows the FTIR spectrum for MOF-5 powders exposed to air with RH = 61% for 0, 24, and 66 h at 22°C. Prior to FTIR analysis, all samples underwent overnight activation (evacuation and heating at 130°C) to remove physisorbed water. Therefore, changes to the FTIR spectrum resulting from exposure should be attributable to irreversible insertion and/or chemisorption of water within the MOF-5 crystal structure. Four new/shifted peaks emerge in the spectrum upon exposure for 66 h, and are labeled with numbers 1 through 4. These peaks suggest a pathway for the reaction of water with MOF-5, and can be assigned to specific bonds illustrated in Figure 5.8(6). At low water loadings, water molecules are expected to be physically adsorbed near the Zn cluster, panel (b). Irreversible insertion of water into the framework is expected to occur at higher loadings, and is consistent with the emergence of peaks 1 and 2, in which molecular water bonds to Zn, displacing oxygen from the linker, panel (c). More specifically, peak 1 at 3600 cm^{-1} can be assigned to O-H stretching in a water molecule that is adsorbed at a Zn site. Similarly, the broad peak from 3400 to 3000 cm^{-1} (labeled '2') can be traced to an O-H stretch, but in which the hydrogen also participates in a H-bond, presumably with the displaced oxygen attached to the linker. The peak at position 3 arises from C=O stretching in a carbonyl group, while peak 4 is also due to C=O stretching, but where the oxygen additionally participates in a hydrogen bond, presumably with a hydrogen from molecular water.

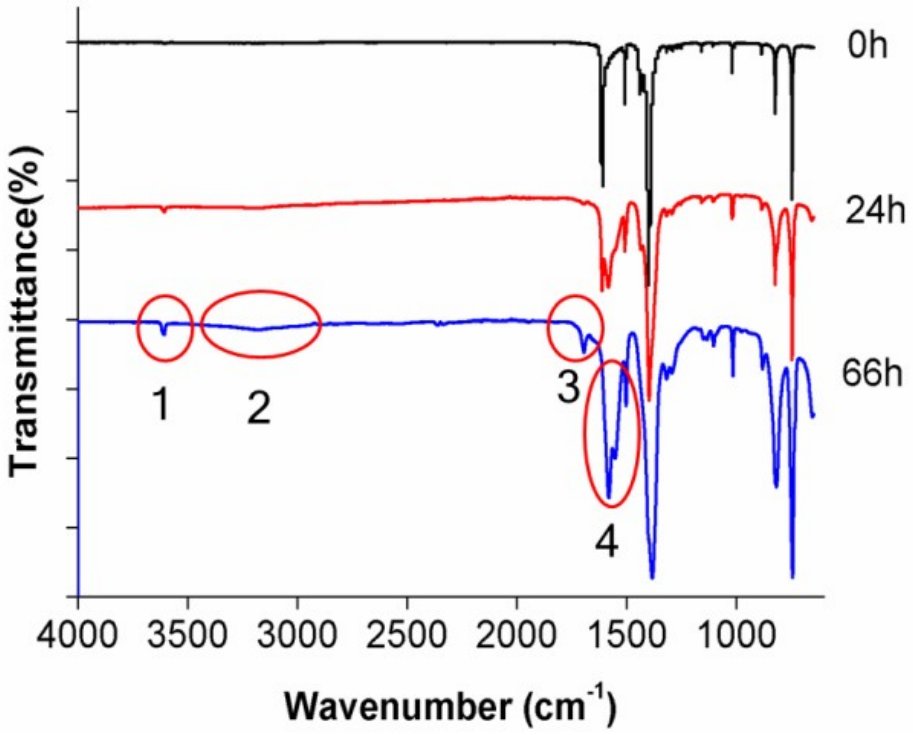

Figure 5.8(5) FTIR spectra for MOF-5 powders exposed to air with RH = 61% for 0 h, 24 h, and 66 h at 22°C.

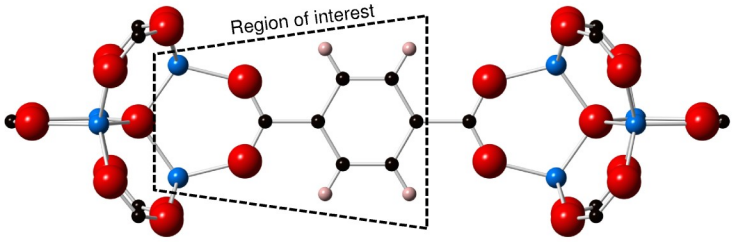

(a) Portion of MOF-5 crystal structure

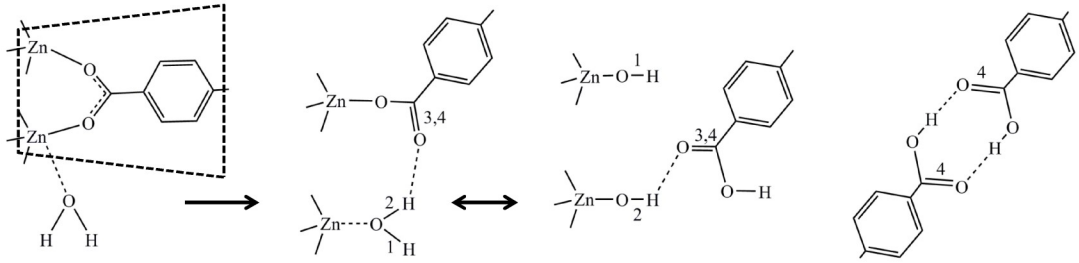

(b) Physisorbed water (c) Water insertion (d) Water dissociation (e) Dimer structure

Figure 5.8(6) (a) Magnification of a portion of the MOF-5 crystal structure. Red represents O, blue: Zn, black: C, green, H. The trapezoid represents the region of interest for water interactions with MOF-5, as shown in the lower four panels. (b) Physisorption of water near the Zn cluster. (c) Insertion of molecular water into the MOF-5 framework via bonding to Zn and displacement of the BDC linker. (d) Water insertion and dissociation, resulting in a hydroxyl group bonding to Zn and carboxylic acid at the terminus of the linker. (e) An example of a carboxylic acid dimer that may contribute to peak 4 in the FTIR spectra. Numbers 1 – 4 refer to bonds associated with peaks in the FTIR spectrum in Fig. 5.8(5).

Panels (d)-(e) depict additional reactions that involve the dissociation of water, and which based on the FTIR spectrum, we speculate may co-exist. As an initial step, hydrogen from dissociated H_2O bonds with oxygen from the BDC linker to form carboxylic acid, while the remaining hydroxyl group bonds with Zn, panel (d). In addition, if several carboxylic acids are formed, then two of these groups from separate linkers may join to form a dimer structure, panel (e); this structure would provide another source for peak 4. In this case the two participating BDC linker fragments are totally disconnected from their respective metal clusters due to water insertion reactions.

The previous discussion suggests that MOF-5 is unstable in the presence of water. This is to be expected based on earlier studies which involved exposure to liquid water or more extreme humidity conditions. However, for the moderate humidity levels examined here, powders exposed for periods ranging from ~30 minutes to 2 hours do not experience a significant degradation in surface area or H_2 storage capacity. This suggests that kinetics play a role in the degradation process. We next examine how the morphology of the material – i.e., powders vs. pellets – impacts the rate of MOF-5 degradation in humid environments.

5.8.7 Effects of humidity – Compacted MOF-5 pellets

MOF-5 pellets: A highly-densified MOF-5 powder structure may present fewer or less facile pathways for the infiltration of water vapor into the MOF, potentially reducing the degradation observed for powders. In this section we characterize the stability of MOF-5 pellets with respect to humidity, and compare their performance to that of powders.

Figure 5.8(7) shows the excess gravimetric H_2 adsorption in MOF-5 pellets (density~0.36 g/cm^3) following exposure to the same two humidity conditions used previously for powders (RH = 45% and 61% at 22°C). Exposure times were 0.5 h, 2 h, 24 h and 66 h. Similar to the powder results, increasing the relative humidity from 45 to 61% has a large effect on the MOF's hydrogen capacity. For example, H_2 uptake in pellets is not significantly reduced after 24 h exposure to RH=45% (panel a). However, after an identical exposure time at

RH=61%, H_2 capacity drops by ~50% relative to uptake in the unexposed system, panel (b). Because gravimetric uptake is related to geometric properties of MOFs such as specific surface area and micropore volume, a loss in hydrogen capacity can also presumably be related to a comparable loss in these quantities, as previously discussed.

Another observation relates to the "kinetic stability" of the densified MOF. Here kinetic stability refers to the rate of degradation/decomposition of the MOF at a given RH, temperature, and exposure time. We first recall that in powders the exposure time at which a significant decrease in excess hydrogen uptake was observed at RH = 45% was 2 h. In contrast, for pellets a much longer exposure time of ~24 hours is required to achieve a comparable loss in H_2 capacity. Similar trends hold for longer exposure times: powders exposed to RH = 45% for 66 hours exhibit a H_2 capacity of 3 wt.%, whereas for pellets the uptake is significantly higher, 4.1 wt.% (panel a). This behavior also carries over to samples exposed to the higher humidity RH = 61% environment: after 2 h exposure, powder MOF-5 has an H_2 capacity of 4.9 wt.%, while for pellets the capacity is essentially unchanged from that of the unexposed material, 5.6 wt.%.

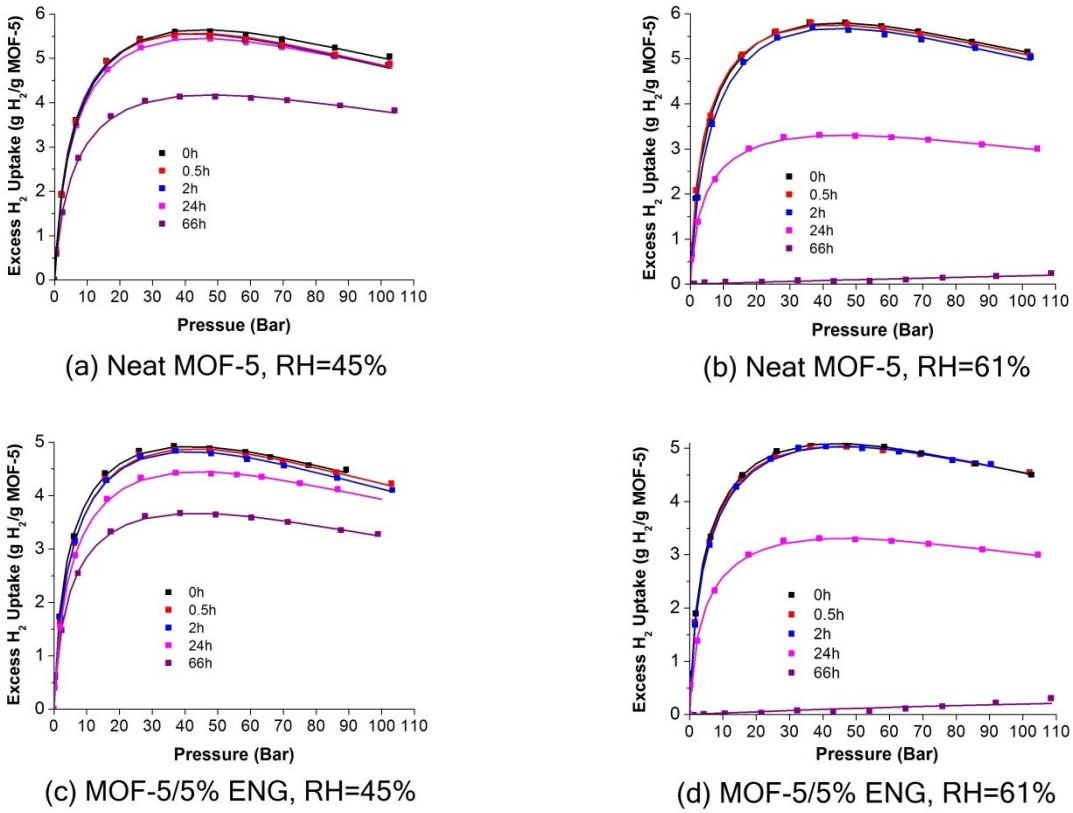

Figure 5.8(7). Excess gravimetric H2 adsorption amount for MOF-5 pellets (density ~0.37 g/cm3) exposed to a humid environment for 0.5h, 2h, 24h and 66h, respectively. (a) Pure MOF-5 pellet, RH=45%; (b) Pure MOF-5 pellet, RH=61%; (c) MOF-5/5%ENG pellet, RH=45%; (d) MOF-5/5%ENG pellet, RH=61%. Symbols represent experimental data, lines are fits to the data using the Unilan isotherm model

We speculate that the improved resistance of the pellets to water-induced degradation results from reduced water permeation into the pellets. Permeation is proportional to both the concentration and the diffusivity of water, and in principle the higher density of the pellets may impact both of these quantities. Nevertheless, given a high enough RH combined with a long exposure time, pellets will ultimately degrade to the point where all of their gas storage capacity is lost, Fig. 5.8(7b). This data indicates that densification can slow – but not stop – the degradation of MOF-5 upon exposure humid environments.

As a final comparison we briefly consider the impact of expanded natural graphite (ENG) additions on the stability of MOF-5 pellets. Our earlier studies have shown that ENG tends to accumulate at the interfaces between MOF-5 particles during compaction. As these interfaces may present facile diffusion pathways for water

molecules into MOF pellets, we hypothesize that interfacial ENG may impede water transport, and thereby slow degradation resulting from water entry into the pellet. To test this hypothesis, humidity exposure tests were also performed on ENG-containing pellets. Pellets synthesized from a physical mixture of MOF-5 and 5 wt.% ENG were exposed to RH of 45% and 61%, and then subjected to H_2 uptake testing, Figs. 5.8(7c-d). As evident from the results, the MOF-5/ENG pellet shows similar robustness to that of the pure MOF-5 pellets.

5.8.8 Water-insertion mechanisms in MOF-5: Introduction

In principle, density functional theory (DFT)-based calculations should provide a highly-accurate description of the bond-breaking processes present during MOF hydrolysis. However, these calculations remain a challenge due to the large number of atoms in the computational cell (106 atoms in the MOF-5 primitive cell; 424 in the conventional cell). For this reason, cluster approximations or structure simplifications are commonly adopted to make the calculations tractable.

The goal of our calculations is to elucidate the connection between water uptake in MOF-5 and its hydrolysis. This is accomplished by calculating the energetics of water insertion as a function of water coverage. Distinguishing features of our approach are the use of a van der Waals-aware density functional and full treatment of the MOF crystal structure (i.e., without structure simplifications or cluster model approximations). As a first step we calculate the thermodynamics of water adsorption at various sites in MOF-5. Subsequently, the energetics for hydrolysis are evaluated as a function of the local coverage of water near the Zn-O insertion point. Water insertion is found to be exothermic only after a critical number of H_2O molecules are adsorbed in close proximity on a given Zn-O cluster. This finding corroborates experimental observations of an induction period – presumably associated with nucleation of small, adsorbed water clusters – preceding hydrolysis. Finally, the reaction pathway for water insertion into the framework was evaluated in the presence of explicit, adsorbed water molecules. For coverages where insertion is thermodynamically favorable, the barrier for insertion is predicted to be low, only 0.17 eV. Such a small barrier indicates the likelihood for rapid hydrolysis at moderate humidity levels, in with our experimental measurements.

5.8.9. Adsorption of Isolated Water Molecules.

Figure 5.8(8a) shows the conventional unit cell of MOF-5. The crystal structure consists of BDC linkers and Zn_4O metal-oxygen clusters. Five distinct sites were explored for water adsorption. These sites are illustrated as large purple spheres in Fig. 5.8(8b) and labeled with Greek letters. The three sites α, β, and γ refer to sites on the Zn-O cluster, while δ and ε refer to sites on the benzene ring in the linker. Site α is the closest site to the central oxygen in the Zn cluster; this site is also equidistant to 3 of the Zn atoms bonded to the central oxygen. Site β is closest to one of the four Zn atoms in the cluster, and is equidistant to three of the four oxygens bonded to Zn. Site γ is proximate to two oxygens bonded to Zn. On the linker, site δ is centered above the face of the benzene ring. Site ε is positioned at the edge of the benzene with equal distances to two hydrogen atoms. Table 5.8(1) lists the number of each type of site on a single metal cluster or linker. In total, there are 20 adsorption sites on the metal cluster and 12 sites on the linker.

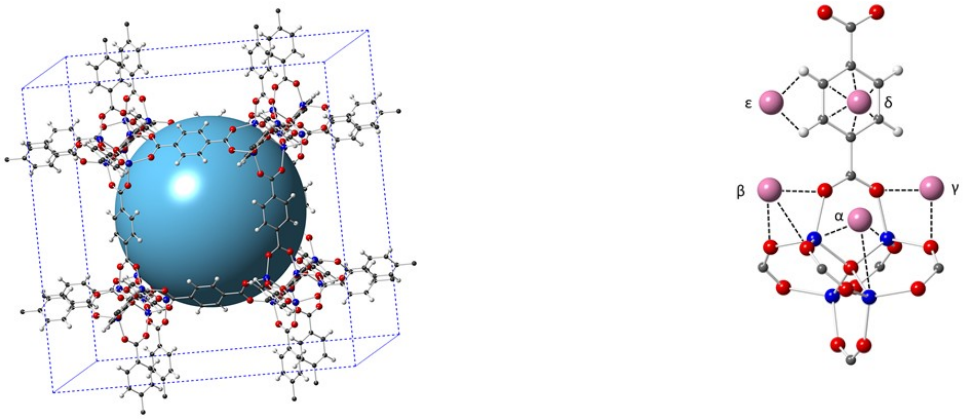

(a) (b)

Figure 5.8(8). (a) Conventional unit cell of MOF-5. Red spheres represent Oxygen, blue: Zn, grey: C, white: H. (b) Magnification of the metal cluster and organic linker from panel (a). The purple spheres represent 5 distinct sites for water adsorption, and are labeled with Greek symbols

Location	Site Name	Number of Sites
Zn-O cluster	α	4
	β	4
	γ	12
Linker	δ	6
	ε	6

Table 5.8(1). Number and location of each type of adsorption site depicted in Fig. 5.8(8b)

Figure 5.8(9a) plots the adsorption energy, E_{ad} , for a single water molecule for each adsorption site as a function of the exchange-correlation functional employed (PBE-GGA and vdW-DF2). The vdW-DF2 functional predicts more exothermic binding energies than does the GGA across all of the binding sites. This difference is particularly large for the α site, where the binding predicted by the GGA is approximately 0.2 eV weaker. The weaker binding observed for the GGA is consistent with earlier calculations involving CO2 and CH4 adsorption in MOFs, and can be attributed to the lack of van der Waals interactions in this functional. More generally, the range of binding energies predicted by the vdW-DF2 across all sites (~0.23 eV) is significantly wider than for the GGA; in the latter case the adsorption energies are clustered around -0.15 eV. This trend has also been observed for the adsorption of small molecules in other MOFs. A final difference between the functionals pertains to the site preference for H_2O adsorption. The α site is predicted to be the most stable site for adsorption by the vdW-DF2 functional, whereas the GGA predicts the β site to have the largest binding energy. The present calculations predict an adsorption energy at the β site of -0.19 eV for the GGA functional; this

Figure 5.8(9b-d) tabulates bond distances between the proximal oxygen atom in an adsorbed water molecule and various atoms in the MOF. This is done for adsorption sites located on the metal cluster (sites α, β, γ) and as a function of the exchange-correlation functional. In all cases the bond lengths are greater than 3Å, consistent with a weak, physisorption interaction. Distances predicted by the vdW-DF2 functional are systematically shorter than those from the GGA; this is expected given the larger adsorption energies reported in Fig. 5.8(9a).

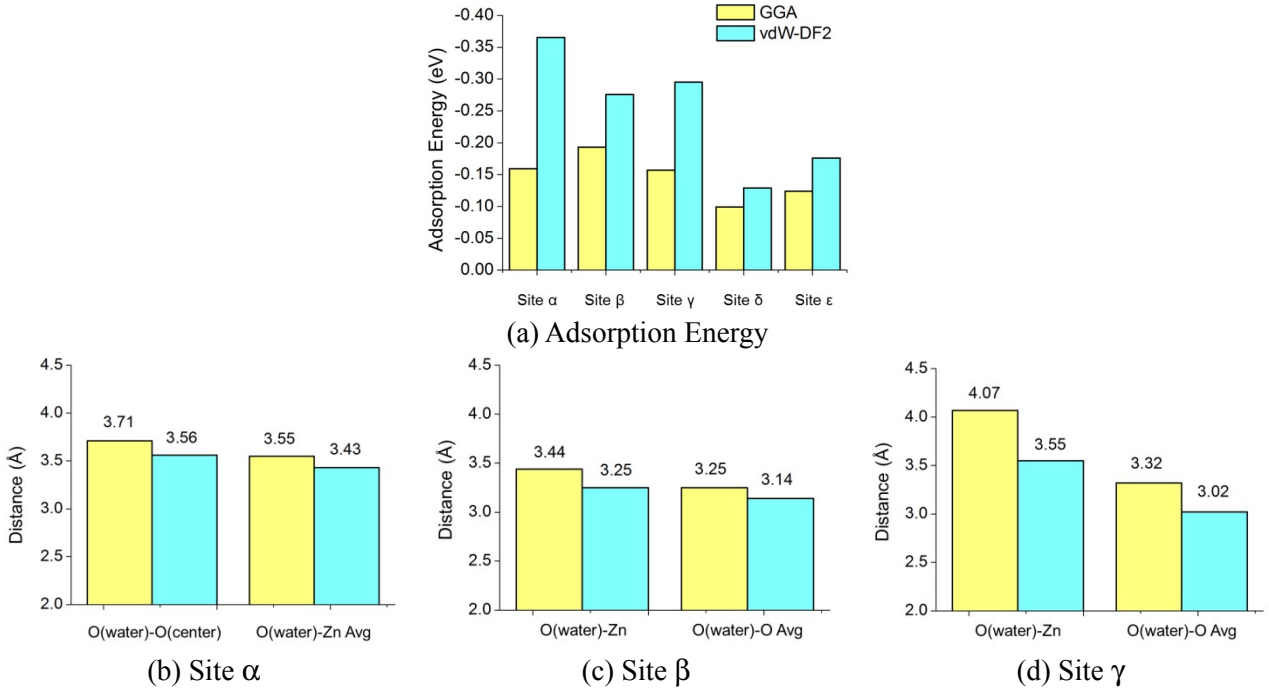

Figure 5.8(9). (a) Calculated adsorption energies for water as a function of exchange-correlation functional and adsorption site in MOF-5. (b-d) Calculated distance from proximal O in an adsorbed water molecule to various atoms in MOF-5 for adsorption sites located on the metal cluster (sites α, β, and γ).

5.8.10 Adsorption of Multiple Water Molecules.

In reality, multiple water molecules can be adsorbed simultaneously on MOF-5 upon exposure to humid air. According to our measurement in Sec. 5.8.5, the saturation water loading in MOF-5 is ~13 wt.% when exposed to air with relative humidity exceeding 50%. Assuming all water molecules preferentially fill the most energetically favorable adsorption sites (α, β, γ sites residing on the Zn-O cluster), this loading corresponds to the adsorption of approximately 5 water molecules per metal cluster. We aim to determine the dependence of water adsorption energies on the Zn-O cluster as a function of coverage and adsorption geometry. To accomplish this, multiple water molecules were placed at α, β, and γ sites on the same Zn-O cluster. Coverages of 1 to 4 molecules were examined. We adopt a naming scheme where the number and identity of filled sites specifies the coverage and adsorbed configuration. For example, the configuration identified as "αα" contains two water molecules adsorbed on α sites. Similarly, "αβγ" corresponds to a configuration where three water molecules are adsorbed in α, β, and γ sites simultaneously. Given the large number (~1,300) of possible configurations for even a small number of adsorbed molecules on a single Zn-O cluster, a systematic enumeration of all configurations was not attempted. Rather, a subset of configurations in which the adsorbed molecules were clustered (i.e., adsorbed at predominantly adjacent sites) was explored. Our preference for these configurations is based on the expectation that water-water interactions are energetically favorable at higher coverages.

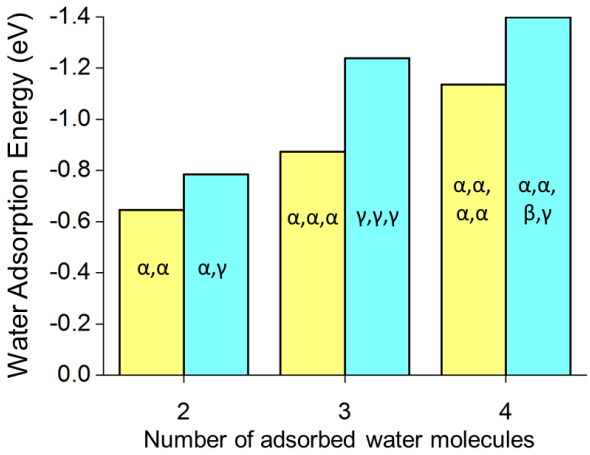

Figure 5.8(10). Calculated total adsorption energy for water on a single SBU as a function of coverage and adsorption configuration. For each coverage the yellow bar (left) represents the adsorption energy in the case where water molecules are widely separated by filling only α sites. (α sites were previously identified as the most favorable sites for the adsorption of isolated H_2O molecules.) Blue bars (right) represent the adsorption energy for the most energetically favorable water distribution identified amongst many candidate adsorbed geometries. Adsorption geometries are labeled inside each bar.

Site α has the lowest adsorption energy for a single water molecule. If water molecules interact weakly, then we expect that only α sites will be filled. Figure 5.8(10) compares the total adsorption energies for the lowest energy adsorbed configurations identified by our search to configurations in which only α sites are filled. For the highest loading considered, 4 water molecules, the total adsorption energy assuming only α sites are occupied is -1.14 eV. For this configuration the distance between adjacent H2O molecules is large, 5.74 Å, signaling that H_2O-H_2O interactions are likely weak. In contrast, a configuration in which H_2O is adsorbed with the configuration ααβγ yields a lower (i.e., more exothermic) adsorption energy of -1.40 eV. In this case the water cluster adopts a more compact arrangement, with H_2O-H_2O distances given by: 2.86 Å (α-β); 4.83 Å (α-γ); 2.97 Å (β-γ). A similar trend holds for loadings of 2 and 3 molecules: adsorption is preferred in configurations that involve nearby αγ and γγγ sites (on average, the γ-γ distance is 2.9 Å). As anticipated, these data suggest that water-water interactions play an important role during the adsorption process: incoming water molecules preferentially adsorb at adjacent sites rather than filling only α sites, which are more widely separated. This tendency is consistent with the type V isotherm measured in our study of water uptake in MOF-5 earlier in Section 5.8.5; such an isotherm indicates the presence of sizeable water-water interactions.

5.8.11 Water Insertion

Having determined the geometries and adsorption energies for small water clusters in MOF-5, we now examine the energetics of water insertion into the framework as a function of water coverage. Prior experiments indicate that hydrolysis of MOF-5 occurs more rapidly at higher water loadings, and is proceeded by an induction period, presumably owing to the nucleation of small water clusters. The exothermicity for water insertion was assessed by evaluating the insertion energy: $\Delta E = E_{final} - E_{initial}$. In this expression $E_{initial}$ corresponds to a low-energy configuration of n adsorbed water molecules on a given metal cluster, as previously described. E_{final} represents the energy of a related structure in which one of the adsorbed molecules is inserted as a molecular unit into the MOF by breaking a Zn-O bond. Water insertion will be favorable if $\Delta E < 0$. Several candidate final (inserted) configurations were considered, including various displacements and twists of the linker following Zn-O bond scission. ΔE was calculated for coverages ranging from 1 to 4 water molecules.

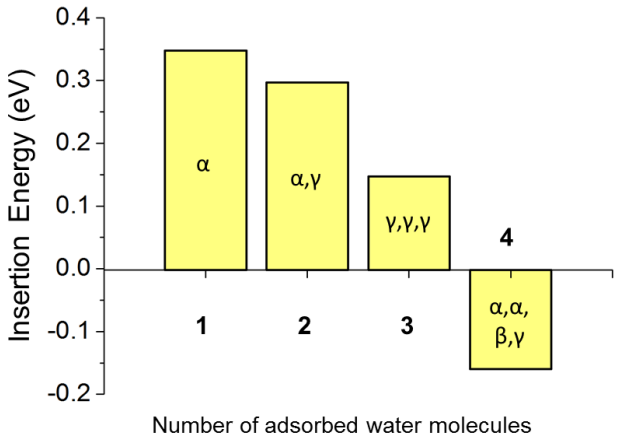

Figure 5.8(11). Water insertion energy in MOF-5 as a function of coverage on a Zn-O cluster. The labels within in each bar indicate the configuration of adsorbed H_2O before insertion.

The insertion energy for water into MOF-5 as a function of coverage is shown in figure 5.8(11). With only one molecule adsorbed water insertion is endothermic: $\Delta E = 0.35$ eV. Insertion becomes increasingly less endothermic as the size of the water cluster grows to 2 or 3 molecules. Finally, insertion becomes exothermic when the cluster size reaches 4 molecules, with ΔE=-0.16 eV. The observation that water insertion is exothermic only at higher coverages is roughly consistent with experimental observations of rapid degradation in MOF-5 upon exposure to air containing relatively high concentrations of water (50% relative humidity or higher). Although experiments suggest that degradation is most rapid at a loading equivalent to 5 molecules per cluster, entropic effects could shift some molecules to sites on the linker. Such an effect would bring the predicted computational loading into even better agreement with experiments.

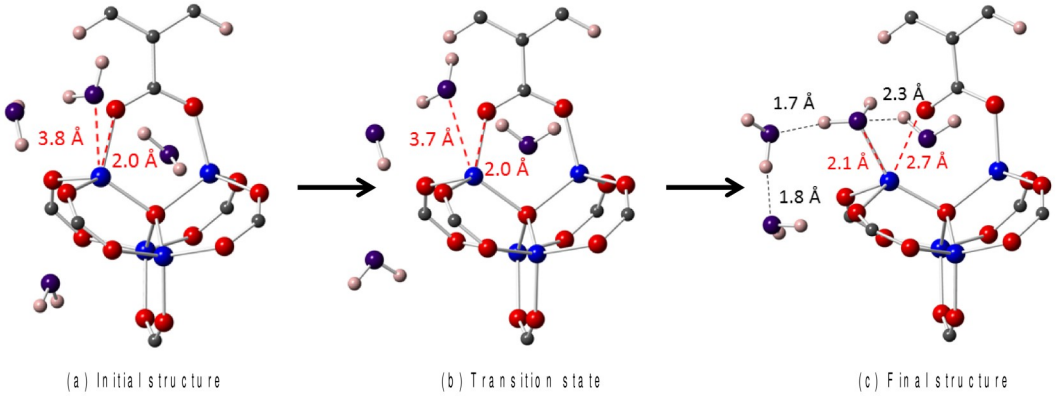

Figure 5.8(12). Water insertion process in MOF-5. (a) Magnification of MOF-5 structure with 4 water molecules physically adsorbed near the Zn-O cluster. (b) Transition state. (c) Final MOF-5 structure containing a Zn-O bond broken via the insertion of a single water molecule. The color scheme for MOF atoms is the same as in Fig. 1(b); O atoms in the water molecules are purple to distinguish them from oxygen in the MOF (blue). Black dashed lines/text indicate hydrogen bond lengths between H and O in adjacent water molecules. Red lines/text illustrate Zn-O bond distances.

The reaction pathway for water insertion is illustrated in figure 5.8(12); the energy profile for this pathway is plotted in Figure 5.8(13). The initial state for the reaction is shown in (a), where four water molecules are physically adsorbed at α, α, β, γ sites, which is the same low-energy configuration reported in Fig. 5.8(10). Upon approaching the transition state, shown in (b), the water molecule occupying the β site migrates towards the Zn atom. Finally, (c) represents the final state where the water has been inserted into the framework by breaking a Zn-O bond. The inserted molecule forms a new bond of length 2.1 Å between Zn and O(water). The original (now broken) Zn-O(MOF) bond lengthens to 2.7 Å from its initial value of 2.0 Å. The O(MOF) stranded by water insertion subsequently forms a double bond with its neighboring C, forming carbonyl group. Meanwhile the 3 adsorbed water molecules remain in close proximity to the inserted molecule, forming a "water chain" with inter-molecular H-O distances of 1.7 to 2.3 Å. These distances are consistent with inter-molecular H-O bond lengths typical of hydrogen bonding in water, ~2.0 Å.

Returning to the energy profile for water insertion, we note that the activation barrier for this process is small, only 0.17 eV. The calculated activation energy for water insertion is used in conjunction with classical rate theory to estimate the time required for hydrolysis of MOF-5 upon exposure to humid air under conditions similar to those used in our recent experimental study [26]. In that study, MOF-5 powders exhibited negligible surface area and hydrogen uptake capacity after 48 hours of exposure to humid air with 61% relative humidity (RH).

The number of water molecules N inserted into 1 g of MOF-5 in time t can be expressed as:

$$N = pAZt \cdot \exp\left(\frac{-E_a}{kT}\right)$$

Here A is the theoretical specific surface area of MOF-5 (3,800 m^2/g), Z represents the number of collisions/adsorption attempts between gas phase water molecules and the pore surface of MOF per unit area-second, p is the probability that adsorbed water occupies sites with a loading and configuration amenable to insertion (such as the low-energy ααβγ configuration described above), and E_a is the activation energy for insertion from that configuration.

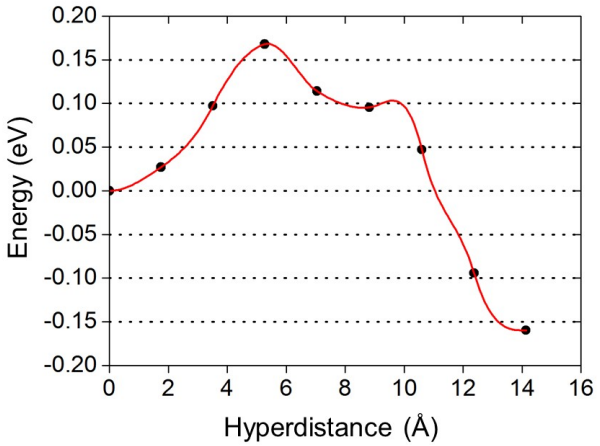

Figure 5.8(13). Calculated energy barrier for the insertion of a water molecule into MOF-5. The insertion process breaks a Zn-O bond, and occurs in the presence of 3 additional adsorbed water molecules adsorbed on the metal cluster.

The rate theory calculation indicates that for a loading of 4 water molecules per cluster, on average approximately 290 hours of exposure time is needed for water insertion to occur. This estimate is in reasonable agreement with the exposure time (~48 hours) needed to significantly degrade the surface area and hydrogen uptake properties of MOF-5 powders at a slightly higher loading of 13 wt.% H_2O (equivalent to about 5 H_2O molecules per cluster) which is the saturation coverage resulting from exposure to air with RH = 61%. Moreover, our estimate is likely an upper bound to the time needed for hydrolysis, as it relates only to a specific local loading and adsorption geometry (ααβγ); it is likely that other configurations and higher loadings also lead to water insertion.

The mechanisms considered above all relate to the insertion of water in molecular form. In addition, calculations were preformed to examine the energetics for dissociative water insertion. For this scenario, a relaxed structure was generated in which the original Zn-O bond present in MOF-5 was broken and replaced by Zn-OH(water) and O–H(water) bonds. However, the energy of this hypothetical structure was found to be much higher (~1 eV) compared with that of the initial structure, indicating water dissociation is not energetically favored in this configuration.

5.8.12 Conclusions

The effect of MOF-5 exposure to environments with high water concentrations was investigated by both a designed experiment and DFT calculations. Measurements indicated that water adsorption in MOF-5 is consistent with a type 5 isotherm, with a steep rise in uptake at a "threshold" level of about 50% relative humidity. Below the threshold only minor degradation is observed for exposure times up to several hours, indicating that MOF-5 is more stable than commonly thought under moderately humid conditions. In contrast, irreversible degradation can occur in a matter of minutes at higher humidity. FTIR spectroscopy suggests that molecular and/or dissociated water is inserted into the skeletal framework after long exposure times. Densification into pellets was observed to slow the degradation of MOF-5 significantly, and may present an opportunity to extend the stability window of some MOFs.

Using *ab intio* calculations, we examined the energetics associated with water adsorption and insertion into MOF-5 as a function of surface coverage. A distinguishing feature of our study was the inclusion of dispersion interactions – which are expected to play an important role in molecular adsorption – and modeling of the full periodic unit cell of MOF-5. A comparison of a van der Waals-aware functional (vdW-DF2) and a conventional gradient-corrected functional (PBE-GGA) revealed important qualitative and quantitative differences regarding the energetics and site preference for water adsorption. The vdW-DF2 functional favors water adsorption on the SBU, rather than on the linker. This differs from the trend predicted by the PBE-GGA, which exhibits a more uniform distribution of adsorption energies on both the linker, and SBU.

The DFT calculations indicated that the thermodynamics of water insertion into MOF-5 is coverage dependent: Insertion becomes thermodynamically favorable only when a critical number of water molecules (4 or more) are co-adsorbed as relatively compact clusters on the same structural building unit of the MOF. This observation is in good agreement with our experimental measurements, which show that hydrolysis is slow at low water coverages and is preceded by an incubation period; we speculate that the latter process owes to the nucleation and growth of water clusters of sufficient size on a given SBU. Once a sufficient coverage has been achieved, the insertion of molecular water into Zn-O bonds proceeds with a low activation barrier, consistent with a rapid hydrolysis reaction.

Our calculations lend further support to the notion that the rate of MOF degradation depends strongly on the operating environment. While it is now clear that some MOFs are unstable to hydrolysis in an absolute sense, under low-to-moderate humidity conditions the rate of hydrolysis can be slow enough to allow exposure for several days without significant degradation.

5.9 Computational Screening of MOFs

5.9.1 Introduction

Increasing emphasis on the development of sustainable transportation technologies has highlighted the need for high-density energy storage.[1] In the case of fuel cell vehicles (FCV), the energy storage problem can be traced to challenges associated with storing low density gaseous H_2.[2] While several approaches to storing hydrogen have been explored, (including, for example, liquefaction, physical compression, absorption in condensed phases, *etc.*), one of the more appealing options is the reversible adsorption of H_2 on high surface area materials.[2] Sorbents generally exhibit high cycle life and fast kinetics, yet are restricted to low operating temperatures due to weak H_2/sorbent interactions. In addition, the high gravimetric capacities typical of some sorbents rarely coincide with high volumetric densities. Consequently, the search for optimal sorbent materials has emerged an extremely active area of research. In particular, the class of materials known as coordination polymers (CPs), of which a

subset are termed metal-organic frameworks (MOFs), has recently attracted intense interest as hydrogen storage materials.[3-5]

MOFs are crystalline materials containing a metal atom or metal cluster bonded to organic linkers.[6-9] Thanks to their record setting surface areas, gas selectivity, and permanent, open pore geometries, MOFs have emerged as promising materials for gas storage and separations,[10] as well as for other applications.[11] MOFs are highly tunable in both structure and composition, as both metal clusters[12,13] and linkers have the potential to be varied amongst several possibilities. In principle, such tunability could enable the development of an adsorbent capable of storing H_2 at near ambient conditions and with high gravimetric and volumetric densities. Nevertheless, the extreme flexibility in MOF design also presents challenges: while a large variety of compounds are possible,[14,15] the synthesis and testing of significant numbers of compounds can be time-consuming and costly. To further complicate matters, existing materials databases (such as the Cambridge Structural Database[16]) generally do not distinguish CPs or MOFs from the large and growing number of molecular compounds.

In recognition of the bottlenecks associated with experimental materials discovery, a small number of studies have employed computational methods to rapidly characterize[17,18] or screen for promising porous materials.[15,19,20,21,22] For example, recent work[15] has screened 137,953 hypothetical MOFs for CH_4 uptake[15,21,22] and CO_2 capture[20] by interchanging 3 metals (comprising 5 metal centers) and 102 carboxylic acid derived ligands. In related work, smaller databases of MOFs were screened for use in gas separation applications.[21,22]

In the present study we significantly expand the space of screened compounds by exploiting the 550,000+ *known* organic compounds contained within the Cambridge Structural Database (CSD).[16] The CSD contains thousands of MOFs,[14] yet it appears that many of these have not been tested for gas storage applications. An advantage of this approach is that it relies on existing compounds rather than on hypothetical materials that may prove difficult to synthesize. To facilitate a computational assessment of these properties, we use data mining and structural routines to identify, "cleanup," and rapidly characterize MOFs within the CSD. The isolation of such structures enables rapid prediction of their performance and allows us to address fundamental questions regarding their properties. For example: *Which MOFs have the highest theoretical H_2 capacity, and what common features do they share? Can high surface and high volumetric density of stored H_2 be achieved simultaneously?* Answering these questions will accelerate the discovery of optimal MOFs for hydrogen storage applications.

Here we demonstrate such an approach by searching for MOFs exhibiting high hydrogen storage capacities.[2] A subset of ~22,700 compounds is generated from the CSD using search and filtering algorithms, followed by routines for the removal of guest molecules or fragments thereof. The resulting structures are characterized with respect to their surface area[23] and pore volume. Application of the empirical correlation between H_2 excess uptake and surface area allows for the theoretical total hydrogen storage capacity to be estimated for the subset of ~4,000 compounds exhibiting non-trivial internal porosity. This approach is relatively efficient as it does not require the evaluation of interatomic potentials or expensive isotherm simulations – only geometric features of the crystal structure need to be assessed. Moreover, by comparing theoretical capacities we avoid experimental complications associated with incomplete solvent removal; this allows for consistent comparisons across compounds and analysis of tradeoffs and trends that could be difficult to isolate using (potentially noisy) experimental data.

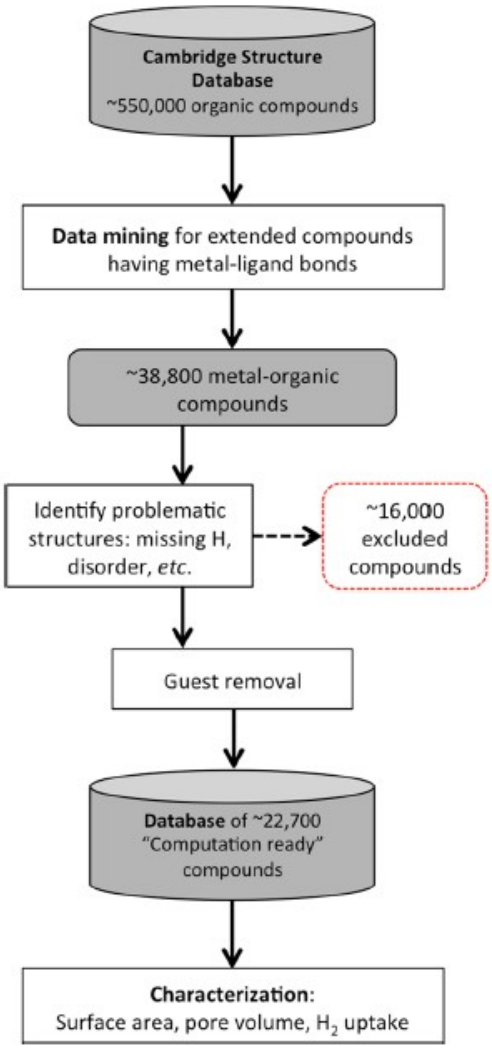

Figure 5.9(1). Flow diagram summarizing the processing and analysis of crystal structure data from the CSD.

Our screening identifies several known, yet overlooked compounds having high hydrogen storage densities exceeding 10 wt. % and 58 g/L (total H_2, at 77K and 35 bar). These compounds are suggested as promising candidates worthy of additional experimental characterization. More importantly, screening also reveals a maximum in the distribution of volumetric vs. gravimetric uptake data, beyond which additional increases in surface area result in decreasing volumetric capacity. Such a tradeoff implies that H_2 storage in MOFs will not benefit from further improvements in surface area alone. Rather, materials development efforts should aim to simultaneously achieve moderate mass densities and surface areas, while ensuring framework robustness upon solvent removal.

5.9.2 Methodology

5.9.2.1 Structure Searching

A flow diagram summarizing the key steps in our MOF screening scheme is given in Fig. 5.9(1). As a first step, MOF crystal structures were identified and extracted from the CSD. The CSD is a database containing over 600K crystal structures, 550K of which are organic compounds (top box in fig. 5.9(1)). Because the rate of structural depositions in the CSD doubles roughly every 9 years,[14] and doubles approximately every 4 years for MOFs,[14] we sought to develop methods to identify MOFs which could be reused upon subsequent updates to the CSD. To facilitate structure analysis, all compounds of interest were translated from the native crystallographic information file (CIF) format of the CSD to explicit xyz atomic coordinates using the Atomic Simulation Environment (ASE),[24] a Python code for structural analysis.

A labeled dataset of previously identified MOFs[14] (2nd box in Fig. 5.9(1)) was employed to verify data features that indicate MOFs. By using these features we were able to identify MOFs in the labeled set with >95% recall. That is, had we known these features beforehand and searched the labeled dataset, we would have found >95% of the structures. Those features were: structures that contain carbon, a metal, a ligand, and a metal-ligand bond; and structures labeled as an extended structure. For this search, we defined a metal to include all metals to the right of the diagonal along (Al to Po), the f-block metals, but not the alkali metals. Ligands are defined as elements that can form bonds between metal and organic components, and we included the elements B, N, O, Si, P, and S in our search.

To identify the presence of a metal-ligand bond we evaluated pair distances between each atom within the crystallographic a unit cell. To determine whether a given pair atoms i and j are bonded we compare their geometric distance (d_{ij}) to a set of known atomic bond radii (r). These radii are computed averages from the CSD and required use of a broadening term $\sigma = 0.5$ Å, to take into account bond length variation: $d_{ij} < r_i + r_j + \sigma$. Our initial search implementing these criteria identified approximately 38,800 metal-organic compounds, Fig. 5.9(1).

Our analysis of the data contained within the CSD revealed several examples of structural irregularities. These include: missing hydrogen, missing atom coordinates (i.e., fractional coordinates labeled with a '?'), ionic species, and partial site occupancies arising from high symmetry conformations. (Since in the latter case the CSD does not generally provide site occupancies, we found that atomic coordinates which are too close to be physically bonded (< 0.7 A) often served as a good indicator of symmetry-related disorder.) We observe that disorder is often present in structures having large unit cells or thermal conformational degrees of freedom, both traits common to MOFs. Missing atoms are often solvent or hydrogen. Compounds containing ionic species were also excluded from the database to avoid charge imbalance; these ionic species often appear in conjunction with guest molecules that are later removed. Since our procedure examines more files than a human can realistically process, automated identification and isolation of potentially troublesome structures was necessary. Scanning for these problematic features resulted in the identification and isolation (i.e., removal) of ~16K compounds, e.g. see the red box in Fig. 5.9(1).

5.9.2.2 Guest Removal

The next step in our processing involved the removal of unbounded guest molecules from the remaining structures. Guests typically consist of residual solvent incorporated into the MOF pores during crystallization. To maximize porosity and surface area it is desirable to remove guests from the structure, for example, by evacuation and heating. In some cases guest removal is not complete; hence, the crystal structure data within the CSD can contain (partially resolved) positions of solvent atoms. As our goal is to estimate the maximum theoretical capacity of MOFs for H_2 storage, we developed an algorithm to remove these guests and thereby create pristine (i.e., solvent free) MOFs.

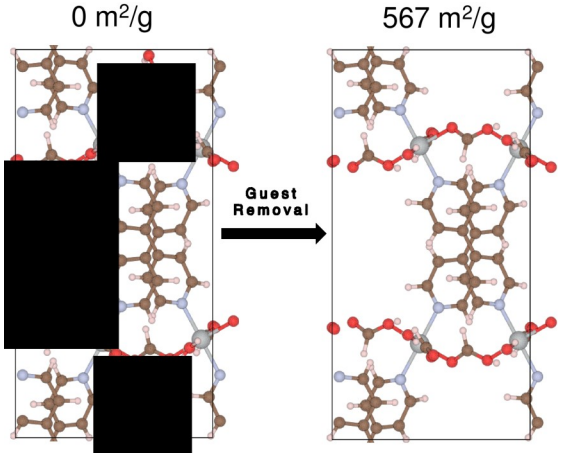

Figure 5.9(2). Example of the automated removal of guest molecules from the compound FIFPAM, and the resulting increase in surface area. The circles indicate unconnected components (water molecules) in the MOF's molecular graph

Our guest removal algorithm operates by constructing a molecular graph of the structure by processing the distances d_{ij} between each pair of atoms, then expanding the connectivity to a periodic cell. In this way the

connectivity of the metal organic framework and all other bonded components were identified. We postulated that the set of bonded atoms could be split into two distinct sets, one containing the metal-organic framework and the other containing all other components. Those components not part of the metal's bonded network are presumed to be guest molecules and are removed.

For gas storage applications it is desirable that the adsorbent material consist of a semi-rigid, 3-D periodic framework of covalently bonded atoms. However, less interesting compounds consisting of 1-D or 2-D building blocks that are held together by hydrogen bond networks or van der Waals forces can also appear in the dataset. These compounds contain multiple connected components lists containing metals, and may complicate the guest removal algorithm. To filter out the 1-D and 2-D compounds, we reasoned that a 3-D framework should have a single connected component list containing all metals in the unit cell. To test this hypothesis, we applied this assumption to our labeled set, and found it true for >95% of the set cases. (Of course, interpenetrated MOFs can have multiple metal lists, and one disadvantage of this approach is that it excludes these compounds from our dataset.) We found that so long as the structure was an extended 3D MOF, our method removed solvents and guests correctly. As a further check on the method's accuracy, we examined the most promising MOF structures by hand to ensure these were free of errors. An example of successful guest removal is shown in Fig. 5.9(2), where the guests are comprised of water molecules. More generally, we observe that structures whose authors used the PLATON SQUEEZE[25] function to refine their structures before submission to the CSD typically produced a crystal structure free from guest molecules. The final step in cleaning up the structures involved removing terminal oxygen atoms bonded to metal sites. These atoms appear to be components of incompletely resolved water molecules that are missing H atoms.

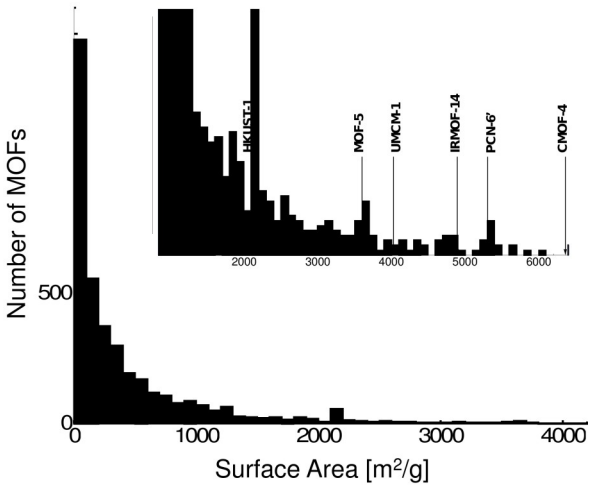

Figure 5.9(3). Number of MOFs having a given surface area. Labels highlight selected common MOFs. The inset magnifies the distribution for MOFs having surface area > 1000 m^2/g. The peak in the distribution near 2100 m2/g is due to multiple entries for HKUST-1.

5.9.2.3 Surface Area, Porosity, and Theoretical H_2 Uptake

With the removal of unbounded guests we have amassed a database of approximately 22,700 "computation ready" compounds amenable to property characterization (Fig. 5.9(1)). For gas storage applications, two key properties of an adsorbent are surface area and porosity. Surface area is significant because it relates to the number of possible sites at which adsorption can take place. In fact, the excess gravimetric uptake arising from adsorption correlates strongly with surface area in a wide range of porous materials.[26] Likewise, porosity determines the amount of free space available to host gas phase (or "bulk") molecules of the adsorbate. By combining the adsorbed and bulk quantities of adsorbate one can estimate the total amount of a gas stored within a given adsorbent. Thus as a next step we calculate the surface areas and porosities for all compounds in our database.

For surface area calculations we adopt the geometric accessible surface area approach described in Ref. 23. The method was validated by comparing calculated surface areas from the dataset compounds against previous

applications of the method.[23] Following convention, we use a probe of N_2 of 3.681 Å diameter; unit cell lattice parameters were read from the CIF file without further modification. Figure 5.9(2) demonstrates how the calculated surface area increases after the removal of guest molecules. To calculate the porosity we used the CALC SOLV function within the PLATON code[25] and a H_2 probe molecule.

In previous work on H_2 adsorption in micro-porous carbons, a linear relationship (i.e., the so-called "Chahine rule")[26] was observed between surface area and excess hydrogen uptake, n_{excess}, at 77 K and 35 bar. Upon further investigation, this relationship was found to hold across a wide class of porous materials, including MOFs.[27,28] It is possible to estimate the *total* amount of H_2 stored by a given MOF by augmenting n_{excess} with n_{gas}, the amount of gas phase hydrogen present in the MOF's pore, $n_{gas} = \rho_{H2} \times V_{pore}$. Here ρ_{H2} is the density of hydrogen at 77K and 35 bar (11.5 kg/m^3), and V_{pore} is the volume within the pores of the crystallographic unit cell as calculated by PLATON. The total uptake can be described by the following equation:

$$n_{tot} = n_{ex} + n_{gas} = C \cdot SA + \rho_{H2} \cdot V_{pore} \quad (1)$$

where C is the proportionality constant (0.021 mg H_2/m^2) linking surface area (SA) with excess uptake.[28] We note that this proportionality constant is valid only for a specific temperature and pressure, in this case 77 K and 35 bar. Dividing n_{tot} by the mass or volume of the unit cell yields, respectively, the total gravimetric (units of g H_2 per g MOF) and total volumetric uptake (units of g H_2 per L of MOF) of H_2.

We emphasize that our estimate of total H_2 uptake refers to the *maximum theoretical uptake on a materials basis*. That is, we assume a pristine MOF in which all solvent molecules have been removed, and furthermore take V_{pore} to be the micropore volume within a *single crystal monolith* of the MOF. (In other words, the theoretical volumetric density of stored H_2 is based on the single crystal MOF density: Volumetric density = gravimetric density × single crystal density.) Although MOF synthesis procedures are continually improving (resulting in less solvent retained within the pores),[29] and densification has shown promise for improving MOF density,[30,31] it is unlikely that MOF media used in a commercial storage system will adopt a single crystal morphology and be completely free from guest molecules. In addition, gravimetric and volumetric losses will arise from the mass and volume associated with the storage system: e.g., pressure vessel, balance of plant components, *etc*. Hence, our estimates represent an upper bound to the H_2 storage performance. Nevertheless, such estimates are of value because they can distinguish "dead-end" materials – i.e., materials that do not at least exceed system-level targets on a materials-only basis – from those that show promise. Moreover, the use of theoretical capacities facilitates comparisons between compounds by avoiding experimental complications associated with incomplete (or inconsistent) solvent removal. This allows for the identification of tradeoffs and trends that may be difficult to isolate using experimental data derived from different synthesis conditions.

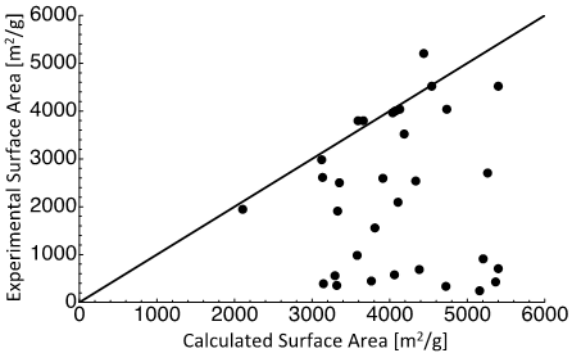

Figure 5.9(4). Comparison of calculated surface areas with experimentally measured surface areas for selected MOFs. The diagonal line indicates perfect agreement between theory and experiments.

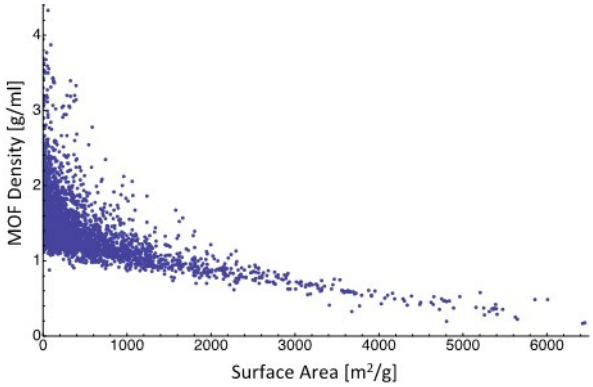

Figure 5.9(5). MOF mass density vs. calculated surface area

5.9.3 Results and Discussion

5.9.3.1 Surface Area, Density, and Porosity

After the removal of guest molecules, calculation of the surface areas for all compounds reveals that the database contains 4026 MOFs with non-zero surface areas; 568 of these exhibit moderately high surface areas > 1000 m^2/g. A histogram illustrating the number of compounds with a given surface area is shown in Fig. 5.9(3). The distribution is sharply peaked at low surface areas, and exhibits a long tail out to values in excess of 5000 m^2/g. The presence of a small number of compounds having large surface areas is consistent with recent experimental measurements showing that a handful of compounds have surface areas in the range of 5000-6000 m^2/g.[3]

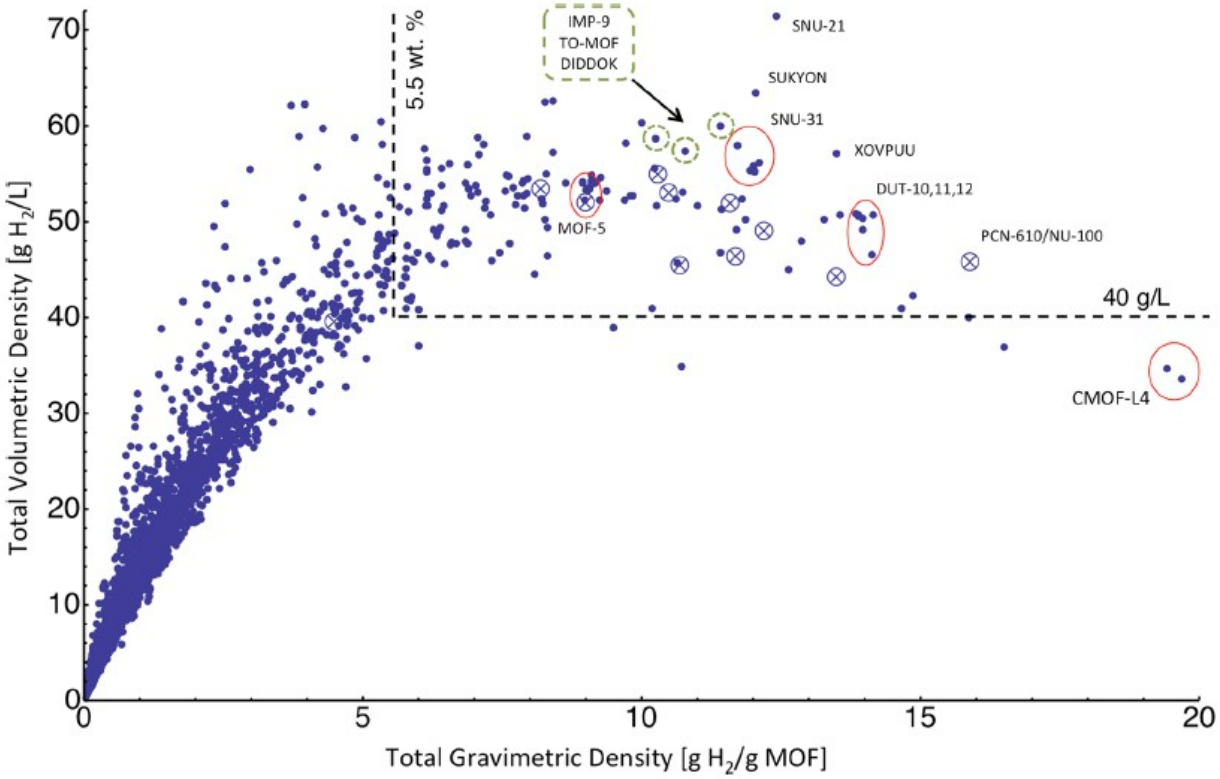

Figure 5.9(6). Theoretical total (adsorbed + gas phase H_2 at 77K and 35 bar) volumetric and gravimetric density of stored H_2 in ~4000 MOFs mined from the CSD. The data account only for the mass and volume of the MOF media; mass and volume contributions from the system are neglected. For comparison, the region bounded by the dashed lines represents the DOE 2017 targets for H_2 storage systems. Crossed circles represent common MOFs with incomplete or disordered crystal data in the CSD; structures for these compounds were constructed by hand. Additional data for the top-performing MOFs is given in Table 5.9(1).

Since surface area directly relates to gravimetric excess uptake, and is therefore a key component in estimating total H_2 stored (Eq. 5.9.1), it is important to assess the degree to which calculated surface areas correlate with experimental measurements, the latter being most commonly based on BET theory. Since the experimental BET surface area depends on the pressure range used in its estimation, as well as on the purity and defect structure of the MOF, care should be exercised in making direct comparisons between theory an experiment; a thorough discussion of these issues is provided in Ref. 23. Fig. 5.9(4) plots the experimental BET surface area *vs.* the calculated surface area for a subset of MOFs whose surface areas have been measured experimentally. The general trend in the data is for the computed surface areas to exceed the experimentally measured areas: that is, the majority of points fall on or below the diagonal line in Fig 5.9(4). The trends in Fig. 5.9(4) can be explained as follows: the optimization of synthesis procedures over time has resulted in significant improvements to the surface area of MOFs, for example through more complete removal of guests or unreacted reactants.[29] Hence, those MOFs exhibiting good agreement between the calculated and measured surface area represent compositions in which essentially all solvent has been removed. On the other hand, compounds that fall below the diagonal line

in Fig. 5.9(4) represent cases where solvent was either not completely removed, or for which the process of solvent removal results in a change in the MOF structure, such as framework collapse. We expect that the agreement between calculated and measured surface areas will improve as synthesis procedures evolve. As an example we cite the evolving surface area of MOF-5, which is perhaps the most heavily studied MOF. Early efforts targeting the synthesis of MOF-5 did not achieve maximal surface areas. Only after an optimal procedure was identified[29] did the measured surface area (~3800 m^2/g) approach the theoretical value (~3656 m^2/g). We conclude that the calculated surface area represents a reasonable upper bound to both the experimentally achievable surface area and, through the Chahine rule, the excess gravimetric density of stored H_2.

In addition to gravimetric density, the volumetric density of stored H_2 is another important, but relatively unappreciated, performance metric. Recent MOF synthesis efforts appear to focus on maximizing surface area and gravimetric performance at the possible expense of volumetric density. The product of gravimetric density and the mass density is equal to the volumetric density; and from the Chahine rule we know that gravimetric density is proportional to surface area, Eq. 5.9.1. *Therefore to simultaneously maximize gravimetric and volumetric performance, compounds having both high surface areas and high mass densities are needed*. Do these materials exist? To answer this, Figure 5.9(5) plots the mass density *vs*. calculated surface area for the database MOFs. Figure 5.9(5) shows that MOF density decreases with increasing surface area. The decrease is rapid and nonlinear for surface areas less than 1000 m_2/g, and then transitions to a roughly linear relation for surfaces areas in excess of 2000 m^2/g. The inverse relationship between SA and density indicates the potential for a tradeoff between volumetric and gravimetric H_2 density; this will be discussed in more detail below. Interestingly, extrapolation of the linear relationship between density and surface area results in an intercept of ~7750 m^2/g, corresponding to the surface area of a hypothetical MOF having a density of zero. This value is somewhat smaller than the ~10,500 m^2/g upper limit for a hypothetical MOF consisting of infinitely long linkers derived from benzene rings[32], and may therefore represent a more realistic estimate of the maximum surface area attainable by MOFs.

To estimate the total H_2 contained within a MOF is necessary to quantify the amount of pore space available for gas phase (bulk) H_2. Similar to surface area, these distributions are peaked at moderate values for pore volume or void fraction, with very long tails extending out to higher values. The data confirms that very few compounds exhibit extremely high porosity.

5.9.3.2 Theoretical H_2 Storage

Figure 5.9(6) plots the theoretical total H_2 uptake (at 77 K and 35 bar) for the database compounds having non-zero surface areas. In several cases the data points corresponding to noteworthy compounds are highlighted. The calculated values are compared with the DOE 2017 hydrogen storage system targets of 5.5 wt. % and 40 g H_2/L, depicted as the rectangular region in the upper-right corner of the plot.[2] Table 5.9(1) summarizes the properties of 78 high-performing compounds identified by screening with gravimetric capacities greater than 7.5 wt. % [(g H_2/g MOF) × 100]. Of these high gravimetric compounds, nearly 8% appear to be variants of MOF-5, while 52% contain Zn-based clusters and 28% contain Cu clusters. The limited diversity in metal content suggests that opportunities may exist to expand the composition space via metal substitution.

Several features of Fig. 5.9(6) warrant discussion. First, it is clear that the vast majority of porous compounds exhibit relatively low H_2 uptake. Nevertheless, our screening identifies several dozen that surpass the targets on a theoretical, materials-only basis, Table 5.9(1). Second, and perhaps more importantly, the distribution of volumetric capacities exhibits a concave downward shape when plotted *vs.* wt. %. That is, at capacities below ~5 wt. % the volumetric and gravimetric densities are positively correlated. However, upon continuing to higher wt. % the volumetric density approaches a maximum of ~ 64 g/L at 8-12 wt. %, and then decreases for gravimetric densities greater than ~12 wt. %. The decrease in volumetric density at high gravimetric densities is consistent with the density/surface area trade-off suggested in Fig. 5.9(5). We conclude that MOFs having extreme surface areas greater than ~5,500 m^2/g cannot meet the DOE volumetric target (assuming the storage system will have a non-zero volume). Instead, the most promising compounds occur at lower surface areas of 3100-4800 m^2/g, Table 5.9(1), resulting in both high gravimetric values of 8-12 wt. % and volumetric densities of 50 – 64 g/L. This suggests that development of new MOFs should not exclusively target high surface areas, but instead focus on achieving moderate mass densities (> 0.5 g/cm^3) in conjunction with high surface areas.

We now discuss the properties of noteworthy MOFs that emerge from our screening. We begin with MOF-5, which is arguably the most widely studied MOF. As such it serves as a useful benchmark against which we validate our methodology. As previously discussed, optimization of the MOF-5 synthesis protocol has resulted in a continual increase in its surface area, with the highest measured values being similar to those predicted by theory. In addition, MOF-5 is unique in that it is perhaps the only system for which *total* H_2 uptake has been reported on an essentially pristine compound.[29] The measured values of the pristine MOF-5 of 8.4 wt.% and 54.4 g/L (35 bar, 77K) compare very favorably with the 8.9 wt. % and 54.1 g/L predicted by our methods. It should be noted the pristine material has higher performance than the BASF MOF-5 although is difficult to practically synthesize, which was the reason the HSECoE system and material development were based on the BASF material performance. We conclude that our screening approach yields reliable predictions of total H_2 uptake.

Turning now to less common compounds, the MOF identified as having the highest theoretical performance is SNU-21, Fig. 5.9(7).[33] This compound is projected to achieve 12.4 wt. % and 71.4 g/L. It has a moderately high theoretical surface area of 5208, yet maintains a mass density of 0.58 g/cm^3. The desolvated versions of this compound, SNU-21H and SNU-21S, have had their surface area and hydrogen uptake properties measured experientially, but the reported values [695 (21H) & 905 (21S) m^2/g, ~5 wt. % total at 77K and 70 bar;[33] fall far below the theoretical expectations. Given that the measured surface area is far below the theoretical one, it is possible that: some solvent has been retained in the pores, pore-collapse has occurred, the structure is (partially) interpenetrated or has degraded in some way. Therefore, further gains in performance could be realized if the synthesis of a pristine compound could be achieved.

In addition to showing the theoretical performance for well-studied compounds, our screening revealed that there are many "understudied" or "overlooked" MOFs: that is, many MOFs have been synthesized, yet relatively few have had their gas adsorption properties measured. Within this subset of MOFs there exist some with potentially exceptional gas storage properties. These compounds are assembled in the top half of Table 5.9(1). For example, Fig. 5.9(6) identifies CMOF-L4[34] as having the highest theoretical gravimetric uptake overall at greater than 19 wt. %. Nevertheless, there appear to be no reported measurements of its hydrogen adsorption properties. Consistent with its high gravimetric H_2 density, this MOF is predicted to have the highest overall surface area, ~6400 m^2/g, which exceeds that of PCN-610/NU-100[35,36] on a theoretical basis. Despite these exceptional properties, the low density (0.17-0.18 g/L) of CMOF-L4 results in a mediocre volumetric density (~34 g/L) that falls below the DOE target.

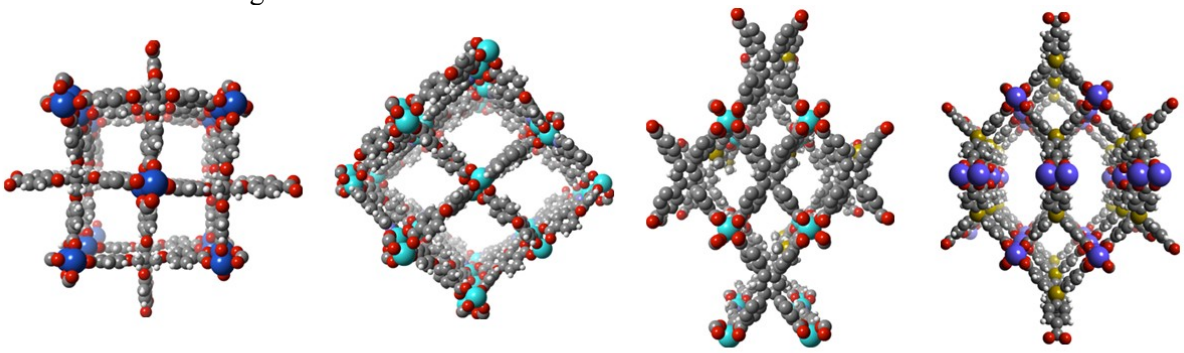

Figure 5.9(7). Crystal structures, CSD identifiers, and MOF names (if known) for four of the top performing MOFs identified by screening.

The absence of hydrogen uptake measurements in CMOF-L4 could potentially be explained by its unstable structure: the pores in this MOF were found to collapse upon removal of guest molecules.[33] Consequently, we expect that the surface area and H_2 capacity of the experimentally realized compound should be much lower than the theoretical prediction. The probability for structure collapse appears to increase as the surface area increases, suggesting that important avenues for MOF research are realizing/stabilizing structures susceptible to collapse, or at least predicting which structures can be realized in pristine, solvent-free form.

Finally, our screening also uncovers several other promising compounds for which *no* H_2 uptake measurements have been reported. They include (using their CSD identifiers): DIDDOK,[37] ENITAX (IMP-9),[38] and LURGEL

(TO-MOF).[39] The crystal structures for these MOFs are illustrated in Fig. 5.9(7). Their positions in the total uptake plot, Fig. 5.9(6), are indicated with green dashed circles, and it can be seen that they fall near the maximum of the data distribution. Table 5.9(1) summarizes their properties; their common features include relatively high mass densities (0.53 – 0.57 g/cm^3), high (but not extreme) surface areas (4162 – 4651 m^2/g), gravimetric densities of 10.2 – 11.4 wt. %, and high volumetric densities of ~60 g/L. All of these compounds appear to have stable structures (i.e., do not exhibit pore collapse upon solvent removal). Because these MOFs have received only minimal experimental scrutiny, they represent targets of opportunity for more extensive synthesis and testing.

5.9.4 Conclusions

We have demonstrated an efficient, automated approach to screening the 600,000+ entry Cambridge Structure Database for porous, metal-organic compounds (i.e., MOFs) useful for hydrogen storage. Our approach employs routines for virtual solvent removal, and leverages the established empirical correlation between excess hydrogen uptake and surface area. Consequently, the method is highly efficient since it does not require the evaluation of interatomic potentials or expensive isotherm simulations. Excluding compounds with disorder or missing atoms, we assemble a database of more than 4,000 solvent-free structures for which we assess porosity, surface area, and total theoretical H_2 uptake (gravimetric and volumetric). Since our approach relies only on known compounds, it may present advantages to those based on hypothetical compounds that may prove difficult to synthesize.

Analysis of the relationship between MOF mass density and surface area reveals that density decreases with increasing surface area, indicating that a tradeoff exists between gravimetric and volumetric H_2 storage. The concave downward shape of the volumetric *vs.* gravimetric uptake distribution further supports this conclusion: volumetric H_2 density reaches a maximum for surface areas in the range of 3100-4800 m^2/g, but then decreases for those compounds having extreme surface areas greater than 5,500 m^2/g. The data suggests that development of new MOFs should not exclusively target high surface areas, but instead focus on achieving moderate mass densities (> 0.5 g/cm^3) in conjunction with high surface areas.

Our screening identifies several compounds with promising properties. While some of these have had their experimental H_2 uptake tested, many appear to have undergone no testing whatsoever. Of these, SNU-21 emerges at the highest-performing candidate, achieving densities of 12.4 wt. % and 71.4 g/L. However, experimental measurements on this compound have not achieved these high levels of performance, presumably due to incomplete solvent removal. In addition, the compounds having CSD identifiers (common names) DIDDOK, ENITAX (IMP-9), and LURGEL (TO-MOF) are highlighted as “targets of opportunity” given their high H_2 densities (10.0 – 11.4 wt. % and ~60 g/L) and absence of uptake measurements.

Looking to the future, we suggest that research efforts targeting MOFs for gas storage emphasize the challenges of structure stability/pore collapse and solvent removal. Many promising compounds in our dataset exhibit these deficiencies, and we believe these issues warrant additional effort to quantify the factors that determine whether a given compound can be realized in a robust, solvent-free form.

5.9 Bibliography (for Section 5.9 only)

(1) Chu, S.; Majumdar, A. *Nature* **2012**, *488*, 294.
(2) Yang, J.; Sudik, A.; Wolverton, C.; Siegel, D. J. *Chemical Society reviews* **2010**, *39*, 656.
(3) Sculley, J.; Yuan, D.; Zhou, H.-C. *Energy & Environmental Science* **2011**, *4*, 2721.
(4) Suh, M. P.; Park, H. J.; Prasad, T. K.; Lim, D. W. *Chemical reviews* **2012**, *112*, 782.
(5) Murray, L. J.; Dinca, M.; Long, J. R. *Chemical Society reviews* **2009**, *38*, 1294.
(6) Ferey, G. *Chem. Soc. Rev.* **2008**, *37*, 191.
(7) Rowsell, J. L. C. Y., O. M. *Microporous Mesoporous Mat.* **2004**, *73*, 3.
(8) Batten, S. R. N., S. M.; Turner, D. R. *Coordination Polymers: Design, Synthesis, and Application*; Royal Society of Chemistry: Cambridge, UK, 2009.
(9) *Design and Construction of Coordination Polymers*; Hong, M.-C. C., L., Ed.; John Wiley & Sons, Inc.: Hoboken, New Jersey, 2009.
(10) Li, J.-R.; Kuppler, R. J.; Zhou, H.-C. *Chemical Society reviews* **2009**, *38*, 1477.
(11) Meek, S. T.; Greathouse, J. A.; Allendorf, M. D. *Advanced Materials* **2011**, *23*, 249.
(12) Koh, H. S.; Rana, M. K.; Hwang, J.; Siegel, D. J. *Physical Chemistry Chemical Physics* **2013**, *15*, 4573.
(13) Caskey, S. R.; Wong-Foy, A. G.; Matzger, A. J. *J Am Chem Soc* **2008**, *130*, 10870.
(14) Ockwig, N. W.; Delgado-Friedrichs, O.; O'Keeffe, M.; Yaghi, O. M. *Accounts of Chemical Research* **2005**, *38*, 176.
(15) Wilmer, C. E.; Leaf, M.; Lee, C. Y.; Farha, O. K.; Hauser, B. G.; Hupp, J. T.; Snurr, R. Q. *Nat Chem* **2012**, *4*, 83.
(16) Allen, F. H. *Acta Crystallographica Section B* **2002**, *58*, 380.
(17) First, E. L.; Floudas, C. A. *Microporous and Mesoporous Materials* **2013**, *165*, 32.
(18) Haldoupis, E.; Nair, S.; Sholl, D. S. *Physical Chemistry Chemical Physics* **2011**, *13*, 5053.
(19) Lin, L.-C.; Berger, A. H.; Martin, R. L.; Kim, J.; Swisher, J. A.; Jariwala, K.; Rycroft, C. H.; Bhown, A. S.; Deem, M. W.; Haranczyk, M.; Smit, B. *Nat Mater* **2012**, *11*, 633.
(20) Wilmer, C. E.; Farha, O. K.; Bae, Y.-S.; Hupp, J. T.; Snurr, R. Q. *Energy & Environmental Science* **2012**, *5*, 9849.
(21) Haldoupis, E.; Nair, S.; Sholl, D. S. *J Am Chem Soc* **2010**, *132*, 7528.
(22) Watanabe, T.; Sholl, D. S. *Langmuir* **2012**, *28*, 14114.
(23) Düren, T.; Millange, F.; Férey, G.; Walton, K. S.; Snurr, R. Q. *The Journal of Physical Chemistry C* **2007**, *111*, 15350.
(24) Jacobsen, S. R. B. a. K. W. *Computing in Science & Engineering* **2002**, *4*, 56.
(25) Spek, A. L. *Journal of Applied Crystallography* **2003**, *36*, 7.
(26) Panella, B.; Hirscher, M.; Roth, S. *Carbon* **2005**, *43*, 2209.
(27) Pavlishchuk, S. V. K. a. V. V. *Theoretical and Experimental Chemistry* **2009**, *45*, 75.
(28) Karl J. Gross, K. R. C., Steven Barcelo, Abhi Karkamkar, Justin Purewal, Shengqian Ma, Hong-Cai Zhou, Pierre Dantzer, Kevin Ott, Tony Burrell, Troy Semeslberger, Yevheniy Pivak, Bernard Dam, and Dhanesh Chandra *Recommended Best Practices for the Characterization of Storage Properties of Hydrogen Storage Materials*, 2012.
(29) Steven S. Kaye, A. D., Omar M. Yaghi, and Jeffrey R. Long *J Am Chem Soc* **2007**, *129*, 14176.
(30) Purewal, J.; Liu, D.; Sudik, A.; Veenstra, M.; Yang, J.; Maurer, S.; Müller, U.; Siegel, D. J. *The Journal of Physical Chemistry C* **2012**, *116*, 20199.
(31) Purewal, J. J.; Liu, D.; Yang, J.; Sudik, A.; Siegel, D. J.; Maurer, S.; Müller, U. *International Journal of Hydrogen Energy* **2012**, *37*, 2723.
(32) Schnobrich, J. K.; Koh, K.; Sura, K. N.; Matzger, A. J. *Langmuir* **2010**, *26*, 5808.
(33) Kim, T. K.; Suh, M. P. *Chem Commun (Camb)* **2011**, *47*, 4258.
(34) Liqing Ma, J. M. F., Carter Abney and Wenbin Lin *Nature Chemistry* **2010**, *2*, 838.
(35) Farha, O. K.; Yazadyn, A. O.; Eryazici, I.; Malliakas, C. D.; Hauser, B. G.; Kanatzidis, M. G.; Nguyen, S. T.; Snurr, R. Q.; Hupp, J. T. *Nat Chem* **2010**, *2*, 944.

(36) Yuan, D.; Zhao, D.; Sun, D.; Zhou, H.-C. *Angewandte Chemie International Edition* **2010**, *49*, 5357.
(37) Kondo, M.; Irie, Y.; Miyazawa, M.; Kawaguchi, H.; Yasue, S.; Maeda, K.; Uchida, F. *Journal of Organometallic Chemistry* **2007**, *692*, 136.
(38) Robert P. Davies, R. L., Paul D. Lickiss, Karen Robertson, and Andrew J. P. White *Crystal Growth and Design* **2010**, *10*, 4571.
(39) Tendai Gadzikwa, O. K. F., Christos D. Malliakas, Mercouri G. Kanatzidis, Joseph T. Hupp, and SonBinh T. Nguyen *J Am Chem Soc* **2009**, *131*, 13613.
(40) Shengqian Ma, D. S., Michael Ambrogio, Jacqueline A. Fillinger, Sean Parkin, and Hong-Cai Zhou *J Am Chem Soc* **2007**, *129*, 1858.
(41) Xi-Sen Wang, S. M., Daofeng Sun, Sean Parkin, and Hong-Cai Zhou *J Am Chem Soc* **2006**, *128*, 16474.
(42) Grünker, R.; Senkovska, I.; Biedermann, R.; Klein, N.; Klausch, A.; Baburin, I. A.; Mueller, U.; Kaskel, S. *European Journal of Inorganic Chemistry* **2010**, *2010*, 3835.
(43) Schnobrich, J. K.; Lebel, O.; Cychosz, K. A.; Dailly, A.; Wong-Foy, A. G.; Matzger, A. J. *J Am Chem Soc* **2010**, *132*, 13941.
(44) Yasuhide Inokuma, T. A. a. M. F. *Nature Chemistry* **2010**, *2*, 780.
(45) Liu, T. F.; Lu, J.; Lin, X.; Cao, R. *Chem Commun (Camb)* **2010**, *46*, 8439.
(46) Yanxiong Ke, D. J. C., Daofeng Sun, and Hong-Cai Zhou *Inorganic Chemistry Communication* **2006**, *45*, 1897.
(47) Prior, T. J.; Bradshaw, D.; Teat, S. J.; Rosseinsky, M. J. *Chemical Communications* **2003**, 500.
(48) Christina A. Bauer, T. V. T., Thomas B. Settersten, Brian D. Patterson, Vincent H. Liu, Blake A. Simmons, and Mark D. Allendorf *J Am Chem Soc* **2007**, *129*, 7136.
(49) Wollmann, P.; Leistner, M.; Stoeck, U.; Grunker, R.; Gedrich, K.; Klein, N.; Throl, O.; Grahlert, W.; Senkovska, I.; Dreisbach, F.; Kaskel, S. *Chem Commun (Camb)* **2011**, *47*, 5151.
(50) Schaate, A.; Roy, P.; Godt, A.; Lippke, J.; Waltz, F.; Wiebcke, M.; Behrens, P. *Chemistry* **2011**, *17*, 6643.
(51) Omar K. Farha, C. D. M., Mercouri G. Kanatzidis, and Joseph T. Hupp *J Am Chem Soc* **2010**, *132*, 950.
(52) Han, Y.; Li, X.; Li, L.; Ma, C.; Shen, Z.; Song, Y.; You, X. *Inorganic chemistry* **2010**, *49*, 10781.
(53) Mei-Jin Lin, A. J., Nathalie Kyritsakas and Mir Wais Hosseini *CrystEngComm* **2009**, *11*, 189.
(54) Eun-Young Choi, P. M. B., Richard W. Novotny, Hyun-Tak Son, Chunhua Hu, and Wonyoung Choe *Inorganic Chemistry Communication* **2009**, *48*, 426.
(55) Andrew P. Nelson, O. K. F., Karen L. Mulfort, and Joseph T. Hupp *J Am Chem Soc* **2009**, *131*.
(56) Haneul Yim, E. K., and Jaheon Kim *Bulletin of the Korean Chemical Society* **2010**, *31*, 1041.
(57) Li, Y.; Song, D. *CrystEngComm* **2011**, *13*, 1821.
(58) Biradha, K.; Fujita, M. *Chemical Communications* **2001**, *0*, 15.
(59) Norberto Masciocchi, S. G., Valentina Colombo, Angelo Maspero, Giovanni Palmisano, Behnam Seyyedi, Carlo Lamberti, and Silvia Bordiga *J Am Chem Soc* **2010**, *132*, 7902.
(60) Park, H. J.; Cheon, Y. E.; Suh, M. P. *Chemistry* **2010**, *16*, 11662.
(61) Stergiannakos, T.; Tylianakis, E.; Klontzas, E.; Froudakis, G. E. *The Journal of Physical Chemistry C* **2010**, *114*, 16855.
(62) Shuting Wu, L. M., La-Sheng Long, Lan-Sun Zheng, and Wenbin Lin *Inorganic chemistry* **2009**, *48*, 2436.
(63) Eddaoudi, M.; Kim, J.; Rosi, N.; Vodak, D.; Wachter, J.; O'Keeffe, M.; Yaghi, O. M. *Science* **2002**, *295*, 469.
(64) Sun, D.; Ke, Y.; Mattox, T. M.; Ooro, B. A.; Zhou, H. C. *Chem Commun (Camb)* **2005**, 5447.
(65) Kenji Sumida, M. R. H., Satoshi Horike, Anne Dailly, and Jeffrey R. Long *J Am Chem Soc* **2009**, *131*, 15120.
(66) Grunker, R.; Senkovska, I.; Biedermann, R.; Klein, N.; Lohe, M. R.; Muller, P.; Kaskel, S. *Chem Commun (Camb)* **2011**, *47*, 490.

(67) Ma, L.; Jin, A.; Xie, Z.; Lin, W. *Angew Chem Int Ed Engl* **2009**, *48*, 9905.
(68) Wang, X. S.; Ma, S.; Yuan, D.; Yoon, J. W.; Hwang, Y. K.; Chang, J. S.; Wang, X.; Jorgensen, M. R.; Chen, Y. S.; Zhou, H. C. *Inorganic chemistry* **2009**, *48*, 7519.
(69) Koh, K.; Van Oosterhout, J. D.; Roy, S.; Wong-Foy, A. G.; Matzger, A. J. *Chemical Science* **2012**, *3*, 2429.
(70) Sun, D.; Collins, D. J.; Ke, Y.; Zuo, J. L.; Zhou, H. C. *Chemistry* **2006**, *12*, 3768.
(71) Song, X.; Zou, Y.; Liu, X.; Oh, M.; Lah, M. S. *New Journal of Chemistry* **2010**, *34*, 2396.
(72) Park, H. J.; Suh, M. P. *Chemistry* **2008**, *14*, 8812.
(73) Jennifer K. Schnobrich, O. L., Katie A. Cychosz, Anne Dailly, Antek G. Wong-Foy, and Adam J. Matzger *J Am Chem Soc* **2010**, *132*, 13941.
(74) Zheng, B.; Liang, Z.; Li, G.; Huo, Q.; Liu, Y. *Crystal Growth & Design* **2010**, *10*, 3405.
(75) Denysenko, D.; Grzywa, M.; Tonigold, M.; Streppel, B.; Krkljus, I.; Hirscher, M.; Mugnaioli, E.; Kolb, U.; Hanss, J.; Volkmer, D. *Chemistry - A European Journal* **2011**, *17*, 1837.
(76) Duan, J.; Bai, J.; Zheng, B.; Li, Y.; Ren, W. *Chem Commun (Camb)* **2011**, *47*, 2556.
(77) Zhao, D.; Yuan, D.; Yakovenko, A.; Zhou, H. C. *Chem Commun (Camb)* **2010**, *46*, 4196.
(78) Cheon, Y. E.; Suh, M. P. *Chem Commun (Camb)* **2009**, 2296.
(79) Park, T. H.; Cychosz, K. A.; Wong-Foy, A. G.; Dailly, A.; Matzger, A. J. *Chem Commun (Camb)* **2011**, *47*, 1452.
(80) Liu, B.; Sun, C.; Chen, G. *Chemical Engineering Science* **2011**, *66*, 3012.
(81) Tan, C.; Yang, S.; Champness, N. R.; Lin, X.; Blake, A. J.; Lewis, W.; Schroder, M. *Chem Commun (Camb)* **2011**, *47*, 4487.
(82) Chavan, S.; Vitillo, J. G.; Gianolio, D.; Zavorotynska, O.; Civalleri, B.; Jakobsen, S.; Nilsen, M. H.; Valenzano, L.; Lamberti, C.; Lillerud, K. P.; Bordiga, S. *Physical Chemistry Chemical Physics* **2012**, *14*, 1614.

5.10 Imaging the Microstructure and Hydrogen Permeation in MOF-5 Pellets

5.10.1 Introduction

Ideally, the densification of MOF powders should not degrade other aspects of performance. For example, densification should not significantly slow the transport or permeation of hydrogen within the pellet. Additionally, the microstructure of the pellet should be relatively homogeneous, and not contain large variations in density or in the distribution of 2nd phase additions intended to enhance thermal conductivity (such as ENG).

An example illustrating the first scenario is the so-called MATI ("modular adsorption tank insert") hydrogen storage system. The MATI system uses several large diameter MOF-5 pucks as the storage media. During refilling, it is desirable to fill the tank with hydrogen very quickly, typically in less than 5 minutes. The large quantity of hydrogen to be stored, combined with the desire to store it rapidly, raises concerns that use of densified media may slow the uptake process (compared to a system using powder-based media). In this case it is desirable to characterize the hydrogen penetration pathway during adsorption and desorption. In situ imaging of hydrogen permeation in MOF-5 pucks could provide such information.

To cite another example, in a large scale MOF-5/ENG pellet it is desirable to have a uniform distribution of ENG within the pellet to maximize the enhancement to thermal transport. More generally, maintaining a highly uniform density throughout the MOF compact will lead to optimal performance.

In this section several imaging analysis techniques are used to characterize densified forms of MOF-5, such as pucks and pellets. Neutron imaging radiography is used to measure the transient hydrogen distribution during adsorption and desorption. Neutron tomography reveals the three-dimensional

distribution of ENG (expanded natural graphite) particles in MOF-5/ENG pellets. Finally, the density of MOF-5 pellets are analyzed using x-ray tomography. The application of these imaging techniques provides new insights into the properties and performance of densified MOF media.

5.10.2 Method

Table 5.10(1). Sizes and compositions of pellets used in neutron imaging and micro CT experiments.

	Diameter (mm)	Height (mm)	Composition
Radiography 1	6.35	5	Pure MOF-5
Radiography 2 & tomography	26.8	10	MOF-5+10% ENG
MicroCT	31	10	Pure MOF-5

Pelletized versions of MOF-5 were examined, with and without ENG additions. Composite MOF-5/ENG pellets were synthesized by adding ENG to MOF-5 to achieve pellets having a mass fraction of 5 wt.% ENG. A SPEX 8000M Mixer/Mill was filled with the MOF-5/ENG mixture and shaken in the milling machine for 20 seconds without milling balls. The powders were loaded into a cylindrical die and pressed.

Three types of pellets were used during neutron imaging and microCT experiments; the diameter and composition of pellets summarized shown in Table 5.10(1). For pellet density characterization experiments, three varieties of pellets were formed from MOF-5 powders that were pre-filtered using meshes with hole diameters of 2mm, 1.18mm, and 0.841mm, respectively.

Beam Tube 2 (BT-2) at the NIST Center for Neutron Research (NCNR) was used for all neutron imaging measurements.

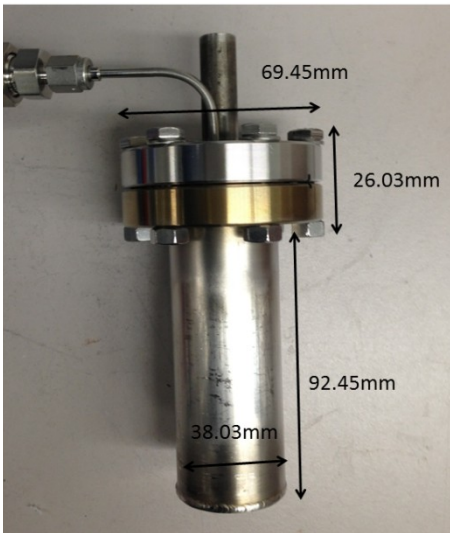

Figure 5.10(1) Vessel used in NIST neutron imaging experiment. Dimensions are shown in the graph.

In our experiment, the vessel, sample holder and sample ring are all made of stainless steel. The structure and size of the vessel are shown in Figure 5.10(1).

For MicroCT measuremtns, specimens were placed in a 34 mm diameter tube and scanned using a microCT (µCT100 Scanco Medical, Bassersdorf, Switzerland). Scan settings were: voxel size 11.4 µm, 70 kVp, 57 µA, 0.5 mm AL filter, 1250 projections / 180 degrees and integration time 500 ms.

5.10.3 Results and discussion

During the adsorption of hydrogen in a MOF-5-based storage system, hydrogen will permeate MOF-5. Neutron imaging radiography was used during the adsorption/desorption processes to measure the transient distribution of hydrogen in real time.

In the present experiment a small hydrogen storage vessel was used to represent the tank. The vessel was filled with small, randomly-oriented pellets of nominally pure MOF-5, and hydrogen adsorption/desorption cycling was performed at a temperature 77 K. The inlet/exit for hydrogen was at the top of the vessel.

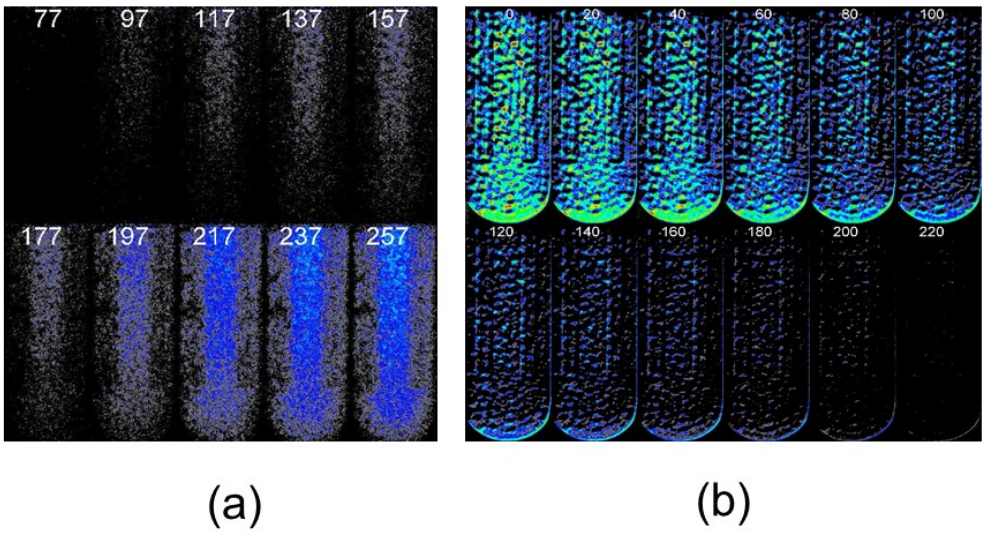

Figure 5.10(2). (a) Temporal evolution of the hydrogen density distribution in a vessel containing MOF-5 pellets during adsorption. (b) Hydrogen density distribution during desorption. Red represents high hydrogen density, while black represents low hydrogen density.

Figure 5.10(2) shows the transient hydrogen density distribution during adsorption and desorption using a color-code scheme (black = low/no hydrogen density; red = high hydrogen density). The first panel, Figure 5.10(2a) and numbered as frame 77 in a time-ordered sequence is dark. This indicates the presence of little/no hydrogen present in the vessel. As the adsorption progresses in the following frames a color change is observed in the radiography image, indicating that hydrogen is accumulating inside the sample holder.

A closer look reveals a non-uniform distribution of hydrogen in the vessel. For example, the data shows a higher concentration of hydrogen at the top of the vessel, where hydrogen enters. Also, there is a higher concentration near the center of the vessel (along the central vertical axis) than along the edges. This distribution suggests that as hydrogen enters the vessel it is first adsorbed by the pellets near the top entrance. It then spreads more slowly from the top to the bottom.

The image sequence shows the transient hydrogen density distribution during desorption. In a small region close to the bottom of the vessel a higher hydrogen density appears to be present. This is likely an artifact of small movements of the vessel during the imaging process.

The transient distribution of hydrogen in a larger MOF-5 puck was also imaged. Neutron radiography images for hydrogen uptake in such a puck are shown in Figure 5.10(3). Similarly, black represents low hydrogen density, and red represents high density. At low pressure (0.2-0.3 bar) Fig. 5.10(3) shows that only a small amount of hydrogen is adsorbed. When the pressure was increased to 3 bar, the color intensity of the radiography image has increased to light blue, indicating increasing adsorbed hydrogen density. As the pressure reaches 9.2 bar, the hydrogen density increases further. In all frames the hydrogen density appears to be uniform across the puck, indicating fast diffusion within the solid.

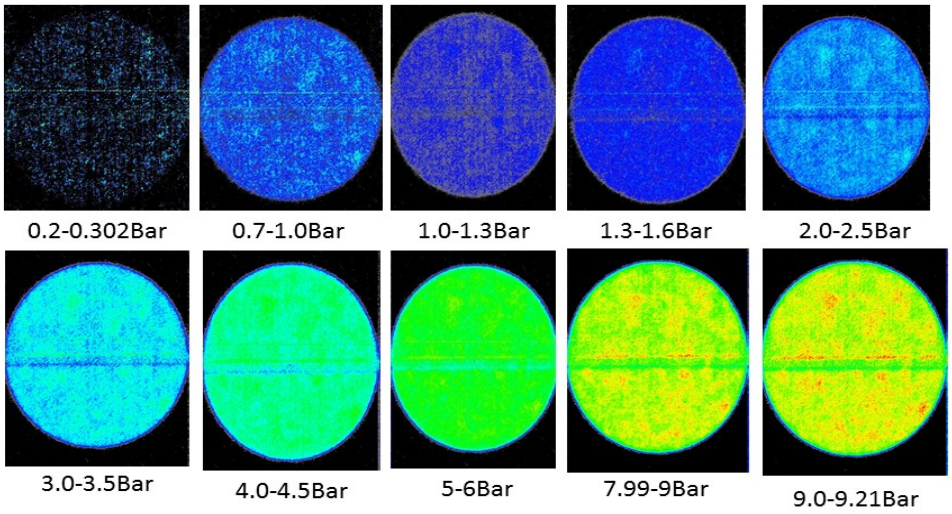

Figure 5.10(3). Transient hydrogen density distribution of a MOF-5 puck. Red stands for higher density, and black stands for lower density.

To quantify the permeation process in more detail, Figure 5.10(3) shows the hydrogen density as a function of pressure and distance to the center of the pellet. The x-axis represents the distance from pellet center, and the y-axis is the calculated adsorbed hydrogen density averaged over a given ring. Data from images collected at different pressures are included in the graph. It is clear that the average hydrogen density increases as the hydrogen pressure in the sample holder increases. At any given pressure the hydrogen density curve is almost flat across the pellet from center to rim, indicating uniform adsorption within the pellet. This behavior is consistent with the uniformly-colored pellet images shown in Figure 5.10(2).

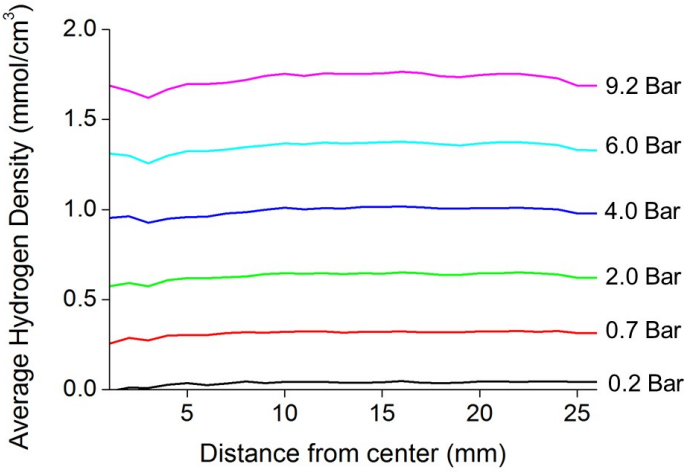

Figure 5.10(3). Average adsorbed hydrogen density as a function of hydrogen gas pressure and radial distance from pellet center.

Figure 5.10(4) shows a cross sectional image for a MOF-5 pellet including 10% ENG obtained from neutron imaging tomography. The color bar below the image shows the correspondence between color and attenuation coefficient. ENG particle has an attenuation coefficient of 0.612 cm^{-1}, which is represented by blue in the image. It can be seen that ENG particles are distributed across the pellet cross section, forming network inside the pellet. This network can improve the pellet's thermal conductivity, as demonstrated by previous studies.

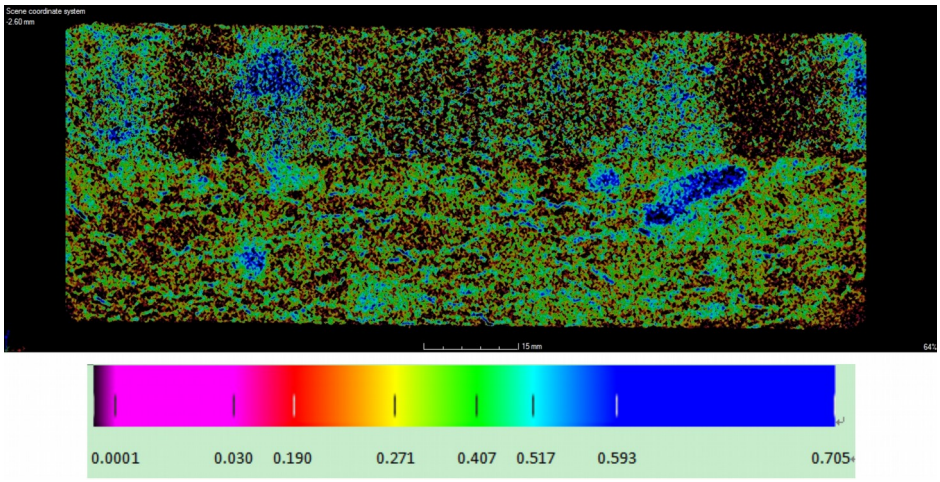

Figure 5.10(4). Tomography of MOF-5/ENG pellet using neutron imaging technique. The color bar shows the attenuation coefficient.

The hydrogen storage media in the MATI system consists of densified "pucks" of MOF-5. These pucks have been compacted to a nominal density of 0.4 g/cc, which is 2 to 3 times the density of tapped powder. We expect that the best performance for these systems will be achieved when the density variation within the pucks is small. The spatial density distribution can be measured using x-ray computed tomography (microCT).

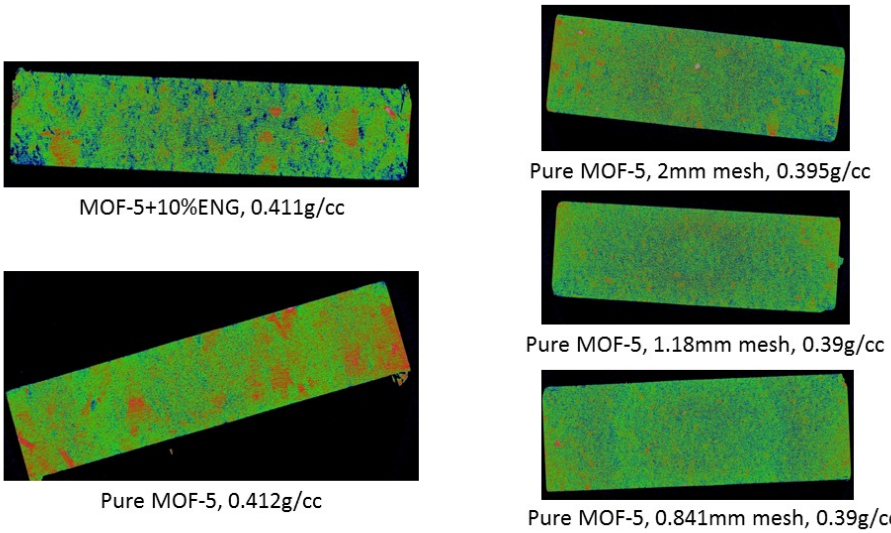

Figure 5.10(5). MicroCT tomography images for a MOF-5/ENG pellet, and for several pure MOF-5 pellets fabricated using powders filtered with different mesh sizes. Blue represents regions of low density, while red represents high density.

Figure 5.10(5) shows several microCT tomography cross-sectional images of MOF-5 pellets having different compositions and pre-treatment conditions. The upper left image corresponds to a MOF-5 pellet containing 10 wt.% ENG. Based on the imaging analysis, this pellet has a relatively large density variation, as evidenced by the presence of regions with either high (red) or low (blue) density. The lower left image of a pellet made from pure MOF-5 also shows large density variation.

To minimize these density variations, a pre-treatment process in which the powders are filtered using meshes of different pore diameter was explored. The resulting tomography images for the pellets made from filtered powders are shown on the right of Figure 5.10(5). MOF-5 powders for these pellets were filtered with meshes having diameters of 2mm, 1.18mm and 0.841mm. No obvious extreme density regions are observed in the filtered systems. Table 5.10(2) summarizes the standard deviations of the densities of MOF-5 pellets synthesized with and without powder filtering. The standard deviation of the pellet synthesized from the smallest aperture mesh (0.841mm) is almost 1/3 of the pellet for which no pre-meshing was performed.

Table 5.10(2). Standard deviation in the density of pellets with different filtering pre-treatment. The sizes listed in the left column refer to the aperture size of the mesh used to filter MOF-5 powders before pressing into pellets.

Pellet	Std (g/cc)
No mesh	0.0271
2mm	0.0246
1.18mm	0.0114
0.841mm	0.0107

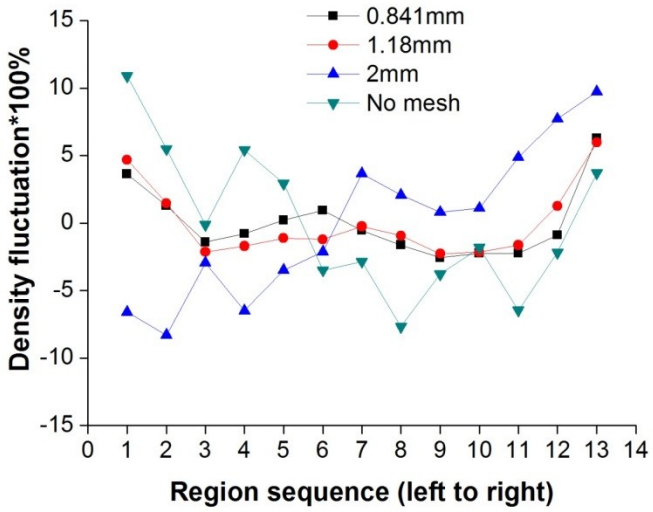

Figure 5.10(6). Density fluctuation percentage across the cross sections of MOF-5 pellets using different pre-meshing treatments.

The density variation across the cross section of MOF-5 pellets is plotted in Figure 5.10(6). Here the rectangular sample cross section was divided into 13 smaller regions from left to right, and the average density of each region, defined as ρ_n, was calculated. This density was then compared to the average density of the entire cross section, ρ_n. Density fluctuations, F, are plotted along the y-axis. If the pellet is very uniform, then ρ_n in each region should be very close to ρ_n, which in turn gives F values

very close to 0. Density fluctuations in the pellet with 0.841mm and 1.18mm pre-treatment meshing are small, within 2%, except for the two regions at the rim. This indicates that making pellet with meshed MOF-5 powders can improve the density uniformity.

5.10.4 Conclusion

In this study we introduced several imaging analysis method to characterize densified versions of MOF-5, such as pucks and pellets. Neutron imaging radiography is used to characterize the transient hydrogen distribution during adsorption and desorption. In these experiments two types of MOF-5 samples were examined: small MOF-5 pellets, and larger MOF-5 pucks. The adsorbed hydrogen density can be monitored both qualitatively and quantitatively. Neutron tomography was used to characterize the ENG network pellets containing 2nd phase additions. Finally, microCT was used to analyze density variations within MOF-5 pellets synthesized using different compositions and pre-treatment conditions. Pellet made from filtered powders exhibited the lowest density variations. The successful application of those imaging analysis methods points out potential ways to improve the performance of systems based on densified MOF media.

6.0 OEM Assessment/Perspective

Ford believes that hydrogen-powered fuel cell vehicles may be an important long-term solution for improving energy security and diversifying our energy sources, as well as for reducing greenhouse gas emissions, if hydrogen fuel emerges as a viable low-carbon energy carrier. Ford has been working on fuel cell vehicle development and technology demonstration for more than a decade. From 2005 to 2009, we participated in a technology demonstration program partially funded by the U.S. Department of Energy (DOE), as well as in other government-supported demonstration programs in Canada and Europe. A total of 30 Ford Focus FCVs were in operation in these programs. These vehicles were tested to demonstrate technical feasibility, performance durability and reliability. For example, they were subjected to driving tests at sub-zero temperatures and high altitudes to prove vehicle performance under a range of customer-encountered driving environments. By 2009, these vehicles had accumulated more than a million driving miles without significant technical problems, thereby demonstrating the reliability of fuel cell powertrain systems in real-world driving conditions. The data collected from this fleet have been critical to the further development of Ford's fuel cell technology. Based on the knowledge gained in this first generation of fuel cell technology, we have completed development and laboratory validation of additional generations of fuel cell technologies.

Even with the advances we have made in hydrogen technology over the past 10 years, we still have challenges to overcome before hydrogen FCVs can compete in the market with current vehicle technology. Ford recognizes on-board hydrogen storage as one of the critical challenges to the commercial viability of hydrogen FCVs. The previous demonstration vehicles used compressed gaseous hydrogen storage at 350 bar and current vehicles have improved the storage by increasing the pressure to 700 bar. However, the high-pressure tanks required for this storage use expensive carbon fiber for reinforcement. In addition, the current tanks are large and difficult to package in a vehicle without unacceptable losses in passenger or cargo space. Therefore, we are interested in research on materials-based hydrogen storage technology especially at lower operating pressures, which may ultimately achieve higher energy density and lower cost. The results of the HSECoE allow us to have a better perspective of the system engineering challenge with each material-based storage technology.

As extensively analyzed in the HSECoE, each material-based storage system has their respective advantages and disadvantages. Complex metal hydrides have the potential for improved volumetric, although this was not shown with the HSECoE sodium alanate system. Further, the HSECoE system had a poor gravimetric density. Beyond these parameters, the kinetics and reversibility of complex metal hydrides can be a concern. Chemical hydrogen is an interesting storage technology since it uses a liquid

fuel feedstock which can be desirable as a similar media replacement for the current liquid fuel infrastructure The system developed within the HSECoE based on ammonia borane had attractive gravimetric and volumetric properties although the regeneration and fuel cost remain barriers for this material-based technology.

Adsorbents seem to have properties that are the most competitive with 700 bar compressed storage, even though still not able to achieve the DOE USDRIVE targets. The HSECoE adsorbent system with MOF-5 was able to provide gravimetric and volumetric densities approaching a 700 bar compressed system, but although at 7x less in operating pressure. The reduced operating pressure could easily provide a ripple effect towards not only lowering the cost of the on-board system, but also lowering the cost of H_2 delivery infrastructure. In fact, the cost of the system has been estimated to have a slight advantage over a 700 bar compressed system at high economies of scale.

The challenges with adsorbents relate to the need for cryogenic operating temperatures, such as the uncertainty of safety testing, insulation robustness, and liquid hydrogen pathway. Further opportunities for integration of these material-based storage systems into a complete vehicle could provide additional benefits (or offsets for certain parameters) such as the potential thermal sink for the fuel cell propulsion system which has heat rejection limitations. Overall, the HSECoE has made progress with these material-based system although not enough in the near term to displace compressed 700 bar. But the gap has been reduced and there is still significant potential for improvement.

7.0 Summary: Lessons learned and potential next steps

7.1 Scaled-up production of MOFs

The work performed in this project demonstrated that it is possible to produce sufficient quantities of an adsorbent material matching or exceeding MSC-30/AX-21 in terms of hydrogen storage capacity. Scaled MOF-5 synthesis trials at BASF were carried out in a 1000 L-scale reactor to produce several kg of MOF-5 per batch. Initially, the kg-scale MOF-5 batches showed deviations compared to laboratory-scale MOF-5 batches. MOF-5 crystals were considerably smaller for the kg-scale batches. This affected the MOF's filterability and resulted in long filtration times during which MOF-5 degraded. Ultimately, three scaled synthesis trials (200 L) were carried out to produce about 10 kg MOF-5 powder (denoted as the 200 L batches). These 200 L batches of MOF-5 had surface areas and hydrogen storage capacities equal to, or even slightly higher than, the lab-scale MOF-5 batches.

While there are a number of commercially available MOFs, most of these materials are developed as drop-in alternatives for zeolites in mainstream applications like separations and heterogeneous catalysis. Examples are ZIF-8, Al-MIL-88a, and UiO-66, all of which have exceptional thermal and chemical robustness, but do not have sufficient surface area or pore volumes for on-board H_2 storage. Of the MOFs available in more than lab-scale quantities, only two (MOF-5, MOF-177) have the potential to outperform the benchmark activated carbon MSC-30.

We demonstrated that MOF-5 outperforms MSC-30 at the system level in both gravimetric density and in volumetric density. For a powder-based Type III system operating at $P_{max} = 60$ bar and $T = \left(40\,\mathrm{K} - 120\,\mathrm{K}\right)$ is 5.5 wt. % for MSC-30 versus 7.3 wt. % for MOF-5, the projected volumetric densities for the systems are: 27 g H_2/L (MSC-30) and 31 g H_2/L (MOF-5). MOF-5 also holds an advantage over MSC-30 in terms of densification; MOF-5 can be compacted without the use of binders, whereas MSC-30 cannot. Use of binders lowers the surface area and hydrogen storage capacity. Furthermore, MOF-5 possesses a balance of both gravimetric and volumetric storage density. This is important from a vehicle packaging viewpoint, because driving range is more sensitive to the volumetric storage capacity of an adsorbent material than to the gravimetric capacity.

7.2 Adsorbent packing efficiency

During the course of the project, we explored a number of processes for efficiently packing an adsorbent powder within the fixed internal volume of a high-pressure tank. Efficiency, as defined here, denotes maximizing the fraction of internal tank volume occupied by the adsorbent micropore volume (the active region where H_2 density is enhanced), and minimizing the non-active free space.

We found that simple mechanical compaction was effective at forming desolvated MOF-5 powder into high-density pellets or puck-shaped monoliths. By this method alone, we can increase volumetric H_2 storage at 77 K, 100 bar in MOF-5 from 36 g/L to 45 g/L. The upper limit for H_2 storage in the crystal pore structure of MOF-5 is calculated at 54 g/L (at 35 bar). Achieving this value would have required large, defect-free MOF-5 crystals, which was out of the scope of work for this project. We found that compacting MOF-5 beyond a density of roughly 0.4 g/cm^3 did not produce any additional gains in volumetric storage, due to the loss of pore volume.

While most compaction studies were performed under inert atmosphere in a glovebox using a small pellet press, it was relatively easy to scale-up compaction to 22 g pucks using a custom-built punch and die set. Compacting MOF-5 yields solid blocks of material which are robust enough to handle, thereby simplifying packaging, maximizing volumetric storage capacity and (as described below) improving heat transfer properties.

7.3 Hydrogen permeation through compacted MOF-5 powder

Rapid refueling (<5 min) is a key feature of hydrogen fuel cell vehicles. It was important to characterize hydrogen transport kinetics through a compacted MOF-5 adsorbent bed, and to use those properties to simulate refueling times on a high-density MOF-5 adsorbent system.

We built a H_2 permeation test stand and measured the H_2 Darcy permeability in MOF-5 samples in details. The experimental results showed that the H_2 Darcy permeability exponentially decreases with increasing of the MOF-5 packing density. So increasing the packing density of MOF-5 will largely reduce H_2 permeation because external porous channels in MOF-5 for H_2 convection transport are reduced by increasing its packing density. Generally, MOF-5 crystal structure will be destroyed if MOF-5 is packed over 0.5 g/cm^3. If the packing density is lower than 0.3 g/cm^3 the packed MOF-5 pellets cannot firmly keep their shape in the vehicle storage tank. So the packing density range from 0.3 g/cm^{-3} to 0.5 g/cm^{-3} leads to the H_2 permeation from 0.045 to 0.0006 Darcy about100 times difference at 77K. The H_2 permeation of MOF-5 can be slightly improved by adding 5% to 10% ENG at the certain packing density.

7.4 Heat transport in compacted MOF-5 adsorbent systems

Even when using recirculating 80 K hydrogen gas to convectively cool the adsorbent bed, system-level simulation indicate that an effective thermal conductivity of 1 W/m·K is required to meet a 5 min cool-down/refueling time. Unfortunately, porous adsorbents in general, and MOF-5 in particular, are effective insulators. We explored options for increasing the thermal conductivity of MOF-5, at the material level to 1 W/m*K. Further, we demonstrated methods for effectively interfacing the MOF-5 storage media to internal heat exchangers and temperature sensors.

We found that mechanically compacting a blend of MOF-5 and a graphitized, conductive carbon additive (ENG, GPX) yields a monolith with significantly enhanced heat transfer properties. Since graphite has anisotropic heat transfer properties, we noted the textural properties of the carbon additive can affect the properties of the MOF-5/carbon composite.

- Thermal conductivity increases with pellet density due to an improvement interfacial contact between particles
- Expanded natural graphite (ENG), as an additive, is excellent for directional heat conduction within MOF-5 pellets and monoliths. When incorporated into a layered alternating MOF|ENG|MOF compacted structure, it offers about twenty-fold improvement in heat conduction in the ENG planar direction. This design can be scaled up, and combined with an internal aluminum pin matrix. This provides an example of how a MOF-5 monolith can be effectively interfaced with a heat exchanger to minimize contact resistance.
- The thermal conductivity increases with ENG content in both axial and radial directions, with the most significant increases for 5% ENG and 10% ENG. Addition of 1% ENG did not appear to provide a significant improvement in thermal conduction
- The maximum thermal conductivity was achieved for a 0.7 g/cm^3 density and 10 wt.% ENG loading, and was close to 1 W/m·K.
- As expected, there is significant directional affect for ENG-containing pellets. Heat conduction is higher in the radial compared to the axial direction due to alignment of the rod-like ENG particles perpendicular to axial compaction direction.
- GPX (graphene-aggregate carbon powder) is good for isotropic heat conduction in a MOF-5 pellets, and coats individual MOF-5 particles with a conductive layer. Homogeneity is limited by the particle sizes of MOF-5.
- Additions of ENG and GPX lower (slightly) the specific micropore volume, surface area, and hydrogen adsorption properties of the MOF-5/carbon composite relative to neat MOF-5. The effect is identical for both ENG and GPX, and depends only on the carbon loading and pellet density. It originates simply from that fact that the conductive carbons contribute mass to the MOF5/carbon composite, but have a negligible surface area and pore volume.

7.5 Robustness of MOF-5

Carboxylate-based MOFs such as MOF-5 are known to be thermodynamically unstable in humid environments. Water attacks the Zn-O bonds that support the pore structure of MOF-5, degrading the crystallinity, pore volume and surface area. We set out understand in detail the kinetic stability of MOF-5 in humid environments. We measured the MOF-5 degradation rate as a function of exposure duration, exposure level (i.e., the relative humidity) and pellet density.

After measuring water adsorption isotherms for MOF-5, we noted that it is a Type 5 isotherm with the adsorption rising steeply at about 50% relative humidity. Below the 50% RH threshold only minor degradation is observed for exposure times up to several hours, indicating that MOF-5 is more stable than commonly thought under moderately humid conditions. In contrast, degradation occurs in a matter of minutes at higher humidity. Spectroscopic characterization suggests that molecular and/or dissociated water is inserted into the skeletal framework after long exposure times. Densification into pellets was observed to slow the degradation of MOF-5 by reducing the permeation of water through the monolith, and may present an opportunity to extend the stability window of some MOFs.

Our DFT calculations indicated that the thermodynamics of water insertion into MOF-5 is coverage dependent: Insertion becomes thermodynamically favorable only when a critical number of water molecules (4 or more) are co-adsorbed as relatively compact clusters on the same structural building unit of the MOF. This observation is consistent with our experimental measurements, which show that hydrolysis is slow at low water coverages.

7.6 High-throughput screening for promising MOFs

The efforts described in this report have largely focused on a MOF-5-based storage system. This MOF was selected for demonstration based on the best-available data at the time. Nevertheless, literally thousands of MOFs are known, yet relatively few have had their hydrogen storage properties measured. For this reason there is a strong possibility that higher-performing MOFs may exist. The only difficulty is identifying them.

Toward this goal, we have demonstrated an efficient, automated approach for screening the 600 000+ entry Cambridge Structure Database for porous, metal−organic compounds (i.e., MOFs) useful for hydrogen storage. Our approach employs routines for virtual solvent removal, and leverages the established empirical correlation between excess hydrogen uptake and surface area. Consequently, the method is highly efficient since it does not require the evaluation of interatomic potentials or expensive isotherm simulations. Excluding compounds with disorder or missing atoms, we have assembled a database of more than 4000 solvent-free structures for which we assess porosity, surface area, and total theoretical H2 uptake (gravimetric and volumetric). Because our approach relies only on known compounds, it may present advantages to those based on hypothetical compounds that may prove difficult to synthesize.

Analysis of the relationship between MOF mass density and surface area reveals that density decreases with increasing surface area, indicating that a trade-off exists between gravimetric and volumetric H2 storage. The concave downward shape of the volumetric vs. gravimetric uptake distribution further supports this conclusion: volumetric H2 density reaches a maximum for surface areas in the range of 3100−4800 m2/g, but then decreases for those compounds having larger surface areas. The data suggests that development of new MOFs should not exclusively target high surface areas, but instead focus on achieving moderate mass densities (>0.5 g/cm3) in conjunction with high surface areas.

Our screening identified several compounds with promising properties. While some of these have had their experimental H2 uptake tested, many appear to have undergone no testing whatsoever. Of these, SNU-21 emerges at the highest- performing candidate, achieving densities of 12.4 wt % and 71.4 g/L. However, experimental measurements on this compound have not achieved these high levels of performance, presumably due to incomplete solvent removal. In addition, the compounds having CSD identifiers (common names) DIDDOK, ENITAX (IMP-9), and LURGEL (TO-MOF) are highlighted as “targets of opportunity” given their high H2 densities (10.0−11.4 wt % and ∼60 g/L) and absence of uptake measurements.

Looking to the future, we suggest that research efforts targeting MOFs for gas storage emphasize the challenges of structure stability/pore collapse and solvent removal. Many promising compounds in our data set exhibit these deficiencies, and we believe these issues warrant additional effort to quantify the factors that determine whether a given compound can be realized in a robust, solvent-free form.

7.7 Next steps

This project was the first to delve deeply into the engineering properties of the prototype adsorbent MOF-5 (or for that matter, any MOF). Although many useful insights were provided by this effort (summarized above), several challenges remain before an adsorbent-based hydrogen storage system can be viable for automotive applications. These challenges span from the atomic-scale properties of the adsorbent itself to the design and operation of the entire storage device. As the focus of this project was on the storage material, here we summarize key challenges related to developing a suitable hydrogen adsorbent.

An unfortunate characteristic of adsorptive hydrogen storage is that high gravimetric densities typically come at the expense of volumetric density. Although MOF-5 is one of the few MOF compounds that exhibits high gravimetric and volumetric densities simultaneously, the extremely large number of MOFs suggests that superior compounds likely exist. Indeed, this possibility was demonstrated using the high-throughput screening reported in Goldsmith *et al*., where a small number of known, but overlooked, MOFs were projected to surpass the H_2 capacity of MOF-5. A logical next step is to synthesize and test these candidate materials, and to expand the search algorithm to identify others.

This effort is now well underway through a new joint UM/Ford project sponsored by DOE. One challenge to be addressed in this project is realizing a given MOF target in pristine form. To achieve high H_2 capacities, the promising MOFs identified by Goldsmith *et al.* must be synthesized without pore collapse and without the presence of guest molecules within the pore space. The factors that control whether a given MOF structure can be synthesized in this manner are poorly understood. Revealing these factors, and developing activation techniques that can minimize their impact, is a highly important research direction.

In addition to identifying known compounds with the potential to exhibit high hydrogen capacities, an important parallel pathway is the synthesis of totally new compounds. Of course these compounds should demonstrate an appropriate combination of high density and moderately high surface areas, so as to maximize volumetric and gravimetric uptake simultaneously. Beyond this, the enthalpy of adsorption for H_2 on MOFs needs to be increased. This would facilitate the development of storage systems that operate at near room temperature, and likely lower the cost of the on-board system and the forecourt refueling apparatus. These cost benefits would accrue from the minimization of refrigeration and insulation sub-components, which are needed to maintain the low operating temperature (77 K) of a MOF-based storage system. To achieve ambient temperature operation a factor of 3 to 4 increase (15-20 kJ/mol H_2) in the adsorption enthalpy relative to that for MOF-5 (~5 kJ/mol H_2) is needed. Such an increase will most likely require the development of MOFs with special binding sites capable of strong interactions with H_2.

At a larger scale, additional effort is needed to optimize the processing of MOF powders into monoliths or pellets that are dense and robust. The goal is to generate shaped bodies having densities that approach the single crystal density of the MOF. (Although very large single crystals of silicon are routinely manufactured for semiconductor devices, the synthesis of kilogram quantities of MOFs with a single-crystal microstructure appears to be impractical at present.) Maximizing this monolith density will in turn maximize the volumetric density of hydrogen in the storage system. While the present study showed that MOF-5 could be densified without the use of binders, we anticipate that not all MOFs will behave similarly. If binder compounds are needed, they will likely lower volumetric and gravimetric performance. It is necessary to balance these penalties with the desire to have monoliths that are easy to handle and which can survive large-scale manufacturing processes. An additional trade-off in need of optimization is the tendency for pore collapse – i.e. loss of porosity, surface area, and therefore H_2 uptake capacity – at higher densification levels. The present study demonstrated empirically that MOF-5 powders could be processed to ~70-80% of the single crystal density before the onset of plastic deformation and pore collapse. Processing strategies for maximizing density should be further explored.

8.0 Bibliography

[Beckner, 2015] Beckner, M.; Dailly, A. *Applied Energy* **2015**, *149*, 69–74

[Dailly, 2015] Shen, J.; Sulkowski, J.; Beckner, M.; Dailly, A. *Microporous Mesoporous Materials* **2015** 212, 80-90.

[Goldsmith, 2013] Goldsmith, J.; Wong-Foy, A.; Cafarella, M.; Siegel, D. *Chem. Mater.* **2013**, *25*, 3373−3382

[Hirscher, 2014] Oh, H.; Lupu, D.; Blanita, G.; Hirscher, M. *RSC Adv.* **2014**, *4*, 2648

[Kaye, 2007] Kaye, S; Dailly, A.; Yaghi, O.; Long, *J. Am. Chem. Soc.* **2007**, *129*, 14176-14177

[Lupu 2013] Ardelean, O.; Blanita, G.; Borodi, G.; Lazar, M.; Misan, I.; Coldea, I.; Lupu, D. Int. J. Hydrogen Energy, 2013, 38:17, 7046-7055

[Matsunaga, 2002] Matsunaga, N; Hori, M; Nagashima, A *Heat Transfer—Asian Research*, **2002**, *31*, 182-193

[Parilla, 2015] Parilla, P.; Gross, K.; Hurst, K.; Gennett, T. *Recommended Volumetric Capacity Definitions and Protocols for Accurate, Standardized and Unambiguous Metrics for Hydrogen Storage Materials*

[Purewal, 2012] Purewal, J.; Liu, D.; Sudik, A.; Veenstra, M.; Yang, J.; Maurer, S.; Muuler, U.; Siegel, D. *J. Phys. Chem. C* **2012**, *116*, 20199−20212

[Richard, 2009 Adsorption] Richard, M.-A.; Benard, P.; Chahine, R. Adsorption 2009, 15, 43–51

[Richard, 2009 AIChE] Richard, M.-A.; Cossement, D.; Chandonia, P.-A.; Chahine, R.; Mori, D.; Katsuhiko, H. AIChE Journal 2009, 55, 2985-2996

[Rouquerol, 1999] Rouquerol, J., Rouquerol, F., Llewellyn, P., Maurin, G. and Sing, K.S., 2013. *Adsorption by powders and porous solids: principles, methodology and applications*. Academic press.

[Snurr, 2007] Duren, T.; Millange, F.; Ferey, G.; Walton, K.; Snurr, R. *J. Phys. Chem. C* **2007**, 111, 15350-15356

[Voskuilen, 2012] Voskuilen, T.; Pourpoint, T.; Dailly, A. *Adsorption* **2012,** *18*, 239–249.

[Webb, 2001] Webb, P. *Volume and Density Determinations for Particle Technologists*, Micromeritics Instrument Corp., 2/16/01

[Xu, 2013] Xu, C.; Yang, J.; Veenstra, M.; Sudik, A.; Purewal, J.; Ming, Y.; Hardy, B.; Warner, J.; Maurer, S.; Muller, U.; Siegel, D. *Int. J. Hydrogen Energy*, **2013**, *38*, 3268-3274

[Yildirim, 2013] Peng, Y.; Krunglevicuite, V.;Eryazici, I.; Hupp, J.; Farha, O.; Yildirim, T. *J. Am. Chem. Soc.* **2013**, *135*, 11887−11894

[Zhang 2010] Hu, H.; Zhang, L. *Phys. Rev. B* **2010**, *81*, 174103.

[Zhou 2007] Zhou, W.; Wu, H.; Hartman, M.; Yildirim, T. J. Phys. Chem. C 2007, 111, 16131-16137

9.0 Project Publications, Presentations, and Patents

Papers

1. J. Yang, A. Sudik, C. Wolverton, and D. J. Siegel, *High capacity hydrogen storage materials: Attributes for automotive applications and techniques for materials discovery*, Chemical Society Reviews 39, 656 (2010).
2. J. Purewal, D. Liu, J. Yang, A. Sudik, D. J. Siegel, S. Maurer, and U. Muller, *Increased volumetric hydrogen uptake in MOF-5 by powder densification.* International Journal of Hydrogen Energy 37, 2723 (2012).
3. D. Liu, J. J. Purewal, J. Yang, A. Sudik, S. Maurer, U. Mueller, J. Ni, and D. J. Siegel, *MOF-5 Composites Exhibiting Improved Thermal Conductivity*. International Journal of Hydrogen Energy 37, 6109 (2012).
4. J. Purewal, D. Liu, A. Sudik, M. Veenstra, J. Yang, S. Maurer, U. Muller, and D. J. Siegel, *Improved Hydrogen Storage and Thermal Conductivity in High-Density MOF-5 Composites*, Journal of Physical Chemistry C, 116, 20199 (2012) DOI:10.1021/jp305524f
5. J. Pasini, B. Van Hassel, D. Mosher, and M. Veenstra, System Modeling Methodology and Analyses for Materials-based Hydrogen Storage, Int. J. Hydrogen Energy vol. 37, pp. 2874-2884, 2012.
6. C. Xu, J. Yang, M. Veenstra, A. Sudik, J. J. Purewal, Y. Ming, B. J. Hardy, J. Warner, S. Maurer, U. Mueller, and D. J. Siegel, *Hydrogen Permeation and Diffusion in Densified MOF-5 Pellets*, International Journal of Hydrogen Energy, 38, 3268 (2013). DOI:10.1016/j.ijhydene.2012.12.096
7. M. Thornton, A. Brooker, J. Cosgrove, M. Veenstra, and J.M. Pasini. Development of a Vehicle-Level Simulation Model for Evaluating the Trade-off between Various Advanced On-board Hydrogen Storage Technologies for Fuel Cell Vehicles. SAE 2012-01-1227, 2012.
8. J. Goldsmith, A. G. Wong-Foy, M. J. Cafarella, and D. J. Siegel, *Theoretical Limits of Hydrogen Storage in Metal-Organic Frameworks: Opportunities and Challenges*, Chemistry of Materials 25, 3373 (2013). DOI: 10.1021/cm401978e
9. Y. Ming, J. Purewal, D. Liu, A. Sudik, C. Xu, J. Yang, M. Veenstra, K. Rodes, R. Soltis, J. Warner, M. Gaab, U. Muller, and D. J. Siegel, *Thermophysical Properties of MOF-5 Powders*, Microporous and Mesoporous Materials 185, 235 (2014). DOI: 10.1016/j.micromeso.2013.11.015
10. Y. Ming, H. Chi, R. Blaser, C. Xu, J. Yang, M. Veenstra, M. Gaab, U. Müller, C. Uher, D. J. Siegel, *Anisotropic Thermal Transport in MOF-5 Composites,* International Journal of Heat and Mass Transfer, 82, 250 (2015). DOI: 10.1016/j.ijheatmasstransfer.2014.11.053
11. Y. Ming, J. Purewal, J. Yang, C. Xu, R. Soltis, J. Warner M. Veenstra, M. Gaab, U. Muller, and D. J. Siegel, *Kinetic Stability of MOF-5 in Humid Environments: Impact of Powder Densification, Humidity Level, and Exposure Time,* Langmuir, 2015, *31* (17), pp 4988–4995, DOI: 10.1021/acs.langmuir.5b00833
12. T. Semelsberger, M. Veenstra, and C. Dixon, *Room temperature thermal conductivity measurements of neat MOF-5 compacts with high pressure hydrogen and helium*, International Journal of Hydrogen Energy, 41, 4690 (2015). http://dx.doi.org/10.1016/j.ijhydene.2015.12.059
13. Y. Ming, J. Purewal, J. Yang, C. Xu, A. Drews, M. Veenstra, M. Gaab, U. Müller, and D. J. Siegel, *Stability of MOF-5 in a Hydrogen Gas Environment Containing Fueling Station*

Impurities, International Journal of Hydrogen Energy, 41, 9374 (2016). http://dx.doi.org/10.1016/j.ijhydene.2016.03.155

14. Y. Ming, *Robustness and Thermophysical Properties of MOF-5:A Prototypical Hydrogen Storage Material*, PhD Dissertation, University of Michigan, 2015.
15. Y. Ming and D. J. Siegel, *Water Adsorption and Insertion in MOF-5*, *Langmuir*, in revision.

Presentations

1. J. J. Purewal, Hydrogen Storage by MOR-5 Monoliths and Composites: Materials Processing, Thermal Conductivity, and Neutron Imagining, 2011 Materials Research Society Meeting, San Francisco CA, April 2011.
2. A. Sudik, Hydrogen Storage Materials Research & Development, Invited Presentation, University of California – Los Angeles Materials Science & Engineering Department Symposium, Los Angeles CA, May 2011.
3. Justin Purewal, Dongan Liu, Andrea Sudik, Stefan Maurer, Ulrich Mueller, Don Siegel. "Improved Hydrogen Storage and Thermal Conductivity in High-density MOF-5 Composites". 2012 MRS Spring Meeting & Exhibit- Symposium P: Advanced Materials and Nanoframeworks for Hydrogen Storage and Carbon Capture, April 2012, San Francisco, California.
4. D. J. Siegel, "Development of an Advanced Hydrogen Storage System Based on Adsorbent Media, 2012 World Hydrogen Energy Conference, June 2012, Toronto, Canada.
5. D. J. Siegel, U.S. Dept. of Energy, Adsorbent Hydrogen Storage Workshop, Nov. 27, 2012, Washington, D.C.
6. D. J. Siegel, "Adsorption-Based Hydrogen Storage System: An Overview". DOE Hydrogen Storage Materials Requirement U.S. Department of Energy Webinar, June 2013.
7. M. Veenstra. "Onboard Automotive Targets: An OEM Perspective," DOE Materials-based Hydrogen Storage Summit, NREL, January 2015.
8. D. Siegel. "Engineering and Adsorbent-based Hydrogen Storage System: What Have We Learned?," DOE Materials-based Hydrogen Storage Summit, NREL, January 2015.

Patents

R. Blaser, M. Veenstra, and C. Xu, "Adsorbent material with anisotropic layering," US Patent 9 006 137, April 14, 2015.